Technische Universität Dortmund
Experimentelle Physik 5

Dissertation zur Erlangung des akademischen Grades Dr. rer. nat.

Scintillating Fibre and Silicon Photomultiplier Studies for the LHCb Upgrade

vorgelegt von
Mirco Deckenhoff

Dortmund, im Dezember 2015

Gutachter:
Prof. Dr. Bernhard Spaan
Priv.-Doz. Dr. Reiner Klingenberg

Vorsitzender der Prüfungskommission:
Prof. Dr. Heinz Hövel

Vertreterin der wissenschaftlichen MitarbeiterInnen:
Dr. Bärbel Siegmann

Datum der mündlichen Prüfung:
23. Februar 2016

Abstract

The LHCb experiment will perform a major detector upgrade during the Long Shutdown 2 of the LHC, scheduled in 2019 to 2020. The main tracking system is intended to be replaced by the LHCb SciFi Tracker, whose main components are scintillating fibres and silicon photomultipliers. Studies presented in this thesis have contributed to assess the viability of this technology under the harsh operational conditions of the upgraded LHCb detector.

A simulation of scintillating fibres has been developed based on the GEANT4 toolkit. It takes into account the fibre characteristics which have been obtained from measurements by the LHCb SciFi Tracker group and from literature. Simulation studies of several properties such as light yield of particle hits in the SciFi Tracker and radiation effects are presented. The developed simulation program is now being used by several groups of the LHCb collaboration as a tool in research and development as well as to infer parametrisations for the overall detector simulation. Besides the fibre simulation, a measurement of the scintillating fibres' time response is described.

Characterisation measurements of silicon photomultipliers have been conducted to determine the dependence of several parameters on bias voltage and temperature. In particular, the radiation hardness has been tested by irradiations with protons and in long-term studies *in situ* in the LHCb cavern. At 1 MeV-neutron-equivalent fluences of up to $8 \cdot 10^{11}\,\mathrm{cm}^{-2}$, no radiation effects except for a considerable increase in dark count rate and accordingly dark current has been observed. The temperature dependence of radiation-induced dark current shows a significant deviation from that of the initial dark current.

The presented studies have contributed to the *Letter of Intent for the LHCb Upgrade* and the *LHCb Tracker Upgrade Technical Design Report* and have been the base for further research and development by the LHCb collaboration. It has been concluded, that a scintillating fibre tracker with silicon photomultiplier readout is a viable technology for the LHCb upgrade. The LHCb collaboration has therefore decided to completely replace the current downstream tracking system by the LHCb SciFi Tracker.

Kurzfassung

Das LHCb-Experiment wird ein umfangreiches Detektor-Upgrade während des LHC Long Shutdown 2 in den Jahren 2019 bis 2020 durchführen. Das Hauptspurkammern sollen durch den LHCb SciFi Tracker ersetzt werden, dessen Haupkomponenten szintillierende Fasern und Silizium-Photomultiplier sind. Die in dieser Arbeit gezeigten Studien haben dazu beigetragen, die Eignung dieser Technologie unter den anspruchsvollen Betriebsbedingungen des aufgerüsteten LHCb-Detektors zu bewerten.

Unter Verwendung des GEANT4-Toolkits wurde eine Simulation szintillierender Fasern entwickelt. Diese berücksichtigt Fasereigenschaften die aus Messungen der LHCb-SciFi-Tracker-Kollaboration und aus Literaturquellen abgeleitet wurden. Das entwickelte Simulationsprogramm wird aktuell von verschiedenen Gruppen der LHCb-Kollaboration als Hilfsmittel in Forschung und Entwicklung wie auch zur Herleitung von Parametrisierungen für die Gesamtdetektorsimulation verwendet. Neben der Fasersimulation, wird die Zeitmessung von Signalen einer szintillierenden Faser beschrieben.

Charakterisierungen von Silizium-Photomultipliern wurden durchgeführt, um die Abhängigkeit verschiedener Parameter von angelegter Spannung und Temperatur zu bestimmen. Insbesondere wurde die Strahlenhärte in Bestrahlungstests mit Protonen sowie in langfristigen Bestrahlungen in der LHCb-Kaverne *in situ* untersucht. Bis zu einem 1 MeV-Neutronen-äquivalenten Fluss von etwa $8 \cdot 10^{11}\,\mathrm{cm}^{-2}$ wurde keine Beeinträchtigung durch Strahlung außer einer deutlichen Erhöhung der Dunkelzählrate und entsprechend des Dunkelstroms beobachtet. Die Temperaturabhängigkeit des stahleninduzierten Dunkelstroms weicht signifikant von der des Dunkelstroms vor Bestrahlung ab.

Die gezeigten Studien haben zum *Letter of Intent for the LHCb Upgrade* und dem *LHCb Tracker Upgrade Technical Design Report* beigetragen und waren der Ausgangspunkt für weitere Forschung und Entwicklung durch die LHCb-Kollaboration. Es wurde der Schluss gezogen, dass ein Spurdetektor aus szintillierenden Fasern mit Silizium-Photomultiplier-Auslese eine geeignete Technologie für das LHCb-Upgrade ist. Die LHCb-Kollaboration hat daher entschieden, das derzeitige Hauptspurfindungssystem vollständig durch den LHCb SciFi Tracker zu ersetzen.

Contents

1 Introduction **1**

2 LHCb and Its Upgrade **5**
2.1 Physics Motivation 5
2.2 The LHCb Detector And Its Upgrade 7
2.3 LHCb SciFi Tracker 10

3 Scintillating Fibres **15**
3.1 Review of Scintillating Fibre Characteristics 15
3.1.1 Scintillation Mechanism 16
3.1.2 Light Collection 19
3.1.3 Transmission Loss 21
3.1.4 Radiation Effects 30
3.1.5 Timing 35
3.2 Fibre Simulation 37
3.2.1 The Simulation Program 37
3.2.2 Light Collection and Photon Paths 40
3.2.3 Transmission Loss and Wavelength Spectra 45
3.2.4 Dye Concentrations 52
3.2.5 Fibre Response to Particles 55
3.2.6 Radiation Effects 65
3.3 Signal Shape and Propagation Time 83
3.4 Conclusion and Outlook 98

4 Silicon Photomultipliers **101**
4.1 Introduction 101
4.2 Characterisation Measurements 105
4.2.1 Sensors 105
4.2.2 Test Setups 105
4.2.3 Temperature Measurement and Temperature Sensor Calibration 109
4.3 Signal Spectrum 114
4.4 Dark Count Rate 124
4.5 Current-Voltage Characteristic 133
4.6 Radiation Damage 144
4.6.1 Proton Irradiation 144
4.6.2 *In Situ* Irradiation 154

4.7 Conclusion and Outlook 173

5 Conclusion **179**

Appendices **c**

A ^{90}Sr Spectrum c

B Photon Detection Efficiencies c

C UV LED Characteristics . . . . . e

D Proton Irradiations . . . . . e

Bibliography **i**

1 Introduction

The Standard Model (SM) of particle physics [1–3] is a theory of great success. Since its development in the mid 20th century, it has explained almost every experimental observation in the domain of particle physics. All known matter is made up of the particles and interacts according to the fundamental forces described by the model. It has precisely predicted the existence of several phenomena that were observed subsequently. By discovery of the Higgs boson at the Large Hadron Collider (LHC) in the year 2012 [4, 5], the last fundamental particle of the Standard Model was found.

However, despite its accuracy in describing particles and forces on a subatomic level, the Standard Model cannot be considered a complete theory. Gravity, which is negligible in subatomic processes, is not incorporated. Further limitations of the Standard Model are apparent in the observations that will be described in the following.

Astronomical studies show a large discrepancy between visible matter and the mass densities necessary to explain the observations that are being made. It is inferred that about 26 % of our universe is made up of Dark Matter [6] whose nature aside from its gravitational interactions is unknown. At present, there is no particle in the Standard Model which could describe the existence of Dark Matter. Only about 5 % of our universe are observable matter and energy. The residual 69 % consist of Dark Energy which is responsible for the accelerated expansion of our universe but still lacks a physical description apart from this effect.

At the birth of our universe, matter and antimatter should have been created in equal parts in the big bang. Though, only a small amount of antimatter is found today, whereas matter predominates in almost everything we see. In 1967, three necessary conditions to allow for the emergence of today's matter–antimatter asymmetry were proposed by Andrei Sakharov [7]: baryon number violation, a deviation from thermal equilibrium and violation of C- and CP-symmetry, with P and C being the parity transformation and conjugation of charge-like quantum numbers, respectively. However, the CP violation existent in the Standard Model is not sufficient to explain the magnitude of matter-antimatter asymmetry in the universe.

These features demand new theories beyond the reach of the Standard Model, which are referred to as New Physics (NP). The LHC enables the search for signs of New Physics at unprecedented centre-of-mass energies and luminosities. The LHCb experiment [8], located at one of the four interaction points of the LHC, is dedicated to high precision measurements of heavy flavour physics. It aims for indirect evidence of new phenomena in CP violation and rare decays of charm and beauty hadrons.

During LHC Run 1 from 2010 to 2012, the LHCb detector has shown an excellent performance, running at luminosities of up to $4 \cdot 10^{32}\,\mathrm{cm}^{-2}\,\mathrm{s}^{-1}$ which is twice its original design value [9]. The collected data correspond to an integrated luminosity of $3\,\mathrm{fb}^{-1}$. The world's largest sample of exclusively reconstructed charm and beauty decays has been recorded. The data have enabled the LHCb collaboration to obtain many key results such as the first evidence for the rare decay $B_s^0 \to \mu^+\mu^-$ [10]. Running the LHCb detector until 2018 will provide an integrated luminosity of about $8\,\mathrm{fb}^{-1}$.

LHCb measurements have shown the potential to improve the statistical sensitivities to many key observables to levels that are similar or even better than those of current SM theory calculations [11, 12]. However, the data sample necessary to exploit the full LHCb potential cannot be obtained with the current detector. It will be achieved by an upgrade of the LHCb detector, which is proposed to take place in the years 2019 to 2020 during LHC's Long Shutdown 2.

The current first level (L0) trigger rate of 1 MHz prohibits increasing the yield for hadronic channels by operation at higher luminosities. Consequently, the L0 trigger stage will be removed in favour of a triggerless readout at 40 MHz, according to the LHC bunch crossing rate. The design luminosity of the upgraded LHCb detector is $2 \cdot 10^{33}\,\mathrm{cm}^{-2}\,\mathrm{s}^{-1}$. The upgraded detector will be able to record $50\,\mathrm{fb}^{-1}$ over ten years.

The LHCb upgrade comprises the replacement of several components and subsystems of the LHCb detector. The entire downstream tracking system, which in the current detector consists of silicon strip sensors and gas drift tubes, will be replaced by a scintillating fibre (SciFi) tracker with silicon photomultiplier (SiPM) readout. Extensive studies were necessary to assess the viability of this technology under the harsh operational conditions of the LHCb upgrade. It had to be shown that requirements of high tracking efficiency and low noise rate will be met and that the detector will keep this level of performance during the whole period of upgrade data taking in spite of occurring radiation damages. The base of this proof is a sufficient comprehension and knowledge about the characteristics of the two main SciFi Tracker components, scintillating fibres and silicon photomultipliers.

The goal of studies presented in this thesis is to determine the characteristics of scintillating fibres and silicon photomultipliers by simulations and measurements. The results provide input parameters to the simulation of the full SciFi Tracker and thus contribute to performance studies that are necessary to assess the viability of the technology and optimise the detector performance. Chapter 2 briefly reviews the physics goals of the LHCb upgrade and how these can profit from the detector upgrade. An overview of the LHCb upgrade and its detector components is given. The Scintillating Fibre tracker is explained in more detail at the and of the chapter.

Studies of scintillating fibres are presented in Chapter 3. It starts with a discussionof the mechanisms that are responsible for the scintillation yield, the photon propagation and light losses. These mechanisms are included in a comprehensive GEANT4 simulation of scintillating fibres which is described subsequently. Several results obtained from the simulation are shown. In particular, the fibre simulation

is used to enable a cross-check of different radiation tests that have been performed with the scintillating fibres at conditions that are not fully equivalent. Measurements of the time distribution of photons reaching the fibre end have been taken and are compared with simulation results.

Chapter 4 is dedicated to the study of silicon photomultipliers. After a brief introduction of the characteristic parameters, a description of investigated devices and used test setups follows. Discussions of performed SiPM test measurements, data analyses and results obtained from non-irradiated sensors are ordered by the type of characterisation, *i.e.* measurement of signal spectra, dark count rate or current–voltage dependence. The effect of radiation on SiPMs has been studied by sensor irradiations with protons and by long-term *in situ* tests in the LHCb cavern.

Conclusions from scintillating fibre and silicon photomultiplier studies are given at the end of the respective chapter. An overall conclusion is made in Chapter 5.

2 LHCb and Its Upgrade

The LHCb experiment is dedicated to the indirect search for New Physics in heavy flavour physics processes. The LHCb detector upgrade is able to significantly extend the physics reach of studies made with the already well performing detector by a major increase in the acquired data sample. This chapter briefly describes the physics motivation for the LHCb upgrade, with three physics studies being introduced, which provide examples for the benefit from larger data sets. The current LHCb detector and the modifications, which enable the upgraded detector to be read out at 40 MHz and cope with an increased luminosity, are outlined. Studies presented in Chapter 3 and 4 of this work are part of the research and development program for the LHCb SciFi Tracker, a new detector system which is described in more detail in the last section of this chapter.

2.1 Physics Motivation

Precision measurements of heavy flavour physics processes are a promising approach in the search for New Physics (NP). While direct searches are limited by available energies to produce new particles, indirect searches can probe even beyond this energy frontier by measuring the contribution of NP to parameters of *CP* violation and branching fractions of rare decays, mediated by quantum loops [12]. Also, in the case of successful direct searches, LHCb will enable the study of couplings and flavour structure that are not accessible by only using high transverse momentum data [11]. LHCb has a unique pseudorapidity range in the forward direction which is complementary to the general purpose detectors ATLAS and CMS.

The LHCb detector has already shown an excellent performance during LHC Run 1 (2010 to 2012) resulting in several world-leading measurements [9, 11]. Even beyond its core flavour physics programme, LHCb has established itself as general purpose detector in the forward region by measurements in the electroweak and QCD sector. An integrated luminosity of about $3\,\mathrm{fb}^{-1}$ has been recorded at 7 TeV to 8 TeV centre-of-mass energy during this period. Additional $5\,\mathrm{fb}^{-1}$ will be recorded at $\geq 13\,\mathrm{TeV}$ in LHC Run 2 by 2018.

However, the precision of many LHCb measurements is still limited by statistical uncertainties. Therefore, the LHCb upgrade aims for a major increase in data by accumulation of $50\,\mathrm{fb}^{-1}$ with 40 MHz readout over ten years. The estimated sensitivity improvement is about one order of magnitude for many key observables compared to current measurements [12]. Three examples of LHCb key studies are briefly introduced in the following. References [11] and [13] provide a detailed

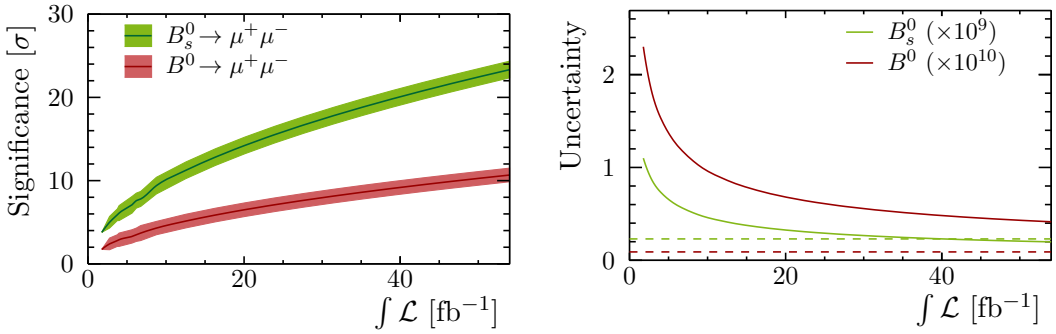

Figure 2.1: Left: Estimated significance of measured $B_s^0 \to \mu^+\mu^-$ and $B^0 \to \mu^+\mu^-$ branching ratios with respect to a background only hypothesis as function of data recorded by LHCb. Right: Expected uncertainties of $B_s^0 \to \mu^+\mu^-$ and $B^0 \to \mu^+\mu^-$ branching ratios. Uncertainties of SM predictions from theory are indicated by dashed lines. Both plots are results from studies presented in Ref. [15].

discussion of these and further measurements, as well as of their benefit from the LHCb upgrade.

The decays $B_s^0 \to \mu^+\mu^-$ and $B^0 \to \mu^+\mu^-$ are highly suppressed in the Standard Model (SM). Due to the absence of direct flavour changing neutral currents, these decays can only occur via higher order topologies such as so-called penguin diagrams. New Physics particles may contribute in these topologies and thus enhance the branching fractions well beyond the SM predictions. First evidence for the decay $B_s^0 \to \mu^+\mu^-$ has been found by LHCb [10], followed by its observation and the evidence for $B^0 \to \mu^+\mu^-$ in a combined analysis of CMS and LHCb data [14]. The results are consistent with the Standard Model. However, larger data sets are necessary to enable a distinct observation of $B^0 \to \mu^+\mu^-$ and high precision measurements of branching fractions, which could reveal possible deviations from the Standard Model predictions. Figure 2.1 shows the estimated significance and uncertainties for both decays as a function of data recorded by LHCb.

In the Standard Model, the Cabibbo-Kobayashi-Maskawa (CKM) matrix [16, 17] determines the coupling strengths of up- and down-type quarks to weak charged currents and thus explains quark mixing. Its complex phase is the only known source of *CP* violation. Measurements of the angle γ of the CKM unitarity triangle are crucial benchmark tests of the Standard Model. Its value is the least precisely known of the three angles of the unitarity triangle. The present uncertainty of γ from the combined analysis of $B \to DK$ decays is about 10° [18] where theoretical uncertainties are negligible [19]. The data sample of 50 fb^{-1} available by the LHCb upgrade will improve the precision of γ measurements to the one degree level [11].

Like $B_{(s)}^0 \to \mu^+\mu^-$, the charm-less decay $B_s^0 \to \phi\phi$ is also forbidden at tree-level. It is dominated by penguin loop transitions which are highly sensitive to NP contributions. Their effects could appear in time-dependent *CP* violation, which is predicted to be close to zero in the SM, and in angular distributions [13]. A

first measurement of the *CP* violating phase ϕ_s in $B_s^0 \to \phi\phi$ has been presented by LHCb in Ref. [20]. The direct extrapolation of sensitivities from this measurement shows that a statistical uncertainty of 0.12 rad can be achieved by the end of LHC Run 2 in 2018 [12]. Increasing the data set to the integrated luminosity of the LHCb upgrade will improve this value to 0.026 rad which is close to the accuracy of the SM prediction from theory.

2.2 The LHCb Detector And Its Upgrade

The LHCb detector [8, 9] is a single-arm forward spectrometer covering an angular range from approximately 10 mrad to 300 mrad (250 mrad) in the bending (non-bending) plane, which corresponds to a pseudorapidity range of $2 < \eta < 5$. It is designed for the study of *CP* violation and rare decays of charm and bottom hadrons. The detector geometry is justified by the fact that in high energy *pp* collisions b- and $\bar{b}$-hadrons are predominantly produced as pairs in the same forward or backward cone.

LHCb is located at one of the four interaction points of the LHC at CERN. The LHC provides colliding proton beams with a design energy of 7 TeV per beam. Each beam consists of proton bunches whose distances correspond to a bunch crossing rate at the interaction points of maximum 40 MHz. The design luminosity of the LHC is $10^{34}\,\mathrm{cm}^{-2}\,\mathrm{s}^{-1}$. However, the maximum luminosity that can be delivered by LHC decreases during the time of a machine fill due to diminishing beam intensities. Consequently, a new fill becomes necessary after a time in the order of hours to provide the high luminosities demanded by the ATLAS and CMS experiments. In 2012, the average fill time was about 6 h with an inter-fill time of about 8 h [21].

At high luminosities, the large number of visible *pp* interactions per bunch crossing, the so-called pile-up, complicates a proper vertex reconstruction and flavour tagging and increases combinatorial background [21]. For this reason, LHCb is operated at reduced luminosity compared to the LHC design. The reduction is achieved by only partially overlapping the two proton beams at the interaction point. This overlap is adjusted according to the decreasing beam intensities, referred to as luminosity levelling, which provides a luminosity being constant within about 5 % during a fill.

In LHC Run 1 (2010 to 2012), LHCb has demonstrated an excellent performance even at luminosities and pile-up exceeding its design values of $2 \cdot 10^{32}\,\mathrm{cm}^{-2}\,\mathrm{s}^{-1}$ and about 0.7 [9]. Most of the recorded data were taken at $4 \cdot 10^{32}\,\mathrm{cm}^{-2}\,\mathrm{s}^{-1}$ and 1.7, respectively [21].

The LHCb upgrade shall enable the data collection of $50\,\mathrm{fb}^{-1}$ integrated luminosity during 10 years of operation [13, 22]. This implies detector operation at an instantaneous luminosity of about $10^{33}\,\mathrm{cm}^{-2}\,\mathrm{s}^{-1}$. Furthermore, a fully flexible software trigger running at the LHC clock rate of 40 MHz is proposed to replace the current two-staged system consisting of the first level trigger (L0) and the high level trigger (HLT). This replacement is necessary because the limitation of the L0 output rate to 1.1 MHz prevents from profiting from higher luminosities. The L0 trigger yield for

hadronic channels saturates at luminosities greater than $2 \cdot 10^{32}\,\mathrm{cm}^{-2}\,\mathrm{s}^{-1}$ [13]. The current L0 trigger is implemented in hardware, its 1.1 MHz output rate is equivalent to the readout rate of current front-end (FE) electronics. Therefore, implementing a 40 MHz readout necessitates the replacement of all FE electronics. However, the proposed software trigger will not only significantly improve the efficiency in sampling data of heavy flavour processes, but also allows for implementation of trigger decisions that even more establish LHCb as a general purpose detector in the forward direction, complementary to the pseudorapidity range of ATLAS and CMS.

Besides the complete replacement of current FE electronics, several subsystems of the LHCb detector have to be modified to cope with the increased luminosity. Upgrade detector components are designed to run at a luminosity of $2 \cdot 10^{33}\,\mathrm{cm}^{-2}\,\mathrm{s}^{-1}$ with an average pile-up of about 5 [23]. Figures 2.3 and 2.2 show side views of the current and upgraded LHCb detector, respectively. Its components are briefly introduced in the following.

The Vertex Locator (VELO) surrounds the interaction region at LHCb. Its task is the determination of primary pp interaction vertices and of the displaced vertices of c- and b-hadron decays. In the upgrade detector, the current VELO will be completely replaced since it does not allow for the more complex pattern recognition requirements at high pile-up, nor will withstand the expected radiation level [24]. The upgraded VELO detector will be a silicon detector based on hybrid pixel sensors. It comprises new radiation hard readout electronics and a re-designed cooling system.

Particle tracking will be realised by the Upstream Tracker (UT) and the Scintillating Fibre (SciFi) Tracker [23] located before (upstream) and behind (downstream) of the bending magnet, respectively, looking from the interaction point. The UT replaces the current Tracker Turicensis (TT) for reasons of radiation hardness, detector occupancy and compatibility with 40 MHz readout. It consists of four high granularity silicon micro-strip layers with an improved coverage of the LHCb acceptance. The SciFi Tracker is a completely new detector technology in LHCb. It will be installed at the three tracking stations T1 to T3, replacing the current Inner Tracker (IT) and Outer Tracker (OT). The SciFi Tracker is discussed in more detail in Sec. 2.3.

Two ring imaging Cherenkov detectors (RICH1, RICH2), whose task is in particular the discrimination of kaons and pions, an electromagnetic calorimeter (ECAL), a hadronic calorimeter (HCAL) and a muon system comprising stations M2 to M5 provide particle identification (PID) in the upgraded LHCb detector [25]. A change of the overall structure of the currently installed RICH detectors is not required. However, the reduced effectiveness of the aerogel, one of the radiators in the present RICH1 detector, at high luminosity in combination with the possible gain achievement by less material in the acceptance have led to the decision to remove the aerogel. The currently used hybrid photo detectors (HPD) have encapsulated 1 MHz readout electronics and thus need a replacement. The proposed photodetectors are commercial multi-anode photomultiplier tubes (MaPMTs). Additionally, a

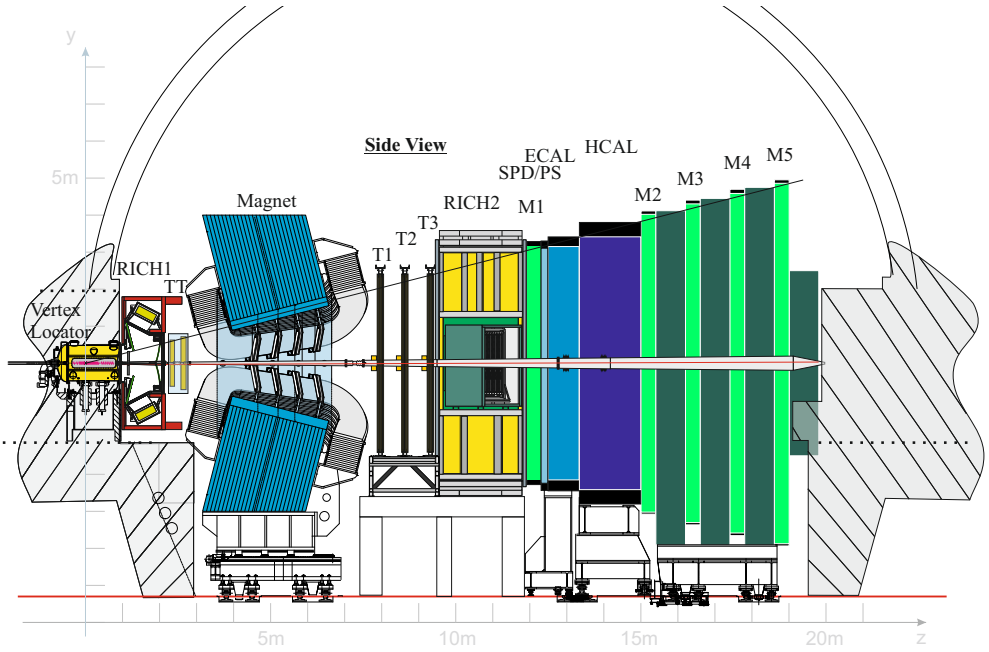

Figure 2.2: Schematic view of the current LHCb detector, taken from Ref. [23].

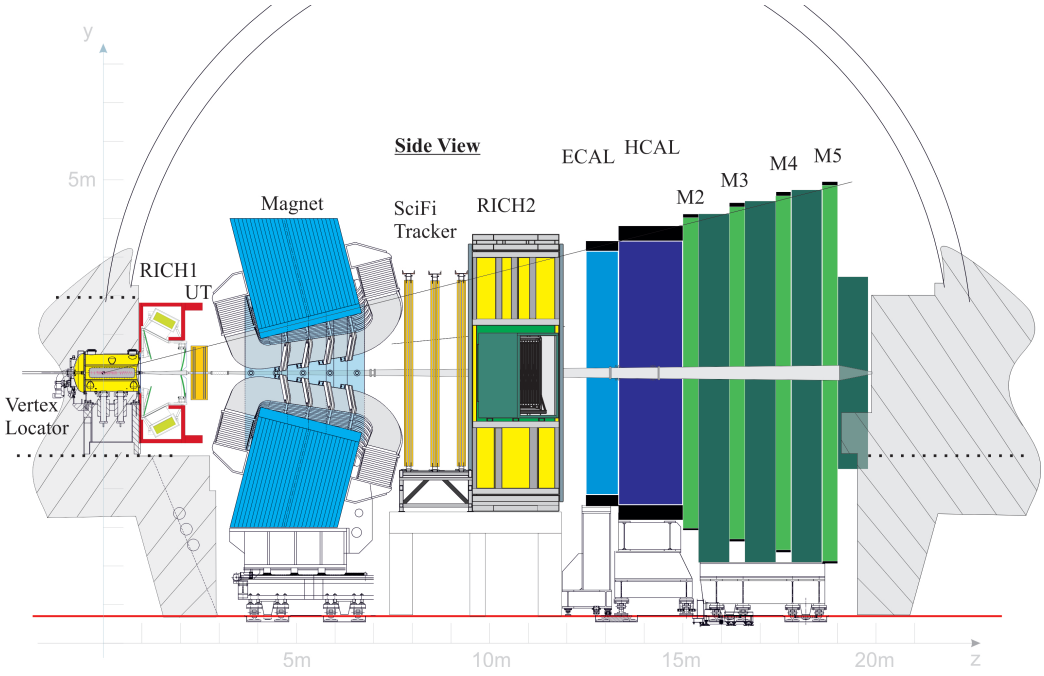

Figure 2.3: Schematic view of the upgraded LHCb detector, taken from Ref. [23].

time-of-flight system is under studies to enable identification of low momentum particles. The calorimeters and the muon detectors M2 to M5 of the current LHCb detector already meet the requirements for the upgrade, except for their readout electronics. The muon station M1 as well as the Scintillating Pad Detector (SPD) and the Preshower (PS) of the current detector will be removed in the upgrade. At present, their task is to enable an adequate L0 trigger decision. An additional shielding will be installed around the beam pipe in front of muon station M2 to prevent the inner region of this station from high occupancies.

2.3 LHCb SciFi Tracker

The purpose of tracking stations upstream (UT in Fig. 2.3) and downstream (SciFi Tracker in Fig. 2.3) of the LHCb dipole magnet is to provide a high precision momentum measurement for charged particles and thus enable precise mass and lifetime resolutions of decayed particles. Additionally, measured track directions are used as input to the photo-ring searches in the RICH detectors.

The downstream tracking detectors are located at three tracking stations (T-stations) T1 to T3. Currently, two detector systems of different technology are operated at the T-stations: the Outer Tracker (OT), based on gas straw tubes, and the Inner Tracker (IT), a silicon strip detector. The OT covers about 99 % of the surface of a T-station. Only the innermost part around the beam-pipe is covered by the IT, where the high track density requires a higher granularity. Each T-station comprises four detector planes with orientations of straws and strips following an (x, u, v, x) scheme. The given coordinates correspond to angles $(0°, +5°, -5°, 0°)$ of straws and strips relative to the vertical axis, which is parallel to the major component of the magnetic field of the dipole magnet. The stereo-angles $\pm 5°$ allow for the determination of track coordinates in the vertical direction additionally to the position in the magnet's bending plane.

Both subsystems, the OT and the IT, have demonstrated their performance in LHC Run 1 [26, 27]. Hit efficiencies greater than 99 % with spatial resolutions of about 200 µm (OT) and 50 µm (IT) in the bending plane were measured. Although the original design considerations implied a maximum detector occupancy of about 10 % in the hottest region of the Outer Tracker, it could be shown that even at occupancies of about 25 % the track finding efficiency remained unaffected due to improvements in the tracking algorithm [23]. However, it is stated in Ref. [13] that, with the current IT-OT design, occupancies will be too high at upgrade luminosities. Consequently, at least the inner part of the T-stations needs a redesign.

It was decided to replace the complete downstream tracking system with a Scintillating Fibre Tracker [23] covering a total area of 360 m^2. The use of a single detector technology has the following benefits. The track reconstruction is simplified and thus becomes potentially faster. Construction, maintenance and operation of a single technology are less expensive in terms of time and cost. There is no need for new OT electronics.

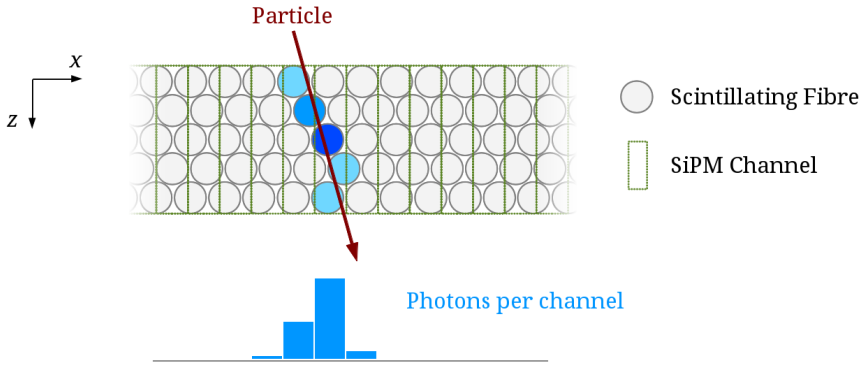

Figure 2.4: Arrangement of scintillating fibres and SiPM channels in a fibre tracker module. The fibre diameter in the LHCb SciFi Tracker is 250 µm. The coordinates given in the figure are those of the right-handed coordinate system of LHCb with beam-pipe direction z and vertical direction y, compare Fig. 2.3.

The sensitive volume of the SciFi tracker is built from 2.5 m long scintillating fibres with a diameter of 250 µm. The fibres are arranged in a mat of multiple fibre layers to increase the detectable light per crossing particle, see Fig. 2.4. The detection of scintillation light is realised at one end face of the fibre mat by Silicon Photomultipliers (SiPM). The proposed devices are arrays of individual channels, each equivalent to a single SiPM. Thus, the photon detection in a particular channel can be associated to a spatial coordinate. The SiPM channel width is 250 µm, equivalent to the fibre diameter. However, a distinct matching of individual fibres and SiPM channels is not possible. The fibre pitch within a layer (horizontal direction in Fig. 2.4) is larger than the fibre diameter to enable a reliable fibre positioning in the production process of a mat and account for possible variations of the fibre diameter.

A typical particle hit yields photon detection in more than one channel. By finding clusters of neighboured channels whose signals exceed certain thresholds and calculating weights according to the respective signal level, a spatial resolution significantly better than 100 µm is achieved. The resolution depends on the number of detected photons because only a few will reach the photodetector which leads to relatively large signal fluctuations. Hence, a mirror is placed at the fibre mat's end face opposite to the SiPM to also detect photons emitted in the direction of the non-instrumented fibre end.

The width of a fibre mat is about 13 cm in the x-direction, *cf.* Fig. 2.4. A standard SciFi Tracker module consists of four times two mats attached to the same light-weight support structure made from plastic and carbon foils. Figure 2.5 shows the arrangement of fibre mats, SiPM readout and mirror in a single module which is a part of a detector plane. Each detector plane will comprise 10 to 12 modules. A detailed review of the LHCb SciFi Tracker and its components including readout electronics, SiPM cooling system, module production *etc.* is provided by the Technical Design Report (TDR) Ref. [23].

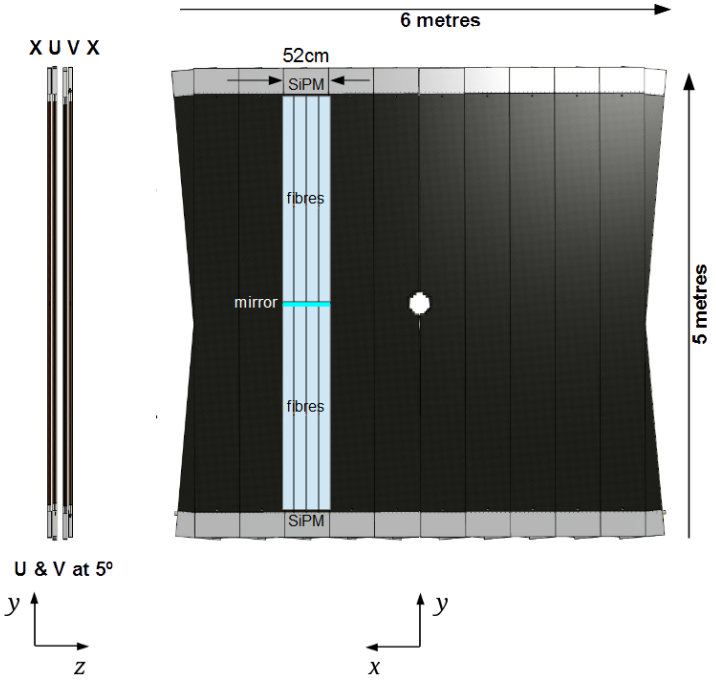

Figure 2.5: Sketch of one station of the LHCb SciFi Tracker comprising four detector planes. The original figure is taken from Ref. [28].

A comprehensive programme of research and development (R&D) has been performed by the LHCb SciFi Tracker group to verify the viability of the technology at the conditions of the LHCb upgrade, and is still being executed to optimise the detector design, readout electronics, cluster finding algorithms, cooling of SiPMs *etc.* In this context, studies of the two main tracker components, the scintillating fibres and the silicon photomultipliers, play an important role.

The number, wavelengths and arrival times of scintillation photons that are reaching the SiPM strongly affect the detector performance. As mentioned before, the achievable hit resolution and also the hit detection efficiency depend on the number of detected photons. In addition to initial light attenuation in the fibre material, radiation damages will further diminish the number of photons reaching the fibre end. The SiPM's detection efficiency is a function of photon wavelength and thus has to comply with the emission spectrum of the used scintillating fibre. The available time for signal integration in the readout electronics is only 25 ns, including dead time, according to the proposed 40 MHz readout rate. Propagation times of light in 2.5 m long fibres and decay times of scintillators and wavelength-shifters have to be considered for an optimal choice of the integration start time and to determine the signal fraction being accounted in the respective integration interval or instead being wrongly associated to previous or subsequent bunch crossings, the so-called spill-over. Furthermore, the distributions of photon directions and exit points at the fibre end may affect the spread over SiPM channels.

These characteristics depend on various fibre properties which are discussed in Chapter 3. The simulation of scintillating fibres using the GEANT4 [29, 30] toolkit helps to understand the complex signal behaviour. The effect of particular fibre properties and of their change, *e.g.* due to radiation damages, can be studied and cross-checked with measurements. The GEANT4 fibre simulation is a valuable input for the overall simulation of the upgrade detector. The measurement of time distributions of photons reaching the fibre end and the comparison with simulation are described at the end of the chapter.

The used SiPMs have to provide sufficient gain, a good photon detection efficiency as well as a low noise rate to achieve high tracking performances. Their operational capability has to be preserved during the data taking period of the upgrade despite the occurring radiation levels. Characterisation measurements are performed to reveal the dependencies of SiPM parameters on applied bias voltage and temperature. In addition to measurements of non-irradiated sensors, tests of SiPMs suffering from proton radiation and from the *in situ* radiation environment of the current LHCb have been conducted. These characterisations are the topic of Chapter 4 of this thesis.

3 Scintillating Fibres

The LHCb SciFi Tracker is the first tracking detector that covers an area of about $360\,\mathrm{m}^2$ with scintillating fibres (SciFi) of 250 µm diameter. Its readout rate of 40 MHz and the radiation levels at which it will be operated are unique for scintillating fibre trackers to date. Studies of light yield, time response and radiation effects were necessary to verify the viability of this technology under the harsh operational conditions after the LHCb upgrade. This chapter comprises a review of mechanisms that determine the signal characteristics of scintillating fibres, the development of a fibre simulation including studies made with it and the measurement of the SciFi's time response.

3.1 Review of Scintillating Fibre Characteristics

Scintillating fibres have become a common technology in high-energy physics. They are used to build calorimeters, beam monitors and tracking detectors. Their main advantages are low costs, only small fraction of insensitive volume, high spatial resolution and fast response time.

The components of these fibres are a core and its cladding. While the core serves as scintillator, the cladding provides light guidance by having a lower refractive index than the core. To improve the light yield fibres may have more than one cladding material, with the lowest refractive index in the outmost layer. This type is referred to as multi-clad fibre. Table 3.1 lists the materials used in scintillating fibres produced by the manufacturer Kuraray.

When a particle traverses the fibre core, it produces scintillation light due to its energy deposition. Photons emitted in a direction that leads to total reflection at the boundary between core and cladding or between inner and outer cladding, respectively, will be captured and guided to the fibre ends, where they can be detected. Figure 3.1 illustrates a particle crossing the fibre core and producing one exemplary photon, which propagates within the fibre.

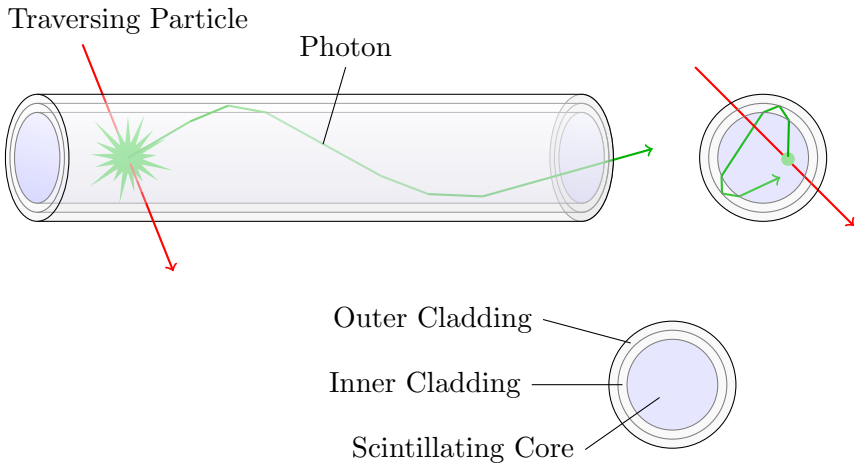

Figure 3.1: Lateral view and cross-section of a multi-clad fibre. The green line shows the path of an exemplary photon, which is produced by a traversing particle, through the fibre. The dimensions are not to scale.

Table 3.1: Materials of scintillating fibres with multiple cladding produced by Kuraray [31]. The refractive index corresponds to the sodium D line.

Component	Material	Refractive Index	Density $\frac{\text{g}}{\text{cm}^3}$	Cladding Width / Total Diameter
Core	Polystyrene	1.59	1.05	
Inner Cladding	Poly(methyl methacrylate)	1.49	1.19	3 %
Outer Cladding	Fluorinated Polymer	1.42	1.43	3 %

3.1.1 Scintillation Mechanism

The production of scintillation light in organic compounds, such as the plastic scintillator polystyrene (PS), is related to the presence of benzene rings. The electrons of these aromatics that belong to the double bonds of unsaturated carbon atoms in a benzene ring form a conjugated π orbital. They are therefore delocalised, *i.e.* not bound to a particular C atom in the ring. The resulting energy levels of these aromatic compounds, including their vibrational sublevels, and some example transitions are schematically shown in Fig. 3.2.

When an ionizing particle loses energy in the scintillator material, it may excite a π-electron from the lowest singlet state S to the first excited electronic state S* or higher modes S**, in which vibrational modes are excited as well. By the process of internal degradation nearly all higher excitations decay rapidly ($< 10^{-11}$ s) to the lowest state of the S* band [32]. The excess energy is transferred to vibrational phonons and thus these transitions are non-radiative.

Further decays of the lowest S* state to the vibrational sublevels of the electronic ground state S can occur radiatively by emission of fluorescent light. The exponential

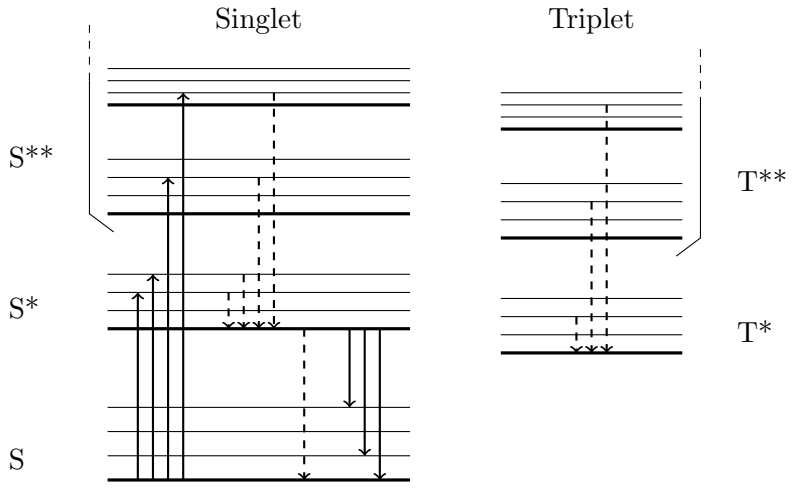

Figure 3.2: Schematic diagram of energy levels in aromatic compounds due to conjugated π orbitals. Each electronic state has vibrational sublevels. The lowest level of a vibrational band that belongs to one electronic state is denoted by a thick line. Continuous arrows indicate radiative, dashed arrows radiationless transitions. [32]

lifetime of these decays is in the order of 1 ns to 80 ns [32]. Since the energy of photons emitted in the decay of S* is below the threshold of a vibronic excitation from the ground state, the scintillator is transparent to its scintillation light.

Transitions between singlet and triplet states are highly suppressed according to multiplicity selection rules. The typical order of magnitude of the suppression factor is 10^8 for excitations from S to T** [32]. However, rare processes like double photon absorption and inter-system crossings S**→T** can lead to a population of higher triplet states. Like singlet states they decay fast and radiationless to the lowest level of T* (Fig. 3.2).

Phosphorescence resulting from a direct transition from T* to the singlet ground state is inhibited by the selection rules and thus not significant. Instead, T* states decay by the triplet annihilation $\mathrm{T^* + T^* \rightarrow S^* + S + phonons}$ with a subsequent transition from S* to S, as described above. The decay time of the annihilation process can be many orders of magnitude larger than the lifetime of the S* state and therefore leads to a delayed emission of fluorescent light [32].

Pure polystyrene shows only poor scintillation characteristics in the context of efficient and fast particle detection. Its fluorescence quantum yield is only 3 % [33] due to competing processes such as internal degradation from S* to the ground state S. Although the major parts of the absorption and emission spectra have no overlap (compare Fig. 3.3), the extinction coefficient ϵ of polystyrene at wavelengths λ with the highest emission intensity I is still sufficient to lead to significant self-absorption of the emitted photons. Neither the interaction length of Rayleigh scattering is negligible at the relevant range of emission energies. A further discussion of transmission losses can be found in section 3.1.3. The decay

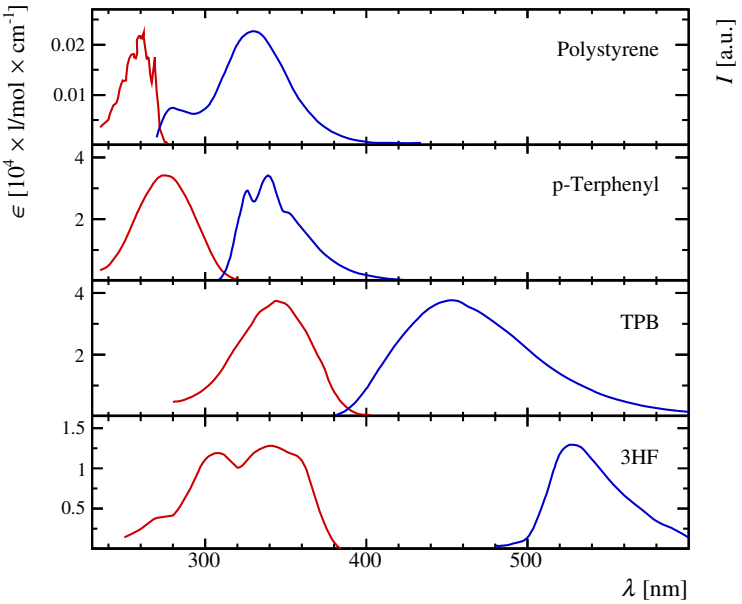

Figure 3.3: Absorption and emission spectra of compounds used in plastic scintillators. Red curves show the decadic molar extinction coefficient ϵ, blue curves the emission intensity (number of photons) I per unit wavelength in arbitrary units. The data for polystyrene, p-terphenyl and TPB refer to solutions in cyclohexane and are obtained from [33]. 3HF is dissolved in polystyrene, data adapted from [35].

time of fluorescent states in polystyrene is about 20 ns [33, 34], which is too slow for applications where a fast data acquisition is necessary. An additional disadvantage is the discrepancy between the polystyrene emission spectrum and wavelength-dependent sensitivity of common photodetectors such as photomultiplier tubes (PMT) and silicon photomultipliers (compare Appendix B).

To improve the scintillation light yield and decay time of polystyrene based plastic scintillators they are doped with additional aromatic molecules. Provided that the emission spectrum of the base polystyrene and the absorption spectrum of the dopant have a good overlap and the distance to a dopant molecule is short, the energy of the excited polystyrene can be transferred to the dopant via non-radiative dipole-dipole interactions, so-called Förster transfer [36, 37]. Typical dopant concentrations in the order of 1 % molar fraction increase the efficiency of this non-radiative transfer to about 100 % [34]. Thus, the scintillation characteristics of the plastic scintillator are dominated by the properties of the dopant, which acts as energy acceptor.

Fig. 3.3 shows the good overlap between the emission spectrum of polystyrene and the absorption spectrum of 1,1,4,4-tetraphenylbutadiene (TPB). However, at TPB concentrations necessary to provide an efficient energy transfer from the polystyrene to the acceptor molecules, the self-absorption of TPB is too high to be used in scintillating fibres. Since this is the case for almost any fluorescent dye, a ternary

system of polystyrene with two different dopants instead of a binary system is often more convenient. For example p-terphenyl, which has a high quantum yield and short decay time, can be used as first dopant in concentrations mentioned before. Photons emitted by the first fluor are subsequently absorbed by the second dopant, *e.g.* TPB or 3-hydroxyflavone (3HF), added in low concentrations of about 0.05 % by weight. By further emission the secondary fluor serves as wavelength-shifter to the most transparent region of the base polystyrene and the peak sensitivity of the photodetector.

3.1.2 Light Collection

The difference in refractive indices of fibre core and cladding leads to fractional trapping of the isotropically emitted photons. Because of the short photon wavelength compared to the dimensions of the fibre, geometrical optics are a valid approximation. Therefore, the critical angle α_c of total internal reflection with respect to the surface normal of the boundary between two media of different refractive indices n_1 and n_2 can be calculated by Snell's law

$$\frac{\sin(\alpha_1)}{\sin(\alpha_2)} = \frac{n_2}{n_1} \ , \tag{3.1}$$

$$\Rightarrow \quad \alpha_c = \arcsin\left(\frac{n_2}{n_1}\right) \ , \text{ with } n_2 < n_1 \ . \tag{3.2}$$

The equations (3.1) and (3.2) are also valid in the presence of an intermediate volume with refractive index n_{imv} between the two media with n_1 and n_2 under the conditions that $n_1 > n_{\text{imv}} > n_2$ and that the surface normals of the two boundaries are parallel.

Hence, considering photons emitted isotropically at the fibre axis, the trapping efficiency $\varepsilon_{\text{trap,axis}}$ for single-clad as well as for multi-clad fibres is

$$\varepsilon_{\text{trap,axis}} = \frac{1-\cos(\theta_c)}{2} = \frac{1}{2}\left(1 - \frac{n_{\text{clad}}}{n_{\text{core}}}\right) \ , \text{ with } \theta_c = 90^\circ - \alpha_c \ , \tag{3.3}$$

where n_{core} and n_{clad} are the refractive indices of the core and the (outer) cladding respectively. In this calculation only the photons emitted into one hemisphere, *i.e.* with angles $0^\circ < \theta < 90^\circ$ relative to the direction of the fibre axis, are taken into account.

Indeed, only an infinitesimal fraction of the scintillation light will be emitted from the fibre axis or in a direction crossing the fibre axis, respectively. However, for single-clad fibres it can be shown geometrically that photons, whose path has a non-zero minimal distance r_{min} from the axis, will also be trapped, if θ is less than θ_c. Photons emitted at an angle θ greater than θ_c undergo total internal reflection, if they fulfil the constraint

$$r_{\text{min}} \geq r_{\text{min,c}}(\theta) = R\sqrt{1 - \left(\frac{\sin(\theta_c)}{\sin(\theta)}\right)^2} \ , \tag{3.4}$$

Table 3.2: Parameter values of the Sellmeier Equation (3.7).

Material	a	b [nm^2]
PS	$1.443\,55 \pm 0.000\,99$	$20\,216 \pm 211$
PMMA	$1.181\,88 \pm 0.000\,66$	$11\,309 \pm 181$
PTFEMA	$0.983\,23 \pm 0.000\,12$	9541 ± 15

where R is the fibre core radius. Thus the trapping efficiency increases with increasing distance of the point of light emission from the fibre axis, compare Section 3.2.2.

If the scintillation light is produced uniformly over the fibre core cross-section, it follows from Equation (3.4) that the θ dependent fraction of trapped photons is

$$\varepsilon_{\text{trap}}(\theta) = \begin{cases} 1 & \text{, if } 0^\circ \leq \theta \leq \theta_\text{c} \text{ ,} \\ 1 - \frac{2}{\pi}\arcsin\left(\frac{r_{\text{min,c}}(\theta)}{R}\right) - \frac{2}{\pi}\frac{r_{\text{min,c}}(\theta)}{R}\sqrt{1-\left(\frac{r_{\text{min,c}}(\theta)}{R}\right)^2} & \text{, if } \theta_\text{c} < \theta \leq 90^\circ \text{ .} \end{cases} \tag{3.5}$$

After [38] this expression can be integrated with respect to $\sin(\theta)\,\mathrm{d}\theta$ analytically, which leads to the total trapping efficiency

$$\varepsilon_{\text{trap}} = \frac{1}{2}\left(1 - \left(\frac{n_{\text{clad}}}{n_{\text{core}}}\right)^2\right) \text{ .} \tag{3.6}$$

For multi-clad fibres the assumptions leading to the equations (3.4) to (3.6) are only valid in the approximation of a small inner cladding width. The normals to the interfaces at the points where a photon reaches the core - inner cladding and inner cladding - outer cladding boundary are not parallel for non-meridional rays. Therefore, the trapping efficiency will be smaller than the values calculated by Eq. (3.6) taking into account all angles $\theta \leq 90^\circ$ or Eq. (3.3) for $\theta \leq \theta_\text{c}$.

The knowledge of refractive indices n is crucial to determine the light collection efficiency of a scintillating fibre. Rayleigh scattering, which leads to transmission losses, is also influenced by n, compare Sec. 3.1.3. However, the refractive index is not constant with photon wavelength λ. Figure 3.4 illustrates the dispersion in the three polymers polystyrene (PS), poly(methyl methacrylate) (PMMA) and poly(trifluoroethyl methacrylate) (PTFEMA). The data points are obtained from Ref. [39] (PS and PMMA) and [40] (PTFEMA), respectively. Fitting a Sellmeier equation [41]of the form

$$n(\lambda) = \sqrt{1 + \frac{a\lambda^2}{\lambda^2 - b}} \tag{3.7}$$

to the data yields the parameter values listed in Tab. 3.2.

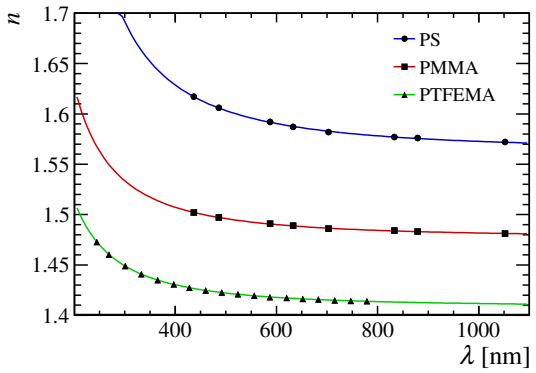

Figure 3.4: Refractive index n *vs.* photon wavelength λ. PS and PMMA data points are taken from [39], PTFEMA from [40]. The curves result from fitting a Sellmeier Equation (3.7) to the respective data.

3.1.3 Transmission Loss

Several sources of photon loss affect the light guidance in the scintillating fibre. These transmission loss factors in plastic optical fibres can be categorised as shown in Tab. 3.3. While the effect of impurities and imperfections in the lightguide structure (extrinsic loss factors) can be minimised by optimisation of the production process, this is not the case for intrinsic losses, which are related to the fibre materials.

Neglecting any possible loss at the material interfaces, the transmission can be described by

$$I(l) = I_0 \cdot \exp\left(-\sum_i a_i l\right) \quad , \tag{3.8}$$

where I_0 is the initial photon intensity, $I(l)$ the intensity after the path length l and a_i are the different loss factors. The photon path length l depends on the covered

Table 3.3: Loss factors in plastic optical fibres [42].

Intrinsic	Absorption	High harmonics of CH absorption Electronic transition
	Scattering	Rayleigh scattering
Extrinsic	Absorption	Transition metals Organic contaminants Absorbed water
	Scattering	Dust and micro voids Fluctuation of core diameter Orientational birefringence Core-cladding boundary imperfections

distance along the fibre axis x and the angle θ relative to this axis by

$$l(x,\theta) = \frac{x}{\cos(\theta)} \ . \tag{3.9}$$

Hence, after inserting (3.9) into (3.8) and multiplication by $\varepsilon_{\text{trap}}(\theta)$, Equation (3.8) has to be integrated over θ to get $I(x)$. However, the resulting expression is only valid for a small range of photon wavelengths since most of the loss factors a_i strongly depend on this quantity.

If possible light loss at the cladding-core interface cannot be neglected, an additional factor $(1-b)^{n_{\text{refl}}}$ has to be accounted for in Equation (3.8), where b is the probability to lose a photon at one single reflection. The mean number of reflections from the cladding-core interface along x is given by

$$n_{\text{refl}}(x,\theta,r_{\text{min}}) = \frac{x\tan(\theta)}{2\sqrt{R^2 - r_{\text{min}}^2}} \ . \tag{3.10}$$

The probability b may depend on the photon wavelength and the angle of incidence at the boundary. Equation (3.10) introduces a further dependency on the value of r_{min}.

The equations (3.9) and (3.10) are only valid for single-clad fibres. They are approximatively correct for multi-clad fibres in the case of a small inner cladding width (compare Sec. 3.1.2). Photons that are reflected from the interface between inner and outer cladding have to cross the boundary of the fibre core where additional losses can occur. The finite probability of Fresnel reflection when photons in the inner cladding arrive at the inner cladding - core interface leads to an increasing influence of the loss factors of the inner cladding material as well as to further deviation from Eq. (3.9) and (3.10).

The fact that scattered photons and those that are re-emitted after absorption can be trapped in the fibre again contributes to the complexity of describing the intensity decrease. In view of the many influences and parameters, Monte Carlo simulations are a reasonable approach to study the loss properties of scintillating fibres, see Sec. 3.2.

The most significant loss factors are briefly discussed in the following.

Molecular vibrations

Absorption due to vibrations of chemical bonds becomes significant at wavelengths beyond 500 nm. The energy levels of these states can be derived from solving the Schrödinger equation for a Morse potential [43].

$$E(v) = h\nu_0\left(v+\frac{1}{2}\right) - h\nu_0\chi\left(v+\frac{1}{2}\right)^2 \ , \tag{3.11}$$

where h is the Planck constant, ν_0 the oscillator frequency, $v \in \{0,1,2,\dots\}$ the quantum number and χ the anharmonicity constant. The energies, which are necessary to excite the v-th harmonic, are therefore

$$h\nu_v = E(v) - E(0) \quad \text{, with } v > 0 \ . \tag{3.12}$$

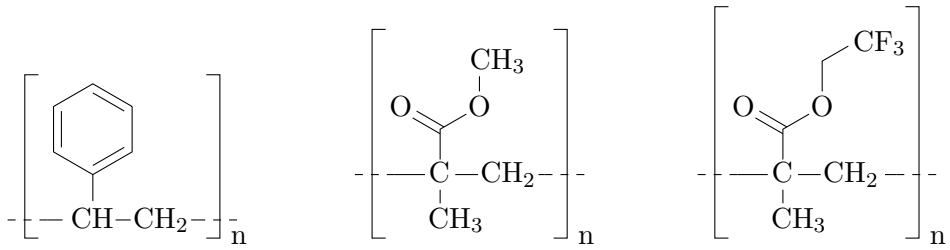

(a) PS (b) PMMA (c) PTFEMA

Figure 3.5: Structural formulae of typical compounds used in plastic optical fibres.

If the fundamental frequency ν_1 and the anharmonicity constant χ are known, the overtones can be calculated by [43]

$$\nu_v = \frac{\nu_1 v - \nu_1 \chi v(v+1)}{1-2\chi} \quad . \tag{3.13}$$

The ratio of the absorption strengths A of the v-th harmonic and the fundamental frequency can be estimated by [43]

$$\frac{A_v}{A_1} = \frac{f(K)_1}{f(K)_v} \quad , \tag{3.14}$$

where

$$f(K)_v = \frac{1}{v(K-2v-1)} \cdot \binom{K-2}{v} \quad \text{, with } K = \frac{1}{\chi} \, . \tag{3.15}$$

Considering the materials in scintillating fibres (compare Fig. 3.5), only the CH bonds show a significant absorption in the relevant wavelength range. However, OH bonds could occur in the fibre due to water absorption or radiation damages. These have an absorption strength similar to CH bonds.

Electronic transitions

Possible transitions between electronic levels of the fibre materials lead to photon absorption even at wavelengths greater than 400 nm. This effect is only significant in the fibre core, since the probability of these transitions is much higher in aromatic than in aliphatic compounds. The main contributor to this kind of absorption is the second dye of the scintillator due to its absorption spectrum at longer wavelengths than the base material (polystyrene) and the first dye, compare Fig. 3.3. In general, the longer wavelength tail of the absorption spectrum a_e can be approximated by an exponential function of the photon energy E_γ with the two parameters p_0 and p_1.

$$a_\mathrm{e} = p_0 \exp\left(p_1 E_\gamma\right) \tag{3.16}$$

Scattering

Density fluctuations and anisotropic dipole orientations in the base material as well as the refractive indices of the dissolved dyes differing from the base material are the sources of Rayleigh scattering in scintillating fibres. The effect of density fluctuations can be calculated by the Einstein-Smoluchowski equation [44–46]

$$a_{\mathrm{r,iso}} = \frac{8\pi^3}{27} \frac{\left(n^2-1\right)^2 \left(n^2+2\right)^2}{\lambda^4} k_{\mathrm{B}} T \beta \quad , \tag{3.17}$$

where n is the refractive index, λ the photon wavelength, k_{B} the Boltzmann constant, T the temperature and β the compressibility at glass transition. Anisotropy of dipole orientations increases the scattering by a so-called Cabannes factor [45, 47] which is about 2.7 for PS and 1.1 for PMMA [47].

Further scattering arises from impurities and geometrical imperfections. In contrast to Rayleigh scattering, it is almost independent of the photon wavelength, if the size of the responsible defects is of the same order or larger than the wavelength.

Boundary effects

Imperfections at the interfaces between core and claddings lead to a reflectivity smaller than one, even in the case of total internal reflection. This effect is significant especially in fibres with small diameter.

Statements about the influence of incident angle and wavelength can be found in Ref. [48] and [49]. The presented results are inconsistent though. While in Ref. [48] the reflection loss is found to comprise two fractions, one that is constant with wavelength λ and a second that follows λ^{-4}, a rough dependence on λ^{-2} is reported in Ref. [49]. There is no influence of the incident angle on the loss reported by Ref. [48]. In contrast, Ref. [49] states losses increasing linearly with the mean angle of incidence. The deviation of reflectivity from one is reported to be of the order of $5 \cdot 10^{-5}$ [48] and $3 \cdot 10^{-4}$ [49] respectively.

In addition, photon loss may occur at the interface between core and inner cladding, if the light is refracted at this boundary and reflected from the inner cladding – outer cladding interface.

Figure 3.6 shows the wavelength dependent light attenuation coefficient $A(\lambda)$ (*cf.* Eq. (3.8)) in pure polystyrene comprising molecular vibrations, Rayleigh scattering and electronic transitions. The parameters p_i which describe these three processes have been determined by fitting the attenuation curve $A(\lambda)$ to data points obtained from Ref. [50, 51].

$$A(\lambda) = a_{\mathrm{e}}(\lambda) + a_{\mathrm{r}}(\lambda) + a_{\mathrm{v}}(\lambda) \tag{3.18}$$

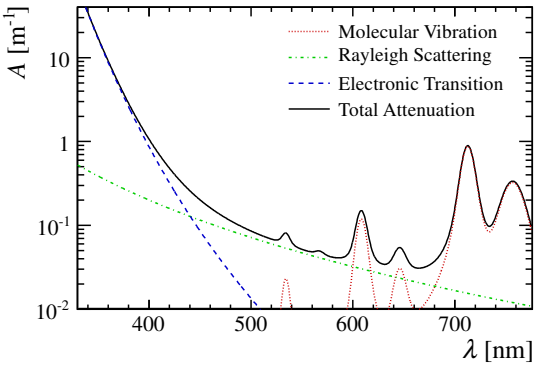

Figure 3.6: Loss mechanisms contributing to the total attenuation in polystyrene.

with indices e, r and v denoting the attenuation by electronic transitions, Rayleigh scattering and molecular vibrations, respectively, and

$$a_{\mathrm{e}}(\lambda) = p_0 \exp\left(p_1 \frac{hc}{\lambda}\right) \tag{3.19}$$

$$a_{\mathrm{r}}(\lambda) = \frac{8\pi^3}{27} \frac{\left(n(\lambda)^2 - 1\right)^2 \left(n(\lambda)^2 + 2\right)^2}{\lambda^4} k_{\mathrm{B}} T \beta p_2 \tag{3.20}$$

$$a_{\mathrm{v}}(\lambda) = \sum_{j=0}^{5} f_{\mathrm{Voigt},j}(\lambda) \tag{3.21}$$

In Equation (3.19) hc denotes the Planck constant times speed of light. The compressibility β of polystyrene is $5.8 \cdot 10^{-10}\,\mathrm{m^2/N}$ [44]. The wavelength dependent refractive index $n(\lambda)$ is calculated by Eq. (3.7) using the parameters shown in Tab. 3.2. The temperature value T is fixed at 295 K in the fit procedure.

Three overtones of each aliphatic and aromatic CH vibrations are considered in Equation (3.21). Each resonance is described by a Voigt function, which is the convolution of a Gaussian and a Lorentz function.

$$f_{\mathrm{Voigt},j}(\lambda) = p_{2j+7} \cdot \left(f_{\mathrm{Gauss},j} * f_{\mathrm{Lorentz}}\right)\left(\frac{1}{\lambda} - \nu_{v(j)}\right) \tag{3.22}$$

$$f_{\mathrm{Gauss},j}(x) = \left(p_{2j+8}\sqrt{2\pi}\right)^{-1} \cdot \exp\left(-\frac{1}{2}\left(\frac{x}{p_{2j+8}}\right)^2\right) \tag{3.23}$$

$$f_{\mathrm{Lorentz}}(x) = \frac{1}{2\pi} \cdot \frac{p_6}{x^2 + \frac{p_6^2}{4}} \tag{3.24}$$

The overtone frequencies $\nu_{v(j)}$ are determined by Eq. (3.13), where the anharmonicity constant is given by parameter p_3 and where p_4 and p_5 are the fundamental

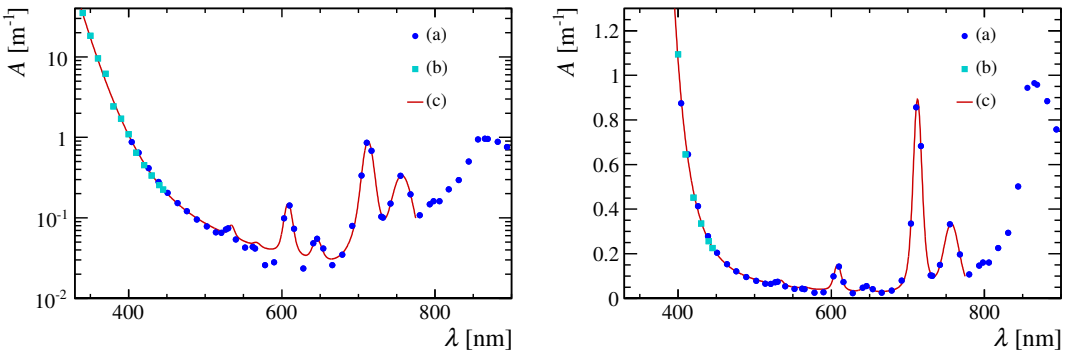

Figure 3.7: Transmission loss A in pure polystyrene *vs.* wavelength λ. Data points are obtained from plots in (a) [50] and (b) [51], respectively. The curve (c) has been determined by fitting Eq. (3.18) to the data. In the left plot the attenuation A is shown at logarithmic scale, whereas the scale is linear in the right plot.

frequencies of aromatic and aliphatic CH bond vibrations.

$$v(j) = \begin{cases} j+5 & \text{, if } j < 3 \\ j+2 & \text{, if } j \geq 3 \end{cases} \tag{3.25}$$

$$\chi = p_3 \tag{3.26}$$

$$\nu_1 = \begin{cases} p_4 & \text{, if } j < 3 \\ p_5 & \text{, if } j \geq 3 \end{cases} \tag{3.27}$$

Since the 7th overtones are only slightly visible, their intensities p_{11} and p_{17} are calculated from the 6th overtones' intensities p_9 and p_{15} with help of Eq. (3.14) and (3.15). The Gaussian widths p_{12} and p_{18} of these two resonances are fixed to those of the 6th overtones p_{10} and p_{16}.

The uncertainties of the attenuation data have been assumed to be $5 \cdot 10^{-3}\,\mathrm{m}^{-1}$ for data obtained from Ref. [50] and $0.03 \cdot A$ for data from Ref. [51]. Only data points in the range of 330 nm to 775 nm are considered in the fit. Figure 3.7 shows the data and the resulting fit curve. The parameter values and their error estimates are presented in Tab. 3.4.

Measured light attenuation data of the scintillating fibre SCSF-78MJ from Kuraray is shown in Fig. 3.8 [23]. The fibre has a diameter of 250 µm. TPB is assumed to be the wavelength-shifting secondary dye due to the similarity of decay times and emission spectra. This assumption is confirmed by Ref. [52] which refers to private communications with Kuraray.

Equation (3.18) is extended by two additional terms to describe the data of the SCSF-78MJ fibre.

$$a_{\mathrm{i}}(\lambda) = p_{19} \tag{3.28}$$

$$a_{\mathrm{e,2nd}}(\lambda) = p_{20} \exp\left(p_{21}\,(410\,\mathrm{nm} - \lambda)\right) \tag{3.29}$$

Table 3.4: Parameters of the wavelength dependent light attenuation in polystyrene. The values and error estimates result from fitting Eq. (3.18) to data obtained from [50] and [51]. Compare figures 3.6 and 3.7.

	Parameter	Value	Unit
Electronic transitions			
p_0		$(7.9 \pm 1.1) \cdot 10^{-10}$	m^{-1}
p_1		6.715 ± 0.045	eV^{-1}
Rayleigh scattering			
p_2		4.010 ± 0.096	–
Molecular vibrations			
p_3	anharmonicity	$(2.068 \pm 0.031) \cdot 10^{-2}$	–
p_4	fundamental frequency, aromatic	$(3.0715 \pm 0.0046) \cdot 10^5$	m^{-1}
p_5	fundamental frequency, aliphatic	$(2.8921 \pm 0.0044) \cdot 10^5$	m^{-1}
p_6	width of Lorentz function	$(1.389 \pm 0.077) \cdot 10^4$	m^{-1}
Aromatic			
5th overtone			
p_7	absorption strength	$(3.143 \pm 0.034) \cdot 10^4$	m^{-2}
p_8	width of Gaussian function	$(0.816 \pm 0.031) \cdot 10^4$	m^{-1}
6th overtone			
p_9	absorption strength	$(0.466 \pm 0.021) \cdot 10^4$	m^{-2}
p_{10}	width of Gaussian function	$(0.975 \pm 0.098) \cdot 10^4$	m^{-1}
7th overtone			
p_{11}	absorption strength	$0.191 \cdot p_9$	m^{-2}
p_{12}	width of Gaussian function	p_{10}	m^{-1}
Aliphatic			
5th overtone			
p_{13}	absorption strength	$(1.628 \pm 0.026) \cdot 10^4$	m^{-2}
p_{14}	width of Gaussian function	$(1.473 \pm 0.054) \cdot 10^4$	m^{-1}
6th overtone			
p_{15}	absorption strength	$(0.102 \pm 0.020) \cdot 10^4$	m^{-2}
p_{16}	width of Gaussian function	$(0.986 \pm 0.333) \cdot 10^4$	m^{-1}
7th overtone			
p_{17}	absorption strength	$0.191 \cdot p_{15}$	m^{-2}
p_{18}	width of Gaussian function	p_{16}	m^{-1}

Table 3.5: Additional parameters of the wavelength dependent light attenuation in scintillating fibre SCSF-78MJ. The values and error estimates are achieved by fitting Eq. (3.30) to data obtained from Ref. [33] and Ref. [23] while p_0 to p_{18} are fixed. The fit result is shown in Fig. 3.8.

Parameter	Value	Unit
Light loss due to imperfections		
p_{19}	$(4.650 \pm 0.178) \cdot 10^{-2}$	m^{-1}
Absorption by secondary dye		
p_{20}	42.9 ± 3.1	m^{-1}
p_{21}	0.1778 ± 0.0047	nm^{-1}

While the first term, a_i, accounts for light loss caused by imperfections in the fibre material and at the material boundaries and is considered to be independent of λ, the second term $a_\mathrm{e,2nd}$ describes the absorption due to electronic transitions in the secondary dye of the scintillator. The resulting equation

$$A(\lambda) = a_\mathrm{e}(\lambda) + a_\mathrm{r}(\lambda) + a_\mathrm{v}(\lambda) + a_\mathrm{i}(\lambda) + a_\mathrm{e,2nd}(\lambda) \tag{3.30}$$

is fitted to those data points shown in Fig. 3.8 that are inside the considered wavelength range of 390 nm to 660 nm.

It is expected that only the fibre core material contributes to the SCSF-78MJ data from Ref. [23]. The data acquisition has been conducted by means of a Hamamatsu C10083CA-2050 photospectrometer [53]. The absolute maximum ratings of this device quote a numerical aperture of 0.22. This is equivalent to an angle of 12.7°. The correspondent angle θ with respect to the fibre axis for photons in the fibre core is 7.9° according to a refractive index of about 1.6. Provided that the coupling of scintillating fibre and measuring device preserves their angular distribution, only those photons are detected that do not penetrate the inner cladding, *cf.* Sec. 3.1.2. Different photon path lengths compared to the distance x along the fibre axis have only a minor effect on the presented SCSF-78MJ data. From Equation (3.9) follows that the maximum deviation of the path length from x is 1 % at $\theta_\mathrm{max} = 7.9°$.

The fitted data include five points of TPB absorption taken from Ref. [33], whose uncertainty is 10 % as given in the reference. The molar concentration is assumed to be $3 \cdot 10^{-2}$ mol/L. In the range of used TPB data its absorption is more than two orders of magnitudes higher than the transmission loss in pure polystyrene. Therefore, the influence of other loss factors than the TPB absorption is negligible in this range.

The parameters p_0 to p_{18} are fixed at the values obtained for polystyrene, see Tab. 3.4. The following numbers for p_{19} to p_{21} and their error estimates are shown in Tab 3.5. Figure 3.8 illustrates the fit result.

Figure 3.9 shows the estimated intrinsic loss (see Tab. 3.3) of PMMA and PTFEMA, which are appropriate cladding materials. The curves are obtained according

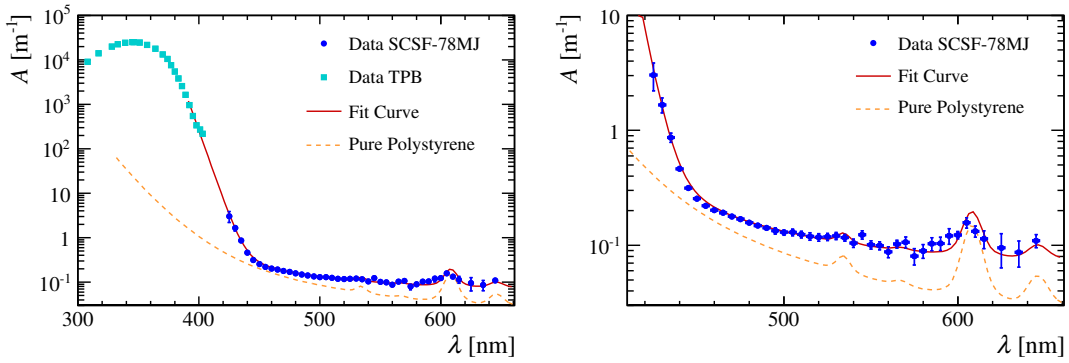

Figure 3.8: Transmission loss A *vs.* wavelength λ in scintillating fibre SCSF-78MJ from Kuraray (250 µm diameter). Data points are obtained from plots in Ref. [23] (SCSF-78MJ) and [33] (TPB), respectively. The plot on the right shows only the wavelength range of measured SCSF-78MJ data.

to Eq. (3.18), in which electronic transitions a_e are ignored due to their small contribution to the light loss in aliphatic compounds in the respective wavelength range.

The Rayleigh scattering strength of PMMA and PTFEMA is smaller compared to polystyrene because of the smaller refractive index, compressibility and anisotropy. The compressibility β of PMMA is $5.2 \cdot 10^{-10}\,\mathrm{m^2/N}$ [44], the Cabannes factor p_2 1.1 [47], the temperature is chosen 295 K. Same values are assumed for PTFEMA, since respective data were not available for this material.

Only aliphatic CH bonds are present in PMMA and PTFEMA. The frequencies and widths of their vibrational overtone absorptions are assumed to be the same as in polystyrene, see Tab. 3.4. Also the absorption strengths are taken from the polystyrene data shown in Tab. 3.4, but corrected with respect to the different densities of aliphatic CH bonds. This correction is done by applying the factor

$$f_{\mathrm{corr},X} = \frac{n_{\mathrm{CH},X}}{n_{\mathrm{CH,PS}}} \frac{\rho_X}{m_{\mathrm{mol},X}} \frac{m_{\mathrm{mol,PS}}}{\rho_{\mathrm{PS}}} \,, \tag{3.31}$$

where n_{CH} is the number of aliphatic CH bonds and m_{mol} the molar mass of the repeating unit. The index X denotes the particular material. Table 3.6 lists the numbers of these parameters for PS, PMMA and PTFEMA. The mass densities ρ are given in Tab. 3.1. The mass density of PTFEMA is assumed to be the same as the value provided for the fluorinated polymer.

The intrinsic light loss in PMMA and PTFEMA is much lower than in pure polystyrene. Hence, extrinsic loss factors such as impurities and geometrical imperfections play a more significant role in these materials.

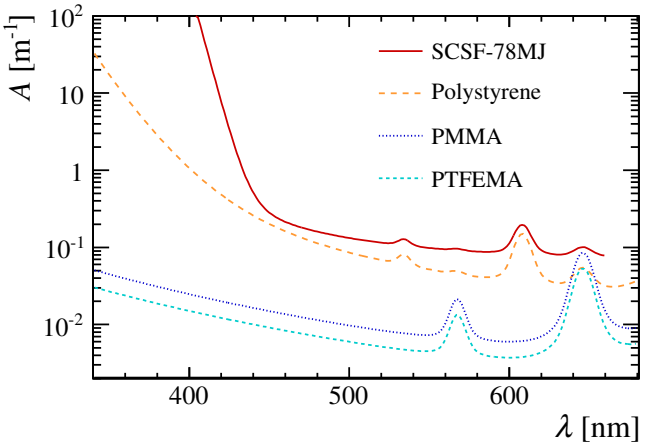

Figure 3.9: Estimated intrinsic loss coefficient of PMMA and PTFEMA *vs.* wavelength. Curves obtained from a fit to polystyrene and SCSF-78MJ data are shown for comparison.

Table 3.6: Number of aliphatic CH bonds n_{CH} and molar mass m_{mol} of the repeating unit. Compare Figure 3.5.

Compound	n_{CH}	m_{mol} [g mol^{-1}]
PS	3	104
PMMA	8	100
PTFEMA	7	168

3.1.4 Radiation Effects

The materials of scintillating fibres which are used in high-energy physics experiments are subject to damages induced by ionising radiation. The degradation of scintillating fibres is caused by free radicals produced via radiolysis and their annealing products. These chemical processes are very complex and still lack in an explicit description.

The lifetime of radicals and the formation of reaction products strongly depends on the composition of the particular material, its geometry and environment. Especially the presence of oxygen affects the annealing process. Surrounding material may have an influence, for example due to the radiation-induced release of gaseous compounds that react with the radicals.

Two different kinds of degradation can occur in scintillating fibres. On the one hand, the fluorescent dyes can experience damages, which decrease the light yield and change the decay time of excited states. On the other hand, the fibre can be affected by the formation of absorption centres, which increase the transmission loss. An observed decrease in the light yield may result from an absorption centre, if its extinction is significant in the wavelength range of the absorption of the secondary dopant and thus competing with the wavelength-shifting process.

The absorption centres observed immediately after short-term irradiation of pure polystyrene are likely associated with benzyl, cyclohexadienyl and possibly other related radicals, which show strong absorption bands in the wavelength range from 250 nm to 320 nm with tails reaching into the region of visible light [54]. Free radicals can annihilate, when two of them are close enough to each other. The necessary migration of radicals is provided by rotations of the polymer and successive hydrogen abstraction reactions [55]. Due to the limited mobility of the radicals within the polymer matrix, the observed annealing in an inert atmosphere is extremely slow at room temperature [54, 55].

In the presence of oxygen, free radicals are oxidised rapidly. The resulting peroxy radicals and subsequent hydroperoxides absorb visible light only very weakly [54]. This explains the annealing in an air atmosphere being orders of magnitude faster than under inert conditions. In thick samples or at high dose rates the oxygen that is dissolved in the inner part of the scintillator will be completely consumed during irradiation. At irradiation in air oxygen will still be available in the part close to the surface due to diffusion into the scintillator. This leads to an inhomogeneous distribution of absorption centres over the scintillator volume.

Dose and dose rate effects can originate from changing concentrations of reactants which are involved in the occurring processes. For example, Reference [55] shows a saturation in the concentration of short-lived absorption centres. The annealing rate increases with the concentration of reactive compounds produced via radiolysis and approximates their production rate. When the dissolved oxygen is completely consumed, the annealing rate becomes negligible and thus the absorption centre increase equals the initial value.

In Ref. [56] the effect of different dose rates on the density of absorption centres in 1 cm thick disks of polystyrene is examined among other studies. No significant effect is observed in inert atmosphere. However, the transmission loss immediately after irradiation of a sample which accumulated a total dose of 100 kGy in oxygen at about $40 \cdot 10^3$ hPa is smaller than in air. The reason is the higher annealing rate during irradiation, if oxygen is available in the material at any time. This condition is equivalent to an irradiation in air at low dose rate. Though, the permanent damage remaining after the annealing period is higher for the sample kept in $40 \cdot 10^3$ hPa oxygen (see Fig. 3.10). This explains why radiation damages are often underestimated when data from short-term irradiations at high dose rates are employed to assume the damage after long-term irradiations at lower dose rates.

Figure 3.10 shows the radiation-induced transmission loss a_{rad} in pure polystyrene and several fibres, which adds to the total attenuation coefficient A (compare Sec. 3.1.3). All the data represent the permanent damage after an annealing period, except for SCSF-78MJ data. These are obtained from measurements which took place during a period beginning one day after the irradiation and lasting for one week [58]. The fibres whose data are shown in Fig. 3.10 consist of a polystyrene core with PMMA cladding. However, even the light guide fibre BCF-98 which has no fluorescent dyes shows a significant deviation from the loss in pure polystyrene.

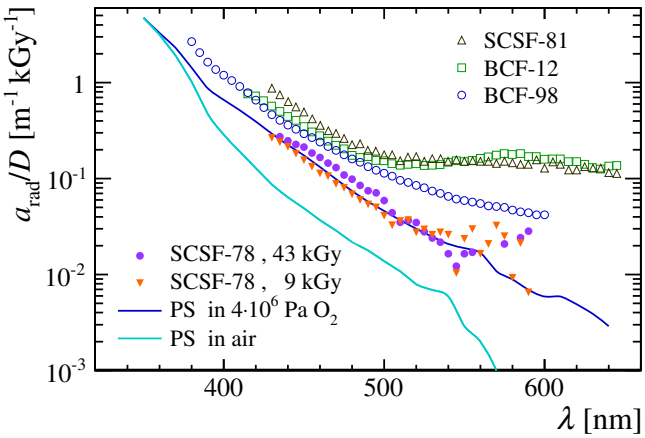

Figure 3.10: Additional radiation-induced absorption coefficient a_{rad} per dose D *vs.* photon wavelength λ in pure polystyrene and several fibres. Data for the scintillating fibre SCSF-81 from Kuraray and the light guide fibre BCF-98 from Bicron (now Saint-Gobain Crystals) are taken from Ref. [57], data for the scintillating fibre BCF-12 (Bicron) from Ref. [55]. The loss coefficients of the scintillating fibre SCSF-78MJ from Kuraray irradiated with two different doses are calculated from attenuation lengths provided by Ref. [58]. Values for pure polystyrene are calculated from transmission data presented in Ref. [56].

These deviations can be caused by several reasons. The respective materials under test have different dimensions, material compositions and surroundings. The various dimensions enable different diffusion rates of oxygen. Furthermore the diffusion into the polystyrene volume of the fibres is restricted by their cladding material and in the case of SCSF-78MJ by additional optical epoxy glue and surrounding PVC [23]. Though, the irradiations of all other fibres have been performed at dose rates and maximal doses, where oxygen is still available throughout the test [57].

The fluorescent dyes and further unknown additives in the commercially available fibres may influence the chemical processes during and after irradiation. They could act as diffusion enhancers or participate as reactants in the chemical reactions and thus lead to different products. The transmission of light through optical fibres is very sensitive to the quality of the core-cladding interface. A radiation-induced quality decrease of this boundary can be one possible reason for higher transmission loss in fibres compared to polystyrene disks.

Table 3.7 shows the properties of irradiations which have been executed to reveal the radiation damages. The applied dose rates vary by about six orders of magnitude. From findings presented in Ref. [57] it must be assumed that at the extremely high dose rate and the doses applied in SCSF-78MJ irradiations the oxygen in the fibre is completely consumed during the test. Furthermore the high dose rate leads to a high concentration of free radicals and thus to an increased probability of radical-radical recombination without intermediate oxidation. This could explain the lower transmission loss compared to all other fibres even after an annealing process.

Table 3.7: Properties of irradiations of polystyrene and fibres which yielded the data shown in Figure 3.10.

Data set	Total dose [kGy]	Dose rate [Gy/h]	Radiation	Reference
SCSF-81	2.2	36	X-ray	[57]
BCF-12	1.1–2.5	42	X-ray	[55]
BCF-98	0.14–6.0	32–128	X-ray	[57]
SCSF-78, 43 kGy	43 ± 7	$\sim 1.8 \cdot 10^7$	22.9 MeV protons	[23]
SCSF-78, 9 kGy	8.8 ± 1.5	$\sim 1.8 \cdot 10^7$	22.9 MeV protons	[23]
PS in $4 \cdot 10^6$ Pa O_2	100	$1 \cdot 10^4$	γ from ^{60}Co	[56]
PS in air	100	$1 \cdot 10^4$	γ from ^{60}Co	[56]

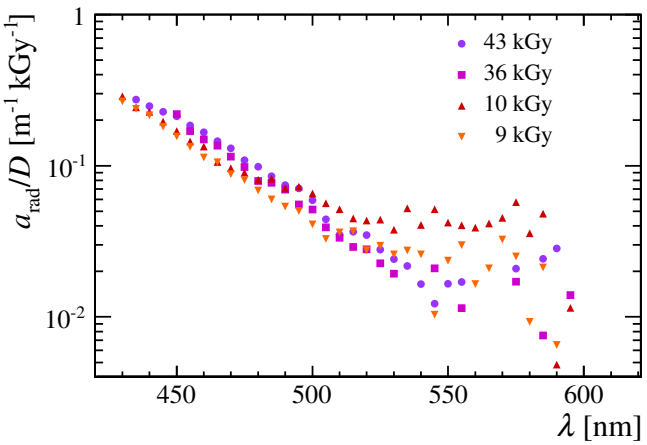

Figure 3.11: Additional radiation-induced absorption coefficient a_{rad} per dose D *vs.* photon wavelength λ in scintillating fibre SCSF-78MJ after accumulation of different doses. The values are calculated from attenuation length data from Ref. [58]. The data points of different doses are consistent with each other within their uncertainties. For the purpose of clarity the uncertainties are not shown.

The radiation-induced absorption coefficient per dose as it occurred in the SCSF-78MJ fibre irradiations is illustrated in Figure 3.11. The data of all four applied doses are consistent with each other with regard to their uncertainties. Hence, it can be assumed that in the studied dose range, with the given dose rate and arrangement of fibres the damage grows linearly with dose.

The degradation of the cladding material affects the light transmission, too. In single-clad fibres the absorption centres developing in the cladding can only be seen by the photons at the reflection from the core-cladding interface. However, in multi-clad fibres the photons that are reflected from the interface between inner and outer cladding have to traverse the inner cladding material.

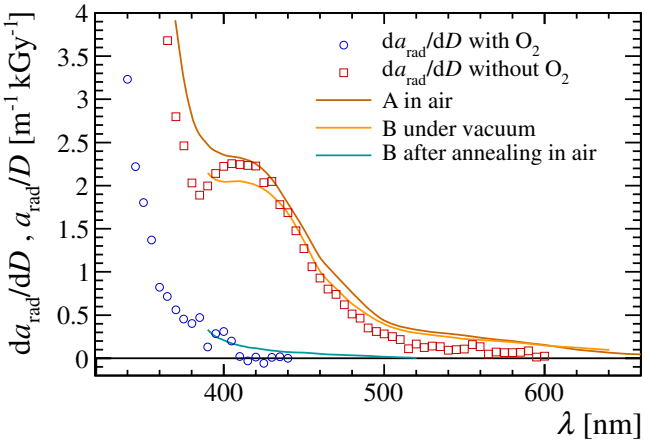

Figure 3.12: Additional radiation-induced absorption coefficient a_{rad} per dose D and derivative $\frac{\mathrm{d}a_{\mathrm{rad}}}{\mathrm{d}D}$ *vs.* photon wavelength λ in PMMA. The values of $\frac{\mathrm{d}a_{\mathrm{rad}}}{\mathrm{d}D}$ are taken from Ref. [57], curves for the 8 mm thick sample A and the 3 mm thick sample B are calculated from data presented in Ref. [60] and [59], respectively.

The oxygen diffusion rate in the common cladding material PMMA is about one to two orders of magnitude lower than in PS [57]. Thus, at the irradiation of the PMMA core light guide fibre FL-51 a complete consumption of dissolved oxygen is already observed after a received dose of a few hundreds of Gy, even at relatively low dose rates [57] (see Tab. 3.8). The increase of radiation-induced light attenuation per dose $\frac{\mathrm{d}a_{\mathrm{rad}}}{\mathrm{d}D}$ is constant at levels which are different before and after the dissolved oxygen is consumed. At wavelengths longer than 370 nm only permanent damages emerge as long as oxygen is present in the fibre. Thus, no further annealing is observed after irradiation. The radicals that are produced while irradiation in the absence of oxygen develop the same permanent damage after annealing in air.

Results of PMMA irradiations obtained from literature are shown in Fig. 3.12. Besides the mentioned values of $\frac{\mathrm{d}a_{\mathrm{rad}}}{\mathrm{d}D}$ from [57], the outcome of tests with 3 mm [59] and 8 mm [60] thick samples of PMMA is visualised. The presented curves are calculated from absorbance [59] and transmission [60] data measured before and after irradiation in vacuum and air, respectively. Due to the low diffusion rate, it is expected that the sample irradiated in air is almost free of oxygen during most of the irradiation time as well. The radiation-induced attenuations per dose $\frac{a_{\mathrm{rad}}}{D}$ immediately after irradiation derived from the two references [59, 60] are in agreement with the values of $\frac{\mathrm{d}a_{\mathrm{rad}}}{\mathrm{d}D}$ for the oxygen free case from [57]. After an annealing period in air of 9 months, the 3 mm thick sample shows a transmission loss per dose, which is similar to $\frac{\mathrm{d}a_{\mathrm{rad}}}{\mathrm{d}D}$ in the presence of oxygen. Table 3.8 gives information about the irradiation properties of the tests presented in [57, 59, 60].

The radiation-induced transmission loss in PTFEMA presented in Ref. [60] has a wavelength dependence which is similar to that of PMMA. Though, the level of absorption immediately after irradiation is lower in PTFEMA than in PMMA. Furthermore a stronger annealing after 7 days recovery is observed in PTFEMA.

Table 3.8: Properties of irradiations of PMMA which yielded the data shown in Fig. 3.12.

Data set	Total dose [kGy]	Dose rate [Gy/h]	Radiation	Reference
$\mathrm{d}a_{\mathrm{rad}}/\mathrm{d}D$ with O_2	1.2	43	X-ray	[57]
$\mathrm{d}a_{\mathrm{rad}}/\mathrm{d}D$ without O_2	0.255	43	X-ray	[57]
A in air	100	410	γ from ^{60}Co	[60]
B under vacuum	150	3000	γ from ^{60}Co	[59]
B after annealing	150	3000	γ from ^{60}Co	[59]

If similar damages are supposed to arise in both materials, these facts might be a result of higher oxygen permeability in PTFEMA compared to PMMA as it is reported for other fluorinated polymers in Ref. [61].

3.1.5 Timing

The time distribution of photons leaving the fibre end is dependent on two major effects. On the one hand, it is affected by the path length distribution (*cf.* Sec. 3.2.2) of photons propagating to the fibre end and the refractive indices of the traversed materials. The minimum propagation time for a photon of 480 nm wavelength, which is travelling inside the PS fibre core parallel to its axis, is 5.36 ns per 1 m fibre length, compare Eq. (3.7) and Tab. 3.2.

The second effect is the decay of excited states in the scintillator's bulk material and the fluorescent dyes. If only the second dopant of a ternary system is excited, *e.g.* by means of UV photons, one observes a curve as shown in Fig. 3.13 (a). In contrast, the curve (b) is measured, if the decay of excited states in the first dopant with a subsequent wavelength-shifting process via the second dopant rules the time distribution. These consecutive decays can be described by

$$\frac{\mathrm{d}I(t)}{\mathrm{d}t} = \frac{\exp(-\frac{t}{\tau_1}) - \exp(-\frac{t}{\tau_2})}{\tau_1 - \tau_2} \quad , \tag{3.32}$$

where I is the light intensity normalised to 1 and τ_i are the decay times of the two fluorescent dyes.

This description neglects the rise time of the scintillation process and the decay of primary excited states in the bulk material polystyrene. The time-dependent Förster transfer rate [62, 63] K_{FT} from the polystyrene to the dye (compare Sec. 3.1.1) and the decay rate K_0 for processes which also occur in the absence of the dopant are given by

$$K_{\mathrm{FT}}(t) = k_{\mathrm{FT}}(t) \cdot N_{\mathrm{S}^*}(t) \ , \tag{3.33}$$

$$K_0(t) = k_0 \cdot N_{\mathrm{S}^*}(t) \ , \tag{3.34}$$

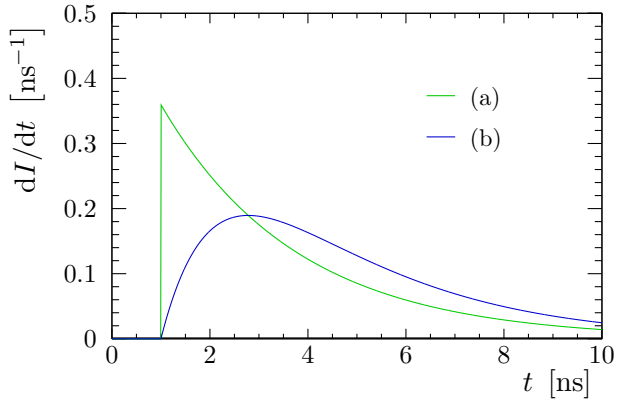

Figure 3.13: Time distribution of photons emitted by a single fluorescent dye (a) and a system of two dyes (b). The used decay time parameters are the fluorescence lifetimes of TPB (2.78 ns) in (a) and (b) and p-terphenyl (1.21 ns) in (b) [33]. The excitation occurs at 1 ns. The total intensity I is normalised to be 1.

with rate coefficients

$$k_{\mathrm{FT}}(t) = \frac{c}{c_0}\,(\tau_0 t)^{-\frac{1}{2}} \ , \tag{3.35}$$

$$k_0 = \frac{1}{\tau_0} \ , \tag{3.36}$$

and the number of excited states in the polystyrene

$$N_{\mathrm{S}^*}(t) = N_{\mathrm{S}^*}(0) \cdot \exp\left(-\frac{t}{\tau_0} - 2\frac{c}{c_0}\sqrt{\frac{t}{\tau_0}}\right) \ . \tag{3.37}$$

In these equations c denotes the concentration of the dopant and τ_0 the lifetime of excited states in the absence of the dye. The so-called critical concentration c_0 of the dye is related to the critical distance R_0 by

$$c_0 = \frac{3}{2}\pi^{-\frac{3}{2}} R_0^{-3} \ . \tag{3.38}$$

The parameter R_0 is defined as the distance between two molecules, where the probability of Förster energy transfer equals the probability of all other decay modes. The time-dependent Förster transfer rate coefficient $k_{\mathrm{FT}}(t)$ and thus the non-exponential decay of excited states as given by Eq. (3.37) follows from the assumption of a uniform statistical distribution of acceptor molecules in the given volume [62].

At high acceptor concentrations the majority of Förster energy transfer will happen within 1 ns. Therefore the shape of scintillation light pulses will be hardly affected by this process and will be dominated by the dopants' decay time constants. In fact, measurements reveal a signal response which can be expressed by Eq. (3.32) [64, 65]. Deviations in the form of an additional slow component are a result of the delayed emission caused by triplet state annihilation [65], see Sec. 3.1.1.

3.2 Fibre Simulation

The mechanisms of energy deposit of particles traversing a scintillating fibre together with the many influences on the light production and propagation shown in the previous section are very complex. Monte Carlo methods are useful to determine the fibre behaviour since an analytical approach is difficult. For this purpose a GEANT4 [29, 30] application has been developed to simulate the processes in a scintillating fibre, which are initiated by a traversing particle.

On the one hand, the simulation aims for a deeper understanding of the general behaviour of scintillating fibres. Manifold properties can be extracted from the simulation output and, in parts, compared with experimental data. Examples are photon path lengths and the resulting propagation times, transmission losses, angular and wavelength distributions and the impact of ionising radiation.

A further goal of the GEANT4 SciFi simulation is the allocation of data, which are used as input for the development of the LHCb SciFi tracking detector. The light pulse shapes, which are recorded at the read-out end of the fibres, and their arrival times affect the design of front-end electronics, since only a restricted time period of 25 ns is available for detection and signal integration (*cf.* Sec. 2.3). The simulation provides signal yields and their fluctuations for single particles depending on their hit position in the detector. These yields may be considered in the overall detector simulation for efficiency, occupancy and, in combination with the time information, spill-over studies. Particularly the degradation of the detector performance in the course of its lifetime, which is caused by ionising radiation, can only be estimated by means of a simulation.

The following section gives a description of the simulation program. In the proximate part of this chapter simulation results and the comparison with theory and experimental data are presented.

3.2.1 The Simulation Program

The GEANT4 SciFi simulation is written in the C++ programming language. The data storage is realised using the ROOT [66] data analysis framework. It was developed with GEANT4 version 9.6 patch 2 and ROOT version 5.34 patch 11.

The program simulates the interaction of particles with a single multi-clad scintillating fibre. While the relative cladding widths, the materials and densities as shown in Tab. 3.1 are implemented in the C++ source code, many other properties are read from text files at the program start. This facilitates flexible use of the application. Different scenarios can be simulated without the need for writing C++ code and compiling it. Reference [67] lists all parameters that are specified via these input text files.

The manufacturer Kuraray does not specify the outer cladding material of their scintillating fibres. However, it is mentioned to be a "fluorinated polymer" [31]. The simulation uses the atomic composition of PTFEMA for the outer cladding, since it

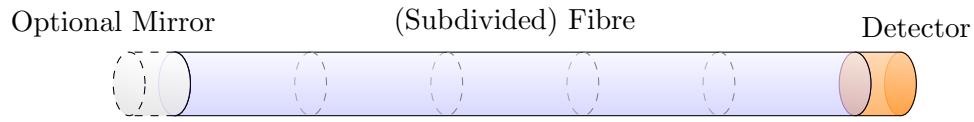

Figure 3.14: Geometry used in the GEANT4 SciFi simulation program comprising a scintillating fibre, a photodetector and an optional mirror. The fibre can be subdivided into sections with different radiation-induced light absorption.

is a common material in fibre optics and its refractive index [40] and density [68] match the values quoted in Tab. 3.1.

Figure 3.14 shows the basic geometry as used in the simulation. At one end face of the scintillating fibre a detector is placed to record incoming photons. The detector material can be chosen as either vacuum or polystyrene. Simulating a detector with properties of vacuum serves to describe the behaviour of photons reaching the fibre end in the case of a small air gap between the fibre and the adjacent medium. The choice of polystyrene will keep the photon momentum as it was in the fibre core, as there will be no Fresnel reflection nor refraction for photons passing from the fibre core to the polystyrene detector. A consideration of materials other than polystyrene can be done with help of recorded photon momentum data.

A mirror with user-defined reflectivity can be set optionally at the opposite fibre end. The number of reflections from the mirror is saved for every photon track that is seen by the detector. Therefore miscellaneous mirror reflectivities can be studied after the simulation run, if this parameter was set to 1 at the program start.

The fibre can be subdivided into an arbitrary number of sections of equal length, *cf.* Fig. 3.14. This allows to simulate inhomogeneous radiation dose profiles along the fibre. For each section the user has to provide a dose level in kGy. User-defined formulae incorporate these numbers for the calculation of radiation-induced absorption in the fibre claddings and core of the respective volume.

The surrounding medium is vacuum. Other materials can be taken into account by adjusting the formula that determines the vacuum's refractive index and its dispersion. In reality most of the light that reaches the fibre surface will be lost due to the poor surface quality, even at an angle of total reflection [64]. The simulation can be adapted to this characteristic by setting the probability of losing a photon at the fibre surface to values in the range from 0 to 1. If the fibre is embedded in a material with a refractive index greater than that of the outer cladding, no total reflection will occur at all.

In the present configuration of the GEANT4 simulation optical photons are subject to the following physics processes.

- Photon generation via
  - *Scintillation*
  - *Cherenkov Radiation*

- Absorption and subsequent generation of a new photon by *Wavelength Shifting (WLS)*
- *Rayleigh Scattering*
- *Absorption*
- Boundary processes
  - *(Fresnel) Reflection*
  - *Fresnel Refraction*
  - *Absorption*

The necessary parameters, *e.g.* the emission and absorption spectra of the scintillation and WLS processes, are made available to the simulation program by means of the mentioned text file, see Ref. [67].

A large data set is acquired during the simulation. Recording numerous parameters of photon tracks seen by the detector enables a variety of studies. These photon parameters are stored in ROOT `TTree` objects and saved to disk in a ROOT data file. While the data of detected photons can be found in the `DetectedPhotons` tree, the properties of photons that are absorbed by the wavelength-shifter are stored in the `OpWlsPhotons` tree. These additional data are necessary to determine the parameters of the full photon track from the location of the primary particle hit to the detector. The detector receives no information about parent particles. Consequently, no information about the absorbed photon is included in the `DetectedPhotons` tree, if the detected photon was generated by the WLS process.

Properties of all optical photons that are created in the simulated events are stored in the `ProducedPhotons` tree. Trapping efficiency studies and comparative analyses of characteristics of primarily generated and detected photons can be conducted with these data. The photon track parameters, which are stored in the `DetectedPhotons`, `OpWlsPhotons` and `ProducedPhotons` trees, are listed in Ref. [67].

Primary particles are specified by `G4GeneralParticleSource` (GPS) macro commands of the GEANT4 toolkit. The commands can be supplied either interactively, when deploying the graphical user interface, or via macro files. The simulation is started in batch mode, if a macro file is provided as an argument at the program call.

A single simulated event is shown in Fig. 3.15. The primary particle is a muon of 200 MeV kinetic energy. A small fraction of the generated photons is trapped and propagates to the mirror and the detector, respectively.

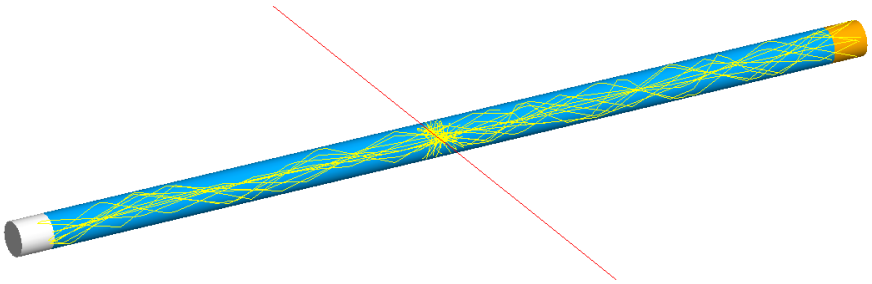

Figure 3.15: Simulated event in a short scintillating fibre (blue). A charged particle (red) crosses the fibre and initiates photon generation. Some of the photons (yellow) are trapped in the fibre and propagate to the mirror (white) and the detector (orange).

3.2.2 Light Collection and Photon Paths

The simulation of a fibre without transmission losses enables the study of light collection and photon paths according to the fibre's geometry and refractive indices. Photons are generated at random distance from the fibre axis, following a uniform distribution over the scintillating core's cross-section. Their momentum directions are distributed isotropically. Only a single photon energy, 2.638 eV (470 nm wavelength), is considered to eliminate the effects of dispersion.

The trapping efficiency $\varepsilon_{\text{trap}}(r, \Delta r)$ is calculated by

$$\varepsilon_{\text{trap}}(r, \Delta r) = \frac{N_{\text{det}}(r, \Delta r)}{p_{\text{gen}}(r, \Delta r)\, N_{\text{gen}}} \ , \tag{3.39}$$

with r being the distance from the fibre axis. $N_{\text{det}}(r, \Delta r)$ is the number of photons that reach one fibre end and originate from

$$r' \in \left[r - \frac{\Delta r}{2}, r + \frac{\Delta r}{2} \right[\ . \tag{3.40}$$

The variables N_{gen} and $p_{\text{gen}}(r, \Delta r)$ denote the total number of simulated photons and their probability to be generated in the interval (3.40). The uncertainty of $\varepsilon_{\text{trap}}(r, \Delta r)$ is estimated by consideration of a binomial distribution.

$$\sigma_{\varepsilon_{\text{trap}}}(r, \Delta r) = \sqrt{p_{\text{det}}(r, \Delta r) \left(1 - p_{\text{det}}(r, \Delta r)\right) N_{\text{gen}}} \ , \tag{3.41}$$

with

$$p_{\text{det}}(r, \Delta r) = \varepsilon_{\text{trap}}(r, \Delta r)\, p_{\text{gen}}(r, \Delta r) \ . \tag{3.42}$$

The obtained trapping efficiencies as a function of r/R, with fibre core radius R, are shown in Figure 3.16. Only photons that do not leave the fibre core are taken into account to study the light collection of a single-clad fibre. To determine the

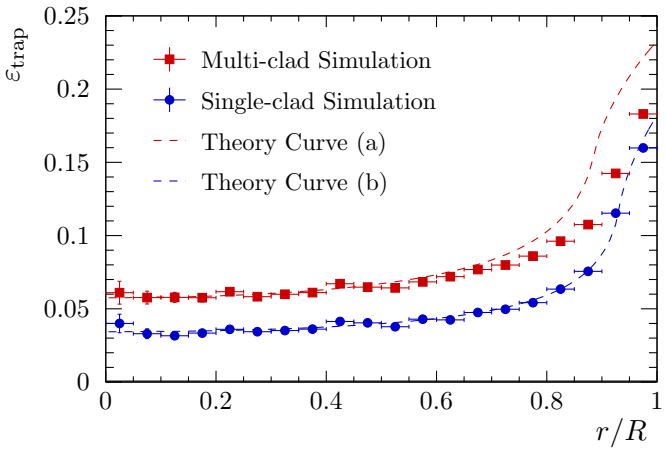

Figure 3.16: Trapping efficiency $\varepsilon_{\text{trap}}$ *vs.* relative distance of the point of photon generation from the fibre axis r/R in single-clad and multi-clad fibres. Theory curves are calculated according to Sec. 3.1.2 with refractive indices of fibre core and (a) outer cladding, (b) inner cladding.

trapping efficiency in a multi-clad fibre, those photons are also considered that may penetrate the inner cladding and undergo total internal reflection at the boundary between inner and outer cladding.

Theory curves are plotted in Figure 3.16 in addition to the values of $\varepsilon_{\text{trap}}$, that are calculated from the simulation output. These curves are obtained by the following method. The ratio of photons that meet one of the two conditions

- being emitted under an angle θ relative to the fibre axis, that is smaller than the angle of total internal reflection θ_{c}
- fulfilling the constraint (3.4)

is calculated as a function of r and θ. A subsequent numerical integration over θ leads to the theoretical trapping efficiency dependent on r.

The simulated trapping efficiencies of a single-clad fibre are well described by the theory curve (b). However, the theoretical description after Sec. 3.1.2 does not account for the refraction of non-meridional light at the boundary between inner cladding and core in multi-clad fibres. Therefore, Figure 3.16 shows a deviation of simulated data points from theory curve (a), which increases with r/R.

A comparison of angular-dependent photon path lengths l from simulation with relation (3.9) is shown in Fig. 3.17a. As in the case of trapping efficiencies, the photons that do not leave the fibre core are well described by the theory curve. The additional photons, that are reflected from the boundary between inner and outer cladding, here referred to as inner-cladding light, or from the fibre surface when being in an air environment, the outer-cladding light, have slightly shorter path lengths. This effect is caused by refraction at the relevant boundaries.

The number of reflections n_{refl} per covered fibre length x of the inner-cladding and outer-cladding photons is decreased by refractions. However, Fresnel reflection

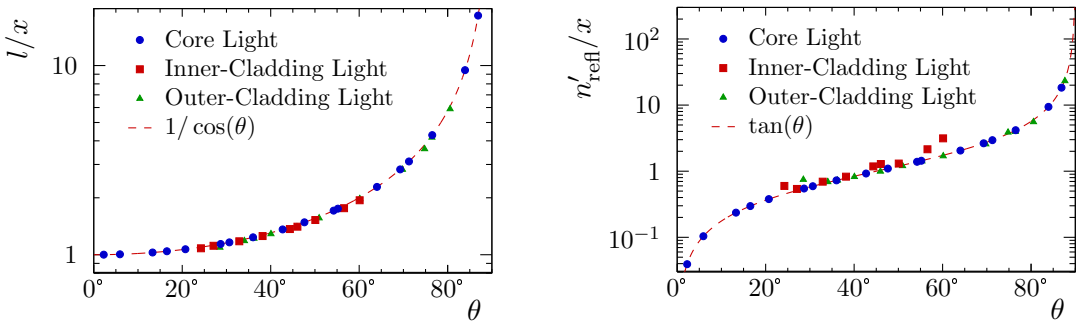

Figure 3.17: Angular dependence of (a) photon path length l and (b) number of reflections n'_{refl} per distance x along fibre axis. For the purpose of clarity, only one randomly chosen data point per 5° and category is drawn.

may occur at interfaces, that are enclosed by those where total internal reflection takes place. This leads to an increase of the number of reflections per length. Hence, deviations from the theory curve (3.10) to smaller and larger values can be expected for inner-cladding and outer-cladding light.

In Figure 3.17b, n'_{refl} is considered instead of n_{refl} to eliminate the dependence on the photon path's minimum distance from the fibre axis r_{min}.

$$n'_{\text{refl}}(x,\theta) = n_{\text{refl}}(x,\theta,r_{\text{min}}) \cdot 2\sqrt{R^2 - r_{\text{min}}^2} = x\tan(\theta) \tag{3.43}$$

The value of R is given by the radius of the outermost boundary that can be reached by core, inner-cladding and outer-cladding light, respectively. Obviously, the number of reflections, and thus the total number of boundary processes, is more influenced by the angle θ than the path length.

The distribution of simulated photon path lengths in Figure 3.18 shows a long tail of large l/x for core and outer-cladding light. In contrast, the distribution of inner-cladding light paths appears to be restricted. This effect can be explained by the non-parallel surface normals at the points where the photons meet the interfaces between core, inner and outer cladding. As a further consequence, inner-cladding light is only observed at angles less than about 65°, *cf.* Fig. 3.17, 3.20.

The fraction of path length covered in the fibre core l_{core}/l of inner-cladding and outer-cladding light is well below 1 due to the non-negligible cladding widths. Therefore, the differences in absorption and radiation damages of core and cladding materials have to be considered for a realistic simulation as well as in the analysis of measured data. The distribution of l_{core}/l is visualised in Fig. 3.19.

The isotropic emission of photons results in angular distributions whose sum corresponds to a sine shape for angles smaller than the critical angle θ_{c} of the considered photons, see Figure 3.20. The number of photons decreases rapidly with θ exceeding θ_{c}. According to (3.4), the distribution function of core light is non-zero at 90°. Also some of the outer-cladding photons, that are emitted at 90°,

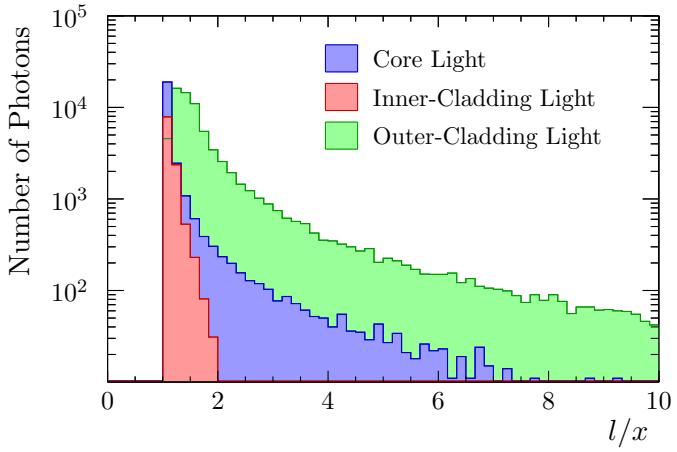

Figure 3.18: Distribution of photon path length l per distance x along fibre axis.

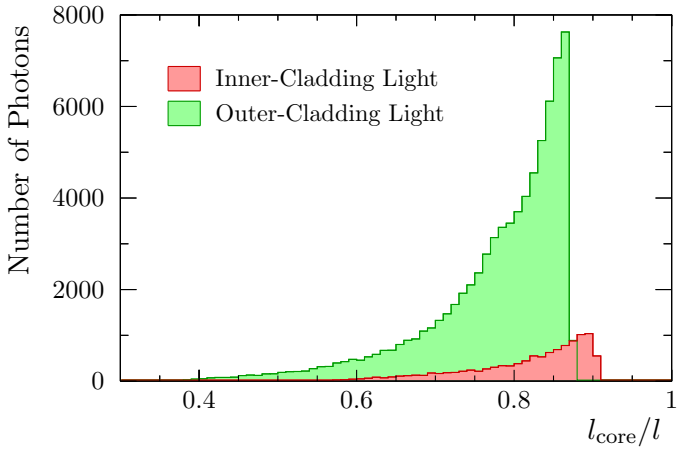

Figure 3.19: Distribution of path length covered in fibre core l_{core} relative to total path length l.

are trapped in the fibre. This is not the case for the inner-cladding light, though, whose maximum angle is about 65° as mentioned above.

Figure 3.21 shows the distribution of the number of total internal reflections $n_{\mathrm{refl,tot}}$, which a photon undergoes while covering a distance x in fibre axis direction. The high number of reflections per meter necessitates a high quality of the boundaries of core and claddings. Already a small deviation of the reflectivity from 1 will result in significant transmission losses, compare Section 3.2.3.

The density of photons far from the excitation point relative to the fibre radius is non-uniform over the fibre cross-section. The majority of photons appears at the outer part of the fibre core, close to the core-cladding interface. Figure 3.22 illustrates this distribution accounting for core and inner-cladding light only.

The only influences on the photon path discussed so far in this section are refractions and reflections at the material interfaces. However, the wavelength-shifting process and Rayleigh scatterings will also affect the photon momentum

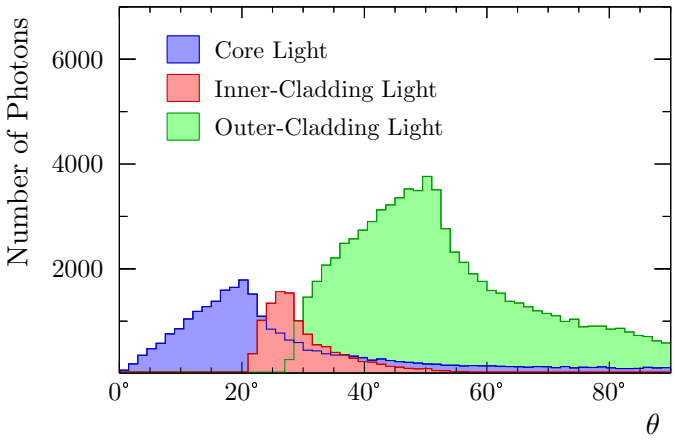

Figure 3.20: Angular distribution of photons trapped in the fibre.

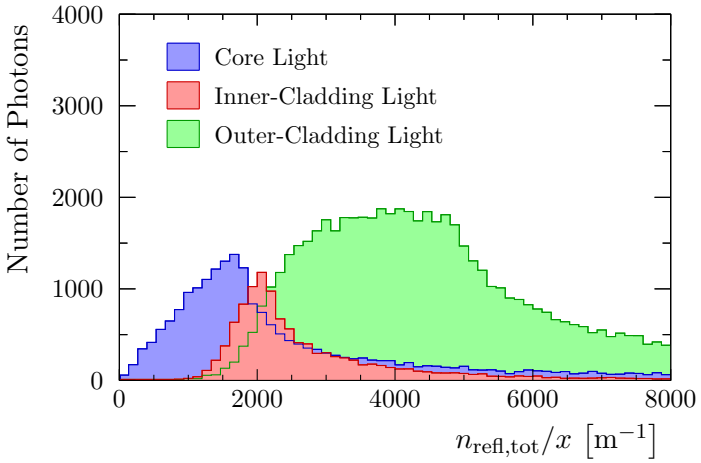

Figure 3.21: Distribution of the number of total internal reflections $n_{\mathrm{refl,tot}}$ per distance in fibre axis direction x.

direction. Their impact is studied by counting the occurrence of these processes on the path from primary photon emission to detection at 1 m distance from the excitation point. For this purpose, a simulation was conducted with consideration of the loss factors of a scintillating fibre from Kuraray of type SCSF-78MJ as discussed in Sec. 3.1.3. The exciting particles are minimum ionising muons with random distance from the fibre axis.

The results are shown in Figure 3.23. About 4 % of detected photons were Rayleigh scattered, 5 % have experienced more than one WLS process. Thus, only small deviations from the presented path length and angular distributions are expected due to these processes. The impact of the primary WLS process on the trapping efficiency will be discussed in Section 3.2.4.

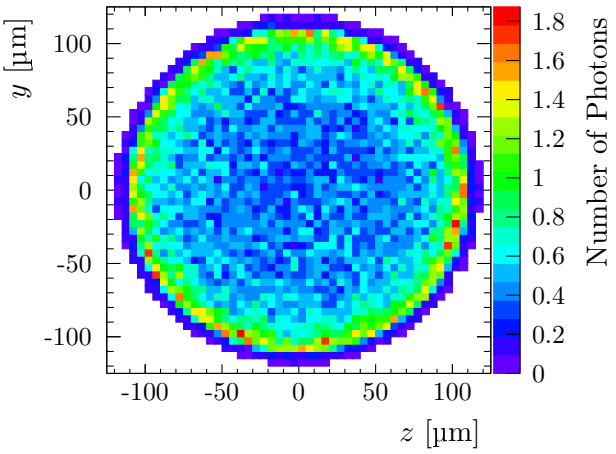

Figure 3.22: Photon density in fibre cross-section at $x = 0.499\,\mathrm{m}$. The number of photons per bin is given per thousands of their total number.

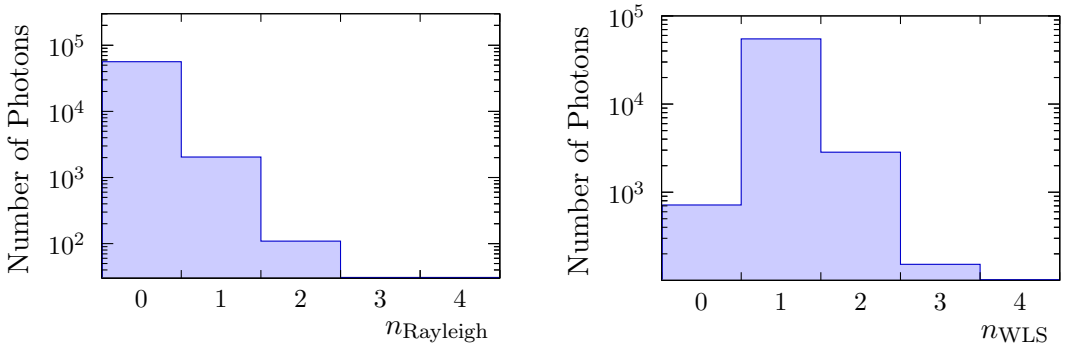

Figure 3.23: Number of (a) Rayleigh scatterings n_{Rayleigh} and (b) wavelength-shifting processes n_{WLS} occurring on the path from primary photon emission to detection.

3.2.3 Transmission Loss and Wavelength Spectra

The number and wavelength spectrum of photons that can be detected at the fibre end is significantly affected by transmission losses. Figure 3.24 illustrates the wavelength spectra generated by the physical processes in a simulated scintillating fibre from Kuraray of type SCSF-78MJ. The scintillation light, which is emitted by the first dye, will be absorbed by the wavelength-shifting second dye. The shorter wavelength part of the spectrum emitted by the WLS dye is completely extinguished after short fibre lengths due to self-absorption. In addition to scintillation light, a traversing charged particle also produces Cherenkov light. This light may be detected at the fibre end, too, but its intensity is only a few percent of the scintillation light intensity.

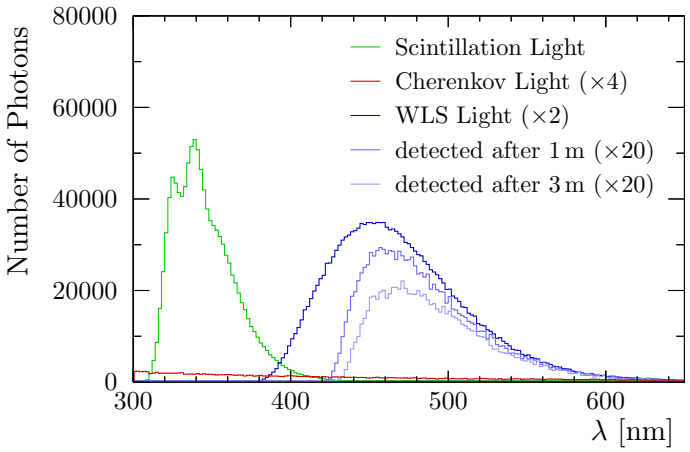

Figure 3.24: Wavelength spectra generated by physical processes in a simulated scintillating fibre of type SCSF-78MJ. Minimum ionising muons serve as exciting particles. Apart from scintillation light data, all distributions are multiplied by a scale factor (quoted in parentheses) to be distinguishable.

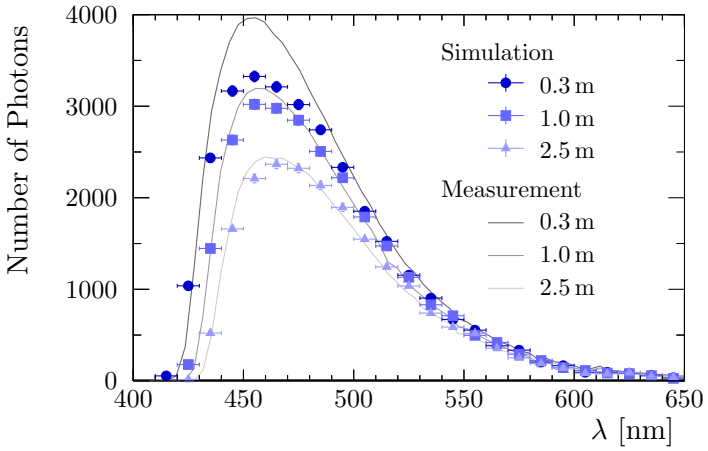

Figure 3.25: Wavelength spectra of photons arriving at the fibre end. Three distances of the excitation point from the fibre end are investigated. Measured curves are scaled in order that simulated and measured data have the same integral at 1 m. Measured data are obtained from Ref. [58].

A comparison of simulated and measured wavelength spectra of photons that have left one fibre end is shown in Fig. 3.25. The simulation only accounts for photons whose angle θ of their momentum direction relative to the fibre axis is less than 12.7° in air. This constraint considers the numerical aperture of the Hamamatsu C10083CA-2050 photospectrometer [53], which is used for the measurements [58]. The simulated data set comprises core and inner-cladding light, only. The measured curves are scaled by a factor, which provides equal integrals over simulated and measured data points at 1 m distance from the excitation point to the fibre end.

While the general shapes of measured and simulated spectra are in good agreement, the signal amplitudes due to the chosen scaling of measured data diverge at 0.3 m. The measured signal exceeds the simulation by 11 %. In contrast, the integrated intensities of measurement and simulation at 2.5 m distance differ only by 0.3 %.

The possible reasons for this divergence are manifold. For example, a small damage or poor fibre quality in the range of 0.3 m to 1.0 m from the fibre end could cause an attenuation which is higher than expected from the simulation. The consideration of outer-cladding light, which is not included in the simulated data, as well as a wider range of angles would increase the ratio of detected photons at 0.3 m and 1.0 m, too. Angles θ, that are larger than according to the numerical aperture of the photospectrometer, could be detected due to possible scattering at the fibre end face or other imperfections of the coupling of fibre and measuring device.

In Section 3.1.3, an attenuation coefficient a_i is employed to describe the deviation of light loss in the scintillating fibre SCSF-78MJ from pure polystyrene, see Equation (3.30) and Figure 3.8. The effect of this additional transmission loss factor compared to only intrinsic losses, including absorption by the wavelength-shifter, is shown in Figure 3.26. The number of detected photons is illustrated as a function of the distance x of the photodetector from the excitation point under several conditions. The shown fit curves and considered transmission losses are explained in the following.

Scintillating fibres are often characterised by fitting an exponential function to measured light intensities at certain distances x. By this means, the attenuation length Λ, as defined in Equation (3.44), is determined. The variable N denotes the number of photons or equivalently the light intensity.

$$N(x) = N_0 \exp\left(-\frac{x}{\Lambda}\right) \tag{3.44}$$

Dashed curves in Figure 3.26 show function (3.44) fitted to the respective data points in $x \in [1\,\mathrm{m}, 3\,\mathrm{m}]$. Resulting N_0 and Λ are given in Table 3.10.

In Figure 3.26a one can see that an observed light attenuation, as expected due to an additional absorption a_AA in the fibre material, can also be a result of a non-zero probability p_BL for photon loss at the material boundaries. The value of a_AA is taken from the fit result for p_{19} in Table 3.5 and can be found in Table 3.9. The probability of photon loss p_BL is applied at every photon hit on a material boundary, *i.e.* also at refraction, not only at reflection. Like a_AA, its value is specified in Table 3.9. Furthermore, Table 3.9 provides θ_max, which is the maximum angle θ of the photon momentum relative to the fibre axis measured in polystyrene, that is considered in the plotted data of the respective figure.

Data presented in Fig. 3.26a correspond to $\theta < 8°$. This constraint considers the numerical aperture of the spectrometer, whose measured data are used to obtain the value of a_i and therefore a_AA, *cf.* Sec. 3.1.3.

Without a restriction in θ, the same values of a_AA and p_BL as used in Fig. 3.26a result in differing light attenuations, see Fig. 3.26b and Tab. 3.10. The attenuation length due to boundary loss is only 62 % of the attenuation length caused by an

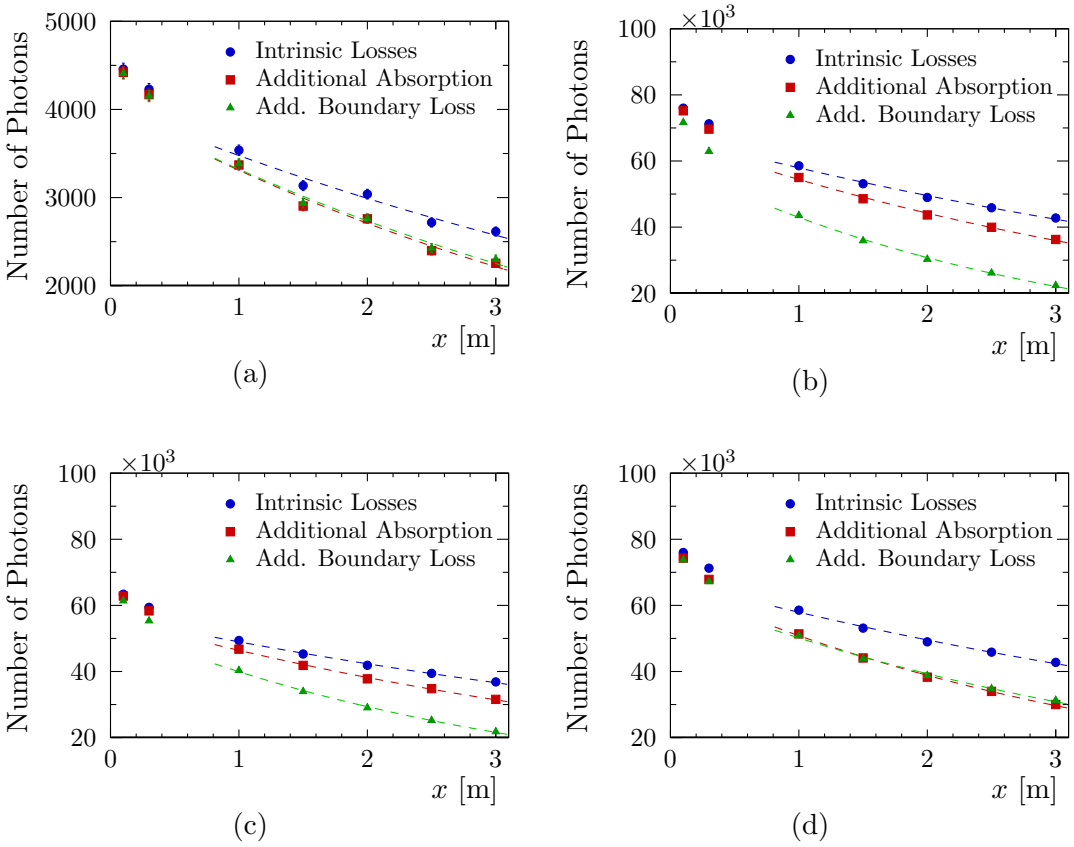

Figure 3.26: Number of detected photons dependent on distance x of excitation point from photodetector. Data points are due to parameters in Tab. 3.9. Figures (a) to (d) correspond to different angular acceptances of the photon detection and different magnitudes of light absorption in the fibre material and loss at boundaries, additional to intrinsic losses. Dashed lines result from fitting an exponential function (3.44) for $x \in [1\,\mathrm{m}, 3\,\mathrm{m}]$.

Table 3.9: Simulation parameters of data shown in Fig. 3.26.

Figure	a_{AA} [m^{-1}]	p_{BL}	$\theta_{\max}$
(a)	$4.65 \cdot 10^{-2}$	$5 \cdot 10^{-5}$	8°
(b)	$4.65 \cdot 10^{-2}$	$5 \cdot 10^{-5}$	90°
(c)	$4.65 \cdot 10^{-2}$	$5 \cdot 10^{-5}$	39°
(d)	$1.00 \cdot 10^{-1}$	$2 \cdot 10^{-5}$	90°

Table 3.10: Results of fitting Eq. (3.44) to data shown in Fig. 3.26.

Figure	Transmission Losses	N_0 [10^3]	Λ [m]
(a)	intrinsic	4.04 ± 0.10	6.64 ± 0.51
	additional absorption	4.05 ± 0.10	4.98 ± 0.30
	additional boundary loss	4.04 ± 0.10	5.14 ± 0.32
(b)	intrinsic	67.72 ± 0.40	6.40 ± 0.12
	additional absorption	66.94 ± 0.41	4.82 ± 0.07
	additional boundary loss	59.94 ± 0.43	3.00 ± 0.03
(c)	intrinsic	56.64 ± 0.36	6.87 ± 0.15
	additional absorption	56.39 ± 0.37	5.13 ± 0.09
	additional boundary loss	54.33 ± 0.40	3.25 ± 0.04
(d)	intrinsic	67.72 ± 0.40	6.40 ± 0.12
	additional absorption	66.54 ± 0.43	3.71 ± 0.04
	additional boundary loss	63.94 ± 0.41	4.12 ± 0.05

additional absorption. This is a consequence of the strong dependence of the number of boundary processes on θ, compare Fig. 3.17. The values of Λ for intrinsic losses and additional absorption do not show strong variations for different $\theta_{\max}$.

The value of $\theta_{\max}$, that is equivalent to the critical angle of total internal reflection at the interface between polystyrene and air with refractive indices $n_{\mathrm{PS}} = 1.6$ and $n_{\mathrm{Air}} = 1$, leads to photon numbers shown in Fig. 3.26c. Therefore, the plotted data correspond to detectable photons, if an air medium is adjacent to the fibre end face and Fresnel reflections are ignored. As it was the case in Fig. 3.26b, the light attenuation is significantly higher for the considered boundary losses compared to the additional absorption.

Attenuation length measurements at real SCSF-78MJ fibres reveal Λ values in the range of 3 m to 4.5 m, with photosensors attached to the fibre end. Since these values are smaller than those observed with the Hamamatsu C10083CA-2050 photospectrometer, boundary loss is assumed to be at least partially responsible for light attenuation, which occurs in addition to intrinsic losses.

Figure 3.27 shows the effect of transmission loss on photon path length and angular distributions. Values of a_{AA} and p_{BL}, that lead to a realistic attenuation length and similar photon numbers, see Fig. 3.26d and Tab. 3.9, 3.10, were chosen for analysing the impact of an additional absorption or boundary imperfections, respectively.

As expected, the path length distribution becomes narrower with increasing x. However, it is more affected by boundary loss compared to additional absorption. The angular distribution is hardly influenced by intrinsic losses and further absorptions, while boundary imperfections lead to a shift to smaller angles.

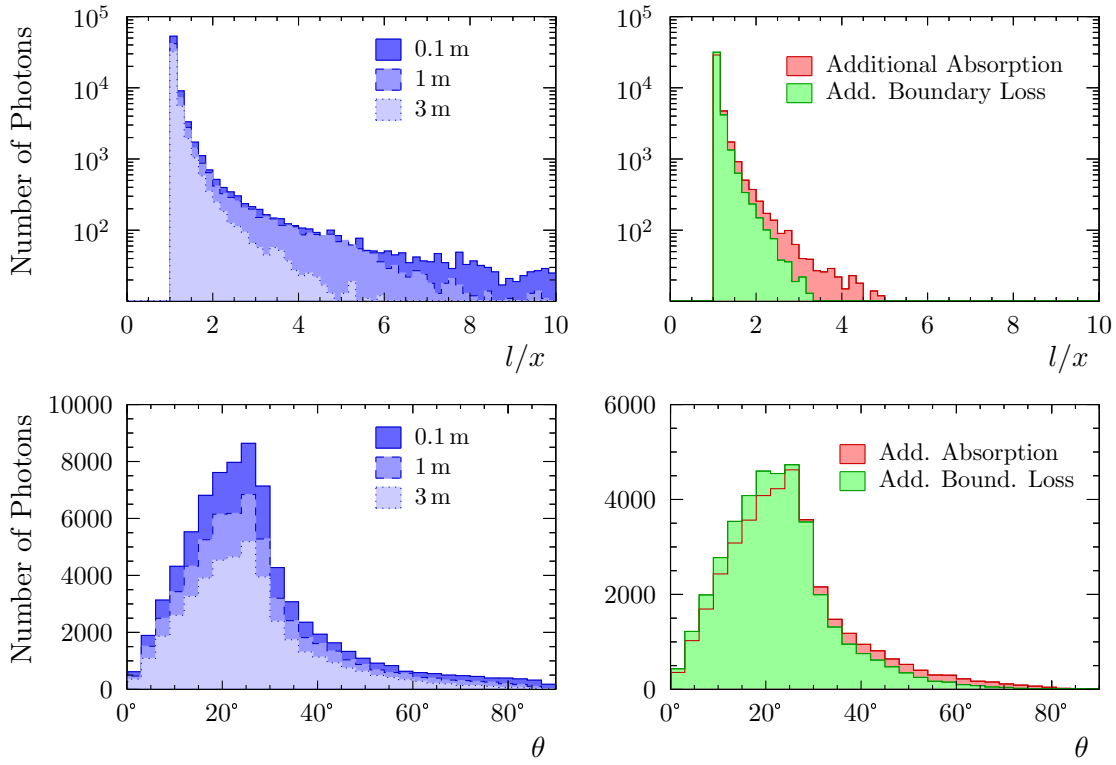

(a) Intrinsic light loss.

(b) Additional loss factors.

Figure 3.27: Distributions of photon path length l per distance x along fibre axis and angle θ . Column (a) shows the dependency on x for three exemplary distances considering only intrinsic light loss. Column (b) visualises distributions due to additional absorption and boundary imperfections, respectively, at $x = 2\,\mathrm{m}$.

A similar behaviour is visible in the probability ε, that a photon reaches one fibre end, shown in Fig. 3.28. The dependency of ε on the relative distance r/R of the photon emission from the fibre axis shows a similar trend with or without intrinsic losses being considered. This dependency on r/R decreases when boundary imperfections are taken into account. Trapped photons, that have been emitted at large r/R, can have larger values of θ (*cf.* Eq. (3.4)) and thus a higher probability to be lost. Consequently, the distribution of photons over the fibre cross-section at its end face is more homogeneous with boundary loss considered instead of an additional absorption, see Fig. 3.29.

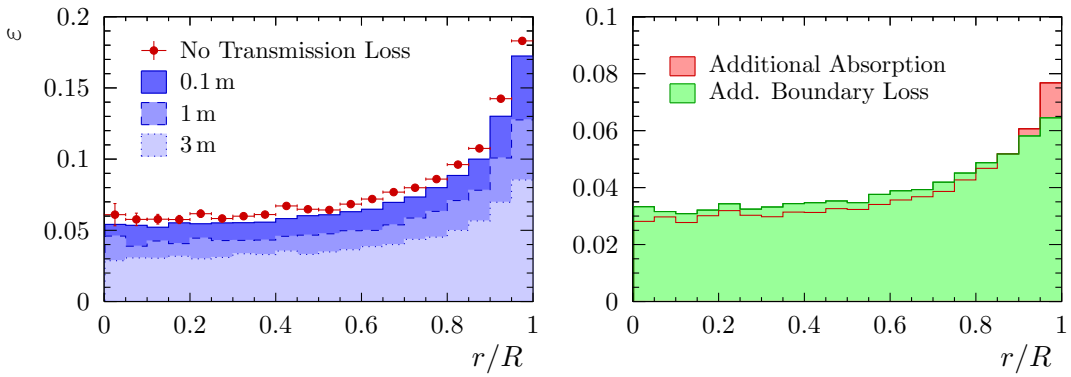

(a) Intrinsic light loss. (b) Additional loss factors.

Figure 3.28: Probability ε of photons to reach the fibre end *vs.* relative distance r/R of emission from fibre axis. (a) shows the dependency on x for three exemplary distances considering only intrinsic light loss. (b) visualises distributions due to additional absorption and boundary imperfections, respectively, at $x = 2\,\mathrm{m}$.

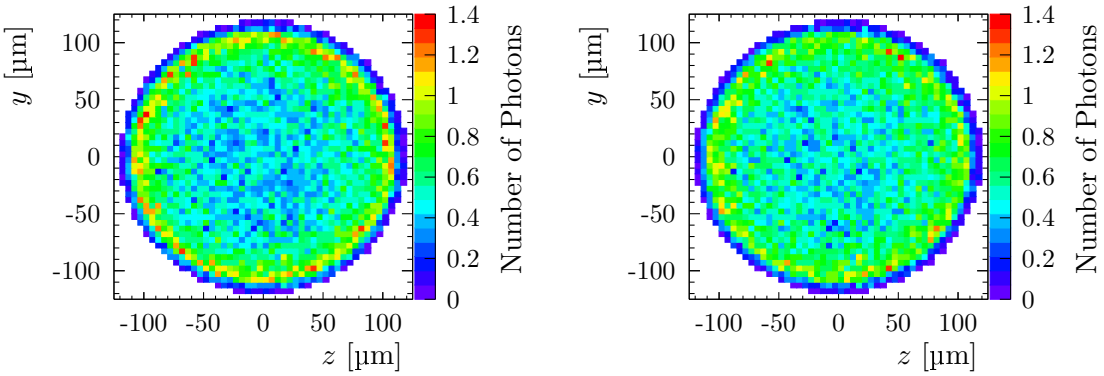

(a) Additional absorption. (b) Additional boundary loss.

Figure 3.29: Cross-sectional distribution of photons at 2 m from the excitation point with extra absorption or boundary loss added to intrinsic photon loss. The number of photons per bin is given per thousands of their total number.

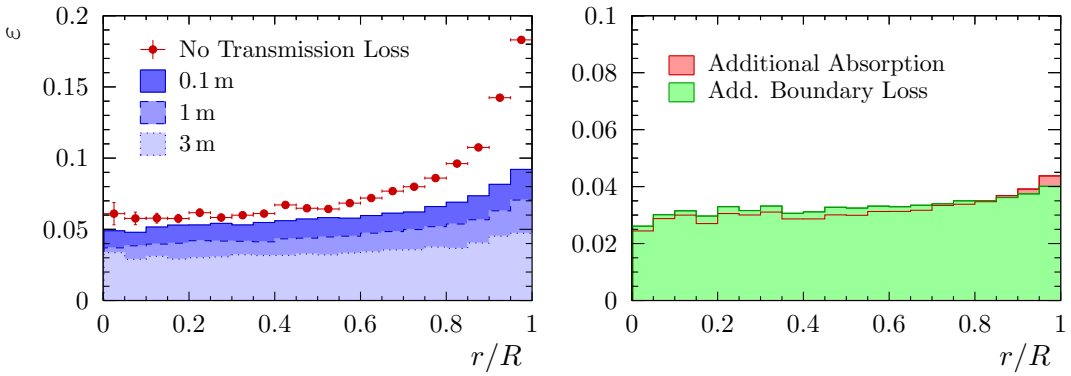

(a) Intrinsic light loss. (b) Additional loss factors.

Figure 3.30: Probability ε of photon detection at the fibre end *vs.* relative distance r/R of primarily emitted scintillation photon from fibre axis. (a) shows the dependency on x for three exemplary distances considering only intrinsic light loss. (b) visualises distributions due to additional absorption and boundary imperfections, respectively, at $x = 2\,\mathrm{m}$.

3.2.4 Dye Concentrations

The detection efficiency ε in Fig. 3.28 is shown as a function of the point of emission of the detected photon. However, almost 100 % of detected photons were emitted by the wavelength-shifting secondary dye, compare Fig. 3.23. Thus, their emission point is different from the origin of the primary scintillation photon, which is absorbed by the wavelength-shifter.

Figure 3.30 illustrates the dependence of detection efficiency on the origin of the primarily emitted scintillation photon. In comparison with Fig. 3.28, the curve increases less at r/R values close to 1. This is caused by the increasing probability of photons to leave the fibre before being absorbed by the WLS dye at closer distances to the surface. The magnitude of this effect is dependent on the amount of the secondary dye, which is dissolved in the fibre core material.

The influence of the concentration of the secondary dye on light yield and transmission loss is studied by variation of the WLS absorption strength, which is used in the simulation. Three values, which correspond to half, nominal and double dye concentration of Kuraray's SCSF-78MJ fibre, are investigated[1]. The resulting distributions of the origin of scintillation photons, that are absorbed by the WLS dye, and of the point of absorption (with subsequent emission) are shown in Fig. 3.31. At a constant number of simulated MIPs traversing the fibre, the total number of wavelength-shifted photons increases with dye concentration. The most homogeneous distribution is achieved with the highest WLS concentration.

Table 3.11 lists the fraction $n_{\mathrm{WLS}}/n_{\mathrm{scint}}$ of scintillation photons, that are absorbed by the wavelength-shifter. Figures in this section do not account for outer-cladding light, since it might be lost due to the fibre's surrounding medium. Fibres are

[1]Dye concentrations of SCSF-78MJ are known from Ref. [69]

Table 3.11: Fraction $n_{\mathrm{WLS}}/n_{\mathrm{scint}}$ of scintillation photons absorbed by WLS dye in SCSF-78MJ fibre with 250 µm diameter at different dye concentrations. Values including outer-cladding light correspond to possible total internal reflection at the surface of a fibre in air.

Concentration	$n_{\mathrm{WLS}}/n_{\mathrm{scint}}$	
	excluding outer-cladding light	including outer-cladding light
double	0.88	0.94
nominal	0.79	0.89
half	0.66	0.83

Table 3.12: Results of fitting (3.44) to data shown in Fig. 3.32.

Dye concentration	N_0 [10^3]	Λ [m]
double	74.7 ± 1.2	5.99 ± 0.30
nominal	67.9 ± 1.0	6.35 ± 0.31
half	59.7 ± 1.1	6.16 ± 0.35

often tested in air, though. For this reason, Table 3.11 also provides values of $n_{\mathrm{WLS}}/n_{\mathrm{scint}}$ that are obtained, if total internal reflection at the outer cladding surface is considered.

The striped pattern of the distributions of scintillation light origins in Figure 3.31 is a result of the excitation by MIPs. For this study, minimum ionising muons were generated at random minimum distance y from the fibre axis with parallel momentum directions. Scintillation photons are generated due to the energy deposit at the MIPs' paths through the fibre core. The WLS process smooths this distribution so that the striped pattern disappears in the plots on the right of Fig. 3.31.

The number of photons that can be detected at distance x from the excitation point is shown in Fig. 3.32. Only intrinsic light loss is considered in the plotted data. An exponential function according to Eq. (3.44) is fitted to data points with $x \in [1\,\mathrm{m}, 3\,\mathrm{m}]$. The resulting parameters N_0 and Λ can be found in Table 3.12. The values of N_0 clearly depend on the concentration of the secondary dye. However, the self-absorption of the wavelength-shifter, which increases with concentration, does not lead to significant differences in the attenuation length Λ. Therefore, particle detection with 250 µm thick SCSF-78MJ fibres might benefit from increased dye concentrations compared to the nominal.

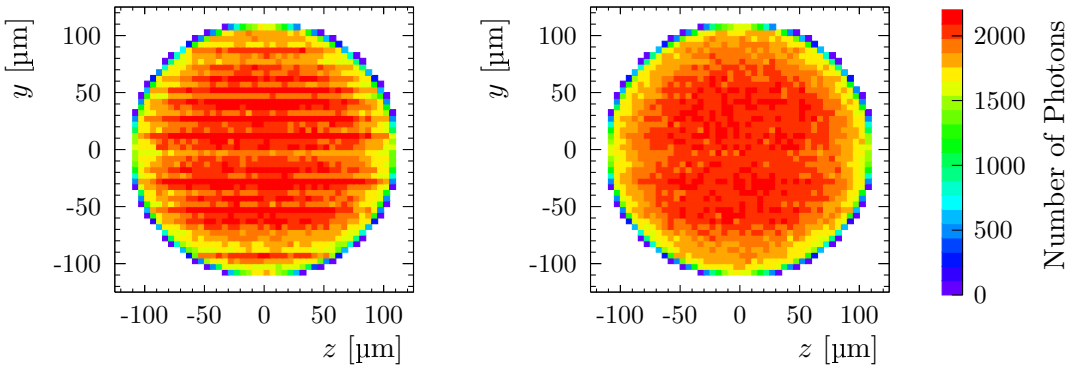

(a) Double WLS Concentration.

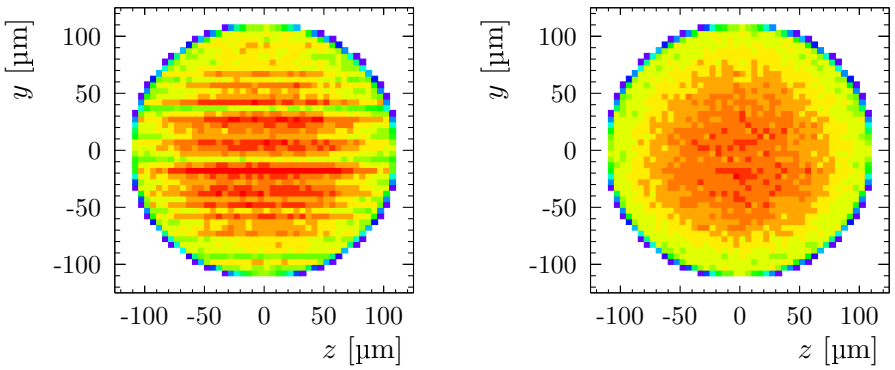

(b) Nominal WLS Concentration.

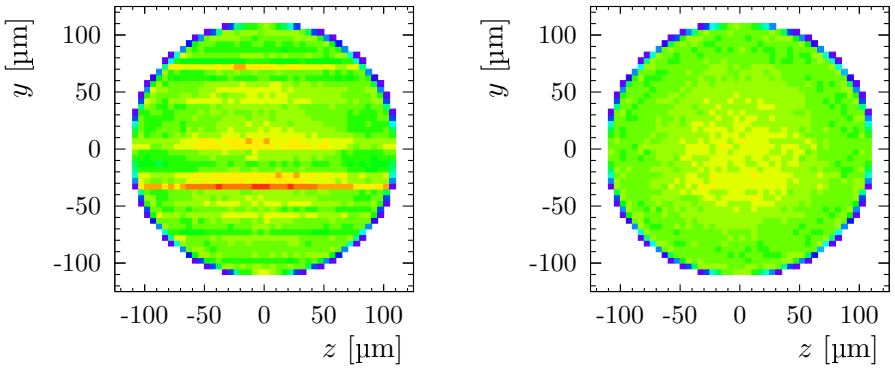

(c) Half WLS Concentration.

Figure 3.31: Distribution of origin of scintillation photons that are absorbed by secondary dye (left column) and of point of their absorption with subsequent photon emission (right column) in fibre cross-section for different secondary dye concentrations in SCSF-78MJ fibre.

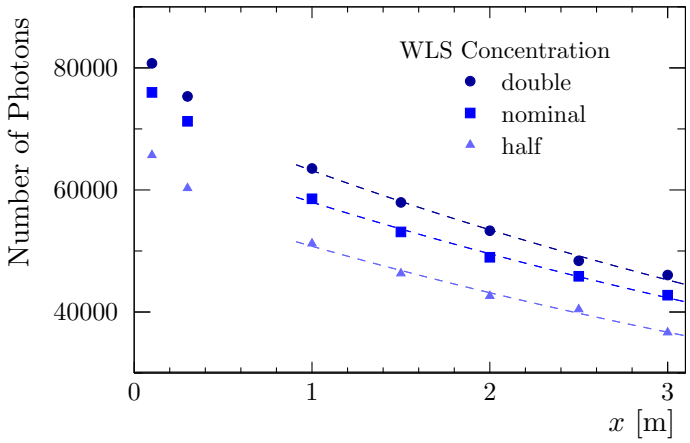

Figure 3.32: Number of detected photons dependent on distance x from excitation point for three dye concentrations. Dashed lines result from fitting an exponential function (3.44) at $x \in [1\,\mathrm{m}, 3\,\mathrm{m}]$.

3.2.5 Fibre Response to Particles

The signal response of scintillating fibres to traversing particles generally depends on the energy deposit specific to the particle's type and energy. Besides the total number of generated scintillation photons per particle hit, the distribution of the photon emission points' distance r from the fibre centre may differ among different particle types. As shown in the previous sections, the value of r is correlated with trapping efficiency, angular and therefore path length distributions as well as with the number of reflections and refractions a photon undergoes. Thus, the light attenuation along the fibre, which is obtained from measurements, may depend on the particles used to excite the scintillation process.

Figure 3.33 shows the simulated distribution of photon emission by the wavelength-shifting dye in a scintillating fibre of type SCSF-78MJ from Kuraray after excitation by different particles. All particles were generated at a fixed positive value of z close to the fibre surface. The value of y was set randomly following a uniform distribution in the range from $-125\,\mu\mathrm{m}$ to $125\,\mu\mathrm{m}$, which corresponds to the fibre radius. The particles' momentum direction at generation time is parallel to the z-axis in its negative direction. Considered particles are minimum ionising, mono-energetic muons ($E_{\mathrm{kin}} = 200\,\mathrm{MeV}$), electrons with energy spectrum of a ^{90}Sr source (*cf.* Appendix A) and mono-energetic UV photons ($E = 3.351\,\mathrm{eV}$ corresponding to $\lambda = 370\,\mathrm{nm}$). The simulated scintillating fibre is placed in vacuum.

Minimum ionising muons lose only a small fraction of there total kinetic energy in the thin fibre. Hence, their trajectory remains approximately unaffected and the probability of energy loss is constant along their path through the fibre core. The resulting energy deposit is constant over the fibre cross-section and the distribution of photon emission by the WLS dye in Fig. 3.33a exhibits a rotational symmetry around the fibre axis x, compare Sec. 3.2.4.

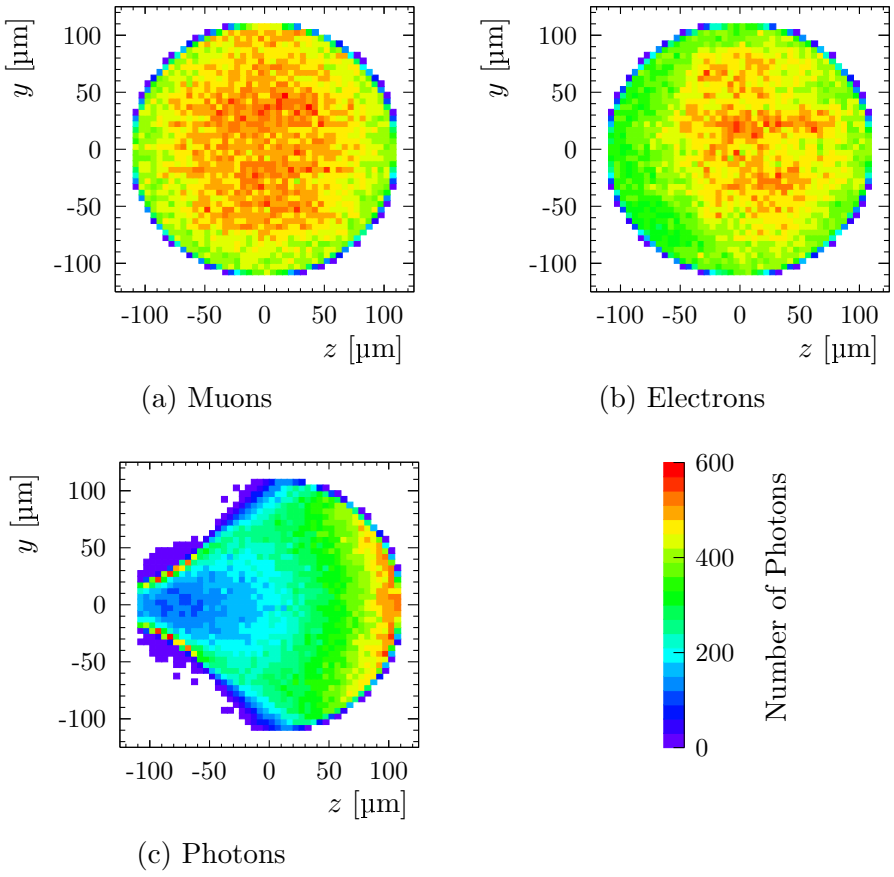

Figure 3.33: Distribution of photon emission by secondary dye in fibre cross-section after excitation of the scintillation process by minimum ionising muons, electrons from ^{90}Sr source and direct excitation of the dye by mono-energetic UV photons. Particles are generated at the right side of the fibre with momentum direction parallel to the z-axis.

Many of the simulated electrons experience multiple scattering or are even absorbed in the fibre due to their energy spectrum. Thus, the photon distribution in Fig. 3.33b is less homogeneous than that of simulated muons. For UV photons the circular fibre cross-section acts as a lens. It follows that parts of the fibre cannot be reached by UV photons and therefore do not emit WLS light.

Despite the diverse distributions of photon emission in the fibre cross-section, the distributions of r/R shown in Fig. 3.34 are similar for the three reviewed particle species. Here the distance of photon emission from the fibre axis r is normalised by the fibre core radius R. The distributions are comparable with a uniform emission over the cross-section.

The ratio of photons that is emitted from a particular interval of r/R depends on the concentration of the WLS dye. The r/R distributions of muons and electrons will approach the linear curve of uniform emission with increasing dye concentration, *cf.* Fig. 3.31. Other effects occur in the case of UV photons. The peak around

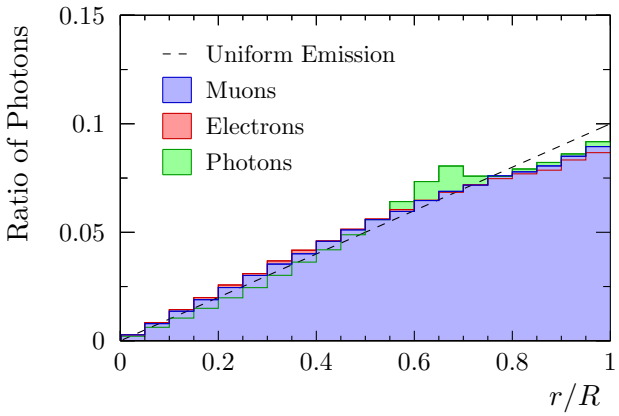

Figure 3.34: Ratio of photons emitted from particular interval of r/R of width 0.05 after excitation by minimum ionising muons, electrons from ^{90}Sr source and mono-energetic UV photons. The dashed line denotes a distribution according to uniform photon emission over the fibre core cross-section.

$r/R = 0.65$, which is a consequence of the light refraction due to the circular cross-section, grows with decreasing dye concentration. It diminishes at higher WLS concentration, while at the same time an excess beyond the distribution of a uniform emission appears at values close to $r/R = 1$. This is caused by the increased probability to be already absorbed by the WLS dye after a short path length in the fibre core.

According to the distributions shown in Fig. 3.34, it can be expected that light attenuation measurements at SCSF-78MJ fibres will lead to comparable results when performed by means of a ^{90}Sr source placed close to the fibre or excitation via a UV LED. The obtained parameters should also be comparable to a fibre excited by particles with small energy deposit such as MIPs, cosmic muons or high-energetic particles which are of interest in a particle physics experiment. This assumption is not necessarily valid if a UV LED is utilised and the fibre has either a WLS dye concentration diverging from the nominal or is not placed in vacuum or air, *e.g.* if it is glued.

The number of photons created by minimum ionising muons in a single fibre is shown in Figure 3.35a. The light yield is set to 8 photons per keV deposited energy. Muons are generated at random minimum distance y of their trajectory from the fibre axis with momentum direction perpendicular to this axis.

The underlying Landau distribution of energy deposition in the fibre core is visible in the right plot of Fig. 3.35a where $|y|$ and therefore the MIP's path length in the core s are constrained. The original Landau distribution of energy deposition is widened by randomising the number of scintillation photons according to a Gaussian distribution whose mean is proportional to the energy deposit. The square root of the mean is chosen as width of the Gaussian distribution. This procedure is motivated by the fact that only a small fraction of energy loss will emerge as scintillation photons.

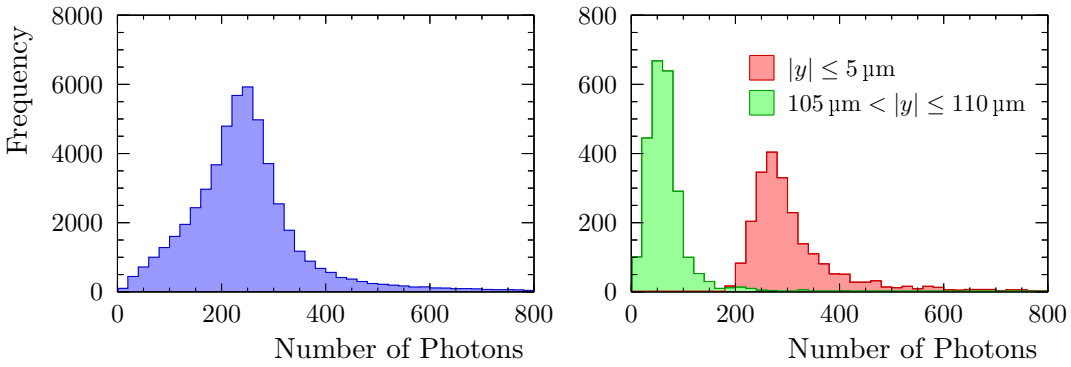

(a) Produced

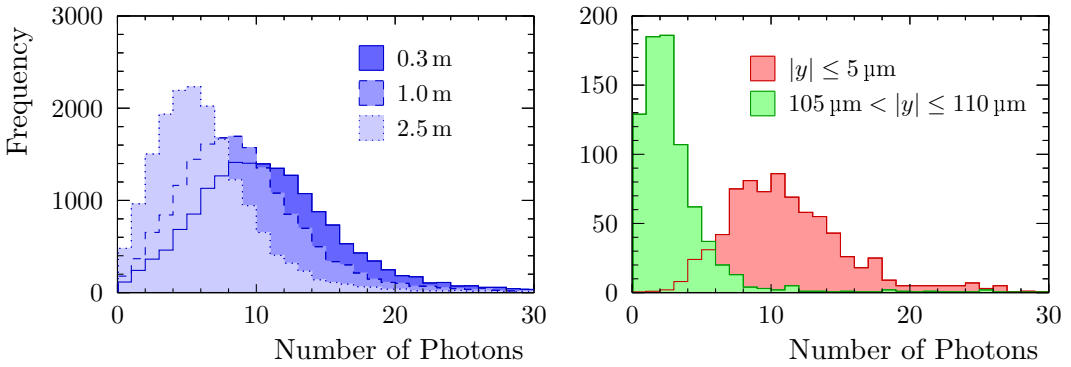

(b) Arriving at fibre end

Figure 3.35: Number of photons produced and arriving at one fibre end per MIP crossing the scintillating core. The number of photons arriving at the fibre end with no restriction of the MIP's minimum distance from the fibre axis $|y|$ (left) are determined for three distances x of the excitation point from the fibre end. Distributions of arriving photon numbers with restricted $|y|$ (right) are obtained at $x = 1.0\,\mathrm{m}$.

As one can expect, the mean number of photons created by a MIP obtained from the simulation follows a curve that is proportional to the particle's path length in the scintillating core s, see Figure 3.36a. The path length is calculated by

$$s(y) = \sqrt{R^2 - y^2}\ . \tag{3.45}$$

The tail at lower photon numbers in the distribution on the left of Fig. 3.35a is a result of shorter path lengths s occurring less frequently than longer when y follows a uniform distribution.

According to the fibre's trapping efficiency and its light attenuation, only a small fraction ε of the number of photons created by a MIP will reach the fibre end. This leads to a further increase of the width of the photon number distribution relative to its mean, see Fig. 3.35b. The value of ε is plotted *vs.* $|y|$ in Fig. 3.36b.

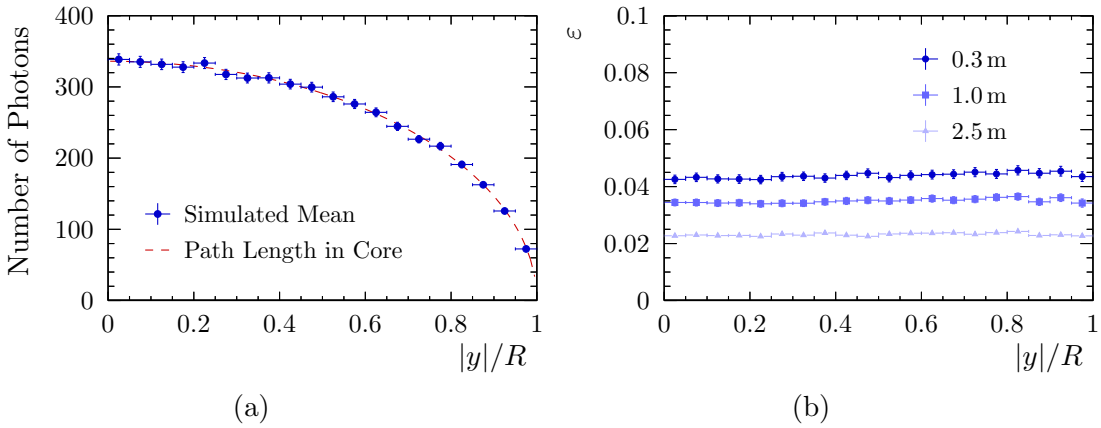

Figure 3.36: Dependencies of mean number of produced photons per MIP (a) and ratio of photons reaching one fibre end ε (b) on distance $|y|$ of the MIP's trajectory from fibre axis. The dashed line in (a) shows a trend proportional to the MIP's path length in the fibre core. Values in (b) are obtained at three distances x of the excitation from the fibre end.

At all three considered distances from the excitation point, ε exhibits only a small dependency on $|y|$. This observation can be explained by two facts. On the one hand, the detector material adjacent to the fibre end was vacuum in the underlying simulation run. Thus, photons with large angle θ relative to the fibre axis will not be able to leave the fibre end due to total internal reflection. However, photons with θ larger than the angle of total internal reflection are responsible for the increase of ε with distance r of the photon's point of emission from the fibre axis, *cf.* Eq. (3.4). On the other hand, the MIP trajectories each cover a range of r, which always comprises the fibre core radius R. Consequently, the curve of ε *vs.* $|y|$ is more even than ε *vs.* r, shown in Fig. 3.30b.

A linear function is fitted to data shown in Fig. 3.36b to quantify the relation between ε and y.

$$\varepsilon(y) = p_0 + p_1 \cdot \frac{|y|}{R} \tag{3.46}$$

The resulting parameter values of p_0 and p_1 are given in Tab. 3.13. According to these fit results, ε increases only by a few percent in the maximum range of $|y|/R$ from 0 to 1, also specified in Tab. 3.13.

Tracking detectors made from scintillating fibres consist of multiple fibre layers, *cf.* Sec. 2.3. Figure 3.37 illustrates the cross-section of a fibre mat comprising five layers of scintillating fibres as it is proposed for the LHC SciFi Tracker. The path length s covered in the scintillating fibre cores depends on the position and direction of the particle's trajectory. Figure 3.38 shows the distribution of s for MIPs having straight tracks within the fibre mat. The considered particles originate from random positions in the horizontal direction of Fig. 3.37. Two angles of incidence φ are taken

Table 3.13: Results of fitting (3.46) to data shown in Fig. 3.36b.

x [m]	p_0 [10^{-2}]	p_1 [10^{-2}]	$\frac{\varepsilon(R)-\varepsilon(0)}{\varepsilon(0)}$
0.3	4.25 ± 0.07	0.26 ± 0.12	6 %
1.0	3.41 ± 0.05	0.18 ± 0.10	5 %
2.5	2.28 ± 0.04	0.07 ± 0.07	3 %

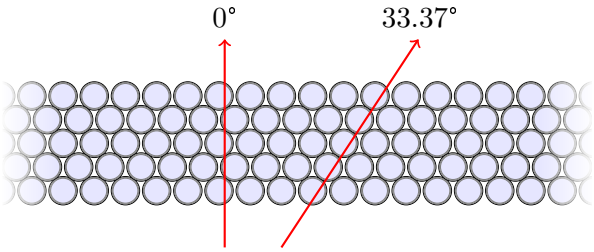

Figure 3.37: Two particles crossing a mat of scintillating fibres under different angles φ relative to the surface normal. The mat is made up from five layers of fibres with a diameter of 250 µm and 275 µm horizontal pitch. The particles' momentum directions are perpendicular to the fibre axes.

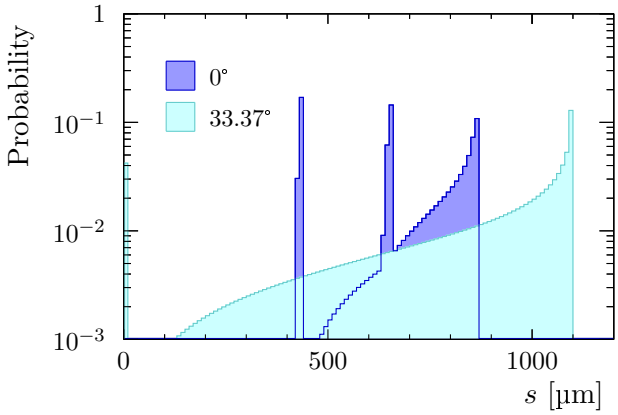

Figure 3.38: Distribution of path length s in fibre core for MIPs crossing a fibre mat under two different angles φ, *cf.* Fig. 3.37. Particles originate from random positions at one side of the mat. The given probability refers to an interval of 10 µm.

into account. In both cases, the MIP trajectories are inside a plane perpendicular to the fibre axes.

While 0° corresponds to the direction of the fibre mat's surface normal, a value of $\varphi = 33.37°$ meets the condition that the minimum distances $|y|$ of the particles from the fibre axes are the same in every layer, see Fig. 3.37. Therefore, the signal response of the fibre mat is similar to that of a single fibre in the second case.

However, due to the cladding width, about 4 % of the particles crossing the fibre mat at 33.37° do not traverse the fibre cores and thus do not produce scintillation light, compare Fig. 3.40b.

The probability of a MIP to cover a distance in the scintillating cores that is inside a particular interval of s, shown in Figure 3.38, peaks at about twice, three and four times the core diameter for $\varphi = 0°$ and at zero and five times the core diameter for $\varphi = 33.37°$. The underlying continuous probability density functions have singularities at these values of s. The distribution of s becomes more complex at angles φ different from the two considered.

The photon number distribution expected from a mat of fibres that is hit by MIPs at the mentioned angles is determined from the simulation of a single scintillating fibre. This is done by classifying MIP trajectories into bins that correspond to consecutive intervals of the minimum distance y from the fibre axes. The width Δy of each bin is 5.5 µm, *i.e.* 1/20 of the fibre core radius R. Figure 3.39 shows one exemplary y interval per considered angle φ. According to a homogeneous particle flux through the fibre mat, an equal number of traversing MIPs is accounted for in each bin.

Only bins within the range of $0 \leq y_{\text{Mat}} \leq 137.5\,\mu\text{m}$ at $z_{\text{Mat}} = 0$ are considered, with 137.5 µm being half the fibre pitch. The coordinate system $(y_{\text{Mat}}, z_{\text{Mat}})$ is specified in Fig. 3.39. Its origin $(0, 0)$ is at the centre of an arbitrary fibre. For the two contemplated angles φ, the restricted range of bins comprises the full distribution of occuring path lengths s due to the fibre mat symmetry.

The photon number resulting from a particle passage through the fibre mat is calculated by addition of photon numbers of five different MIP events from the single-fibre simulation. These MIP events have minimum distances y_i from the fibre axis that are within the y interval corresponding to the bin into which the particle hit has been classified. The enumerator $i \in [1, 5]$ denotes the layer to which the respective fibre belongs.

Figure 3.40 shows distributions of the number of photons arriving at one fibre mat end face obtained from 2500 muon hits each. According to path length distributions shown in Fig. 3.38, the photon number distribution at a perpendicular incidence of the MIP on the fibre mat is narrower than at 33.37°. The mean number of photons per MIP arriving at one fibre mat end face is about 20 % larger for the inclined trajectories compared to the perpendicular. Though, a significant number of particles with $\varphi = 33.37°$ produce no signal at the fibre end. In contrast, no MIP passages with a photon number smaller than four occur at 0° in the simulated data.

Distributions shown in Fig. 3.40 represent the number of photons arriving at one end face of the fibre mat, if light is completely lost at the other end. In the LHCb SciFi Tracker modules, the end face that is opposite to the instrumented one is mirrored to increase the light yield. On the other hand, not all photons reaching the photodetector will induce a signal due to a photon detection efficiency (PDE) significantly less than 1.

These two effects are included in a further simulation, where a mirror is considered at the non-instrumented fibre end. Its reflectivity is set to 0.85, compare Ref. [70].

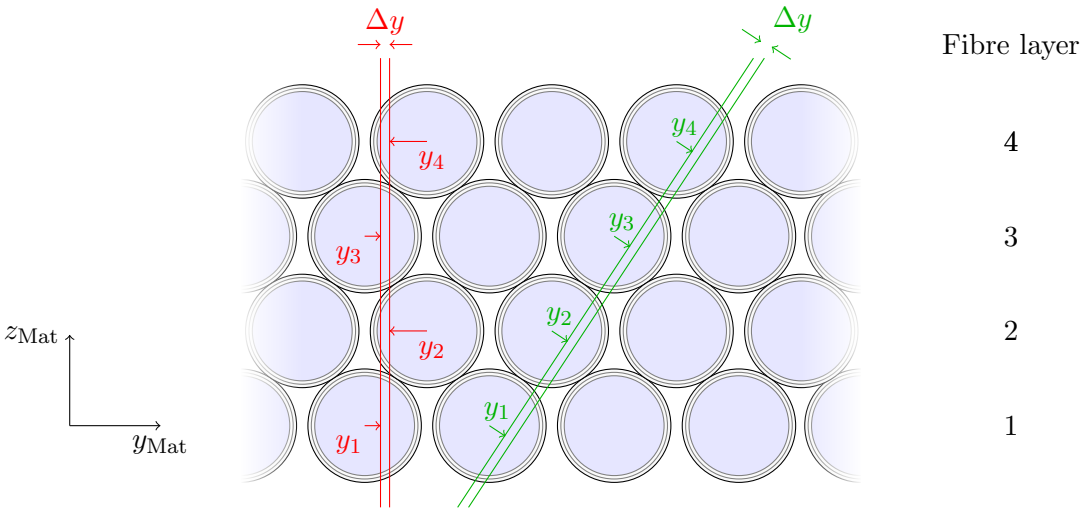

Figure 3.39: Generation of fibre mat response from single-fibre simulation data. For the purpose of visibility the interval dimension Δy is enlarged in the drawing. Only four of five fibre layers are shown.

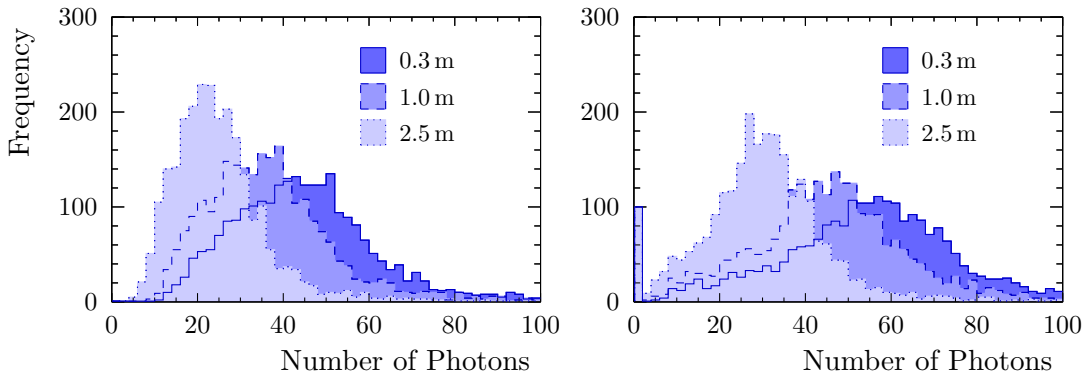

(a) $\varphi = 0°$ (b) $\varphi = 33.37°$

Figure 3.40: Number of photons arriving at one end face when a MIP crosses the fibre mat under an angle φ. Three distances of the excitation point from the fibre end are considered.

The wavelength-dependant PDE of a Hamamatsu SiPM as shown in Ref. [23] is applied to photons reaching the photodetector. It is illustrated in the appendix in Fig. B.2. The resulting distributions of detected photon numbers after excitation close to the mirrored fibre mat end face are shown in Fig. 3.41. Their mean values and standard deviations are given in Tab. 3.14.

Measured data obtained from Ref. [23] are drawn for comparison. They are scaled to have the same integral as the simulated distributions. The data points were acquired from a fibre tracker used as a cosmic ray telescope. The number of photons has been derived from the correspondent charge of the measured signal. Incident angles are restricted to maximum 30°. Therefore, the data correspond to a

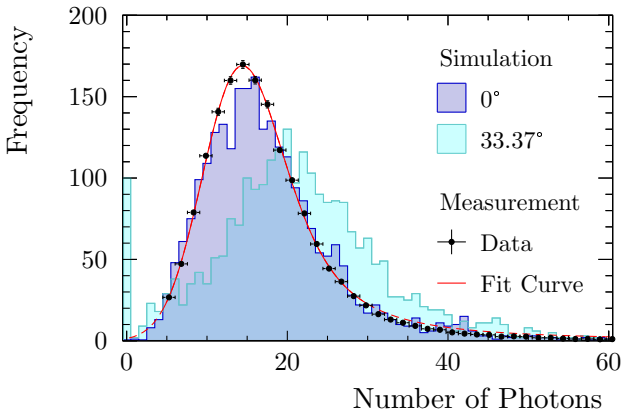

Figure 3.41: Number of photons detected at instrumented end face of fibre mat per MIP crossing under angle φ. The excitation is 2.5 m from the photodetector and close to the mirrored end face. An inefficiency of the photodetector is taken into account. Measured data are obtained from Ref. [23], see text for details.

Table 3.14: Mean value $\langle N \rangle$ and standard deviation σ_N of number of detected photons in Fig. 3.41.

Data	$\langle N \rangle$	σ_N
Simulation 0°	17.68 ± 0.17	8.55 ± 0.12
Simulation 33.37°	21.23 ± 0.22	10.95 ± 0.15
Measurement	17.59 ± 0.04	8.53 ± 0.03

distribution of angles rather than to a single angle as it is the case in the simulated data.

Further difficulties in the comparison of simulated with measured data arise from multiple sources. The measured signal is influenced by the applied clustering algorithm, which may lead to the loss of part of the signal. Pixel cross-talk and saturation effects due to multiple photons hitting the same SiPM pixel also affect the measured signal charge, compare Sec. 4.1. In contrast to simulated data, the measured distribution does not result from the excitation of a 2.5 m long fibre module at its mirrored end. Instead, shorter modules were employed whose signal yield is decreased by reduction of the SiPM gain. The lower SiPM gain is correlated with decreased PDE, which serves to reproduce the stronger attenuation in long fibres.

The convolution of a Gaussian and a Landau distribution is fitted to measured data following Ref. [23]. The fit range is restricted to $[4.5, 29.5]$ to achieve a sufficient description of data in the bulk region. The resulting functional description overestimates the photon number distribution at values above the fit range.

This discrepancy can be explained by the mentioned convolution not being an explicit description of underlying effects. The photon number distribution does

Table 3.15: Results of fitting the convolution of a Gaussian and a Landau distribution to detected photon number distributions in Fig. 3.41. σ_{Landau} is a measure of the width, $\text{MPV}_{\text{Landau}}$ the most probable value of the Landau distribution. The width of the Gaussian distribution is given by σ_{Gaussian}. Area denotes the integral of the function, which results from the convolution.

Data	σ_{Landau}	$\text{MPV}_{\text{Landau}}$	Area	σ_{Gaussian}
Simulation 0°	1.32 ± 0.25	13.15 ± 0.28	$(2.62 \pm 0.07) \cdot 10^3$	5.17 ± 0.36
Simulation 33.37°	1.09 ± 0.41	18.11 ± 0.59	$(2.41 \pm 0.07) \cdot 10^3$	7.64 ± 0.47
Measurement	1.67 ± 0.06	12.86 ± 0.04	$(8.12 \pm 0.05) \cdot 10^4$	3.98 ± 0.08

Data	MPV	FWHM	χ^2/NDF
Simulation 0°	14.93	14.69	20.84/24
Simulation 33.37°	20.16	19.95	50.97/34
Measurement	14.42	12.81	15.52/12

not result from a single Landau distribution as considered in the convolution. It rather originates from an integral of Landau distributions, with most probable values (MPV) depending non-linearly on the path length s in the fibre cores and weighted according to the distribution of s, compare Fig. 3.38. Fluctuations in the number of generated scintillation photons and those resulting from attenuation processes depend on the amount of deposited energy and the initial number of photons, respectively. This is not considered by the fixed width of the convoluted Gaussian.

Despite of these inaccuracies, fitting the convolution of a Gaussian and a Landau distribution in a limited range can provide a sufficient description of the obtained data in this particular range as mentioned above. Therefore, this is also done with simulated data to determine the MPV and the full width at half maximum (FWHM) of these distributions. The fit range limits are set to the first and last bin, respectively, of histograms shown in Fig. 3.41 whose contents are larger than 0.125 of the respective histogram's maximum bin content. The bin content at zero is not considered. Fit results are enlisted in Tab. 3.15. The values of MPV of simulated data with $\varphi = 0°$ and measurement are clearly below the mean photon number of the respective distribution in Tab. 3.14. This fact results from the long tail at high photon numbers, which originates from the Landau distributions of the energy deposit.

3.2.6 Radiation Effects

The upgraded LHCb detector is proposed to collect data from an integrated luminosity of $\int \mathcal{L} = 50\,\mathrm{fb}^{-1}$ during about ten years [13]. The dose accumulated in the fibres in the course of this period is estimated from FLUKA simulations [71]. A maximum of 32 kGy is obtained in the central part of the tracker. So far, two irradiation tests with protons have been conducted by the LHCb SciFi group to investigate the damage in the Kuraray fibre SCSF-78MJ from doses in the order of magnitude of the expected maximum [23, 72]. A third test with fibres placed in the LHCb cavern *in situ* has been made to observe the impact of the expected low dose rates [23].

Running irradiation tests that include both the expected dose and dose rate is not possible due to the duration of the proposed running period. Moreover, an adequate reproduction of expected dose distributions along the fibre is challenging. Therefore, the GEANT4 simulation of scintillating fibres is used to estimate the effect of ionising radiation on the light yield of the LHCb SciFi tracker modules.

Two models of radiation-induced light absorption are utilised to simulate radiation effects. Each considers a material- and wavelength-dependent absorption growing linearly with accumulated dose. Figure 3.42 shows the radiation-induced absorption coefficient a_{rad} per dose D in the core and cladding material as described by two damage models A and B.

Model A follows the observed damage in an SCSF-78MJ fibre shown in Fig. 3.10 and 3.11 to simulate the radiation-induced absorption in the fibre core. At lower wavelengths, the data of PS in $4 \cdot 10^6$ Pa O_2 from Fig. 3.10 are considered since they are similar to SCSF-78MJ data in the range of the latter. A complete consumption of dissolved oxygen during the course of irradiation is assumed in this model, compare Sec. 3.1.4. Therefore, model A takes into account a radiation-induced absorption in the cladding material that is based on the damage in PMMA in absence of oxygen, shown in Fig. 3.12.

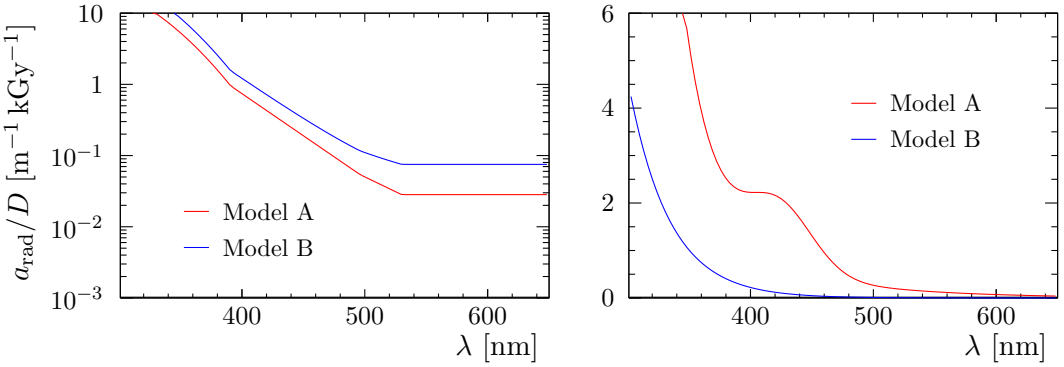

(a) Fibre core. (b) Cladding.

Figure 3.42: Radiation-induced absorption coefficient a_{rad} per dose D *vs.* photon wavelength λ assumed by two models A and B.

Table 3.16: Simulated dose profile of fibre irradiation at CERN PS. The value of x refers to the distance from the instrumented fibre end.

x_{min} [m]	x_{max} [m]	D [kGy]
1.6	2.3	3
2.3	3.0	22

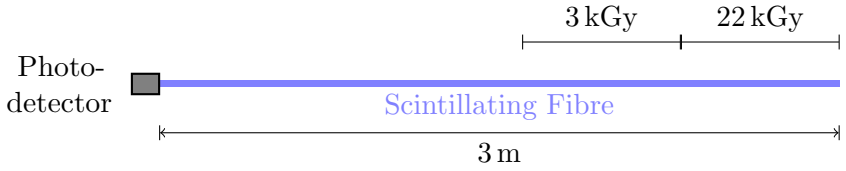

Figure 3.43: Simulated dose profile of fibre irradiation at CERN PS.

Because of the low dose rates, it must be assumed that oxygen will be present in the scintillating fibres of the upgraded LHCb detector constantly as a result of diffusion from surrounding air. The second radiation damage model B is intended for the simulation of these conditions. It approximates the radiation-induced absorption in SCSF-81, BCF-12 and BCF-98 in Fig. 3.10 for simulation of the degrading fibre core material. Damages in the cladding are according to absorption in PMMA with oxygen being available as shown in Fig. 3.12.

The damage models are checked by simulation of the fibre irradiations, which have been performed by the LHCb SciFi Tracker group. Each simulation considers dose distribution, fibre excitation and readout that are equivalent to the corresponding experiment. The same analyses of measurement and simulation are carried out to evaluate the acquired data. Details of each irradiation and a discussion of the combined results are presented in the following paragraphs.

Proton Irradiation at CERN PS

Protons with a momentum of 24 GeV/c from the CERN PS facility were used to irradiate an arrangement of eight parallel fibres of 3 m length [72]. The applied dose profile is specified in Table 3.16 and Figure 3.43. The same dose distribution is accounted to reproduce the test in simulation. Fibres were characterised via excitation by a UV LED with a peak photon wavelength of 385 nm. In the simulation, mono-energetic photons of this wavelength are used. Measured data were corrected for the PDE of a Ketek SiPM. Therefore, the PDE of this device, see Sec. B, is applied to photons arriving at the instrumented fibre end in the simulation.

A probability of $7 \cdot 10^{-6}$ to lose a photon when it reaches a material boundary within the fibre is considered in the simulation. This loss factor adds to transmission losses given by Eq. (3.30) with parameters from Tab. 3.4 and 3.5. The value of

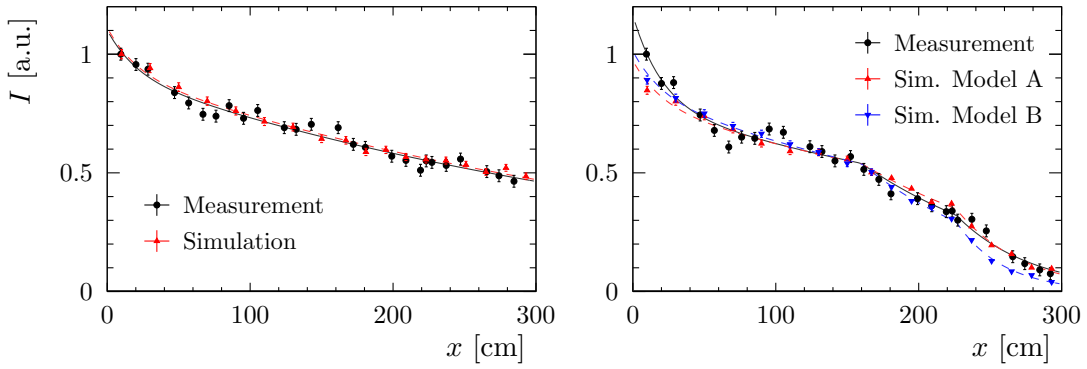

(a) Before irradiation. (b) After irradiation.

Figure 3.44: Measured and simulated data of fibre irradiation at CERN PS. Light intensity I obtained at instrumented fibre end is plotted *vs.* distance x from the photodetector. Curves indicate fit results. Measurement data are taken from Ref. [23].

boundary loss probability is chosen to reproduce the measured data before irradiation by the simulation, see Fig. 3.44a.

Light intensities I shown in Fig. 3.44a are scaled that the first data point of each set equals 1. The same normalisation is used for measured data in Fig. 3.44b. Simulated data are scaled to meet the measurement in the x range from 50 cm to 150 cm with x being the distance from the photodetector.

According to [23], the data before irradiation are analysed by fitting

$$I_{\text{CernPS,no rad}}(x) = I_{0,\text{short}} \exp\left(-\frac{x}{\Lambda_{\text{short}}}\right) + I_{0,\text{long}} \exp\left(-\frac{x}{\Lambda_{\text{long}}}\right) . \tag{3.47}$$

The function

$$I_{\text{CernPS,rad}}(x) = \begin{cases} I_{0,\text{short}} \exp\left(-\dfrac{x}{\Lambda_{\text{short}}}\right) + I_{0,\text{long}} \exp\left(-\dfrac{x}{\Lambda_{\text{long}}}\right) \\ \qquad\qquad \text{if } x \in [0\,\text{m}, 1.6\,\text{m}], \\ I_{\text{CernPS,rad}}(1.6\,\text{m}) \cdot \exp\left(-\dfrac{x - 1.6\,\text{m}}{\Lambda_{\text{long,rad1}}}\right) \\ \qquad\qquad \text{if } x \in \,]1.6\,\text{m}, 2.3\,\text{m}], \\ I_{\text{CernPS,rad}}(2.3\,\text{m}) \cdot \exp\left(-\dfrac{x - 2.3\,\text{m}}{\Lambda_{\text{long,rad2}}}\right) \\ \qquad\qquad \text{if } x \in \,]2.3\,\text{m}, 3.0\,\text{m}], \end{cases} \tag{3.48}$$

is used to describe measured and simulated data after irradiation. In the fit procedures that use simulated data, $I_{0,\text{short}}$ and Λ_{short} are fixed at values obtained

Table 3.17: Parameter values from fitting Eq. (3.47) to measured and simulated data before irradiation. Compare Fig. 3.44a.

	$I_{0,\text{short}}$ [a.u.]	Λ_{short} [m]	$I_{0,\text{long}}$ [a.u.]	Λ_{long} [m]	χ^2/NDF
Measurem.	0.184 ± 0.054	0.20 ± 0.08	0.918 ± 0.022	4.40 ± 0.27	26.8/22
Simulation	0.184 (fixed)	0.2 (fixed)	0.928 ± 0.011	4.43 ± 0.13	15.1/16

Table 3.18: Parameter values from fitting Eq. (3.48) to measured and simulated data after irradiation. Compare Fig. 3.44b.

	$I_{0,\text{short}}$ [a.u.]	Λ_{short} [m]	$I_{0,\text{long}}$ [a.u.]	Λ_{long} [m]
Measurement	0.381 ± 0.063	0.21 ± 0.06	0.783 ± 0.046	4.30 ± 0.86
Sim. Model A	0.184 (fixed)	0.2 (fixed)	0.789 ± 0.012	4.18 ± 0.27
Sim. Model B	0.184 (fixed)	0.2 (fixed)	0.829 ± 0.013	3.70 ± 0.22

	$\Lambda_{\text{long,rad1}}$ [m]	$\Lambda_{\text{long,rad2}}$ [m]	χ^2/NDF
Measurement	1.28 ± 0.12	0.53 ± 0.06	39.5/22
Sim. Model A	1.52 ± 0.10	0.47 ± 0.02	27.4/14
Sim. Model B	1.10 ± 0.05	0.33 ± 0.01	14.1/14

from fits with measured data before irradiation. This approach is necessary to achieve comparable results for Λ_{long} from simulation and measurement, since Λ_{short} and Λ_{long} are highly correlated. The determined values of free parameters in Eq. (3.47) and (3.48) can be found in Tab. 3.17 and 3.18.

The results from both radiation damage models, which are used in the simulation, are compatible with measurement data at the fibre leg that received a dose of 3 kGy. However, they diverge in the region, where 22 kGy were applied. At the higher dose, only model A is consistent with measured data points. Damage model B involves higher transmission loss and thus light intensities continuously less than those of model A and measurement.

Proton Irradiation at KIT

A further irradiation test of SCSF-78MJ fibres with protons was conducted at Karlsruhe Institute of Technology (KIT) [23]. Protons were provided with a kinetic energy of 22.9 MeV. The simulation of one set-up out of two that were used in this test is compared to measurement results. The corresponding dose profile along the fibres is specified in Table 3.19 and shown in Figure 3.45. The light output due to excitation by an UV-LED of 370 nm wavelength is measured before and

Table 3.19: Simulated dose profile of fibre irradiation at KIT. The value of x refers to the distance from the instrumented fibre end.

x_{min} [m]	x_{max} [m]	D [kGy]
0.54	0.78	8.8
0.96	1.20	10
1.34	1.58	43
1.68	1.92	36

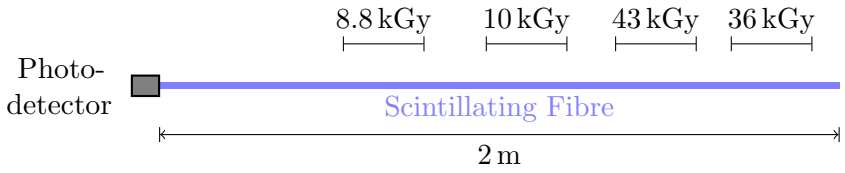

Figure 3.45: Simulated dose profile of fibre irradiation at KIT.

after irradiation. According to the measurement procedure the PDE of a Newport 818-UV photodiode is taken into account, compare Sec. B.

The simulated fibre includes a photon loss probability of $1.95 \cdot 10^{-5}$ at material boundaries. This leads to an attenuation length Λ_0 of $(3.78 \pm 0.14)\,\text{m}$ before irradiation. The value of Λ_0 is obtained by fitting a single exponential function to simulation output that corresponds to a distance $0.5\,\text{m} < x < 2\,\text{m}$ of the excitation point from the fibre end.

In Ref. [23], the ratio of measured light intensities I before and I' after irradiation is evaluated. Measured and simulated ratios $I'(x)/I(x)$ are shown in Fig. 3.46. After irradiation, an additional light absorption at fibre legs that are not considered to be irradiated in the simulation, compare Tab. 3.19, is observed in measurement data. This light loss is indicated by a dotted line in Fig. 3.46. The fibre simulation does not account for damages in these regions. Therefore, the additional light loss observed between groups of data points is included in affected simulation data by a scaling factor.

A single exponential function is assumed to describe the dependency of light output on the excitation point [23]. Thus the intensity ratio is given by

$$I'(x)/I(x) = p_{\text{KIT},0} \cdot \exp\left(p_{\text{KIT},1} \cdot (x_{\text{KIT},0} - x)\right) \ , \tag{3.49}$$

with

$$p_{\text{KIT},1} = \frac{1}{\Lambda'} - \frac{1}{\Lambda_0} \ , \tag{3.50}$$

where Λ_0 and Λ' are the attenuation lengths before and after irradiation. Equation (3.49) is fitted to five groups of data points that correspond to fibre sections

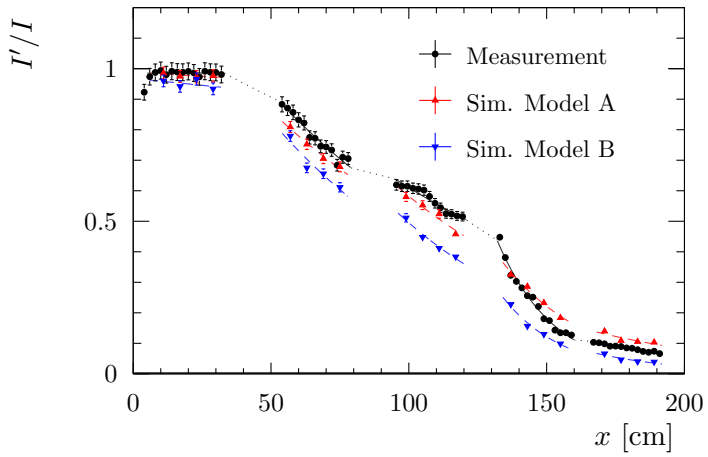

Figure 3.46: Measured and simulated data of fibre irradiation at KIT. Light intensity ratio I'/I of after to before irradiation is plotted *vs.* distance x of excitation from the photodetector. Measurement data are taken from [23].

Table 3.20: Results of fitting Eq. (3.49) to groups of measured and simulated data shown in Fig. 3.46

Data Group	$x_{\mathrm{KIT},0}$ [m]	$p_{\mathrm{KIT},0}$	$p_{\mathrm{KIT},1}$ [m^{-1}]	χ^2/NDF
Measurement				
1	0.05	0.985 ± 0.015	-0.003 ± 0.093	0.72/12
2	0.53	0.893 ± 0.014	1.075 ± 0.105	5.89/11
3	0.95	0.639 ± 0.010	0.915 ± 0.103	5.69/11
4	1.32	0.439 ± 0.007	4.906 ± 0.095	52.6/12
5	1.66	0.107 ± 0.002	1.806 ± 0.103	10.5/11
Simulation Model A				
1	0.06	0.984 ± 0.023	0.049 ± 0.151	0.12/2
2	0.54	0.828 ± 0.019	0.994 ± 0.174	0.55/2
3	0.96	0.612 ± 0.016	1.259 ± 0.195	2.93/2
4	1.34	0.367 ± 0.011	3.155 ± 0.243	2.82/2
5	1.68	0.137 ± 0.006	1.621 ± 0.350	8.05/2
Simulation Model B				
1	0.06	0.963 ± 0.022	0.096 ± 0.151	1.39/2
2	0.54	0.789 ± 0.019	1.275 ± 0.180	4.89/2
3	0.96	0.528 ± 0.015	1.590 ± 0.215	1.29/2
4	1.34	0.253 ± 0.010	4.575 ± 0.319	4.36/2
5	1.68	0.067 ± 0.004	3.063 ± 0.533	6.49/2

with constant dose, compare Tab. 3.19. The value of $x_{\mathrm{KIT},0}$ is fixed to the lower limit of the respective fibre section. Fit curves are plotted in Fig. 3.46 as solid lines for measurement data and dashed lines for simulation. Parameter values are given in Tab. 3.20.

Using damage model A, the simulation yields data similar to measurement, see Fig. 3.46. Values of $p_{\mathrm{KIT},1}$ show a good agreement of measurement and simulation, if model A is considered. Though, the overall level of I'/I in each group of data points is not reproduced precisely.

This discrepancy may be a result of unknown fibre properties or radiation damages, respectively, in regions of x where no data were acquired, as mentioned before. Furthermore, doses measured during the irradiation test have uncertainties of about 20 % [23]. Accordingly, the dose profile used in the simulation (Tab. 3.19) might be incorrect. A deviating dose in a single of the four irradiated sections also affects the measurement results obtained at those fibre sections that are more distant from the photodetector, due to the wavelength dependence of radiation-induced light absorption.

In Situ Irradiation

Scintillating fibres were placed in the LHCb cavern close to the beam pipe to observe radiation damages *in situ* during 2012 [23]. Measurements with six bundles of SCSF-78MJ fibres are compared with the output of corresponding GEANT4 simulations. Four fibre bundles were mounted in the cavern, always two at approximately the same position with respect to the beam pipe. The remaining two bundles were kept non-irradiated as reference. Details about this test will be made available in [73].

The received dose distribution is provided by [74]. Table 3.21 and Figures 3.47 and 3.48 specify the dose profiles used in the simulation. The numbers 1 and 2 identify simulated fibres according to the two mounting positions of irradiated fibre bundles.

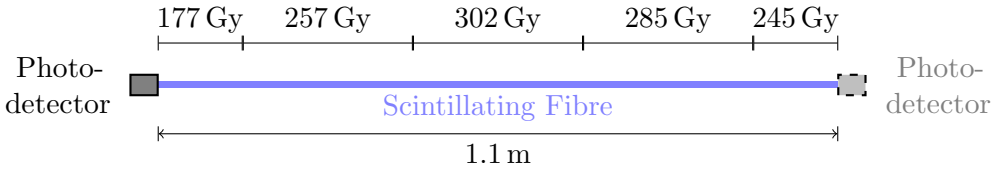

Figure 3.47: Simulated dose profile 1 of *in situ* fibre irradiation.

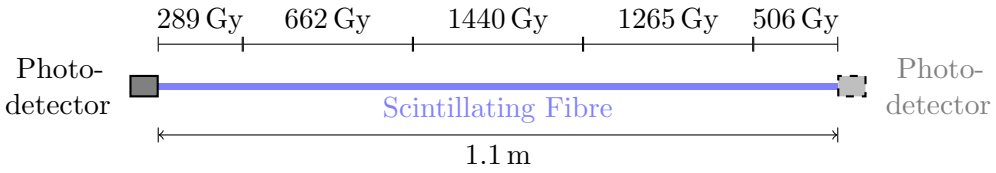

Figure 3.48: Simulated dose profile 2 of *in situ* fibre irradiation.

Table 3.21: Simulated dose profiles of *in situ* fibre irradiation. The value of x refers to the distance from one fibre end.

Dose profile	$x_{\min}$ [cm]	$x_{\max}$ [cm]	D [Gy]
1	0	12.5	177
	12.5	37.5	257
	37.5	62.5	302
	62.5	97.5	285
	97.5	110.0	245
2	0	12.5	289
	12.5	37.5	662
	37.5	62.5	1440
	62.5	97.5	1265
	97.5	110.0	506

In measurement as well as in simulation the light intensity is successively read out at both fibre ends. The utilised device is a Hamamatsu MPPC C11208-01 with PDE given in Sec. B. The scintillation process is initiated by means of a ^{90}Sr source. Its energy spectrum is given in Sec. A. In simulation, the probability of photon loss at material boundaries is set to $2.8 \cdot 10^{-5}$ to achieve results that are consistent with measurements of non-irradiated fibres, see Fig. 3.49a.

An exponential function

$$I(x) = I_0 \cdot \exp\left(-\frac{x}{\Lambda}\right) \tag{3.51}$$

is fit to the data of each simulated fibre and measured fibre bundle with particular photodetector position. The resulting values of I_0 are used to normalise corresponding data and thus make them comparable. The normalised data are illustrated in Fig. 3.49.

Attenuation lengths considered in [23] are the mean $\langle\Lambda\rangle$ of all Λ measurements that correspond to the same dose profile, independent of which fibre end has been read out. The uncertainty of this mean is estimated by the standard deviation of Λ divided by $\sqrt{N}$, with N being the number of considered Λ values. The same approach is used with simulated data except for the calculation of uncertainties. Since only two values of Λ are determined per damage model and dose profile, one per photodetector position, the uncertainty of their mean is calculated by first order error propagation from parameter errors of the fit. Table 3.22 lists determined values of $\langle\Lambda\rangle$. Correspondent curves with I_0 set to 1 are drawn in Fig. 3.49.

Both radiation damage models show less decreased attenuation lengths after irradiation than in measurement, with model B seeming more appropriate to describe the observation. The latter statement is consistent with the assumption

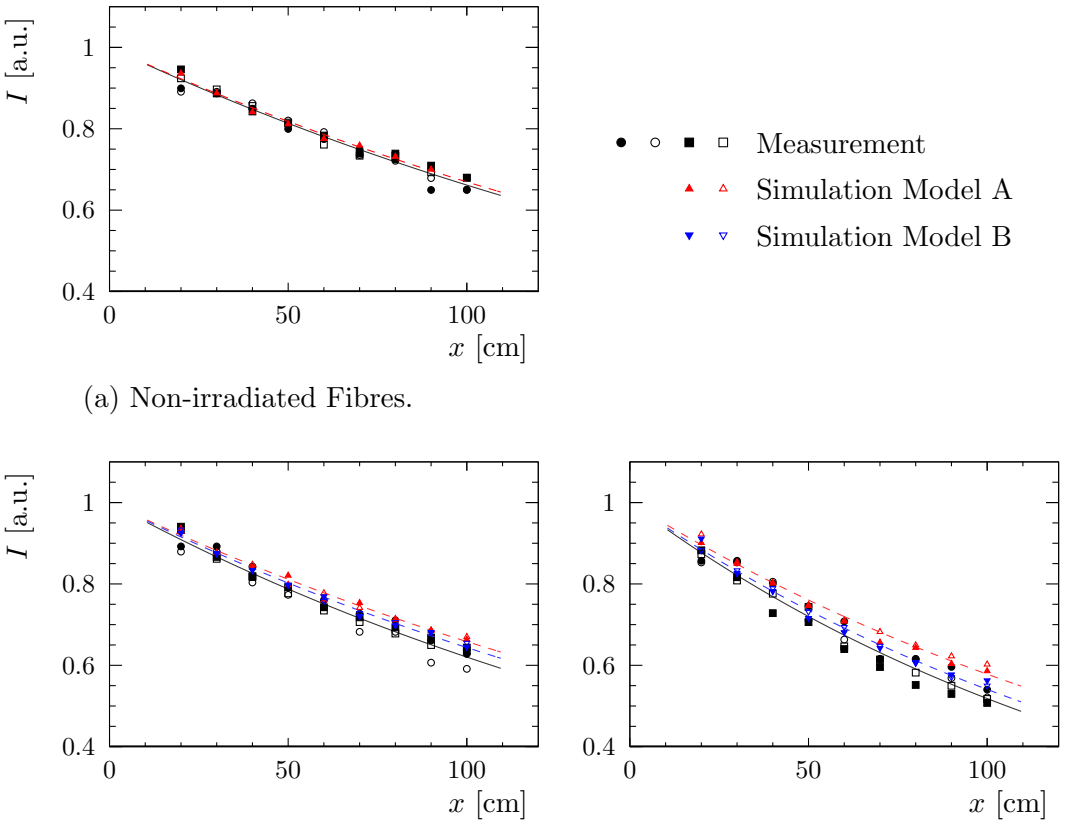

(a) Non-irradiated Fibres.

(b) Dose profile 1.

(c) Dose profile 2.

Figure 3.49: Measured and simulated light intensities I at fibre end depending on distance x of excitation from photodetector in *in situ* test. Circular and square marks identify measurements with different fibre bundles. Filled and open symbols denote data acquired at different fibre ends.

of higher damages at low dose rates caused by oxygen. The fibres tested *in situ* received their total dose during a time period of more than half a year.

However, it is not possible to draw distinct conclusions due to large uncertainties in measured data. The dose estimates for irradiated fibre bundles might deviate by a factor of 2 from the true value [74]. Furthermore, the non-irradiated fibre bundle, which is used as reference, provides only an estimate of the initial state of irradiated fibres with unknown precision.

Combined Results

In the TDR [23], the ratio of attenuation lengths after to before irradiation Λ'/Λ_0 is calculated for each applied dose to combine results of described tests. Although this approach suffers from strong systematic inaccuracies, as discussed below, a suitable simulation should be able to reproduce the outcome.

Table 3.22: Mean attenuation length $\langle\Lambda\rangle$ obtained from measured and simulated data samples depending on dose distribution along fibre.

Data set	$\langle\Lambda\rangle$ [m]
Non-irradiated Fibres	
Measurement	2.42 ± 0.05
Simulation	2.49 ± 0.07
Dose Profile 1	
Measurement	2.09 ± 0.07
Sim. Model A	2.39 ± 0.04
Sim. Model B	2.27 ± 0.04
Dose Profile 2	
Measurement	1.52 ± 0.05
Sim. Model A	1.826 ± 0.025
Sim. Model B	1.627 ± 0.020

Values of Λ'/Λ_0 derived from irradiation tests at CERN PS and *in situ* are calculated using numbers given in Tab. 3.17 and 3.18 and Tab. 3.22, respectively. In the case of proton irradiation at CERN PS, only the long components Λ_{long} are considered. The uncertainty of Λ'/Λ_0 is computed by

$$\sigma_{\Lambda'/\Lambda_0} = \sqrt{\left(\frac{\sigma_{\Lambda'}}{\Lambda_0}\right)^2 + \left(\frac{\sigma_{\Lambda_0}\Lambda'}{\Lambda_0^2}\right)^2}\,, \tag{3.52}$$

with $\sigma_{\Lambda'}$ and σ_{Λ_0} being the uncertainties of attenuation lengths obtained after and before irradiation.

The parameter $p_{\text{KIT},1}$ is used to determine Λ'/Λ_0 from proton irradiations at KIT, compare Eq. (3.49), (3.50) and Tab. 3.20.

$$\Lambda'/\Lambda_0 = \left(p_{\text{KIT},1} \cdot \Lambda_0 + 1\right)^{-1} \tag{3.53}$$

$$\sigma_{\Lambda'/\Lambda_0} = \sqrt{\sigma^2_{p_{\text{KIT},1}}\Lambda_0^2 + p^2_{\text{KIT},1}\sigma^2_{\Lambda_0}} \cdot \left(\Lambda'/\Lambda_0\right)^2 \tag{3.54}$$

Knowledge about the attenuation length and its uncertainty before irradiation is necessary to evaluate Eq. (3.53) and (3.54). This information is not available from data shown in Fig. 3.46. Therefore, Λ_0 is chosen that Λ'/Λ_0 values specified in the TDR [23] are reproduced by measurement data, which the TDR accounts for. The chosen value is 3.7 m, its uncertainty is assumed to be 10 %.

The occurrence of χ^2/NDF values that are given in Tab. 3.20 for measurement data is very unlikely, if both uncertainties of data points are correct and the fitted exponential function is a valid description. It is assumed that the functional description is appropriate within the restricted x range of each group of data used

in the fits. Indeed, the error bars of data points in Fig. 3.46 appear inaccurate. Therefore, parameter uncertainties $\sigma_{p_{\mathrm{KIT},1}}$ are multiplied by $\sqrt{\chi^2/(\mathrm{NDF}-1)}$ before being used in Eq. (3.54) to achieve better error estimates.

Table 3.23 provides the obtained values of Λ'/Λ_0. They are visualised in Figure 3.50. Measured values are in accordance with those given in [23], since they are gained by identical analysis procedures using the same data. Though, uncertainties of results from irradiation at KIT are by a factor 2 to 10 smaller than stated in [23]. The source of error estimates is not specified in the reference.

Using radiation damage model A, simulation results are consistent with measurements of fibres irradiated at CERN PS and KIT. In contrast, model B seems to be the more appropriate to describe data points from *in situ* tests. This might be explained by the extremely different dose rates of 5 kGy/h to 22.5 kGy/h [72], $1.8 \cdot 10^4$ kGy/h [23] and in the order of 10^{-4} kGy/h [74] applied in irradiation tests at CERN PS, KIT and *in situ*, respectively. Though, this conclusion is limited by the large dose uncertainties of *in situ* data discussed in the dedicated section before.

In Ref. [23], four functions $f_{\mathrm{TDR},i}$ with parameters $p_{i,j}$ are considered to describe the dependency of Λ'/Λ_0 on received dose D.

$$f_{\mathrm{TDR},1}(D) = \left(1 + \frac{D}{p_{1,0}}\right)^{-1} \tag{3.55}$$

$$f_{\mathrm{TDR},2}(D) = \left(1 + \left(\frac{D}{p_{2,0}}\right)^{p_{2,1}}\right)^{-1} \tag{3.56}$$

$$f_{\mathrm{TDR},3}(D) = p_{3,0} + p_{3,1} \cdot \log_{10}(D) \tag{3.57}$$

$$f_{\mathrm{TDR},4}(D) = \exp\left(-\left(\frac{D}{p_{4,0}}\right)^{p_{4,1}}\right) \tag{3.58}$$

The result of fitting these functions to data from irradiation at CERN PS and KIT, as it is done in [23], is visualised in Fig. 3.51. The fit allows for dose uncertainties by application of the effective variance method. Table 3.24 lists corresponding χ^2/NDF. In addition, Table 3.24 provides the deviation of simulation model A from measured data, with

$$\chi^2 = \sum_{k=0}^{5} \frac{\left((\Lambda'/\Lambda_0)_{\mathrm{sim},k} - (\Lambda'/\Lambda_0)_{\mathrm{meas},k}\right)^2}{\sigma^2_{(\Lambda'/\Lambda_0)_{\mathrm{sim},k}} + \sigma^2_{(\Lambda'/\Lambda_0)_{\mathrm{meas},k}}} \ . \tag{3.59}$$

The indices sim and meas denote simulated and measured data, respectively, k identifies data associated with a particular dose. Only data from irradiations at CERN PS and KIT are taken into account, as it is done in the fits.

According to numbers in Tab. 3.24, the GEANT4 simulation using damage model A provides the best agreement with measurements. Equation (3.57) is the only of the fitted functions that is likely to be an appropriate description given the χ^2/NDF. However, its curve is the most distant from data points obtained from irradiations in the LHCb cavern. Furthermore, it shows an unphysical behaviour at low and high doses, where it exceeds 1 or reaches negative values, respectively.

Table 3.23: Ratio of attenuation length after to before irradiation Λ'/Λ_0 *vs.* dose D. Underlying measurement data are obtained from Ref. [74] (*in situ*), [72] (CERN PS) and [23] (KIT). The specified dose error of *in situ* data refers to the standard deviation of dose along tested fibres, *cf.* Tab. 3.21. It does not include measurement uncertainties.

D [kGy]	Λ'/Λ_0		
	Measurement	Sim. Model A	Sim. Model B
In situ irradiation			
0.264 ± 0.033	0.865 ± 0.032	0.960 ± 0.032	0.911 ± 0.030
0.941 ± 0.366	0.629 ± 0.025	0.733 ± 0.024	0.653 ± 0.021
Irradiation at CERN PS			
3.0 ± 0.3	0.292 ± 0.032	0.344 ± 0.024	0.248 ± 0.014
22.0 ± 2.2	0.120 ± 0.015	0.106 ± 0.005	0.0748 ± 0.0033
Irradiation at KIT			
8.8 ± 1.5	0.201 ± 0.020	0.210 ± 0.030	0.172 ± 0.021
10 ± 2	0.228 ± 0.023	0.174 ± 0.023	0.143 ± 0.017
43 ± 7	0.052 ± 0.005	0.077 ± 0.006	0.055 ± 0.004
36 ± 7	0.130 ± 0.013	0.140 ± 0.026	0.080 ± 0.013

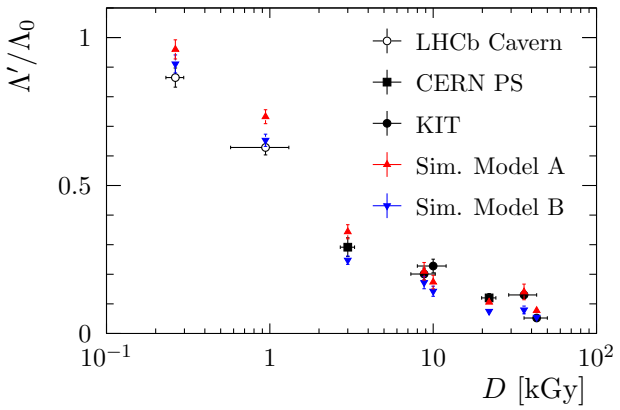

Figure 3.50: Ratio of attenuation length after to before irradiation Λ'/Λ_0 *vs.* dose D. Underlying measurement data are obtained from Ref. [74] (LHCb Cavern), [72] (CERN PS) and [23] (KIT). The specified dose error of *in situ* data (LHCb Cavern) refers to the standard deviation of dose along tested fibres, *cf.* Tab. 3.21. It does not include measurement uncertainties.

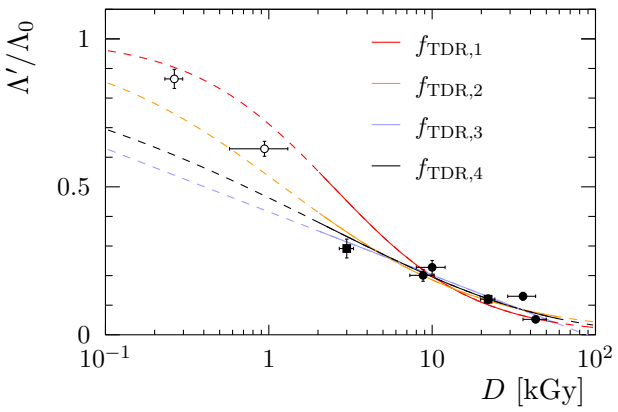

Figure 3.51: Damage models used in [23] to describe Λ'/Λ_0 as a function of D. Dashed parts of the curves are outside the fit range.

Table 3.24: Deviations of fitted damage models used in [23] and simulation model A from measured data. Compare Fig. 3.50 and 3.51.

Model	χ^2/NDF
$f_{\mathrm{TDR},1}$	32.01/5
$f_{\mathrm{TDR},2}$	17.45/4
$f_{\mathrm{TDR},3}$	6.98/4
$f_{\mathrm{TDR},4}$	11.91/4
Simulation Model A	6.33/6

The data point at 36 kGy is an outlier with respect to any of the fitted functions $f_{\mathrm{TDR},i}$. However, it is adequately reproduced by the simulation. This is a result of the wavelength dependence of radiation damages, which is not taken into account in Eq. (3.55) to (3.58). The contribution of photon absorption at short wavelengths to the total attenuation length Λ' observed at the fibre section that is irradiated to 36 kGy is diminished due to the utilised test setup. Corresponding photons are less likely to be registered at the fibre end because of radiation-induced absorption in fibre sections between the investigated and the photodetector, compare Fig. 3.45.

The described effect is an example of systematic inaccuracies in the comparison of irradiation results via the measure Λ'/Λ_0, which are listed in the following.

- Division of Λ' by Λ_0 does not provide a measure that is independent of Λ_0. In fact, radiation-induced damages do not increase existing absorptions by a factor but lead to additional absorption centres. Therefore, fibres with different attenuation lengths before irradiation, *e.g.* caused by extrinsic loss factors, cannot be accurately compared by this approach.

- The light attenuation along optical fibres depends on the path length distribution and the number of reflections and refractions at material boundaries.

Thus, measured values are affected by the distance from the photodetector and the length of the examined part of the fibre.

- Radiation-induced light absorption is strongly wavelength-dependent. Miscellaneous wavelength dependencies of the transparency of the fibre part between the investigated region and the photodetector as well as of the photon detection efficiencies of used sensors will therefore cause different results for Λ' even if at equal radiation damage.

These difficulties can be dealt with by measuring the radiation-induced light absorption, which adds to the absorption before irradiation, as a function of wavelength. Only photons whose path is nearly parallel to the fibre axis should be taken into account in the measurement.

Damage Estimate for the LHCb SciFi Tracker

The impact of radiation-induced absorptions on the light yield of the LHCb SciFi Tracker is studied by the GEANT4 fibre simulation allowing for radiation damage model B. Even though model A provides a better description of results from radiation tests at CERN PS and KIT, it must be assumed that radiation damages evolving in the LHCb detector environment will be significantly larger. Dose rates applied in the mentioned proton irradiations are many orders of magnitude higher than those occurring in the LHCb cavern, compare preceding section. Diffusion of oxygen into the fibres during irradiation was negligible in these tests. In contrast, damage model B is derived from radiation-induced absorptions measured with polystyrene-based fibres similar to the proposed SCSF-78MJ at lower dose rates. Oxygen was available inside the material throughout the underlying irradiation tests, *cf.* Sec. 3.1.4.

Figure 3.52 shows the estimated dose that is received by fibres in the innermost part of the LHCb SciFi Tracker during an operation period corresponding to an

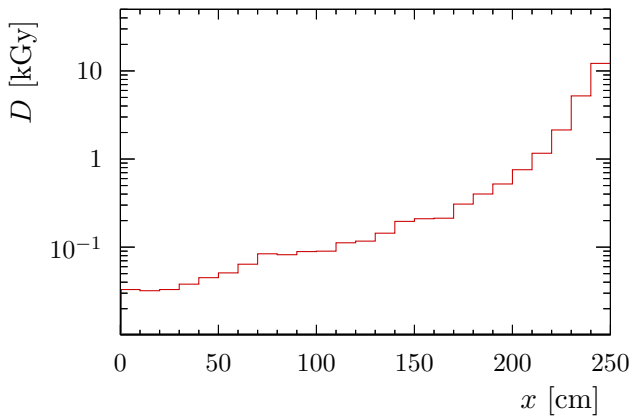

Figure 3.52: Accumulated dose D corresponding to an integrated luminosity of $50\,\mathrm{fb}^{-1}$ *vs.* distance x from the photodetector. Dose values are taken from FLUKA simulation [71] and related to fibres in the innermost part of the detector.

integrated luminosity $\int \mathcal{L}$ of $50\,\mathrm{fb}^{-1}$. The radiation level reaches its maximum at this part of the detector, which is close to the beam pipe, and is obtained from FLUKA simulation [71]. According to Ref. [71], a safety factor of 2 has to be taken into account to allow for uncertainties. Therefore, the impact of radiation corresponding to $100\,\mathrm{fb}^{-1}$ with given doses per proton collision is also discussed in the following.

The discontinuous dose curve shown in Fig. 3.52 originates from the fact that doses are sampled in bins of $10\,\mathrm{cm} \times 10\,\mathrm{cm} \times 0.01\,\mathrm{cm}$ in a Cartesian grid in the FLUKA simulation. The non-zero bin width does not introduce further uncertainties to the fibre simulation, if the following assumptions are satisfied.

- Radiation damages increase linearly with accumulated dose.
- The mean dose of any y-z-plane inside bins that comprise the considered fibre can be found at equal (y, z) coordinate independent of x.
- The considered fibre is located at this particular (y, z) coordinate.
- Simulated excitations are at the points of discontinuity of the given dose curve.

Radiation-induced absorptions that depend linearly on dose lead to an attenuation factor

$$\exp\left(-\int_{s_0}^{s_1} a \cdot D(s)\ \mathrm{d}s\right)\ , \tag{3.60}$$

with a being the absorption per dose and s specifying the photon path. If s_0 and s_1 are at the x limits of a bin, *i.e.* at neighboured points of discontinuity in the dose curve of Fig. 3.52, this expression is equivalent to

$$\exp\left(-a \cdot \langle D\rangle \cdot (s_1 - s_0)\right)\ . \tag{3.61}$$

$\langle D\rangle$ is the mean dose in this bin, which is obtained from the FLUKA simulation. Even if the specified conditions are not perfectly met, it is assumed that the resulting uncertainties are of minor relevance compared to other error sources.

The simulated fibre includes a mirror with reflectivity 0.85 at one end. A probability of photon loss at material boundaries of $2 \cdot 10^{-5}$ is taken into account. The photon detection efficiency of a Hamamatsu SiPM as stated in [23], see Fig. B.2, is applied to photons reaching the instrumented fibre end. Scintillation photons are generated at random (y, z) coordinates inside the fibre core's cross-section with discrete distances x from the photodetector. The distribution of photon emission over the cross-section is equivalent to excitation by minimum ionising particles crossing the fibre at random distance from its centre. Two scenarios concerning photon loss at the fibre end face that is attached to the photodetector are considered. The first implies no light loss at this interface. In the second case, photons whose momentum direction, before leaving the fibre, exhibits an angle greater than 39° relative to the end face normal are lost. This approach corresponds to the presence of an air gap between fibre and sensor, which leads to total internal reflection.

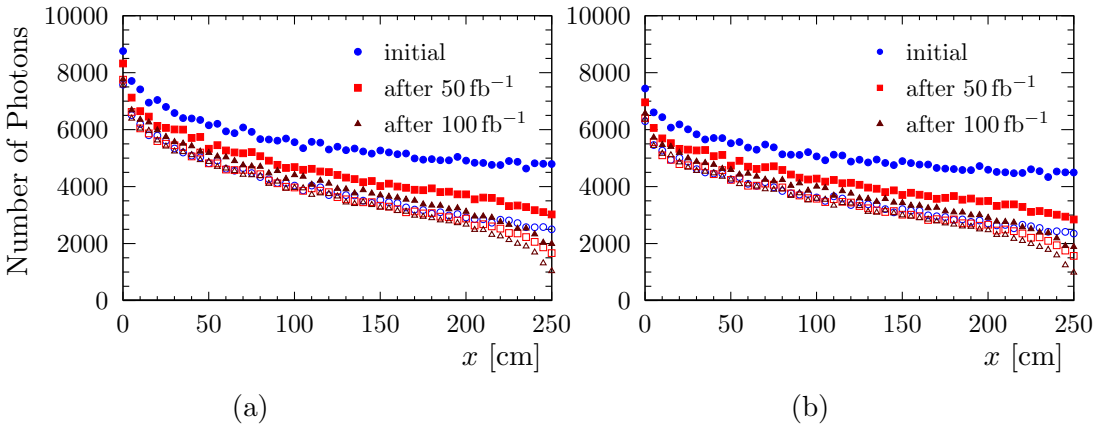

Figure 3.53: Simulated number of detected photons depending on distance x of particle hit from the photodetector in the LHCb SciFi Tracker. The number of scintillation photons generated at each excitation point is 10^5. Open symbols denote direct light only, *i.e.* photons reflected from the mirrored fibre end are not included. In contrast to (a), an additional photon loss due to an air gap between fibre and photodetector is considered in (b).

Table 3.25: Ratio of light intensities after to before irradiation I'/I corresponding to particle hits in the region of maximum radiation damage.

$\int \mathcal{L}$ [fb^{-1}]	I'/I
50	0.63 ± 0.04
100	0.42 ± 0.06

The resulting photon numbers registered at the sensor are plotted in Fig. 3.53. A strong reduction of light yield is observed after irradiation according to the proposed luminosity. The ratio of light intensities after to before irradiation I'/I exhibits a photon loss of about 40 % and 60 % after 50 fb^{-1} and 100 fb^{-1}, respectively, *cf.* Tab. 3.25. These values refer to particle hits close to the mirrored fibre ends, where the maximum damage occurs. Uncertainty estimates given in Tab. 3.25 are calculated from uncertainties of obtained photon numbers N, which are assumed to be $\sqrt{N}$.

Silicon Photomultipliers which are proposed for the LHCb SciFi Tracker are object of current research and development. To achieve a good detector performance the wavelength dependence of the sensors' PDE needs to match the spectrum of photons leaving the fibre. Therefore, it is necessary to determine the latter and its change by radiation damages.

Simulated wavelength spectra of photons reaching the instrumented fibre end are shown in Fig. 3.54. Their mean values are provided in Tab. 3.26. As before a fibre in the detector part where the maximum radiation damage occurs is considered.

Table 3.26: Mean values of photon wavelength spectra shown in Fig. 3.54.

$\int \mathcal{L}$ [fb^{-1}]	including mirrored light	$\langle\lambda\rangle$ [nm]		
		$x = 0.5\,\mathrm{m}$	$x = 1.5\,\mathrm{m}$	$x = 2.5\,\mathrm{m}$
0	yes	485.5 ± 0.5	489.7 ± 0.5	492.5 ± 0.6
0	no	482.7 ± 0.5	487.7 ± 0.6	493.4 ± 0.8
50	yes	485.6 ± 0.5	492.7 ± 0.6	499.3 ± 0.7
50	no	483.1 ± 0.5	489.3 ± 0.7	499.6 ± 1.0
100	yes	485.5 ± 0.6	491.6 ± 0.6	506.0 ± 0.8
100	no	482.9 ± 0.6	488.6 ± 0.7	506.9 ± 1.2

The spectrum's shift to longer wavelengths with increasing distance of excitation from the photodetector is increased after irradiation. The mean wavelength $\langle\lambda\rangle$ of photons coming from the mirrored fibre end changes by about 7 nm and 13.5 nm after $50\,\mathrm{fb}^{-1}$ and $100\,\mathrm{fb}^{-1}$. This is slightly less than the peak's shift which is estimated from Fig. 3.54, since the mean includes the tail of long-wavelength photons which are hardly affected by radiation-induced absorption.

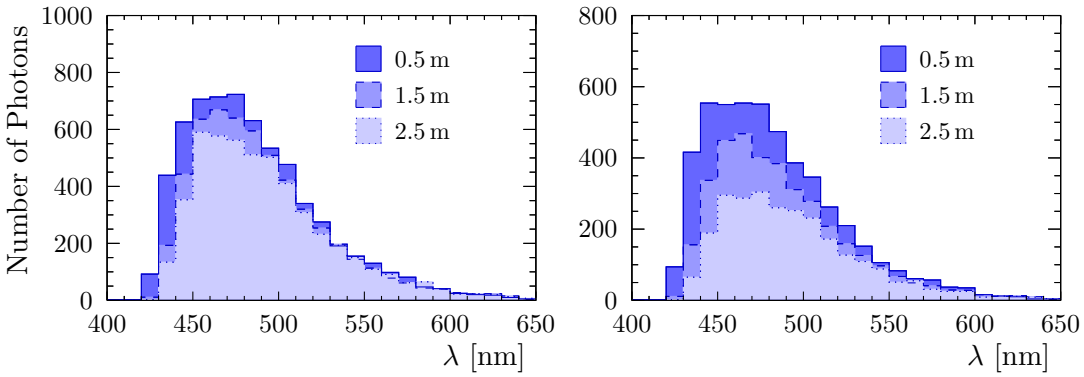

(a) before irradiation

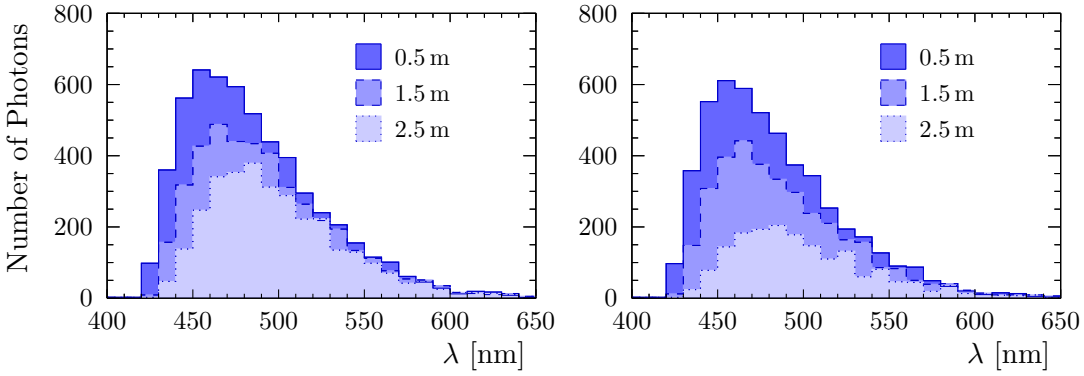

(b) after 50 fb^{-1}

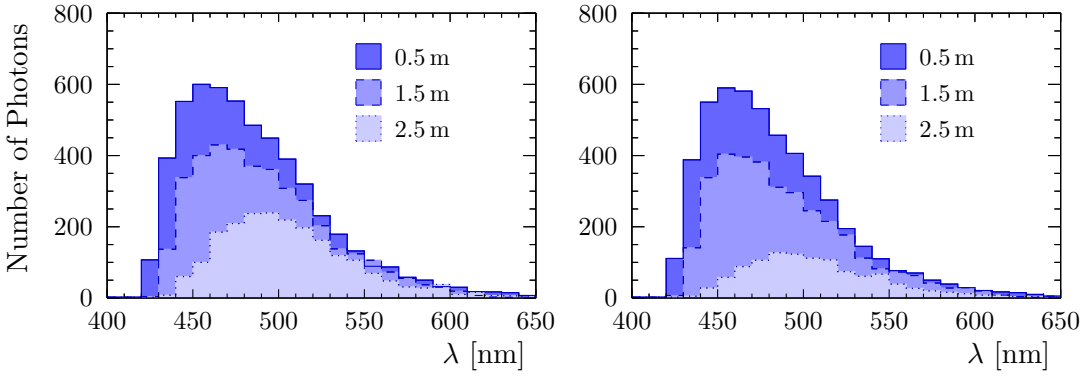

(c) after 100 fb^{-1}

Figure 3.54: Photon wavelength spectra depending on distance of particle hit from instrumented fibre end before and after irradiation. Plots on the right represent direct light only.

3.3 Signal Shape and Propagation Time

Signal shapes and propagation times of scintillation light pulses are critical properties in the context of detector performance of the LHCb SciFi Tracker. The proposed trigger rate of 40 MHz [13] allows for a maximum signal integration over 25 ns. Photons that generate a signal in subsequent time intervals will be wrongly associated with events originating from later proton bunch crossings. This so-called spillover diminishes the efficiency of track reconstruction and potentially leads to the creation of ghost tracks.

Besides the shape of electrical signals created by the used SiPM and readout electronics, knowledge of the time distribution of photons arriving at the instrumented fibre end is necessary to evaluate the impact of these effects. This time distribution is investigated by measurement and simulation of light pulses that are generated by excitation of a scintillating fibre SCSF-78MJ from Kuraray.

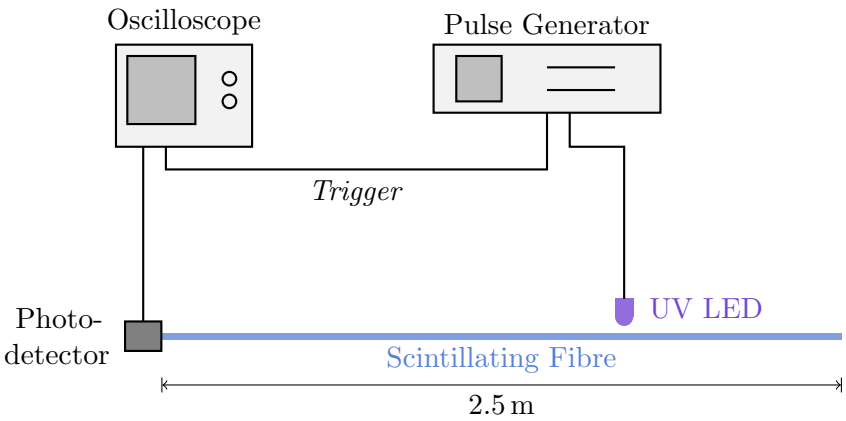

Figure 3.55: Schematic view of setup to measure time distribution of photons arriving at one fibre end.

Figure 3.55 visualises the utilised measurement setup. A 2.5 m long scintillating fibre is excited by means of a UV LED at several distances x from the photodetector. The UV LED is powered by an Agilent 81110A pulse/pattern generator at a rate of 100 kHz. The chosen pulse shape of its output voltage is shown in Fig. 3.56a. The resulting current pulse at the LED which approximates to a step function is also plotted. It is derived from the current-voltage characteristic of the UV LED given in Appendix C. Furthermore, light pulse shapes are calculated from the current-dependent light output of the LED, compare Fig. C.1b. These are shown in Figure 3.56b corresponding to four different maximum output voltages of the pulse generator. The fibre volume that is excited by means of the UV photons is limited to an extent of 5 mm along the fibre axis by use of a screen.

Voltage pulses at the output of the pulse generator and therefore LED light pulses have a fix delay with respect to a trigger signal that is generated by the same device. The trigger initiates a digital oscilloscope of type LeCroy SDA 5000A to acquire

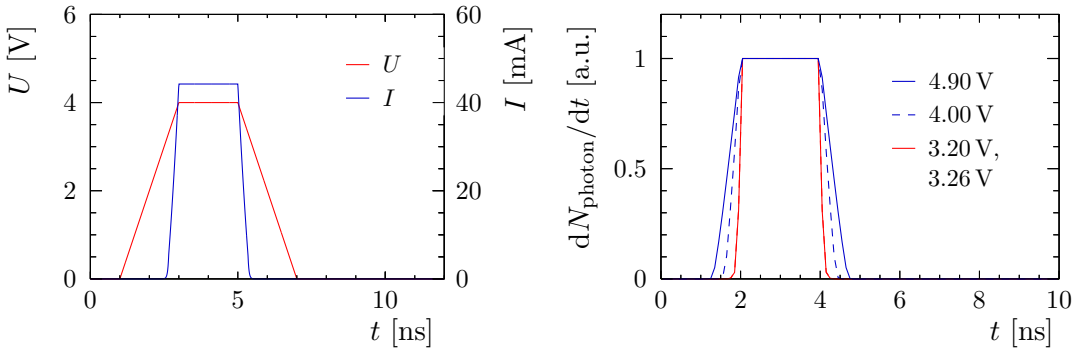

Figure 3.56: Exemplary theoretical voltage and current pulses U and I occurring at the UV LED (a) and shapes of light pulses $\frac{\mathrm{d}N_{\mathrm{photon}}}{\mathrm{d}t}$ emitted by the diode at different maximum voltages (b). Curves are derived from chosen pulse generator settings and characteristics of the LED, see App. C. The photon numbers N_{photon} in (b) are scaled such that all curves have the same maximum. Only one curve is drawn for 3.20 V and 3.26 V, since they are indistinguishable at the given scale.

the analogue output of the used photodetector module. The photodetector signal is recorded at a rate of 10 samples per nanosecond for 500 ns.

A Hamamatsu MPPC module C11208-02 is used for photon detection at the fibre end. Figure 3.57 shows the voltage pulse $U_{\text{single PE}}$ that is observed at its analogue output in the case of a pixel breakdown.[2] The curve represents the mean of 508 recorded dark counts which are equivalent to the signal of single photons. The relatively large width of the voltage pulse does not allow for the desired time resolution for single photons in the order of 1 ns by recording the times of rising pulse edges, since pulses of consecutive photons strongly overlap. Instead, the time distribution of photons arriving at the fibre end is obtained via deconvolution of recorded signals, which is explained in the following.

The voltage pulse $U_{\mathrm{SciFi}}(t)$ that is measured at the output of the photodetector after excitation of the scintillating fibre can be described by the convolution

$$U_{\mathrm{SciFi}}(t) = \left(\frac{\mathrm{d}N_{\mathrm{photon}}}{\mathrm{d}t} * U_{\mathrm{resp}} \right)(t) \ , \tag{3.62}$$

with $\frac{\mathrm{d}N_{\mathrm{photon}}}{\mathrm{d}t}(t)$ being the time distribution of photons resulting from fibre properties and $U_{\mathrm{resp}}(t)$ being an adequate response function. The response function has to comprise the time characteristic of the LED pulse as well as the behaviour of the photodetector. If $U_{\mathrm{resp}}(t)$ is known, $\frac{\mathrm{d}N_{\mathrm{photon}}}{\mathrm{d}t}(t)$ can be obtained by deconvolution of the measured signal $U_{\mathrm{SciFi}}(t)$.

[2] Details about working principle and characteristics of silicon photomultipliers (SiPM) can be found in Chapter 4

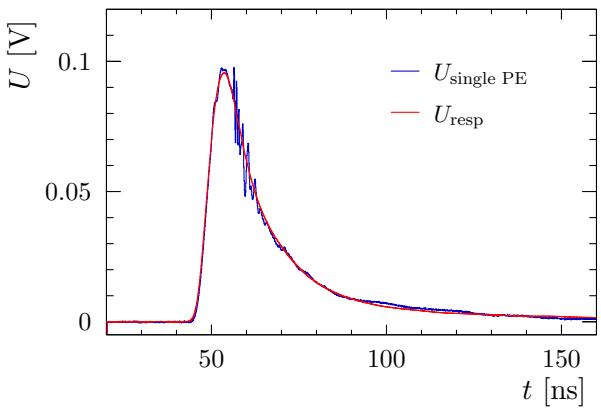

Figure 3.57: Voltage pulses measured at the analogue output of the MPPC module. The signal $U_{\text{single PE}}$ corresponds to the detection of a single photon. The curve U_{resp} is measured via direct illumination of the photosensor by the pulsed UV LED. It is normalised to have the same integral as $U_{\text{single PE}}$.

In principle, the response function $U_{\text{resp}}(t)$ is easily determined by direct illumination of the photodetector with the pulsed UV LED without intermediate fibre. However, it is not possible to use the same pulse heights for powering the UV LED in both cases, excitation of the fibre and illuminating the photosensor directly. As a result of the small ratio of detected scintillation photons to initially generated LED light, peak voltages of about 4.0 V have to be set at the pulse generator's output in the case of fibre excitation to yield photodetector signals comparable to those of direct illumination at about 3.2 V. The light pulse shape is affected by differing peak voltages due the non-linear voltage dependence of the LED's light intensity, *cf.* Fig. C.1. This effect is visualised in Figure 3.56b. From shown curves it can be estimated that the influence on resolution of the sought distribution $\frac{\mathrm{d}N_{\text{photon}}}{\mathrm{d}t}$ is less than 0.5 ns and 0.8 ns, if peak voltages of 4.0 V and 4.9 V, respectively, are used to excite the fibre, while the response function has been measured with a maximum pulse generator voltage in the range of 3.2 V to 3.26 V.

The response function $U_{\text{resp}}(t)$ is acquired in four measurements with direct illumination of the MPPC sensor by the UV LED. Each of the four measurements is a record of numerous LED pulses. The number of light pulses $N_{\text{LED pulse}}$, the used maximum pulse generator voltage $U_{\text{LED,max}}$ and the mean photon equivalent $\langle \text{PE} \rangle$ of the measured voltage pulses are provided in Tab. 3.27. The latter is calculated by division of the time-integrated oscilloscope record by the integral of $U_{\text{single PE}}$. The function $U_{\text{resp}}(t)$ used in the deconvolution approach is the mean of all recorded MPPC voltage pulses. It is illustrated in Fig. 3.57. The curve is similar to the single photon equivalent $U_{\text{single PE}}(t)$.

The deconvolution procedure is realised by an implementation of the Richardson-Lucy algorithm [75, 76]. It is executed with a number of 2000 iterations. To reduce high-frequent noise in measured voltage samples, both U_{SciFi} and U_{resp} are convolved with a Gaussian function of 0.5 ns width before deconvolution. This is equivalent to

Table 3.27: Maximum voltages $U_{\mathrm{LED,max}}$, number of recorded LED pulses $N_{\mathrm{LED\ pulse}}$ and mean photon equivalent detected per pulse $\langle \mathrm{PE} \rangle$ in measurements to determine U_{resp}.

Measurement	$U_{\mathrm{LED,max}}$ [V]	$N_{\mathrm{LED\ pulse}}$	$\langle \mathrm{PE} \rangle$
1	3.20	1947	1.81
2	3.26	1591	3.39
3	3.20	1246	1.99
4	3.26	1053	3.47

Eq. (3.62) according to the associativity of the convolution operation. Furthermore, the data size of both voltage curves is reduced from 5000 to 1000 data points, *i.e.* to one value per 0.5 ns, by calculating the mean of five consecutively sampled voltages each. The benefits are a further reduction of noise and less computing time for execution of the deconvolution algorithm. The time resolution of the deconvolution result for $\frac{\mathrm{d}N_{\mathrm{photon}}}{\mathrm{d}t}(t)$ is hardly affected by this decrease in sample rate as discussed below.

To prevent from artefacts appearing at times close to 0 when the excitation is near the photodetector, $U_{\mathrm{resp}}(t)$ is shifted by 5 ns to earlier times t. This leads to a shift of the deconvolution result by the same value to larger t. The photon number is fixed to 0 for times $t > 62.5$ ns, since no scintillation light is expected to reach the MPPC later than this limit.

The described approach is tested by convolution of two exemplary distributions $\frac{\mathrm{d}N}{\mathrm{d}t}(t)$ with $U_{\mathrm{resp}}(t)$ and subsequent application of the deconvolution procedure. The considered distributions are a delta peak and an exponential function with 2.8 ns decay time. No noise is added to the convolution result $U_{\mathrm{conv}}(t)$.

In the case of the delta peak, the reconstructed distribution is slightly asymmetric and shows a standard deviation of 0.66 ns. Also the reconstructed exponential decay function deviates from its original distribution. In both cases, the reconstructed distribution follows the same curve only with higher density of bins in t, if the data size of U_{resp} and U_{conv} is kept at 5000 points instead of being reduced to 1000. Thus the resolution of determined distributions is assumed to be limited by the deconvolution procedure itself. It seems to be unaffected by the decrease in data size of measured voltage curves.

Figures 3.58a and 3.58b show the response function $U_{\mathrm{ref}}(t)$, the result $U_{\mathrm{conv}}(t)$ of its convolution with a delta peak and an exponential decay, respectively, and the reconstructed distributions of N. The latter are compared with binned representations of their original distributions in Fig. 3.58c and 3.58d.

Timing measurements of the scintillating fibre are taken at two conditions. First, the fibre end face opposite from the photodetector is unmachined. Therefore, only a small number of photons undergoing total internal reflection at this interface to surrounding air will be recognised as delayed signal at the photodetector. When

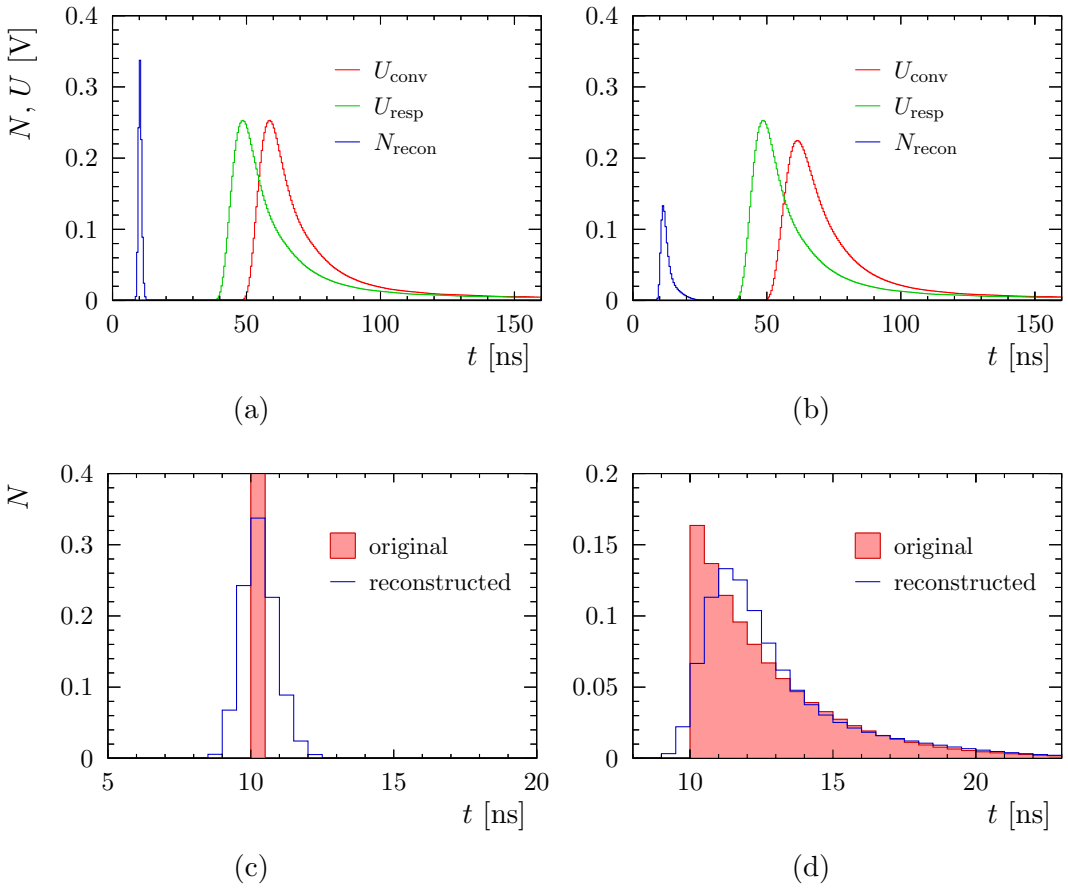

Figure 3.58: Test of the deconvolution approach with delta distribution (a),(c) and exponential decay function (b),(d). Both distributions of N have an integral of 1. Top plots show the response function U_{resp}, its convolution U_{conv} with the respective distribution and the deconvolution result N_{recon}. Bottom plots provide a comparison of the deconvolution results with binned versions of the original distributions.

the first run of measurements is concluded, the fibre end is vacuum metallised with aluminium to increase the amount of reflected light. However, the fibre exhibits an damage somewhere in the range of 37.5 cm to 50 cm from the photodetector that affects light transmission after metallisation, compare Fig. 3.60. The voltage pulse height used to power the UV LED is increased from 4.0 V before metallisation to 4.9 V after treatment of the fibre end to receive a sufficient number of photons despite this degradation.

At each excitation point x, the fibre response to more than 1600 UV LED pulses is recorded to determine the corresponding mean voltage pulse $U_{\text{SciFi}}(t)$ occurring at the output of the photodetector. Figure 3.59 shows measured signals $U_{\text{SciFi}}(t)$ before and after metallisation of the fibre end face for an excitation at $x = 1\,\text{m}$. The response function $U_{\text{resp}}(t)$ and the time dependence of photon number N_{photon},

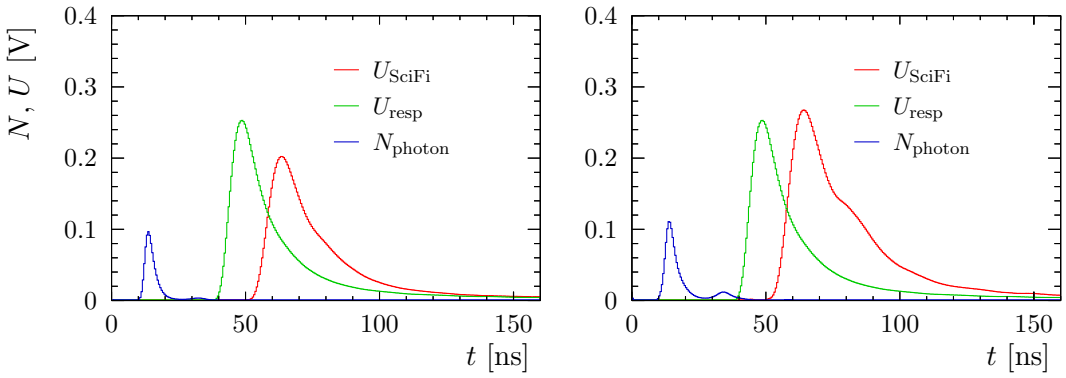

Figure 3.59: Measured MPPC output U_{ScFi} corresponding to fibre excitation at $x = 100\,\mathrm{cm}$. Plots (a) and (b) show acquired curves before and after metallisation of the fibre end, respectively. Deconvolution results for photon number distributions N_{photon} as well as the used response function U_{resp} are also drawn. U_{SciFi} and N_{photon} are scaled by a factor of 2 in (a) and 5 in (b) for the purpose of visibility.

which is obtained via the deconvolution approach, are also presented in the figure. At the chosen scale, the reflected light is hardly visible with the raw fibre end. After metallisation, $U_{\mathrm{SciFi}}(t)$ shows a small excess at its tail corresponding to reflected photons, see Fig. 3.59b. These photons appear as a second peak in $N_{\mathrm{photon}}(t)$ after application of the deconvolution process.

The GEANT4 simulation of scintillating fibres (*cf.* Sec. 3.2) is used to study timing properties in comparison with results obtained from measurements. The material properties of an SCSF-78MJ fibre, as shown in previous sections, are used as input parameters. In measurements, it is not possible to attach the fibre immediately to the sensitive area of the photodetector. As a consequence, only photons with a limited angle relative to the fibre axis will be recognised by the MPPC module, although, the fibre cross-section is smaller than the MPPC's sensor area. In simulation, this effect is roughly taken into account by only considering photons with angles smaller than 30° after leaving the fibre. The fibre is simulated with and without a mirror placed at its non-instrumented end corresponding to the measured fibre with and without aluminium coating. The simulated mirror has a reflectivity of 0.4 to produce an output similar to measurement.

Two different decay times of the wavelength-shifting dye are studied in simulation. The manufacturer Kuraray states a decay time of 2.8 ns [31] for SCSF-78 fibres, which agrees with the natural fluorescent lifetime of TPB [33]. However, decay processes of excited states additional to fluorescence may possibly occur in the investigated fibre. These would decrease both the quantum yield and the observed decay time. For example, values of 0.60 and 1.76 ns, respectively, have been observed for TPB dissolved in cyclohexane [33]. Therefore, a decay time of 2.2 ns is simulated in addition to the mentioned value of 2.8 ns to achieve an estimate from comparison

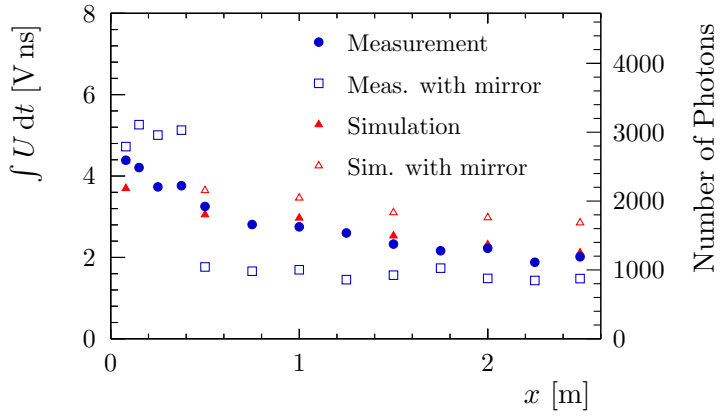

Figure 3.60: Detected light intensity in measurement ($\int U\ \mathrm{d}t$) and simulation (Number of Photons) *vs.* excitation point x.

with measurements, if decay processes besides fluorescence have to be taken into account for a proper description of the considered fibre.

The detected light intensity as a function of distance x of the excitation from the fibre end is shown in Fig. 3.60. Simulation and measurement without mirror exhibit comparable light attenuations with increasing x. Measurements after the metallisation process clearly deviate from all other data due to the light loss between 37.5 cm and 50 cm.

Time distributions of the photon number N_{photon} from measurement and simulation are shown in Figures 3.61 to 3.64. Measured distributions are shifted by 1 ns to smaller t which maximises the overlap with simulated curves in Fig. 3.61. Illustrated curves from simulation have been convolved with $U_{\mathrm{resp}}(t)$ and subsequently deconvolved by the described procedure. This approach facilitates a comparison of measurement and simulation results. It introduces the uncertainties of deconvolution results, which have been revealed by test distributions, *cf.* Fig. 3.58, to simulation output. All curves are normalised to have the same integral of 1. Simulation results for decay times of 2.2 ns are only shown at logarithmic scale, since they are hardly distinguishable from those corresponding to 2.8 ns at a linear scale.

Simulations and measurements of a fibre without mirror show a good agreement, see Fig. 3.61 and 3.62. At logarithmic scale, the small amount of photons reflected from the untreated fibre end is visible as distinct peak for excitations at $x \leq 100$ cm and also at $x = 150$ cm in measurement. Some measured distributions exhibit a third maximum which is consistent with photons successively reflected from both fibre ends before detection. This diminutive effect does not appear in simulation since photons arriving at the instrumented fibre end are erased to avoid excessive computing time. The presented distributions might hint at a better description of measurements by a simulated decay time of 2.2 ns. However, a clear evidence cannot by derived from the given results.

The signal shapes obtained from measurements with a metallised fibre end face deviate from simulations of a fibre including a mirror, see Fig. 3.63, 3.64. However,

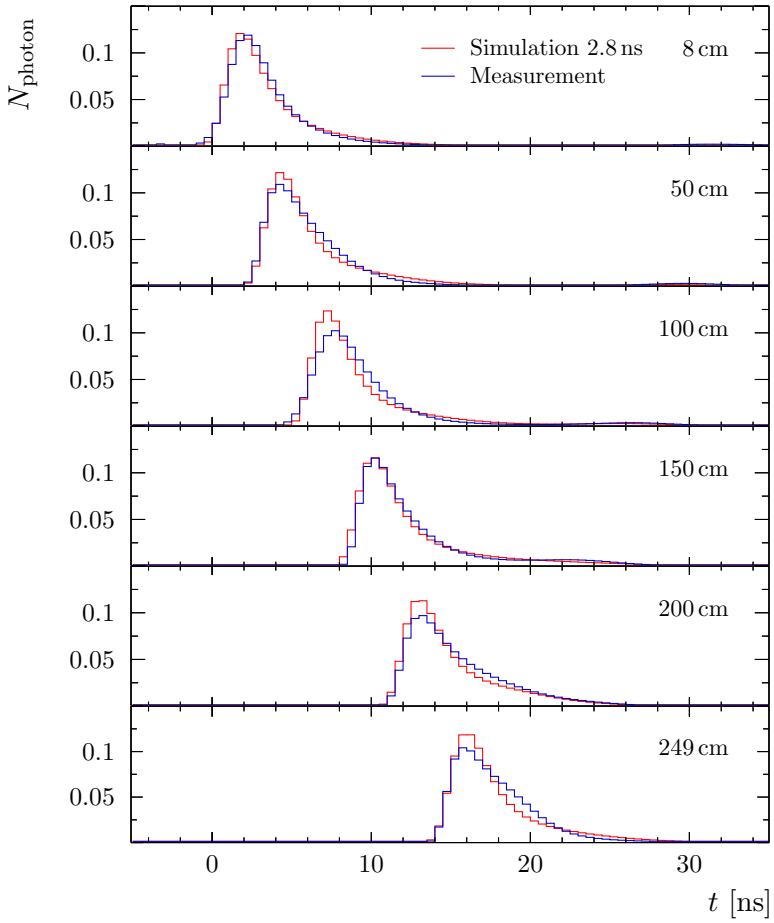

Figure 3.61: Measured and simulated time distributions of photon number N_{photon} with untreated fibre end. Results from several excitation positions x are shown. Simulated data are due to the decay time given in the legend. They include uncertainties resulting from the deconvolution process, see text. Each distribution is normalised so that the sum over all bins is 1.

the arrival time t of the main peak at the photodetector is similar in measurement and simulation. Reflected light occurs at later times in measurement than in simulation. This could be explained by defects observed at the metallised fibre. The light loss between 37.5 cm and 50 cm, *cf.* Fig. 3.60, is likely to be caused by photon scattering. Photons that are emitted at larger angles relative to the fibre axis than detectable could still be seen by the photodetector when being scattered to smaller angles at the defect. These photons potentially have longer path lengths and thus longer propagation times. The damage clearly reduces the intensity of reflected light when the fibre is excited at $x = 8$ cm. Furthermore, the defect could induce reflections and thus explain the increased trailing edge of the main peak

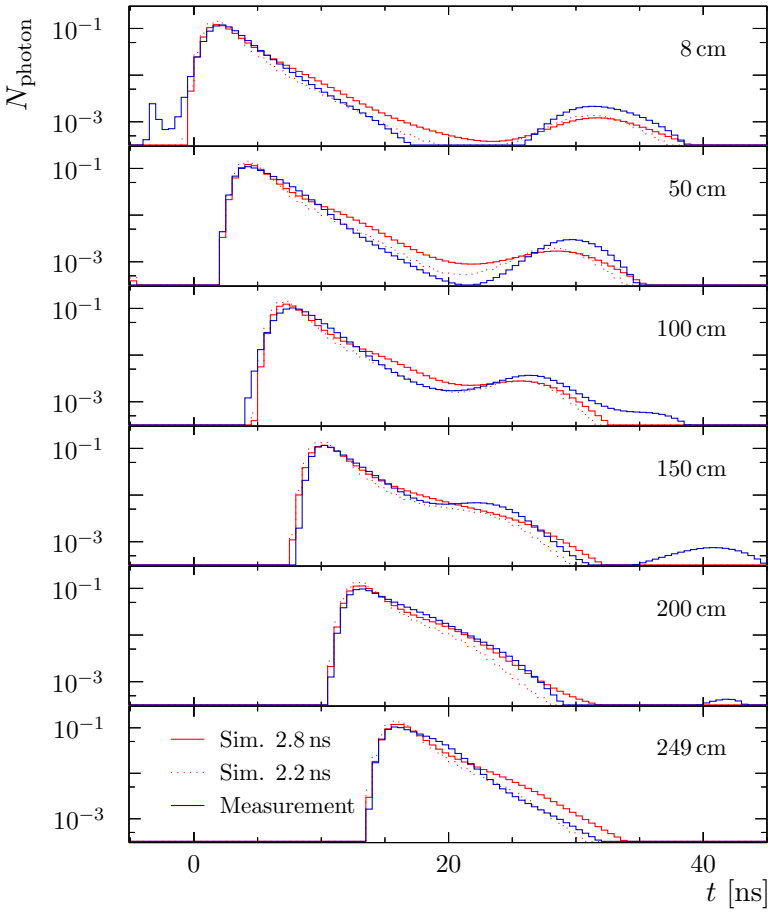

Figure 3.62: Measured and simulated time distributions of photon number N_{photon} with untreated fibre end plotted at logarithmic scale. Results from several excitation positions x are shown. Simulated data are due to the decay time given in the legend. They include uncertainties resulting from the deconvolution process, see text. Each distribution is normalised so that the sum over all bins is 1.

at excitations at 8 cm and 50 cm. Similar to measurements before metallisation, a third peak can be observed which is due to reflections from both fibre ends.

Times t corresponding to maxima of N_{photon} are plotted as a function of distance x of the excitation from the detector in Figure 3.65. The shift by 1 ns, which is applied to measured distributions in Fig. 3.61 to 3.64, is not included. Therefore, measured data points lie above simulated points. Additionally to peak times of simulated distributions as shown in Fig. 3.61 to 3.64, times of maxima in the simulation results are plotted, where no convolution and deconvolution has been applied. Hence, these data points are not affected by artefacts due to the analysis approach. Values of x greater than 2.5 m refer to the path length of reflected photons, projected to the fibre axis.

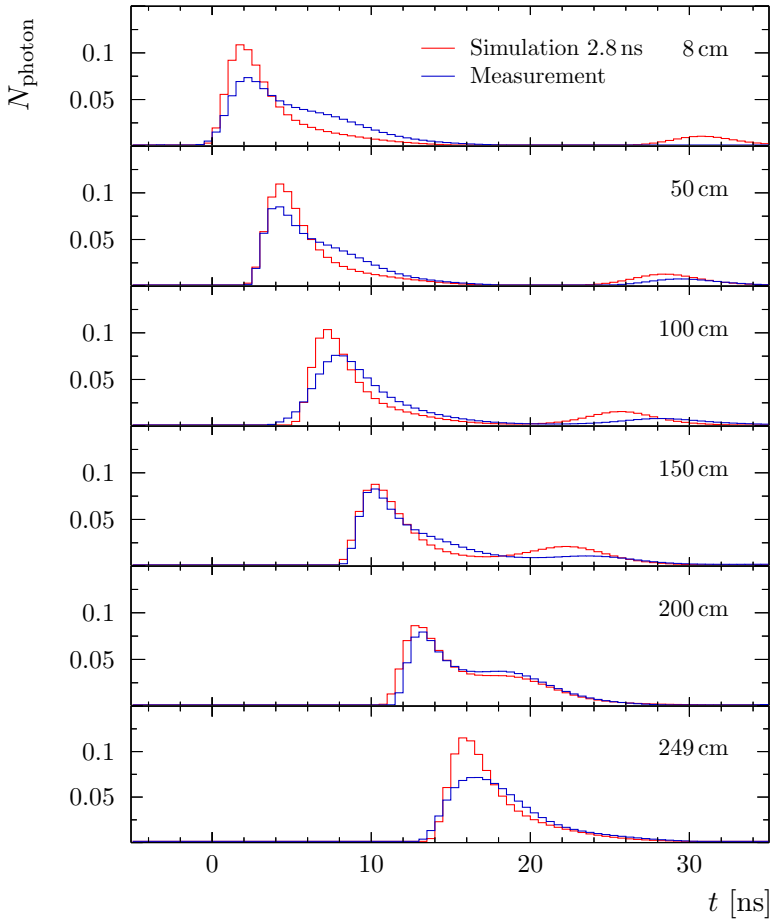

Figure 3.63: Measured and simulated time distributions of photon number N_{photon} with mirrored fibre end. Results from several excitation positions x are shown. Simulated data are due to the decay time given in the legend. They include uncertainties resulting from the deconvolution process, see text. Each distribution is normalised so that the sum over all bins is 1.

A linear function

$$t(x) = t_0 + p \cdot x \tag{3.63}$$

is fitted to data shown in Fig. 3.65. The determined parameters are the propagation time p of the signal peak per fibre length and a time offset t_0. Results are listed in Tab. 3.28 and 3.29. Stated parameter uncertainties result from uncertainties in t which are estimated to be 0.25 ns according to half bin width of determined time distributions. Data points, that correspond to peaks of reflected signal, show larger deviations. Therefore, uncertainties given in Tab. 3.29 are likely to be underestimated, especially in the case of measurements with metallised fibre end.

Propagation times p derived from measured and simulated data are close to 6.0 ns/m if only the direct signal is taken into account. Similar values are obtained

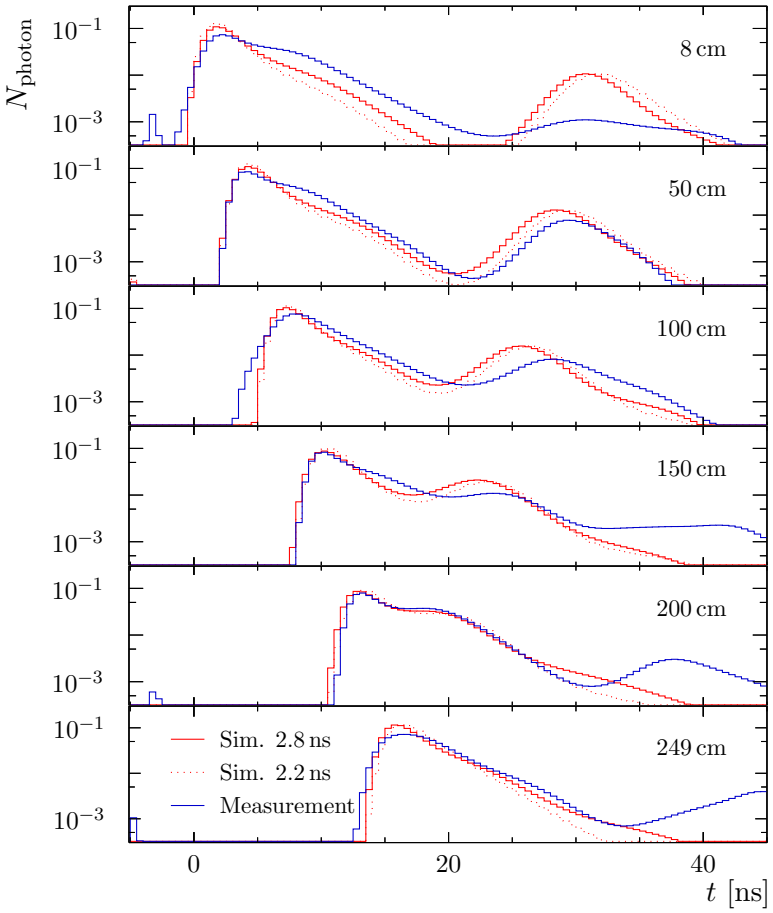

Figure 3.64: Measured and simulated time distributions of photon number N_{photon} with mirrored fibre end plotted at logarithmic scale. Results from several excitation positions x are shown. Simulated data are due to the decay time given in the legend. They include uncertainties resulting from the deconvolution process, see text. Each distribution is normalised so that the sum over all bins is 1.

from simulation with reflected light peaks included. Measurement results incorporating reflected signals exhibit slightly larger propagation times. However, these are the most affected by scatter of t which is not considered in the given uncertainty estimate.

The convolution of simulated time distributions with U_{resp} and following application of the deconvolution approach leads to an increase of t_0 by about 1 ns, while p is not significantly affected. Measured t_0 deviate from values from simulations including deconvolution artefacts by about 1 ns. This discrepancy is considered to be a systematic effect of the measurement procedure, since values of p are consistent, at least for direct light, and time distributions corresponding to a non-mirrored fibre are similar in measurement and simulation, *cf.* Fig. 3.61, 3.62.

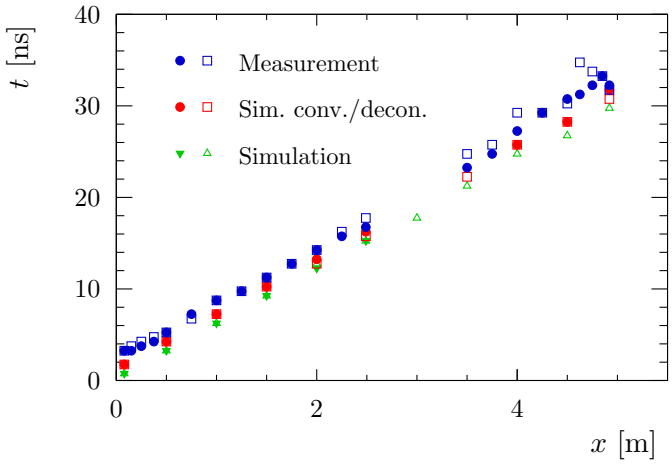

Figure 3.65: Arrival times t of signal peaks at the photodetector as function of fibre length x from the excitation to the instrumented fibre end. Open symbols denote results from fibre with mirrored end face. The abbreviation conv./decon. refers to simulation data being convolved with U_{resp} and subsequently deconvolved to include correspondent uncertainties.

Table 3.28: Parameter results of fitting Eq. (3.63) to data shown in Fig. 3.65 for $x \leq 2.5\,\text{m}$, *i.e.* taking into account direct light only.

Data	t_0 [ns]	p [ns/m]
Measurement	2.49 ± 0.12	5.85 ± 0.09
Measurement with mirror	2.57 ± 0.12	5.95 ± 0.09
Sim. conv./deconv.	1.25 ± 0.19	6.01 ± 0.12
Sim. conv./deconv. with mirror	1.38 ± 0.19	5.78 ± 0.12
Simulation	0.25 ± 0.19	6.02 ± 0.12
Simulation with mirror	0.22 ± 0.19	6.10 ± 0.12

Table 3.29: Parameter results of fitting Eq. (3.63) to data shown in Fig. 3.65 including mirrored light.

Data	t_0 [ns]	p [ns/m]
Measurement	2.09 ± 0.09	6.26 ± 0.03
Measurement with mirror	2.13 ± 0.09	6.44 ± 0.03
Sim. conv./deconv.	1.11 ± 0.14	6.13 ± 0.05
Sim. conv./deconv. with mirror	1.12 ± 0.14	6.04 ± 0.05
Simulation with mirror	0.34 ± 0.14	5.97 ± 0.05

Photon detection is restricted to particular angles of emission from the fibre end in the discussed measurements and simulations. However, a close attachment of fibres to photosensors with thin passivation layers is proposed for the LHCb SciFi Tracker to maximise the photon detection efficiency and hence the angular acceptance. Larger emission angles of photons imply larger path lengths and thus longer propagation times in the fibre, though.

This effect is studied in simulation by cancelling the constraint of only detecting photons with angles less than 30° relative to the fibre axis. Resulting photon distributions are visualised in Fig. 3.66. Indeed, distributions without angular constraint show a slightly larger width, especially with increasing x, and a longer propagation time of the signal peak than those corresponding to limited emission angles.

A further effect has to be considered to obtain time distributions of photons arriving at the photodetector as occurring in the SciFi Tracker. The peak emission wavelength of the used LED of about 370 nm is appropriate to excite the secondary WLS dye in the fibre core only. Its absorption by the primary dopant or the bulk polystyrene is negligible. In contrast, energy of ionising particles in the SciFi Tracker will be mainly deposited in the polystyrene matrix. This leads to photon emission by the primary dopant after non-radiative energy transfer from polystyrene. Therefore, the decay time of this dye has to be taken into account, compare Sec. 3.1.5.

Figure 3.66 shows simulated distributions where a decay time of the primary dopant of 1.21 ns, according to p-terphenyl [33], has been considered. As expected, these distributions exhibit a larger width and shifted peaks with respect to those corresponding to excitation by UV photons. It follows that, for particle hits as close as or closer than 100 cm from the instrumented fibre end, the majority of reflected light will arrive at $t > 25$ ns and thus appear as spill-over signal in the subsequent bunch crossing event, if signal integration starts at $t = 0$ ns.

The spill-over effect will be further increased due to the time response of the SiPM and readout electronics, which is not included here. In addition, the decay of triplet states which are excited by ionising particles, causes delayed emission of photons. This phenomenon is not studied in this paper either, since no correspondent information is available for the contemplated fibre SCSF-78MJ.

Times t corresponding to maxima of distributions shown in Fig. 3.66 are plotted *vs.* covered fibre length x. As before, Equation (3.63) is fitted to obtain the propagation time p of the signal peak. Obviously, fluctuations in the photon numbers per bin of evaluated distributions imply an uncertainty of the observed peak time that is larger than half a bin width, which was considered before. Hence, the uncertainty of parameters t_0 and p is estimated from the residual sum of squares obtained in the fit. Results are listed in Tab. 3.30. The numbers depict the increase in p when larger photon angles are included as well as the shift of maxima to later times if the primary dye is taken into account, occurring as larger t_0.

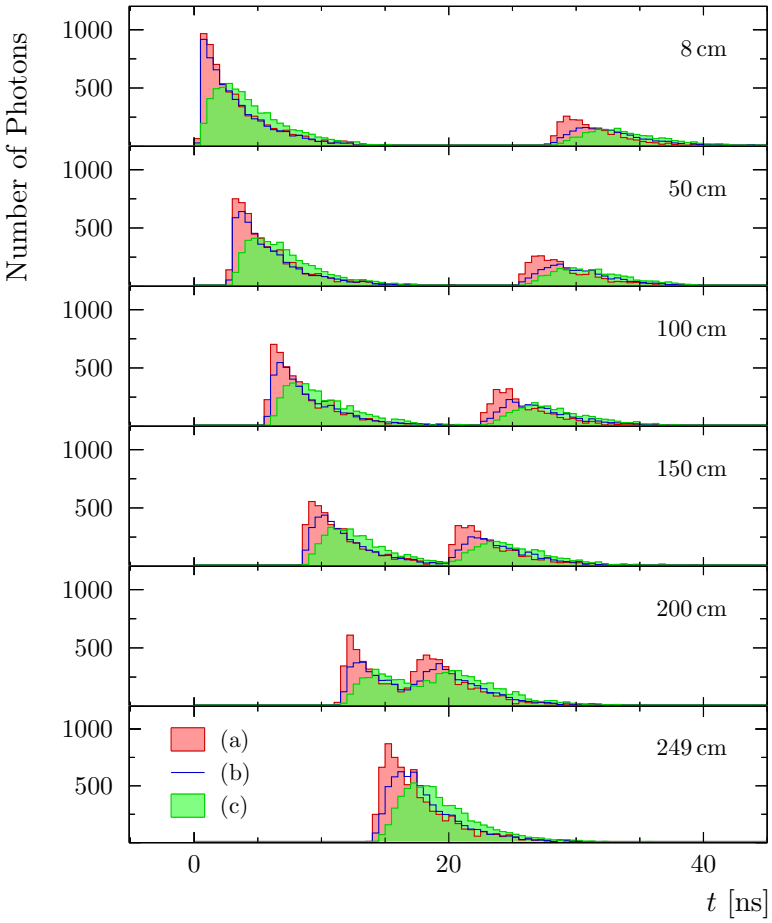

Figure 3.66: Simulated time distribution of detected photon number at several excitation positions x. A mirror with reflectivity 1 is used. Curves (a) and (b) are due to fibre excitation by UV photons. Only photons emitting from the fibre at angles smaller than 30° relative to the fibre axis are considered in (a). For better comparison, this curve is scaled by a factor of 3. Distribution (c) is observed at excitation by ionising particles.

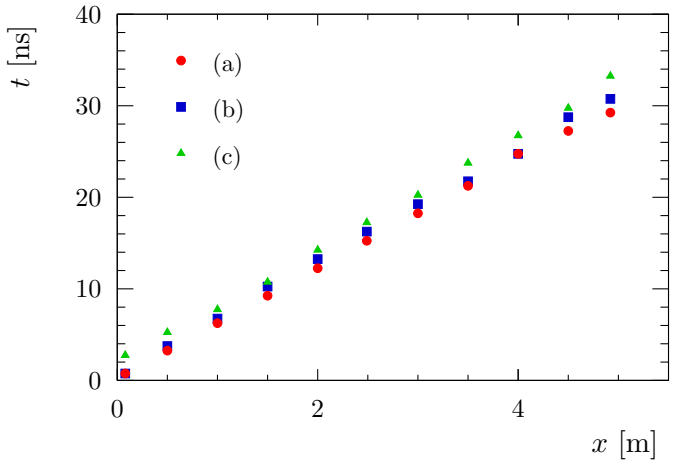

Figure 3.67: Simulated arrival times t of signal peaks at the photodetector as function of fibre length x from the excitation to the instrumented fibre end. Data are obtained from distributions (a), (b) and (c) shown in Fig. 3.66.

Table 3.30: Parameter results of fitting Eq. (3.63) to data shown in Fig. 3.67.

Data	t_0 [ns]	p [ns/m]
UV photons, angular cut	0.31 ± 0.14	5.98 ± 0.05
UV photons	0.68 ± 0.21	6.15 ± 0.07
Ionising particles	1.76 ± 0.23	6.28 ± 0.08

3.4 Conclusion and Outlook

Review of Scintillating Fibres

The deeper understanding of scintillating fibres as well as the realisation of a detailed fibre simulation demand the consideration of various physical processes. A review of these processes has been compiled to provide an overview of photon generation, capture and loss mechanisms. Theoretical models were fitted to data of refractive indices and wavelength-dependent absorption coefficients from literature and from measurements of the LHCb SciFi group. The contributions from different loss mechanisms to the total photon loss have been determined in this analysis. Knowledge about emission and absorption intensities of fluorescent dyes, that are dissolved in the fibre, is needed for a detailed SciFi simulation. However, manufacturers usually don't publish the used compounds and concentrations. The identification of the wavelength-shifting dye used in the SCSF-78MJ fibre from Kuraray and an estimate of its concentration have been achieved by consideration of the fibre's absorption spectrum, the emission spectrum at its end face and the decay time information.

Development of Scintillating Fibre Simulation

A comprehensive simulation of scintillating fibres has been developed using the GEANT4 toolkit. It has been designed to allow for an easy adjustment of fibre parameters such as emission spectra or refractive indices. The produced output data comprise an extensive set of variables which enables to study various fibre characteristics. The program is a valuable tool for SciFi Tracker R&D and is being used by different groups in the LHCb collaboration. Some of its applications are the investigation of alternative wavelength-shifters and fibre diameters (CERN), simulating the signal response of a fibre mat (Heidelberg, Lausanne) and comparison of different radiation models (Dortmund). Beyond the R&D programme, the simulation provides data that are used to infer parametrisations of photon yields, wavelength spectra and time distributions of signals resulting from particle hits in the LHCb SciFi Tracker. These parametrisations are necessary to generate an accurate detector response in Monte-Carlo data production.

Understanding Scintillating Fibres

In this work, the fibre simulation has been employed to study a large variety of characteristics such as spatial photon distributions, photon path lengths, light attenuation and radiation effects. These studies contribute to a better understanding of fibre measurements as shown by the following example. Traditionally, the attenuation length of a scintillating fibre is considered to rate its quality, *e.g.* in Ref. [23, 31]. However, it has been shown that this parameter is an imprecise measure. Neither the photon path length per fibre length nor the number of boundary interactions per fibre length are given by a discrete value but instead by distribution functions. In addition, absorption coefficients are dependent on the

photon wavelength which also occurs according to a continuous emission spectrum. As a consequence, it has been considered to use exponential expressions only as approximation for a clearly defined range of distances from the excitation point to the fibre end. The simulation shows that the measured attenuation length still depends on the angular and wavelength acceptance of the photodetector and on the light loss intermediate of the tested fibre range and the instrumented fibre end. These effects have thus to be taken into account when comparing respective measurements.

Wavelength Spectra, Dye Concentrations and Fibre Mat Response

The wavelength spectra obtained from the simulation are in good agreement with measurements. It has been shown how the concentration of the wavelength-shifting dye affects the light yield and it is concluded that the current baseline fibre in the LHCb SciFi tracker design, SCSF-78MJ, might profit from a higher dye concentration. In the case of MIPs traversing the fibres, the output of the simulation program can be used to determine the signal response of a full fibre mat by geometrical considerations. The resulting photon number distributions depend in a complex manner on the angle of particle incidence. The simulation results agree with data from measurements that were taken with cosmic muons at normal incidence.

Irradiation Tests

Scintillating fibres have been simulated according to the dose profile, excitation method and readout of irradiation tests that were performed by the LHCb SciFi group. Models derived from literature have been taken into account to simulate the occurring radiation damages. The obtained simulation results reproduce the measured data more precisely than previously used simplistic parametrisations.

Damages resulting from the high dose rate tests are best described by a damage model that assumes no oxygen being present in the fibre. However, radiation damages in LHCb occur at many orders of magnitude lower rates. Therefore, it must be considered that oxygen diffusion is able to balance the consumption by radiation-induced radicals. The resulting permanent availability of oxygen induces a stronger deterioration of the fibre.

Radiation Damage Estimate for the LHCb Upgrade

The above developed simulation is used to estimate the radiation damage due to the running conditions of the upgraded LHCb detector. The simulation result for particle hits in the central region of the detector, which is the most irradiated, indicates a decrease of about 40 % in the number of detected photons compared to the initial state. This photon loss increases to about 60 %, if the recommended safety factor of two for dose estimates is taken into account. The spectrum of detectable photons will be shifted to longer wavelengths by the radiation-induced light absorption.

Timing

In the LHCb SciFi Tracker, signals will be measured by consecutive integrations over 25 ns. The signal fraction of a single particle hit, that will be recorded during a particular integration period, is dependent on the photon arrival times at the SiPM. These arrival times and their dependence on the hit location have been studied by simulation and measurement. However, measured waveforms were dominated by the signal response of the photodetector. Separation of the contributions from the fibre and the photodetector to the measured signal shape has been achieved by application of the Richardson-Lucy deconvolution algorithm. The simulation results are in agreement with the measurement. The obtained signal propagation times are used in the overall SciFi Tracker simulation.

4 Silicon Photomultipliers

Only a few scintillation photons, in some cases less than ten per particle hit, will reach the photodetectors of the LHCb SciFi Tracker. Silicon photomultipliers (SiPM) have been proposed to detect these small signals. The main characteristics of SiPMs are introduced in Sec. 4.1. Subsequently, characterisation measurements of these photo-sensors are presented. In particular, radiation effects have been studied to enable an assessment of their viability at conditions of the upgraded LHCb detector.

4.1 Introduction

The silicon photomultiplier (SiPM) is a semiconductor device which enables the measurement of small light intensities at single photon level. Its internal gain is in the order of 10^5 to 10^7. The main advantages of this photodetector, besides its high gain, are good photon detection efficiency (PDE), low bias voltage (25 V to 75 V), low power consumption, compactness, robustness, insensitivity to magnetic fields and to accidental illumination and good timing properties [77, 78].

The SiPM is an array of Geiger mode avalanche photodiodes (G-APD), *cf.* Fig. 4.1. These diodes are operated at reverse bias voltage higher than their breakdown voltage. Consequently, a photon generating an electron-hole pair in the depletion zone of the diode may trigger an avalanche that will persist and thus lead to a significant, permanent diode current. A so-called quenching resistor (R_q) is connected to each photodiode in series. In case of a diode breakdown, the voltage drop at the resistor results in a decrease of the diode voltage below the breakdown voltage. The avalanche is quenched and the diode current is stalled. The released charge per breakdown is independent of the number of initially generated electron-hole pairs which motivates the denotation *Geiger mode*.

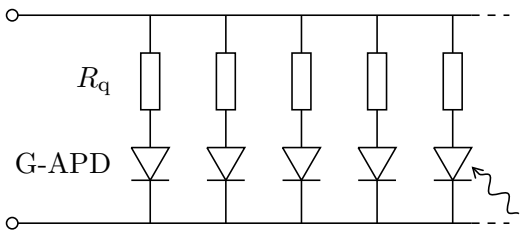

Figure 4.1: Schematic diagram of a Silicon Photomultiplier.

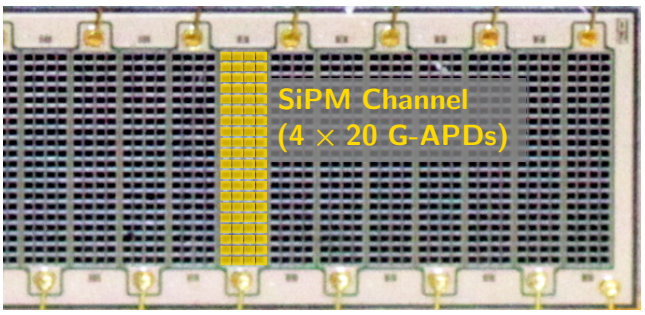

Figure 4.2: Detail view of a Hamamatsu SiPM array (see Sec. 4.2.1). Yellow rectangles identify the G-APD pixels of one exemplary channel which is equivalent to a single SiPM. The channel width is 250 µm in horizontal direction.

The photodiodes are pixels visible on the device's surface, see Figure 4.2. The SiPM signal charge is proportional to the number of fired pixels, *i.e.* of G-APDs where an avalanche was triggered. Since two or more simultaneously incoming photons might hit the same pixel, the expectation value of the number of fired pixels N_{fired} is given by

$$\langle N_{\text{fired}} \rangle = N_{\text{pixel}} \cdot \left(1 - \exp\left(-\frac{\varepsilon_{\text{PD}} N_{\text{photon}}}{N_{\text{pixel}}} \right) \right) \ , \tag{4.1}$$

with the total number of G-APD pixels N_{pixel}, the number of incoming photons N_{photon} and the PDE ε_{PD}.

The photon detection efficiency ε_{PD} can be expressed as a product of three factors.

$$\varepsilon_{\text{PD}} = \varepsilon_{\text{GF}} \cdot \varepsilon_{\text{Q}} \cdot \varepsilon_{\text{BD}} \tag{4.2}$$

The geometric fill factor ε_{GF} is the ratio of the sensitive area of pixels to the total sensor area. It is limited by the quenching resistor, which is usually located at the semiconductor's surface, and the distance between pixels that is necessary to provide electrical and optical insulation. The probability of a photon to generate an electron-hole pair within the depletion zone of the diode's p-n junction is given by the quantum efficiency ε_{Q}. It is dependent on the photon wavelength and the particular doping profile of the SiPM. The third factor, ε_{BD}, is the probability of a generated electron-hole pair to initiate an avalanche breakdown. This breakdown efficiency is a function of over-voltage U_{over}, which is defined as excess of bias voltage U_{bias} over the breakdown voltage U_{BD}.

$$U_{\text{over}} = U_{\text{bias}} - U_{\text{BD}} \tag{4.3}$$

The SiPM gain G is the number of elementary charges e that are released in a single avalanche breakdown. It is determined by the change of reverse diode voltage U_{diode} in the course of a breakdown and the capacitance of the G-APD C_{diode}.

$$G = \frac{1}{e} \int_{U_{\text{BD}}}^{U_{\text{bias}}} C_{\text{diode}} \, \mathrm{d}U_{\text{diode}} \tag{4.4}$$

The depletion layer capacitance is defined by

$$C_{\mathrm{diode}} = \frac{\mathrm{d}Q_{\mathrm{diode}}}{\mathrm{d}U_{\mathrm{diode}}} \ , \tag{4.5}$$

with Q_{diode} being the depletion charge of the diode.

For an abrupt p-n junction, the capacitance's dependence on U_{diode} is given by

$$C_{\mathrm{diode}} \propto \left(U_{\mathrm{BI}} + U_{\mathrm{diode}} - \frac{2k_{\mathrm{B}}T}{e} \right)^{-\frac{1}{2}} \ , \tag{4.6}$$

as long as the diode volume is not fully depleted. The built-in potential U_{BI} of a p-n junction in silicon is about 0.8 V [79]. The temperature-dependent term $2k_{\mathrm{B}}T/e$ reaches a value of about 50 mV at room-temperature. Therefore, it is negligible compared to typical bias voltages.

The gain can be approximated by

$$G \approx \frac{1}{e} \cdot C_{\mathrm{diode}}(U_{\mathrm{BD}}) \cdot U_{\mathrm{over}} \propto U_{\mathrm{over}} \tag{4.7}$$

or

$$G \approx \frac{1}{e} \cdot C_{\mathrm{diode}}(U_{\mathrm{bias}}) \cdot U_{\mathrm{over}} \propto \frac{U_{\mathrm{over}}}{\sqrt{U_{\mathrm{BI}} + U_{\mathrm{bias}}}} \tag{4.8}$$

by using first order terms of a Taylor series centred at U_{BD} or U_{bias}, respectively. While Eq. (4.8) relies on the validity of Eq. (4.6), the approximation (4.7) can also be used with different C-U relations. However, both approximations differ only by a few percent at realistic over-voltages.

Common G-APDs have, instead of a single abrupt junction, a doping profile that leads to a depletion width that is nearly independent of the bias voltage. For these so-called "reach-through" diodes, C_{diode} is therefore constant and the gain is given by

$$G \approx \frac{1}{e} \cdot C_{\mathrm{diode}} \cdot U_{\mathrm{over}} \ . \tag{4.9}$$

Even though the G-APD pixels are electrically insulated from each other, a fired diode is able to trigger an avalanche breakdown in a neighbouring cell. This cross-talk effect is caused by optical photons that are emitted from the carriers in an avalanche. The photons may reach the depletion layer of an adjacent diode and thus initiate a further breakdown there. A fraction of $2.9 \cdot 10^{-5}$ photons with energy higher than 1.14 eV per carrier crossing the junction is reported in [80].

Delayed signal pulses can be observed subsequently to a breakdown. These after-pulses are caused by the release of charge carriers that have been trapped during the primary breakdown. Reference [81] quotes two independent time constants of 15 ns and 82 ns describing the occurrence of after-pulses.

In addition to photo-generated avalanches, a breakdown can also be triggered by thermal generation of free carriers in the depletion layer. Besides carrier diffusion,

the presence of defects in the depletion zone enables electron transitions from the valence band to the conduction band. The corresponding dark count rate r_{dark} is dependent on the defect concentration and on the size of the depleted volume. Defect levels close to the mid band gap are the most efficient generation centres. The temperature dependence of r_{dark} resulting from these defects can be derived from Shockley-Read-Hall (SRH) statistics [82, 83] and is given by

$$r_{\text{dark}} \propto T^2 \exp\left(-\frac{E_{\text{G}}}{2k_{\text{B}}T}\right) , \tag{4.10}$$

with band gap E_{G}. However, deviations from this temperature dependence may be observed due to trap-assisted tunnelling in the high-field region of the p-n junction [84].

The suitability of SiPMs for fibre readout in the LHCb SciFi Tracker is depending on their characteristics as described in the following. The particle hit detection efficiency and the spatial resolution depend on the number of photons that are detected by the SiPM, *cf.* Sec. 2.3, and thus on its PDE. Fake hits which deteriorate the tracking performance may result from the SiPM's dark count rate. Pixel cross-talk and random coincidence of thermal breakdowns or after-pulses can lead to signals that exceed the thresholds set in the data acquisition. SiPMs in the LHCb SciFi Tracker have to be radiation hard in terms of providing a sufficient gain, PDE and low noise rate throughout the full LHCb upgrade data taking period. Studies of the mentioned SiPM characteristics as functions of over-voltage, temperature and radiation level are presented in the following sections of this chapter.

4.2 Characterisation Measurements

4.2.1 Sensors

Characterisation measurements have been performed with silicon photomultipliers having a structure as proposed for the LHCb SciFi Tracker, compare Sec. 2.3. Devices from the two manufacturers Hamamatsu[1] and KETEK[2] are investigated. All tested sensors consist of G-APD pixels whose dimensions are roughly 50 µm × 50 µm. The studied Hamamatsu SiPMs comprise two commercially available products, MPPC S10362-11-050U and MPPC S11028-050, as well as 32-channel SiPM arrays. The latter are all of the same type, MPPC 5883, and were originally produced for the PEBS experiment [85]. Figure 4.2 shows a detail view of this sensor type. The characterised KETEK SiPMs are 32-channel arrays as well. These are three different, customised prototypes that were produced for research and development for the LHCb SciFi Tracker.

The tested devices are listed in Table 4.1. In the following, Hamamatsu SiPM arrays of type MPPC 5883 are denoted by a device name starting with a capital H, *e.g.* HZ5-7-A, while single-channel Hamamatsu SiPMs are identified by their product number given in Tab. 4.1. Identifiers of KETEK SiPMs begin with the character W.

Table 4.1: Geometry of tested SiPMs.

Sensor	Channels	Pixels per channel	Pixel size [µm^2]
Hamamatsu MPPC			
5883	32	4×20	58 ×55
S10362-11-050U	1	20×20	50 ×50
S11028-050	1	20×20	50 ×50
KETEK	32	4×22	57.5×60

4.2.2 Test Setups

Various test setups have been established to execute SiPM characterisation. Schematic diagrams of these setups are shown in Fig. 4.3, 4.4, 4.5 and 4.6. Setup A was designed for laboratory measurements and irradiation tests with proton beams (see Sec. 4.6.1). B is only used for characterisation in the laboratory. Setups C and D have been developed for long-term, *in situ* irradiation tests in the LHCb cavern and are also used in laboratory measurements.

[1]Hamamatsu Photonics K.K., Japan
[2]KETEK GmbH, Germany

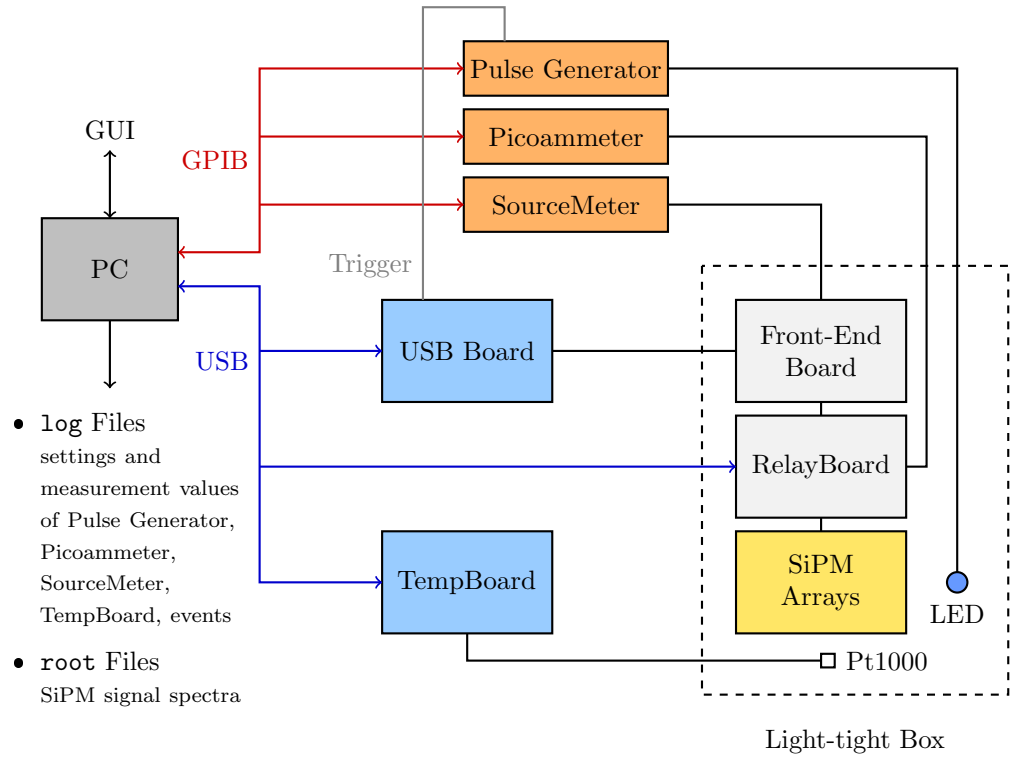

Figure 4.3: SiPM test setup A.

Measurement setup A (Fig. 4.3) enables the characterisation of SiPM arrays. A front-end (FE) board is used that provides read-out of four 32-channel arrays. Sampled SiPM signals are digitised on a back-end board. In Fig. 4.3, it is labelled USB board due to the fact that it transfers measured data to a PC via an USB interface. The used front-end and back-end electronics were developed by *I. Physikalisches Institut B, RWTH Aachen University* and *Ecole Polytechnique Federale de Lausanne* for a scintillating fibre tracker described in Ref. [85].

SiPM arrays are connected to the front-end electronics by an intermediate device, the RelayBoard. It offers the possibility to measure the current of single channels of one SiPM array. This is done by 32 relays that are operated via a USB interface. Switching a particular relay establishes a series connection of the corresponding SiPM channel, a Keithley Picoammeter 6487 and the FE board. The SiPM channel is connected directly to the respective FE board input channel, otherwise. The SiPM array whose single-channel currents are to be analysed is chosen by plugging the relays' connector to the appropriate slot on the RelayBoard. All other SiPM arrays are read out by the FE board without intermediate relay switches. The relay was chosen to be used as switching device to avoid the additional voltage drop occurring at electronic switching components.

The SiPM bias voltage is supplied by a Keithley SourceMeter 2400 which also provides measurement of bias voltage and current. A blue LED with peak emission at about 470 nm wavelength is used to illuminate the photo-sensors. It is powered

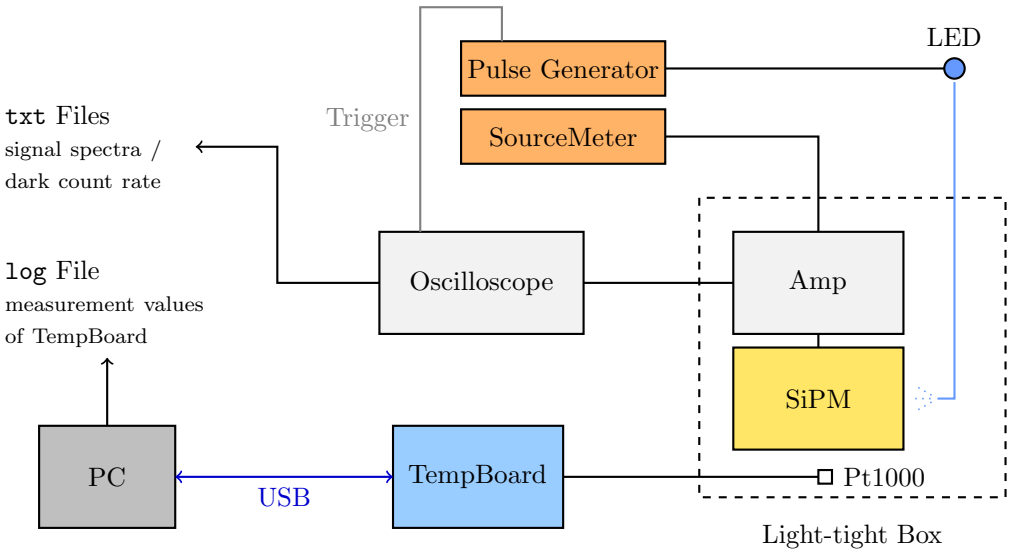

Figure 4.4: SiPM test setup B.

by an Agilent 81110A pulse/pattern generator. LED pulses are triggered by a signal that is sent from the USB board to the pulse generator prior to SiPM pulse sampling on the FE board. The ambient temperature at the SiPM arrays is monitored by means of a so-called TempBoard and Pt1000 temperature sensors, which are described in Sec. 4.2.3.

A computer program has been developed to control device and measurement settings, perform test sequences and save the acquired data. The pulse generator, Picoammeter and SourceMeter are controlled and read out using a GPIB interface. Communication with the USB board, RelayBoard and TempBoard is realised by USB. The program provides a graphical user interface (GUI).

Measured SiPM signal spectra are stored in histograms that are written to `root` files employing the ROOT data analysis framework [66]. Test settings and measurements by the SourceMeter, Picoammeter and TempBoard are stored in plain text files (`log` files).

SiPM signal pulses are also recorded with test setup B, illustrated in Fig. 4.4. However, it provides only a single read-out channel in contrast to 4×32 channels in setup A. The SiPM is connected to an amplifier circuit whose output is sampled by a LeCroy SDA 5000A digital oscilloscope. This allows to investigate the amplified signal waveform, while the front-end board used in setup A samples the signal height of the shaped SiPM pulse at a particular time. Furthermore, the dark count rate can be determined by measuring the number of occurring signal pulses, if the waveform is recorded over a sufficiently long period without illumination of the photodetector. Measured signal spectra and dark count rates are written to plain text (`txt`) files.

Data acquisition with the oscilloscope is initiated by a trigger signal sent from a pulse generator at a fixed rate. In the case of LED signal measurement, the pulse generator powers a blue LED accordingly to the trigger signal. The LED is kept

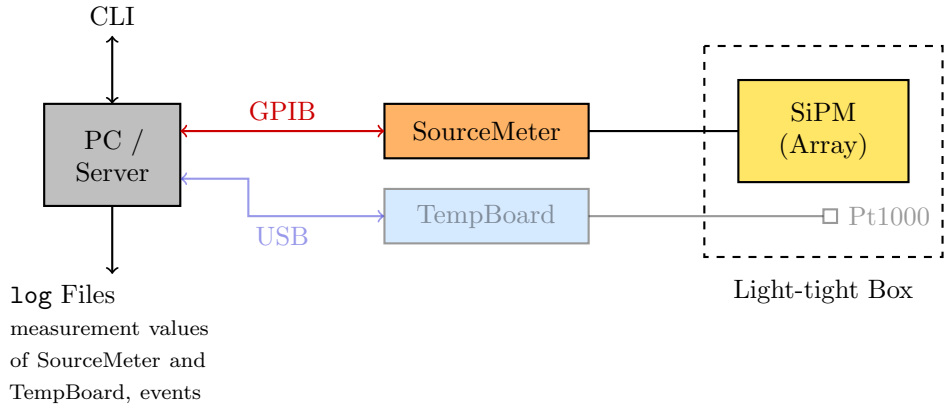

Figure 4.5: SiPM test setup C.

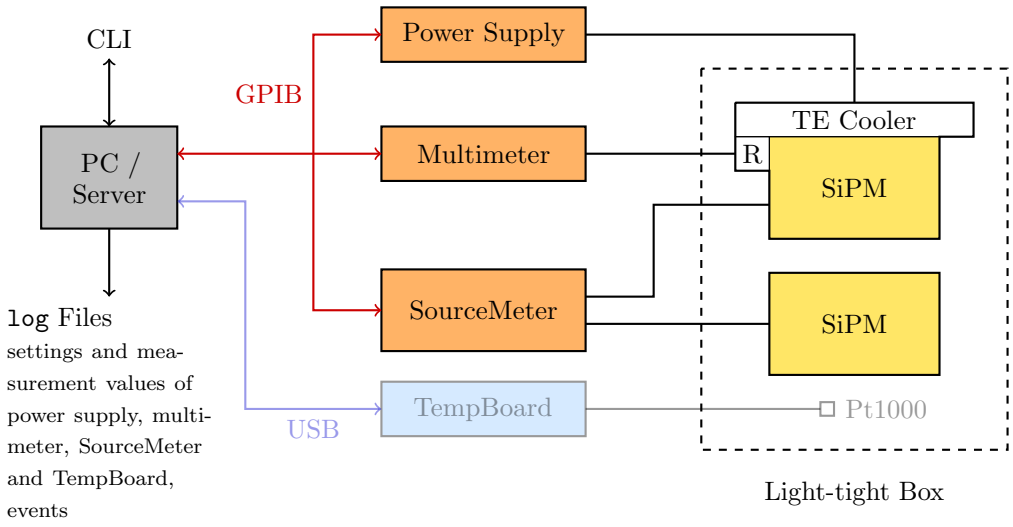

Figure 4.6: SiPM test setup D.

distant from the SiPM under test, since the used signal amplifier reveals a high sensitivity to noise induced by surrounding emitters. The LED's light is guided to the photo-sensor by means of a plastic optical fibre.

A simple measurement setup is shown in Figure 4.5. It is used to determine the current–voltage (I-U) characteristic of SiPMs and its temperature dependence. I-U scans are executed by a computer program utilising a Keithley SourceMeter 2400. A scan is performed at program start and automatically repeated every hour as long as the program is running. This feature enables monitoring the I-U characteristic during long-term irradiation in the LHCb detector cavern, *cf.* Sec. 4.6.2. Temperature measurement using the TempBoard and Pt1000 sensors is only done in laboratory tests, not in the LHCb cavern.

The I-U characteristics of Hamamatsu MPPC S10362-11-050U and MPPC S11028-050 are obtained with help of test setup D which is illustrated in Fig. 4.6. The

mentioned devices have equivalent photo-sensors, *cf.* Table 4.1. However, type S11028-050 makes use of a thermoelectric (TE) cooler and a thermistor, indicated by R in Fig. 4.6, arranged close to the SiPM to control and monitor its temperature.

Both SiPMs are biased by a Keithley SourceMeter 2612 which offers two independent test channels. The TE cooler is powered by a TTi TSX 3510P programmable power supply. Resistance measurements at the thermistor are done using a Philips PM2525 multimeter. All three devices are remotely controlled via a GPIB interface. Measurements and settings, *e.g.* TE cooling power, can be controlled by a computer program via command-line interface (CLI).

Test setup D has been designed for long-term sensor irradiation *in situ*, *i.e.* at the LHCb detector. During the irradiation test, the program runs on a server located in the shielded part of the LHCb cavern. The server is accessible by a network connection which enables online operation.

4.2.3 Temperature Measurement and Temperature Sensor Calibration

Temperature measurements are performed utilising two different sensor types. The majority of temperature data presented in this thesis has been obtained by the employment of Pt1000 sensors. These industrial resistance temperature detectors (RTD) are constructed of platinum with a set point of $1000\,\Omega$ at $0\,°C$. The specification of the Pt1000 RTD is given by the standard DIN EN 60751 [86].

Readout of the Pt1000 sensors is done with help of a dedicated electronics board referred to as TempBoard in this thesis. This board allows for readout of up to 16 sensors, each connected with a 4-wire lead. On the TempBoard a microcontroller controls the consecutive measurement of the 16 channels by means of two multiplexers and an Analog Devices AD7719 analogue-to-digital converter (ADC) [87]. Conversion of the ADC values to temperatures in °C is carried out by the microcontroller, too. After conversion the TempBoard sends the acquired data to a PC via an USB interface. Thus, the user does not get to know the actual resistances of the Pt1000 sensors but only the correspondent temperatures.

Due to possible inaccuracies of the data conversion done by the microcontroller and unknown systematic errors in the resistance measurement itself a calibration of the TempBoard is necessary. To check if the recorded temperatures comply with DIN EN 60751 several different resistors with ohmic resistances are connected to the TempBoard. The resistance values are determined by means of a Keithley 2010 multimeter [88]. When connecting the same resistor to different channels no change in the measured temperature can be observed, thus, no channel-dependent systematic error is assumed. However, a significant discrepancy between the measured temperatures T_{board} and the temperatures corresponding to the connected resistances according to DIN EN 60751, T_{din}, is found. Fig. 4.7 shows the deviation $T_{\mathrm{din}} - T_{\mathrm{board}}$ against T_{board}. These data can be well described by a linear function

$$T_{\mathrm{din}} = ((1.237 \pm 0.003) + (1.00536 \pm 0.00008) \cdot T_{\mathrm{board}}[°\mathrm{C}])\ °\mathrm{C}\ . \tag{4.11}$$

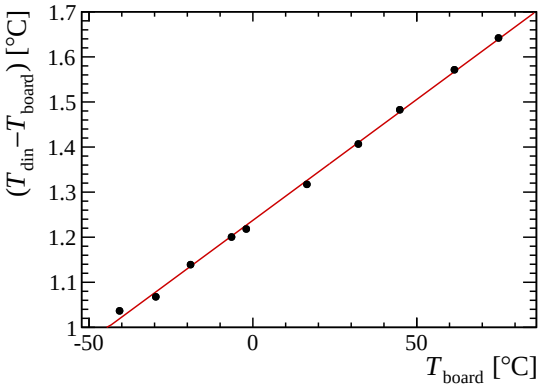

Figure 4.7: Difference between T_{din} corresponding to connected resistors and T_{board} measured by the TempBoard.

All temperature data that are taken utilising the TempBoard are calibrated with help of Eq. (4.11). The error of this calibration $\sigma_{T_{\mathrm{din}}}$ is assumed to be

$$\sigma_{T_{\mathrm{din}}} = \sqrt{\mathrm{RSS/ndf}} = \sqrt{0.000636/8}\,^{\circ}\mathrm{C} = 0.0089\,^{\circ}\mathrm{C}$$

according to the residual sum of squares (RSS) of the fit.

Compared to the uncertainty of calibration by Eq. (4.11), the production accuracy of Pt1000 sensors is a major source of systematic errors. Fig. 4.8 shows calibrated data taken with six sensors at two different temperatures (a) and (b). The distributions are in good agreement with the specification for type F 0,3 elements with a limiting deviation of

$$\Delta T_{\mathrm{Pt1000}} = \pm\,(0.3 + 0.005 \cdot |T[^{\circ}\mathrm{C}]|)\ ^{\circ}\mathrm{C} \quad [86].$$

The deviations of numerous sensors are expected to form a rectangular distribution within the limits given by $\Delta T_{\mathrm{Pt1000}}$. Thus, the total uncertainty σ_T of temperature measurements performed with Pt1000 sensors readout by the TempBoard can be estimated by

$$\sigma_T = \sqrt{\left(\frac{2 \cdot |\Delta T_{\mathrm{Pt1000}}|}{\sqrt{12}}\right)^2 + \sigma^2_{T_{\mathrm{din}}}}\ . \tag{4.12}$$

Considering the mean temperatures in Fig. 4.8 (a) and (b), respectively, this relation leads to $\sigma_T(4.43\,^{\circ}\mathrm{C}) = 0.19\,^{\circ}\mathrm{C}$ and $\sigma_T(22.78\,^{\circ}\mathrm{C}) = 0.24\,^{\circ}\mathrm{C}$ compared to the standard deviations $\sigma_{(\mathrm{a})} = 0.17\,^{\circ}\mathrm{C}$ and $\sigma_{(\mathrm{b})} = 0.13\,^{\circ}\mathrm{C}$ of these two distributions. So, in this special case the systematic uncertainties seem to be slightly overestimated by Eq. (4.12). But, since the means of the measured data in Fig. 4.8 are not necessarily equal to the real temperatures, the systematic uncertainties might be greater than the standard deviations from the mean values.

Another sensor type than the Pt1000 is used to monitor the temperature of the Hamamatsu MPPC S11028-050 [89]. This device contains a thermistor inside its package close to the photo sensor. The characteristics of the thermistor are provided

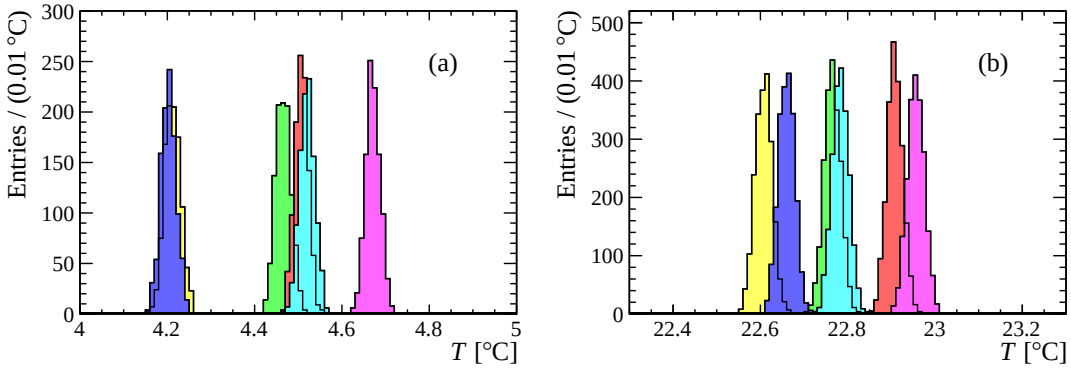

Figure 4.8: Calibrated data of six Pt1000 elements at two different temperatures shown in (a) and (b).

by Hamamatsu in the data sheet in two different ways. On the one hand, the correlation between resistance and element temperature is shown by a data plot. On the other hand, parameters of the following expression are specified, where R_{25} is the thermistor resistance at 25 °C.

$$R(T) = R_{25} \exp\left(B_{25/50}\left(\frac{1}{T} - \frac{1}{298.15\,\mathrm{K}}\right)\right) \tag{4.13}$$

The parameter values stated by Hamamatsu [89] are

$$R_{25} = 9\,\mathrm{k\Omega} \quad , \quad B_{25/50} = 3410\,\mathrm{K}\ .$$

Using these parameters leads to a description of the temperature–resistance relation that is different from the data plot shown in the same data sheet, what is a result of the bad accuracy of Eq. (4.13) when considering a wide temperature range. To get a sufficiently precise temperature information, calibration measurements are performed and the Steinhart-Hart equation (4.14) (see Ref. [90]) is fitted to the data.

$$T^{-1} = A + B\log(R[\Omega]) + C\left(\log(R[\Omega])\right)^3 \tag{4.14}$$

Resistances seen at the thermistor are measured with a Philips PM 2525 multimeter [91], to which the thermistor is connected via a 4-wire lead. Since the temperature sensor is enclosed by the device package, it is not possible to place another sensor directly at the thermistor's position for calibration. For this reason, three Pt1000 sensors are attached to the package's surface, instead. Because the ambient temperature T_a, which is measured via the Pt1000 sensors, may differ from the thermistor temperature inside the device T_i, the following considerations are made to achieve a feasible calibration, though.

The derivative of the inner temperature with respect to time is approximated to be proportional to the difference between outer and inner temperature.

$$\frac{\mathrm{d}T_\mathrm{i}}{\mathrm{d}t}(t) = \big(T_\mathrm{a}(t) - T_\mathrm{i}(t)\big) \cdot \mathrm{const} \tag{4.15}$$

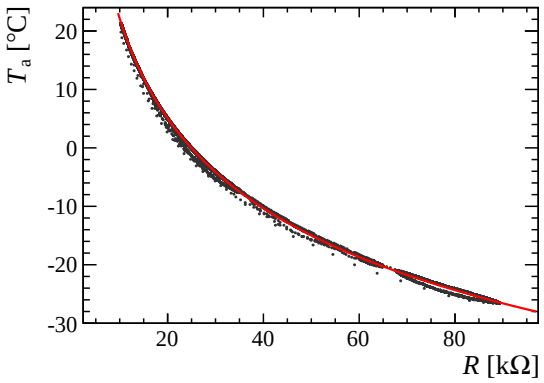

Figure 4.9: Ambient temperature measured at package surface *vs.* thermistor resistance. The red curve shows the result of fitting the Steinhart-Hart equation (4.14) to the data points.

Considering times t_0 and t_1 with identical T_i this leads to

$$T_\mathrm{i}(t_0) = T_\mathrm{i}(t_1) = \frac{T_\mathrm{a}(t_1) \cdot \left(\frac{\mathrm{d}T_\mathrm{i}}{\mathrm{d}t}(t_1)\right)^{-1} - T_\mathrm{a}(t_0) \cdot \left(\frac{\mathrm{d}T_\mathrm{i}}{\mathrm{d}t}(t_0)\right)^{-1}}{\left(\frac{\mathrm{d}T_\mathrm{i}}{\mathrm{d}t}(t_1)\right)^{-1} - \left(\frac{\mathrm{d}T_\mathrm{i}}{\mathrm{d}t}(t_0)\right)^{-1}} \ . \tag{4.16}$$

Provided that the data are acquired with a constant sampling rate, for a measured resistance R that may occur at two different times t_0 and t_1 the expectation of T_a is

$$\langle T_\mathrm{a} \rangle \,|_R = \frac{T_\mathrm{a}(t_0) \cdot \left|\frac{\mathrm{d}R}{\mathrm{d}t}(t_0)\right|^{-1} + T_\mathrm{a}(t_1) \cdot \left|\frac{\mathrm{d}R}{\mathrm{d}t}(t_1)\right|^{-1}}{\left|\frac{\mathrm{d}R}{\mathrm{d}t}(t_0)\right|^{-1} + \left|\frac{\mathrm{d}R}{\mathrm{d}t}(t_1)\right|^{-1}} \ . \tag{4.17}$$

By multiplying the numerator and denominator of this fraction by $\left(\frac{\mathrm{d}T_\mathrm{i}}{\mathrm{d}R}\right)^{-1}$ it follows that

$$\langle T_\mathrm{a} \rangle \,|_R = T_\mathrm{i}(R) \ , \tag{4.18}$$

if the sign of $\frac{\mathrm{d}T_\mathrm{i}}{\mathrm{d}t}$ is different at t_0 and t_1. Since the number of derivatives $\frac{\mathrm{d}T_\mathrm{i}}{\mathrm{d}t}|_{R'}$ with positive and negative signs must be equal at any R', if T_i, and thus R, is identical at the beginning and the end of a measurement, Eq. (4.18) is valid in this case. Hence, the Steinhart-Hart equation (4.14) is fitted to data points (R, T_a) adopting the least squares method to determine $T_\mathrm{i}(R)$.

This method provides the parameter values

$$\begin{aligned} A &= (8.2989 \pm 0.0051) \cdot 10^{-4}\,\mathrm{K}^{-1} \ , \\ B &= (2.6792 \pm 0.0007) \cdot 10^{-4}\,\mathrm{K}^{-1} \ , \\ C &= (1.1439 \pm 0.0023) \cdot 10^{-7}\,\mathrm{K}^{-1} \ . \end{aligned}$$

The parameter errors result from weights $\sigma_{T_\mathrm{a}}^{-2}$ due to measurement errors. These weights are fixed at $(0.2\,^\circ\mathrm{C})^{-2}$ to be of the same order of magnitude as given by Eq. (4.12) but with no temperature dependence to prevent the fit result from bias.

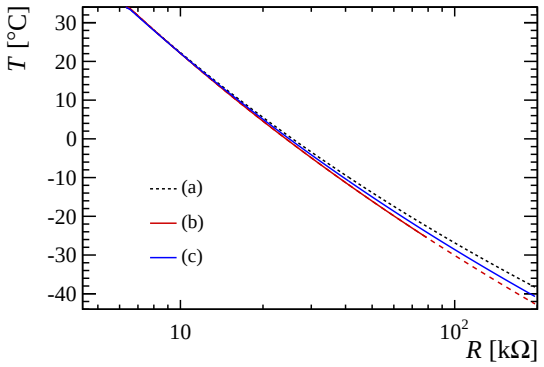

Figure 4.10: Temperature *vs.* thermistor resistance. The dashed, black curve (a) shows a relation due to (4.13) with parameters taken from the data sheet [89]. The red line (b) reproduces the relation as plotted in the data sheet. Its dashed part is an extrapolation according to the Steinhart-Hart equation (4.14). The blue curve (c) shows the result of calibration measurements as explained in the text.

Values lower than $\langle T_\mathrm{a} \rangle$ would have a weight different from values greater than $\langle T_\mathrm{a} \rangle$, otherwise. The uncertainties of the parameter errors are assumed to be quite large, since the parameter results of the fit are highly correlated.

Fig. 4.9 shows measured data and the fit result. For the purpose of clarity only about 1 % of the total data are plotted. The three different temperature–resistance relations according to the exponential expression (4.13), the curve plotted in the data sheet [89] and the calibration using the Steinhart-Hart equation (4.14) are illustrated in Fig. 4.10.

4.3 Signal Spectrum

A typical SiPM signal spectrum is illustrated in Figure 4.11. It corresponds to the illumination by LED pulses with low light intensity. Individual peaks corresponding to the number of fired pixels are clearly visible. The first peak, starting at low ADC count, is obtained when no pixel breakdown occurs during signal measurement. It is thus called pedestal peak or 0 photon, or photo-electron, equivalent (p.e.). Further peaks are referred to as 1 p.e., 2 p.e., *etc.*, as they correspond to the signal generated by the respective number of photons, if each is detected in an individual G-APD pixel of the SiPM.

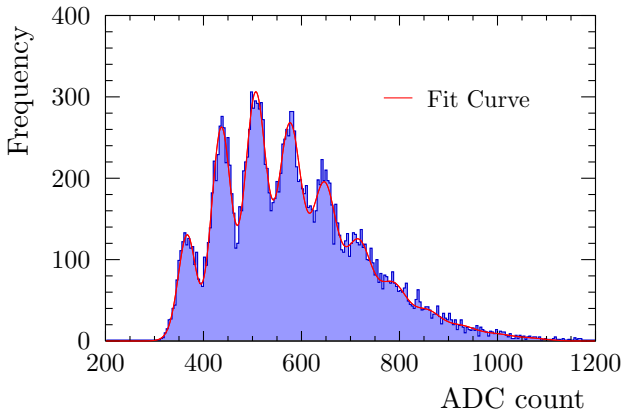

Figure 4.11: Signal spectrum of a single channel of a Hamamatsu MPPC 5883 measured with test setup A, compare Sec. 4.2.1 and 4.2.2.

The signal spectrum is well described by a fit function f_{signal} based on the model described in Ref. [92]. The number of photons detected by the SiPM is assumed to follow a Poisson distribution. After [92], the probability that one initial photon fires k pixels is proportional to $\epsilon_{\text{CT}}^{k-1}$, with ϵ_{CT} being the cross-talk probability. The resulting probability that an avalanche breakdown occurs in n pixels is given by

$$p(n) = \begin{cases} f_{\text{poisson}}(0, \mu_{\text{phot}}) & , \text{if } n = 0 \ , \\ \sum_{i=1}^{n} \binom{n-1}{i-1} \cdot f_{\text{poisson}}(i, \mu_{\text{phot}}) \cdot \epsilon_{\text{CT}}^{n-i} \left(1 - \epsilon_{\text{CT}}\right)^{i} & , \text{if } n > 0 \ . \end{cases} \tag{4.19}$$

The identifiers f_{poisson} and μ_{phot} denote the Poisson distribution and the mean number of detected photons, respectively. If the pedestal peak and the signal that corresponds to exactly one fired pixel are each approximated by a Gaussian distribution f_{gaus} with expectation value μ and width σ, it follows that

$$f_{\text{signal}}(x) = N \sum_{n} p(n)\, f_{\text{gaus}}\left(x, \mu(n), \sigma(n)\right) \ , \tag{4.20}$$

with

$$\mu(n) = \mu_{\text{ped}} + n\,\mu_{\text{gain}}\ , \tag{4.21}$$

$$\sigma(n) = \sqrt{\sigma^2_{\text{ped}} + n\,\sigma^2_{\text{gain}}}\ , \tag{4.22}$$

and total number N of measured SiPM signals x. The subscript $_{\text{ped}}$ identifies parameters of the pedestal peak, $_{\text{gain}}$ denotes those of the signal distribution according to one fired pixel which is equivalent to the SiPM gain G. The value of μ_{gain} corresponds to the distance of signal peaks in the measured spectrum, compare Fig. 4.11.

However, in measurements with the used test setups (*cf.* Sec. 4.2.2), it is observed that the pedestal distribution becomes asymmetric, and also shifted, with increasing light intensity and over-voltage. This effect results from a baseline shift of used shapers and amplifiers at higher output signals. Therefore, an exponentially modified Gaussian distribution $f_{\text{exp-gaus}}$ is considered in Eq. (4.20) instead of f_{gaus}. The distribution $f_{\text{exp-gaus}}$ is the convolution of an exponential, depending on parameter λ which defines the asymmetry, and a normal distribution whose parameters are given by Eq. (4.21) and (4.22).

Signal spectra are measured at several bias voltages to determine the breakdown voltage and the dependence of gain, PDE and cross-talk on the applied over-voltage. A linear dependence of μ_{gain}, and thus of gain G, on bias voltage U_{bias} is observed. According to Eq. (4.9), the function

$$G\,(U_{\text{bias}}) = \mu_{\text{gain}}\,(U_{\text{bias}}) = G' \cdot \underbrace{(U_{\text{bias}} - U_{\text{BD}})}_{=U_{\text{over}}} \tag{4.23}$$

is fitted to values of G obtained from the signal spectrum fits to determine the breakdown voltage U_{BD} and the increase of gain per over-voltage G'.

The breakdown probability ε_{BD} as a function of over-voltage U_{over} can be approximated by $1 - \exp(-\,\alpha_{\text{BD}}\,U_{\text{over}})$ [93]. The quantum efficiency ε_{Q} of sensors with constant depletion layer width and the geometrical fill-factor ε_{GF} can both be assumed to be independent of over-voltage. Therefore, the mean number of incident photons triggering an avalanche breakdown is described by

$$\mu_{\text{phot}}\,(U_{\text{over}}) = \mu_{\text{phot,max}}\,(1 - \exp(-\,\alpha_{\text{BD}}\,U_{\text{over}}))\ . \tag{4.24}$$

The parameter $\mu_{\text{phot,max}}$ corresponds to the mean photon number detected at breakdown probability 1 and includes ε_{Q} and ε_{GF} which cannot be determined with the used measurement setups. The value of α_{BD} determines the dependence of ε_{BD} on U_{over}.

The number of photons generated in the diode during a pixel breakdown is proportional to the number of carriers crossing the junction and thus proportional to the gain G. Cross-talk occurs when at least one of these photons initiates a

breakdown in a further pixel. Therefore, the cross-talk probability is parametrised by

$$\epsilon_{\mathrm{CT}}\left(U_{\mathrm{over}}\right) = \alpha^{*}_{\mathrm{CT}} \cdot G(U_{\mathrm{over}}) \cdot \varepsilon_{\mathrm{BD}}(U_{\mathrm{over}}) \tag{4.25}$$

$$= \alpha_{\mathrm{CT}} \cdot U_{\mathrm{over}} \cdot (1 - \exp(-\,\alpha_{\mathrm{BD}}\, U_{\mathrm{over}})) \ . \tag{4.26}$$

Figure 4.12 shows exemplary results of signal spectrum analyses for four channels of one 32-channel SiPM array from KETEK and Hamamatsu, each. The measurements have been taken utilising test setup A, compare section 4.2.2. Values of μ_{phot} reveal an inhomogeneous light intensity over the 32 channels of array HZ5-7-A during the characterisation. Furthermore, these data points indicate only a small curvature, especially in the case of the Hamamatsu sensor. It follows that $\alpha_{\mathrm{BD}}^{-1}$ must be large compared to the over-voltages in the test.

Cross-talk probabilities ϵ_{CT} of the two exemplary SiPM arrays differ by a factor 10 between the KETEK and the Hamamatsu device. No significant variation of ϵ_{CT} for different channels of the same SiPM array is observed. The relatively wide distribution of ϵ_{CT} that is visible in W2A-1A-2 data in Fig. 4.12 is a result of the parameter uncertainty $\sigma_{\epsilon_{\mathrm{CT}}}$ from the spectrum fit which is about 0.007 for the shown data points.

Spectrum fit results and the derived parametrisations according to Eq. (4.23), (4.24) and (4.26) of six Hamamatsu and three KETEK 32-channel SiPM arrays are shown in Tab. 4.2, 4.3 and Fig. 4.13. For Hamamatsu sensors, the determined increase of gain per voltage G' exhibits no significant dependence on the chosen SiPM channel i. The standard deviation $s_{G'_i}$ of all G'_i values of a single array is of the same magnitude as the mean parameter uncertainty $\left\langle \sigma_{G'_i} \right\rangle$ retrieved from the fits. KETEK sensors show an inter-channel variation of G' that is about three to four times the mean parameter uncertainty. The mean gain increase per voltage of all channels $\langle G'_i \rangle$ differs significantly between tested SiPM arrays. A similar observation is made with the obtained breakdown voltage U_{BD}. The value of G' in Tab. 4.2 is given in ADC count per V. A rough conversion of ADC count read from the electronics of setup A to the correspondent number of carriers is given by Eq. 4.37 in Sec. 4.4.

The front-end electronics used in setup A comprise a 10 kΩ resistor in series with each SiPM array that is connected. Thus, the voltage drop at this resistor which results from the current through the SiPM array needs to be subtracted from the voltage measured with the SourceMeter to determine the sensors' bias voltage. At higher over-voltages this correction is in the order of 0.1 V. However, when multiple arrays are connected to the FE board, as it is the case in most measurements done with Hamamatsu arrays, only the total current through all connected arrays is measured by the SourceMeter. Though, the miscellaneous breakdown voltages and therefore differing over-voltages lead to different SiPM currents, compare Sec. 4.5. Consequently, the subtraction of a voltage drop according to the measured total current divided by the number of connected arrays introduces systematic errors. For this reason, an uncertainty of half the voltage subtraction is taken into account

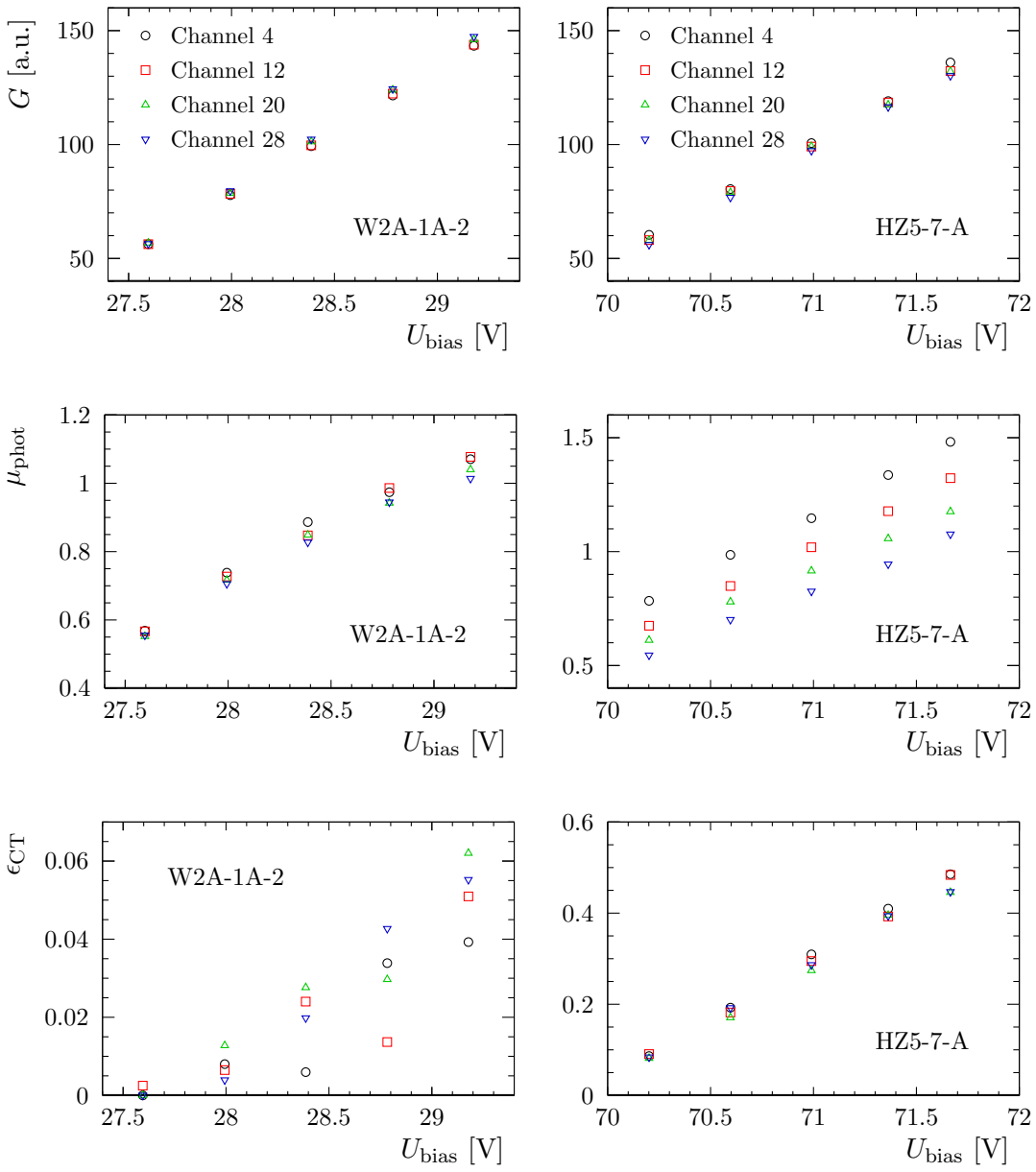

Figure 4.12: Gain G, mean number of incident photons per LED pulse that are detected μ_{phot} and cross-talk probability ϵ_{CT} as a function of bias voltage U_{bias}. Plotted values are obtained from signal spectra of each four out of 32 channels of a KETEK (W2A-1A-2) and a Hamamatsu (HZ5-7-A) SiPM array. Measurements have been taken with test setup A at room temperature.

Table 4.2: Mean value, standard deviation and mean uncertainty of G'_i and $U_{\mathrm{BD},i}$ of 32-channel SiPM arrays from Hamamatsu (HZ5-...) and KETEK (W2...). G'_i and $U_{\mathrm{BD},i}$ are the gain increase and breakdown voltage observed in channel i. Evaluated signal spectra are measured with setup A. The ambient temperature during measurement is given by T.

Sensor	$\langle G'_i \rangle$	$s_{G'_i}$	$\langle \sigma_{G'_i} \rangle$	$\langle U_{\mathrm{BD},i} \rangle$	$s_{U_{\mathrm{BD},i}}$	$\langle \sigma_{U_{\mathrm{BD},i}} \rangle$	T
	[ADC count/V]			[V]			[°C]
HZ5-7-A	51.86	0.66	0.76	69.082	0.028	0.022	20.0
HZ5-7-B	53.76	0.82	1.19	69.228	0.030	0.034	20.0
HZ5-7-D	50.90	0.57	0.73	68.946	0.030	0.024	20.0
HZ5-8-A	49.42	0.93	1.16	69.268	0.039	0.036	22.5
HZ5-8-B	50.76	1.28	1.23	69.186	0.053	0.039	22.5
HZ5-8-D	48.24	0.93	1.06	68.904	0.040	0.040	22.5
W2A-1A-2	56.80	1.09	0.26	26.594	0.013	0.009	21.9
W2B-1B	74.81	1.21	0.33	26.556	0.011	0.008	21.5
W2B-3B-2	40.25	0.97	0.35	26.635	0.034	0.020	21.8

for the measured bias voltage to lower the weight of highly corrected voltages when fitting Eq. (4.23) to the data.

Fitting Eq. (4.24) and (4.26) to the respective data of μ_{phot} and ϵ_{CT} of single SiPM channels does not show significant variations within one array. The obtained fit results of $\mu_{\mathrm{phot,max}}$, α_{BD} and α_{CT} are highly correlated with absolute values of correlation coefficients larger than 0.9, what is a result of measurement uncertainties in combination with the already mentioned small curvature of data points. For this reason, the functions (4.24) and (4.26) are simultaneously fit to the data of all channels of an SiPM array. While the fit parameters $\mu_{\mathrm{phot,max},i}$ consider the possibly different illumination, the same α_{BD} and α_{CT} are used to describe the data of all channels i.

In the fit process, the over-voltage U_{over} in Eq. (4.24) and (4.26) is substituted by the gain G. So μ_{phot} and ϵ_{CT} are considered as functions of measured gain, which is justified by the linearity of $G(U_{\mathrm{over}})$. The values of α_{BD} and α_{CT} in units of V^{-1} are then calculated by Eq. (4.23) using values of $\langle G'_i \rangle$ given in Tab. 4.2.

The results of this fit procedure are provided by Tab. 4.3. Even though a combined fit for all channels of an array and for μ_{phot} as well as ϵ_{CT} data is done, fit parameters are still highly correlated. Therefore, the given uncertainties in Tab. 4.3 must be considered as underestimating the real errors.

In addition to α_{BD} as defined by Eq. (4.24), table 4.3 also provides corresponding values of

$$\alpha'_{\mathrm{BD}} = \alpha_{\mathrm{BD}} \cdot U_{\mathrm{BD}} \ , \tag{4.27}$$

which determine the dependency of $\varepsilon_{\mathrm{BD}}$ on the relative over-voltage $U_{\mathrm{over}}/U_{\mathrm{BD}}$. A

Table 4.3: Parameters α_{BD}, α'_{BD} and α_{CT} derived from signal spectra of 32-channel SiPM arrays from Hamamatsu and KETEK, measured with setup A. Temperatures are the same as in Tab. 4.2.

Sensor	α_{BD} [V^{-1}]	α'_{BD}	α_{CT} [V^{-1}]
HZ5-7-A	0.237 ± 0.005	16.36 ± 0.33	0.407 ± 0.005
HZ5-7-B	0.199 ± 0.006	13.81 ± 0.40	0.467 ± 0.009
HZ5-7-D	0.182 ± 0.005	12.54 ± 0.31	0.474 ± 0.009
HZ5-8-A	0.301 ± 0.008	20.84 ± 0.54	0.371 ± 0.005
HZ5-8-B	0.261 ± 0.009	18.03 ± 0.61	0.404 ± 0.007
HZ5-8-D	0.198 ± 0.007	13.65 ± 0.46	0.481 ± 0.017
W2A-1A-2	0.491 ± 0.011	13.07 ± 0.29	0.0233 ± 0.0005
W2B-1B	0.484 ± 0.010	12.86 ± 0.26	0.0260 ± 0.0006
W2B-3B-2	0.510 ± 0.014	13.59 ± 0.37	0.0017 ± 0.0003

noticeable similarity in α'_{BD} is found for six out of nine characterised SiPM arrays including sensors from Hamamatsu and KETEK.

The small α_{CT} values of KETEK SiPMs indicate a much lower probability of photons generated in an avalanche to reach neighboured pixels compared to the tested Hamamatsu devices. A possible explanation is the relatively thick encapsulation of the Hamamatsu arrays which potentially provides a higher probability for generated photons to reach other pixels via internal reflection. Besides the very thin top coating, the sensor W2B-3B-2 benefits from optical trenches between the G-APD pixels. Its optical cross-talk is further reduced by about a factor 10 relative to the other two KETEK SiPMs.

Figure 4.13 illustrates the results of SiPM array characterisation and the parametrisations according to Eq. (4.23), (4.24) and (4.26). Values of μ_{phot} are divided by the fit result for $\mu_{\mathrm{phot,max}}$ of the particular channel to facilitate a comparison of $\varepsilon_{\mathrm{BD}}$. The cross-talk probability ϵ_{CT} is plotted as function of G to exhibit the differences between tested arrays for similar photon numbers produced in the avalanche.

Signal spectra of single-channel SiPMs S10362-11-050U and S11028-050 from Hamamatsu, see Sec. 4.2.1, and of four channels of array HZ5-7-A are measured using test setup B, see Sec. 4.2.2. The four channels of HZ5-7-A are connected in a parallel circuit and thus act as a single SiPM. The studied SiPM signal is the integral of the amplifier output over about 50 ns. Recording the pulse integral instead of sampling the pulse height diminishes the uncertainty in the measured SiPM signal that is caused by noise frequencies large compared to the integration time.

Two example spectra obtained at different bias voltages are shown in Fig. 4.14. Peaks are more distinct than in spectra measured utilising test setup A due to a narrower pedestal signal, compare Fig. 4.11. However, especially at higher over-voltages, signal in the intermediate range between the major peaks cannot

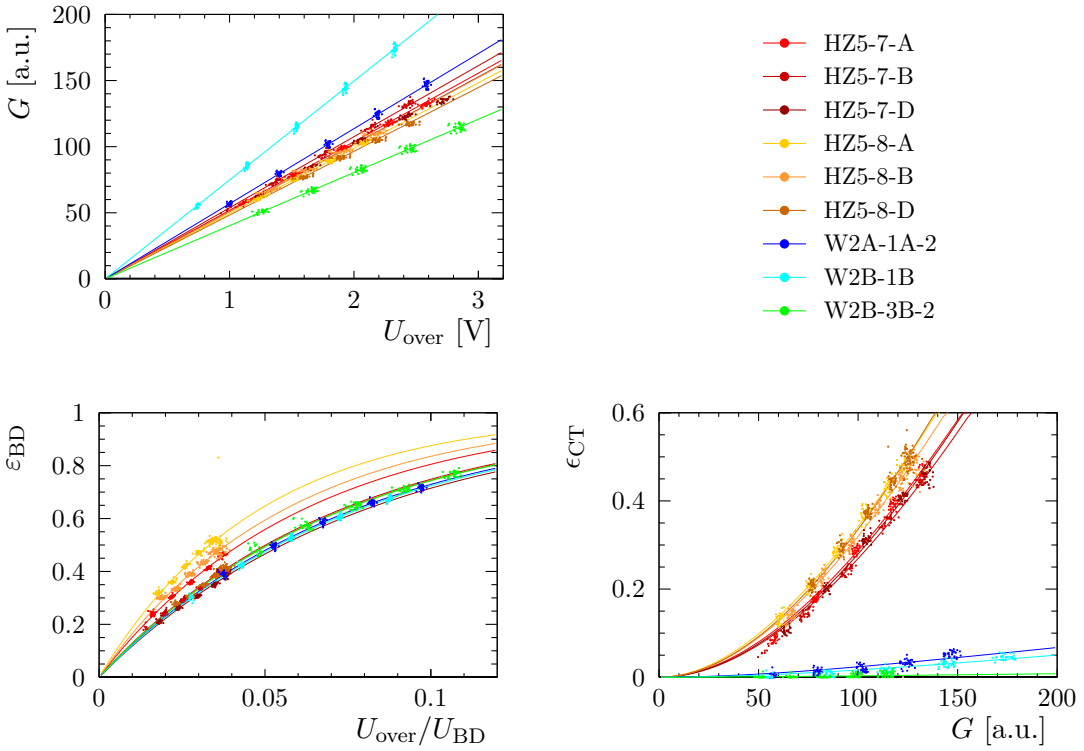

Figure 4.13: Parameters of 32-channel SiPM arrays from Hamamatsu and KETEK obtained from fitting signal spectra of individual channels. Curves are according to Eq. (4.23), (4.24) and (4.26) with parameters given in Tab. 4.2 and 4.3.

be described by fitting a single Gaussian distribution to each photon-equivalent. Therefore, the pedestal signal is described by the sum of two Gaussian functions having the same centre of gravity but different width and normalisation. The pedestal shape is included in other signal peaks via convolution, compare Eq. 4.20 to 4.22. Parameter results from analysing signal spectra measured at room temperature are illustrated in Fig. 4.15.

The temperature dependence of SiPM parameters is studied by keeping devices under test inside a refrigerator volume while acquiring signal data by means of setup B. Cooling the sensor's environment, and not only the device itself, facilitates accurate temperature measurement and prevents from effects due to temperature gradients inside the photo-detector volume. The SiPM array HZ5-7-A is characterised at temperatures in the range from $-25\,^{\circ}\mathrm{C}$ to $25\,^{\circ}\mathrm{C}$, the single-channel sensors S11028-050 and S10362-11-050U are tested at $-5\,^{\circ}\mathrm{C}$ to $25\,^{\circ}\mathrm{C}$.

The breakdown voltage derived from $G(U_{\mathrm{bias}})$ according to Eq. 4.23 has a linear dependence on temperature T as shown in Fig. 4.16. Fitting the relation

$$U_{\mathrm{BD}}(T) = U_{\mathrm{BD}}(0\,^{\circ}\mathrm{C}) + U'_{\mathrm{BD}}\,T \tag{4.28}$$

to the data points leads to parameter values of $U_{\mathrm{BD}}(0\,^{\circ}\mathrm{C})$ and U'_{BD} given in Tab. 4.4. The change of breakdown voltage per temperature variation is consistent for all three

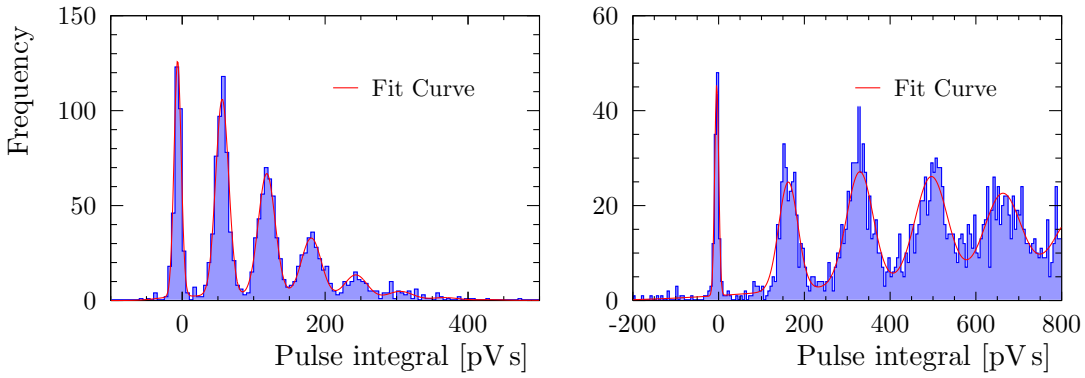

Figure 4.14: SiPM signal spectra of HZ5-7-A measured with test setup B at bias voltages 69.98 V (left) and 71.18 V (right). The ambient temperature during measurement is 21.7 °C.

Table 4.4: Parameter values of $U_{\mathrm{BD}}(0\,^{\circ}\mathrm{C})$ and U'_{BD} determining the breakdown voltage after Eq. (4.28).

Sensor	$U_{\mathrm{BD}}(0\,^{\circ}\mathrm{C})$ [V]	U'_{BD} [mV K^{-1}]
HZ5-7-A	68.0519 ± 0.0034	56.66 ± 0.28
S11028-050	68.562 ± 0.008	55.9 ± 0.8
S10362-11-050U	68.194 ± 0.007	56.7 ± 0.7

sensors within the given uncertainties. The determined values of $U_{\mathrm{BD}}(0\,^{\circ}\mathrm{C})$ could be systematically biased by the limited accuracy of used Pt1000 temperature sensors, *cf.* Sec. 4.2.3. Since all data points potentially have the same temperature offset, an additional uncertainty in $U_{\mathrm{BD}}(0\,^{\circ}\mathrm{C})$ of about 0.01 V must be taken into account, which is estimated by the values of U'_{BD} from Tab. 4.4 and σ_T after Eq. (4.12). Calculating the breakdown voltage of HZ5-7-A at 20.0 °C using Eq. 4.28 leads to a value that is 0.103 V larger than the value stated in Tab. 4.2. This difference is about three times the standard deviation derived from uncertainties of Pt1000 sensors and those given in Tab. 4.2 and 4.4 and thus might be a hint at possible systematic errors in the spectra analyses.

Figure 4.17 shows the dependence of PDE and cross-talk on relative over-voltage for several temperatures. The over-voltage is calculated from measured bias voltages U_{bias} and values of $U_{\mathrm{BD}}(T)$ given by Eq. (4.28). No temperature effect on μ_{phot} and ϵ_{CT} is observed. Variations of both parameters are consistent with their uncertainties. For the purpose of visibility of data points, error bars are not drawn in Fig. 4.17. The uncertainties are of the same magnitude as those plotted in Fig. 4.15. Curves of μ_{phot} and ϵ_{CT} as given by values of α_{BD} and α_{CT} that have been obtained for HZ5-7-A with test setup A (*cf.* Tab. 4.3) are illustrated by dashed lines in Fig. 4.17. Data points do not reveal significant deviations from these curves.

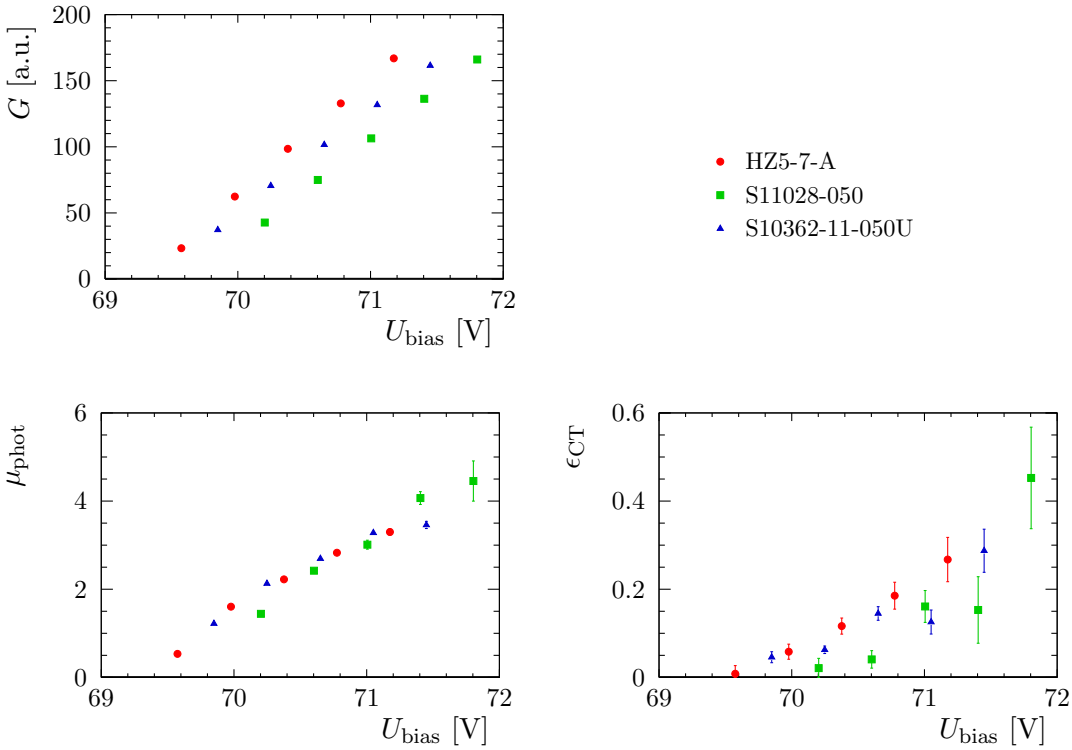

Figure 4.15: Gain G, mean number of detected photons per LED pulse μ_{phot} and cross-talk probability ϵ_{CT} of sensors HZ5-7-A, S11028-050 and S10362-11-050U measured with test setup B at room temperature.

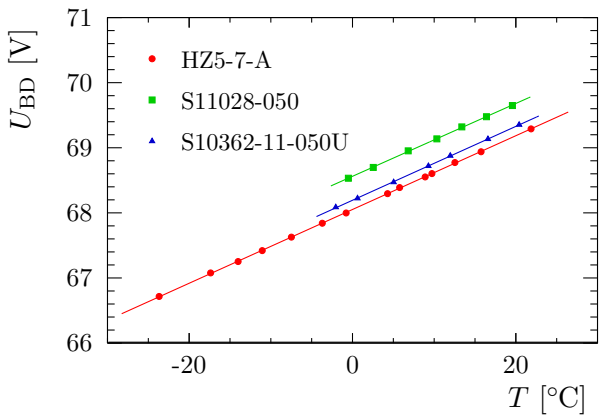

Figure 4.16: Dependence of breakdown voltage U_{BD} on temperature T.

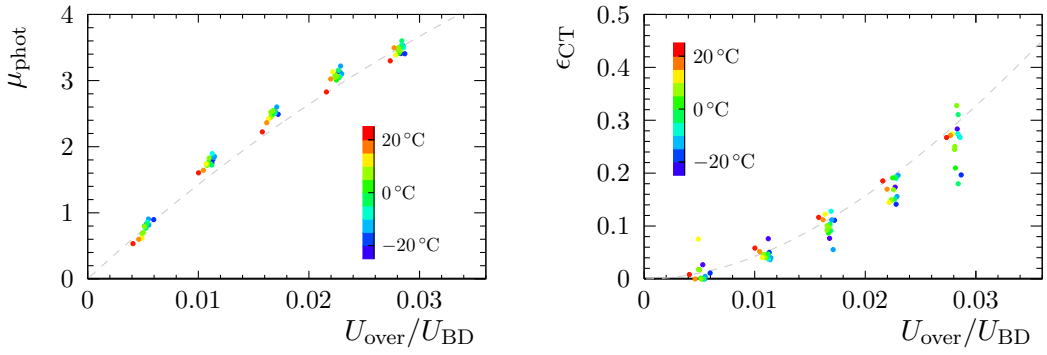

(a) HZ5-7-A

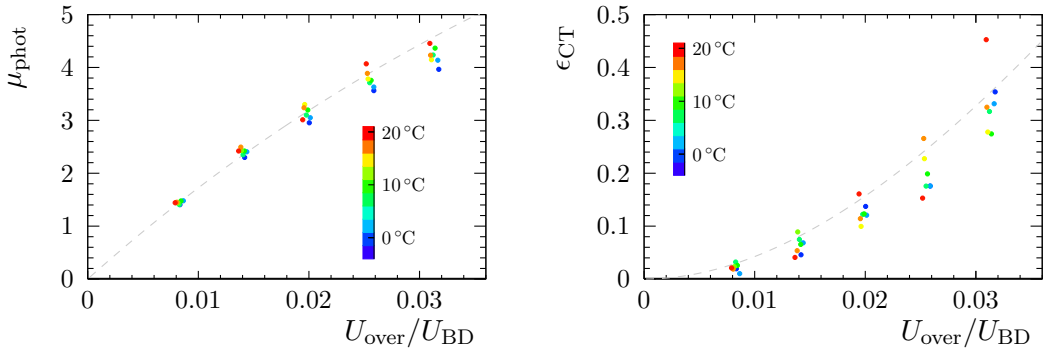

(b) S11028-050

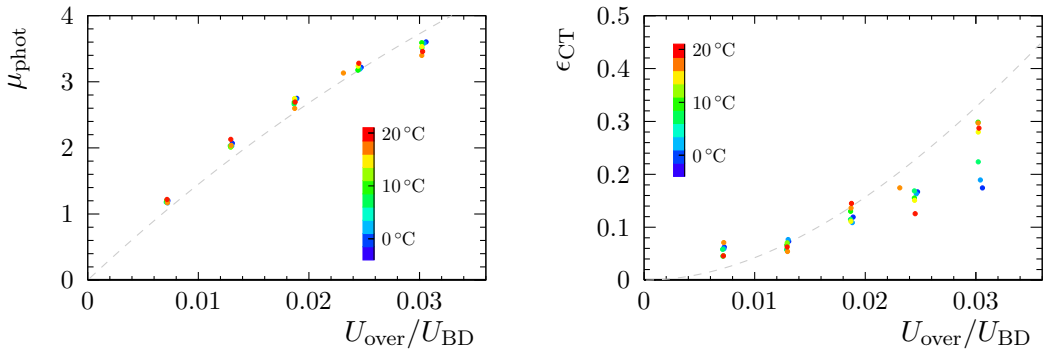

(c) S10362-11-050U

Figure 4.17: Mean number of detected photons per LED pulse μ_{phot} and cross-talk probability ϵ_{CT} of sensors HZ5-7-A, S11028-050 and S10362-11-050U measured with setup B at several temperatures. Dashed lines indicate the corresponding curves obtained for HZ5-7-A with test setup A.

4.4 Dark Count Rate

The number of SiPM pulses per time r_{dark}, that is observed without illumination of the sensor, is measured using test setup B. Single-channel sensors S11028-050, S10362-11-050U and array HZ5-7-A are investigated. Figure 4.18 shows a typical waveform sampled by the digital oscilloscope. The dark count rate (DCR) is obtained by counting signal pulses that exceed a defined threshold. The example comprises a single pulse, as occurring due to thermal avalanche triggering, as well as a series of four SiPM pulses which can be explained by after-pulsing, see Sec. 4.1. Furthermore, the waveform exhibits a noise pulse which is only observed during characterisation of HZ5-7-A and biasses the measured dark count rate.

Dark count rates measured at miscellaneous over-voltages and temperatures are plotted in Figure 4.19. The data of SiPM array HZ5-7-A have been acquired by connecting four channels in parallel. These channels are thus operated as a single SiPM. The impact of noise pulses on the sampled dark count is determined by a measurement at bias voltage 0.13 V below U_{BD}. The DCR of HZ5-7-A is corrected by subtraction of the obtained noise count rate r_{noise} which is 74 kHz.

In SiPM signal spectrum studies, see Sec. 4.3, no significant influence of temperature on PDE and cross-talk probability was found. The after-pulse probability ϵ_{AP} is not affected by temperature, either, as shown later in this section. Hence, it can be assumed that the temperature dependence of r_{dark} is only due to that of the thermal generation of electron-hole pairs in the depleted layer. If the DCR is scaled to a value corresponding to 20 °C via Eq. (4.10), data acquired at different temperatures are in a good agreement, indeed. A value of 1.12 eV is considered for the band gap E_{G} in silicon. Only data points of HZ5-7-A corresponding to the lowest measurement temperatures show larger deviations. However, the mentioned correction of r_{dark} relies on the accuracy of r_{noise} which is larger than the SiPM's dark count rate at these temperatures and might have varied in the course of the test.

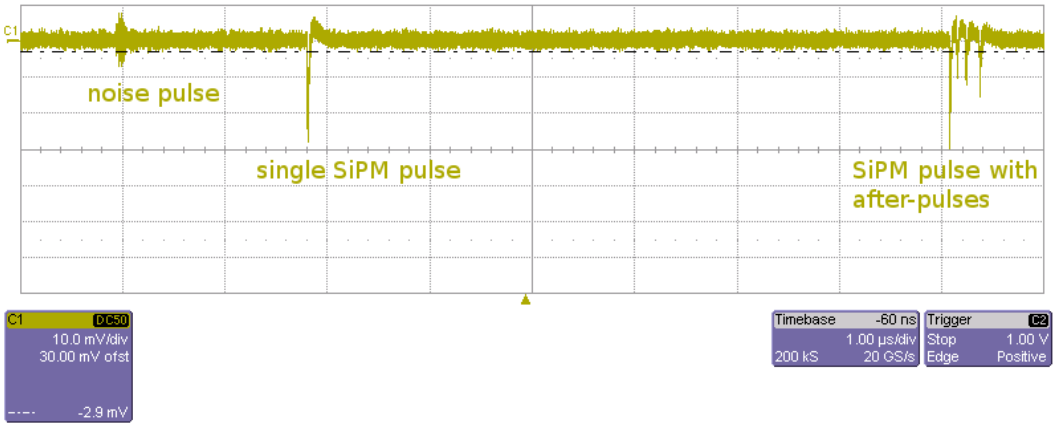

Figure 4.18: Typical waveform sampled by the digital oscilloscope of setup B (see Sec. 4.2.2) during characterisation of SiPM HZ5-7-A.

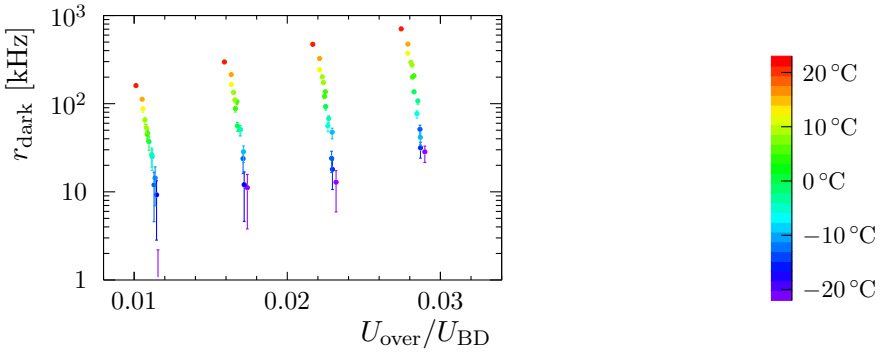

(a) HZ5-7-A

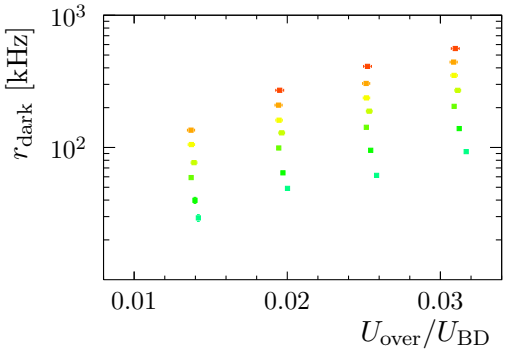

(b) S11028-050

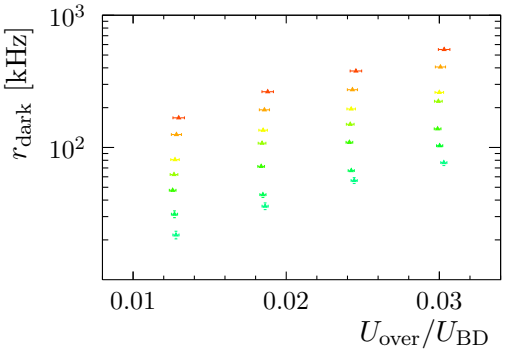

(c) S10362-11-050U

Figure 4.19: Dark count rate r_{dark} measured at different temperatures and over-voltages. Data of HZ5-7-A correspond to the dark count sum of four SiPM channels.

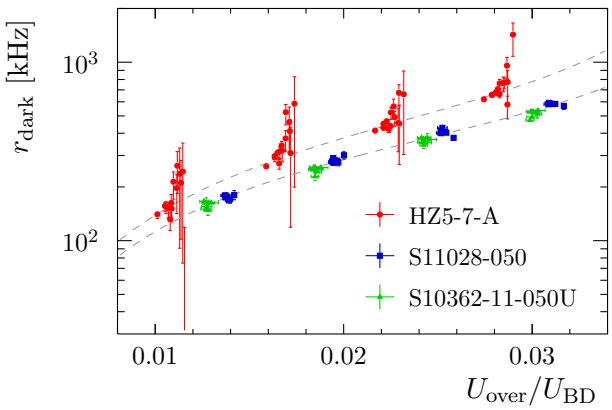

Figure 4.20: Dark count rate r_{dark} scaled to values corresponding to 20 °C by Eq. (4.10). Results of fitting Eq. (4.29) to data of HZ5-7-A and to the collective data of S11028-050 and S10362-11-050U are illustrated by dashed curves.

The measured DCR is approximated by a function of thermal electron-hole pair generation rate $r_{\text{th. gen.}}$, breakdown efficiency $\varepsilon_{\text{BD,dark}}$ and after-pulse probability ϵ_{AP}.

$$r_{\text{dark}} = r_{\text{th. gen.}}\, \varepsilon_{\text{BD,dark}}\, (1 - \epsilon_{\text{AP}})^{-1} \tag{4.29}$$

Primary carrier generation by incident light is more probable at the p-doped side of the G-APD junction than at the n-doped side due to photon absorption. This is not necessarily the case for electron-hole pair generation by thermal excitation via defect levels. Since this process might be more probable to happen at the n-side of the diodes, compared to photon absorption, a lower mean value of breakdown efficiency can be expected for thermally generated carriers. It is explained by the lower ionisation coefficient of holes compared to electrons, see Ref. [94]. An additional factor $(1 - \exp(-\,\alpha_{\text{BD,dark}}\, U_{\text{over}}))$ is used to include this effect in the voltage dependence of the breakdown probability that is considered for dark counts, *cf.* Eq. (4.24).

$$\begin{aligned} \varepsilon_{\text{BD,dark}}(U_{\text{over}}) = &(1 - \exp(-\,\alpha_{\text{BD,dark}}\, U_{\text{over}})) \cdot (1 - \exp(-\,\alpha_{\text{BD}}\, U_{\text{over}})) \\ &\text{with} \quad \alpha_{\text{BD,dark}} > \alpha_{\text{BD}} \end{aligned} \tag{4.30}$$

It has to be noticed that expression (4.30) is not an explicit physical description but an empirical formula to describe measurements.

Similarly to the cross-talk probability ϵ_{CT} (see Eq. (4.26)), the after-pulse probability ϵ_{AP} is assumed to be proportional to the number of carriers released in an avalanche. The after-pulse probability is also increased by cross-talk since carriers might be trapped in each fired pixel and trigger a subsequent breakdown.

$$\epsilon_{\text{AP}}\,(U_{\text{over}}) = \alpha_{\text{AP}} \cdot U_{\text{over}} \cdot (1 - \epsilon_{\text{CT}}(U_{\text{over}}))^{-1} \cdot \varepsilon_{\text{BD,dark}}(U_{\text{over}}) \tag{4.31}$$

The factor $(1-\epsilon_{\text{AP}})^{-1}$ used in Eq. (4.29) results from the possibility of an after-pulse to be itself the source of further after-pulses. It implies the approximation that each SiPM pulse, regardless of being photo-generated or an after-pulse, can cause only one subsequent breakdown directly. Though, two or more trapped carriers can trigger after-pulses independently, especially when being trapped in different pixels as result of cross-talk. Consequently, the used approximation is only valid for after-pulse probabilities clearly below 1.

Function (4.29) is fit to data shown in Fig. 4.20 with free parameters $r_{\text{th. gen.}}$, $\alpha'_{\text{BD,dark}}$ and α'_{AP}. The prime denotes that these parameters are equivalent to those defined by Eq. (4.30) and (4.31) multiplied with U_{BD}. Thus r_{dark} is expressed as a function of relative over-voltage $U_{\text{over}}/U_{\text{BD}}$. The values of α'_{BD} and α'_{CT} are fixed to those of HZ5-7-A given by Tab. 4.3. Data of S11028-050 and S10362-11-050U are described by a single fit function, since they are of the same sensor type and do not show significant differences in the observed dark count rate. The fit results are illustrated by dashed lines in Fig. 4.20. Parameter values are given in Tab. 4.5.

The description of r_{dark} as a function of relative over-voltage using a constant value of α'_{AP} for different temperatures is not fully accurate. The parameter α_{AP} is

Table 4.5: Parameters $r_{\text{th. gen.}}$, $\alpha'_{\text{BD,dark}}$ and α'_{AP} derived from fitting Eq. (4.29) to measured dark count rates shown in Fig. 4.20.

Sensor	$r_{\text{th. gen.}}$ [MHz]	$\alpha'_{\text{BD,dark}}$	α'_{AP}
HZ5-7-A	1.28 ± 0.08	121 ± 19	22.8 ± 2.1
S11028-050/S10362-11-050U	0.953 ± 0.029	146 ± 15	18.48 ± 0.10

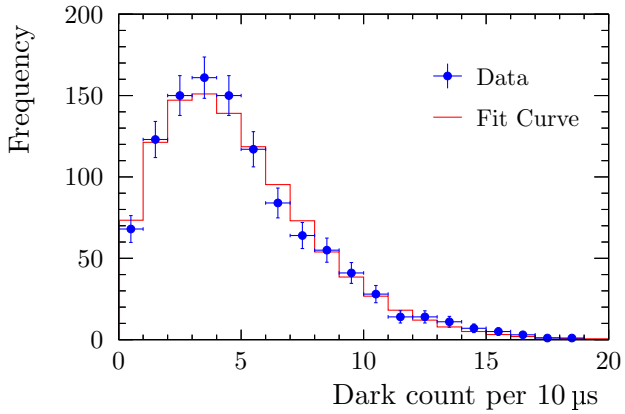

Figure 4.21: Distribution of dark count per sampled waveform of SiPM S11028-050 measured at $U_{\text{over}} = 2.1\,\text{V}$ and $T = 16.7\,°\text{C}$.

used to include the dependence of ϵ_{AP} on the number of free carriers in a breakdown, see Eq. (4.31). The number of carriers is determined by the gain which is a function of the absolute over-voltage, *cf.* Eq. (4.9). Thus, the parameter α'_{AP} providing the dependence on relative over-voltage should vary according to the temperature dependence of U_{BD}. However, a change of temperature by 50 K leads to a change of U_{BD} by only 4 % for the considered Hamamatsu SiPMs.

The approximation of r_{dark} by constant values of $\alpha'_{\text{BD,dark}}$ and α'_{BD} for miscellaneous temperatures is based on the observation of similar dependencies of ε_{BD} on $U_{\text{over}}/U_{\text{BD}}$ for SiPMs with different U_{BD}, see Fig. 4.13. The breakdown efficiency ε_{BD} seems to be rather a function of relative than of absolute over-voltage.

Distributions of the number of dark pulses per time period n_{dark} are analysed to determine the rate of thermally initiated diode breakdowns

$$r_{\text{th. BD}} = r_{\text{th. gen.}}\, \varepsilon_{\text{BD,dark}} \tag{4.32}$$

and the after-pulse probability ϵ_{AP}, independently of the parametrisations (4.30) and (4.31). An example distribution of n_{dark} is visualised in Figure 4.21. Measured data can be described by a function f_{DC} similar to Eq. (4.20). The fit function is a Poisson distribution, which is assumed to describe the occurrence of thermal breakdowns, modified by the probabilities of subsequent after-pulsing.

$$f_{\text{DC}}(n_{\text{dark}}) = N\, p(n_{\text{dark}}) \tag{4.33}$$

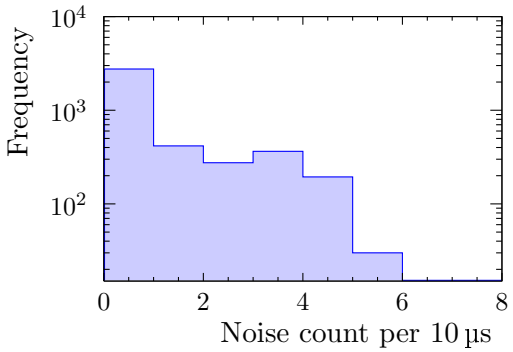

Figure 4.22: Noise count measured with HZ5-7-A at 0.13 V below U_{BD}.

with

$$p(n_{\mathrm{dark}}) = \begin{cases} f_{\mathrm{poisson}}(0, \mu_{\mathrm{th.\,BD}}) & , \text{ if } n_{\mathrm{dark}} = 0 \\ \sum_{i=1}^{n_{\mathrm{dark}}} \binom{n_{\mathrm{dark}} - 1}{i - 1} \cdot f_{\mathrm{poisson}}(i, \mu_{\mathrm{th.\,BD}}) \cdot \epsilon_{\mathrm{AP}}^{n_{\mathrm{dark}} - i} \cdot \ (1 - \epsilon_{\mathrm{AP}})^{i} & , \\ & \text{if } n_{\mathrm{dark}} > 0 \end{cases} \tag{4.34}$$

The sample size is denoted by N. The parameter $\mu_{\mathrm{th.\,BD}}$ is the expectation value of thermal breakdowns occurring in the time of a waveform sample t_{sample}.

$$r_{\mathrm{th.\,BD}} = \mu_{\mathrm{th.\,BD}}\, t_{\mathrm{sample}}^{-1} \tag{4.35}$$

Dark count distributions measured with SiPM array HZ5-7-A comprise threshold excesses due to the observed noise pulses. Therefore, a convolution of function (4.33) and the noise count distribution measured at 0.13 V below U_{BD}, see Fig. 4.22, is fit to the data.

Obtained parameter values of $r_{\mathrm{th.\,BD}}$ and ϵ_{AP} are shown in Fig. 4.23 and 4.25. Data of $r_{\mathrm{th.\,BD}}$ normalised to a temperature of 20 °C using Eq. (4.10) are shown in Fig. 4.24. Function (4.32) with $\varepsilon_{\mathrm{BD,dark}}$ defined by Eq. (4.30) and $\alpha_{\mathrm{BD(,dark)}}\, U_{\mathrm{over}}$ being replaced with $\alpha'_{\mathrm{BD(,dark)}}\, U_{\mathrm{over}}/U_{\mathrm{BD}}$ is fit to the data points. Measurements of sensors S11028-050 and S10362-11-050U are described by a single curve. Fit results are illustrated by grey dashed lines in Fig. 4.24. Corresponding values of $r_{\mathrm{th.\,gen.}}$ and $\alpha'_{\mathrm{BD,dark}}$ can be found in Tab. 4.6. The value of α'_{BD} is fixed to the result for HZ5-7-A obtained from SiPM signal spectra, as it was the case before when fitting r_{dark}.

After-pulse probabilities shown in Fig. 4.25 do not exhibit any significant dependence on temperature. Data of all tested sensors are plotted in Fig. 4.26 to facilitate comparison. A function according to (4.31), (4.30) and (4.26) is fit to the presented data points. In the fit, all parameters are fixed except for α'_{AP}. The values of α'_{BD}, α'_{CT} and $\alpha'_{\mathrm{BD,dark}}$ are taken from signal spectrum analyses of HZ5-7-A (Tab. 4.3) and Tab. 4.6, respectively. Resulting values of α'_{AP} are also shown in Tab. 4.6. A corresponding curve is drawn as dashed line in Fig. 4.26.

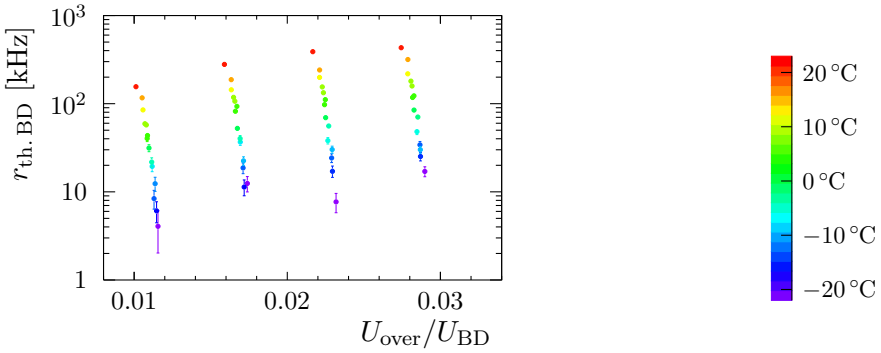

(a) HZ5-7-A

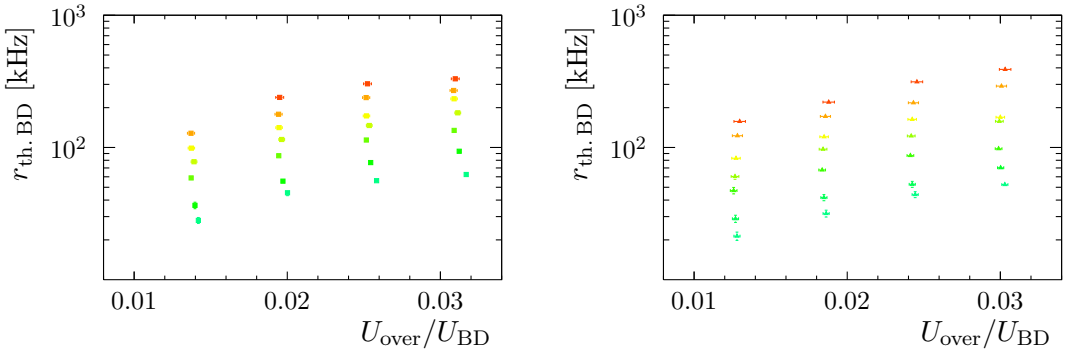

(b) S11028-050

(c) S10362-11-050U

Figure 4.23: Rate of thermally initiated diode breakdowns $r_{\mathrm{th.\,BD}}$ obtained from analysing dark count distributions.

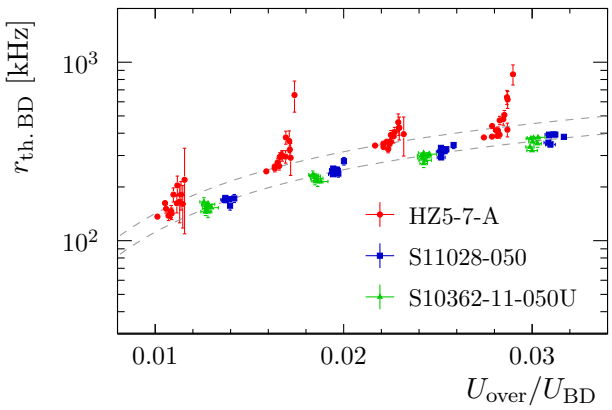

Figure 4.24: Rate of thermally initiated diode breakdowns $r_{\mathrm{th.\,BD}}$ normalised to $T = 20\,°\mathrm{C}$. Results of fitting Eq. (4.32) to data of HZ5-7-A and to the collective data of S11028-050 and S10362-11-050U are illustrated by dashed curves.

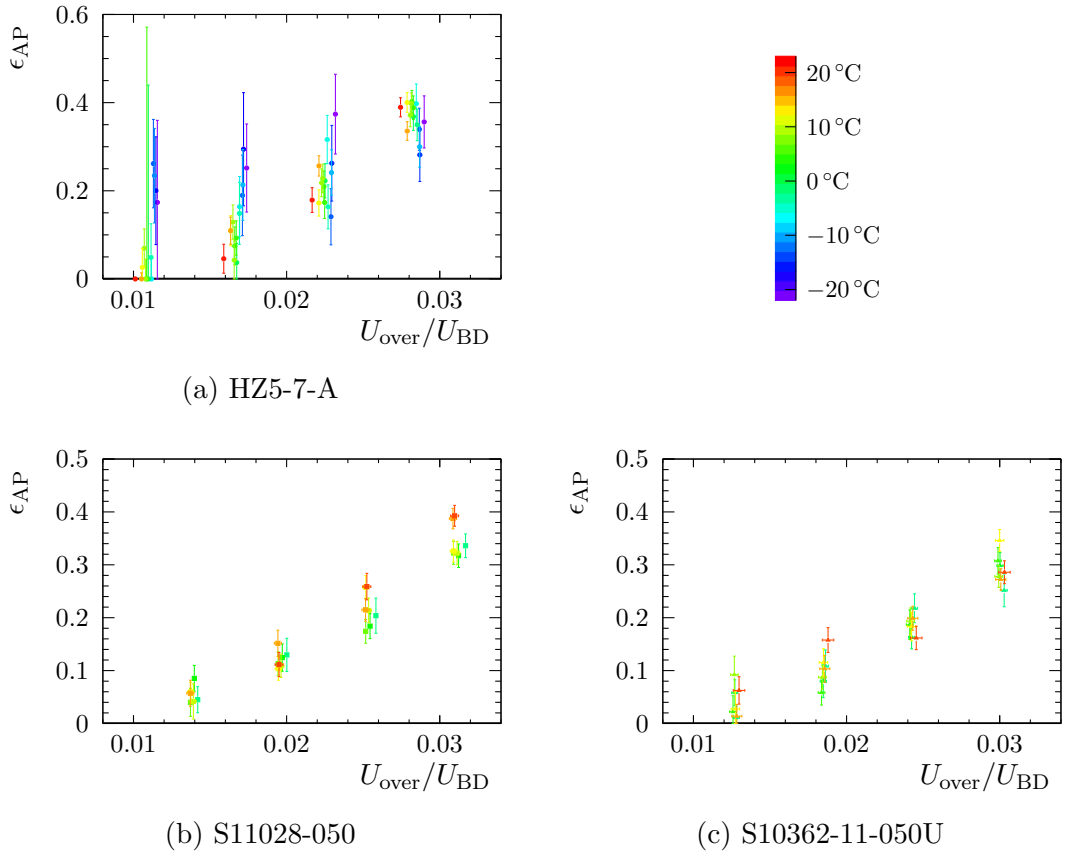

(a) HZ5-7-A

(b) S11028-050

(c) S10362-11-050U

Figure 4.25: After-pulse probability ϵ_{AP} obtained from analysing dark count distributions.

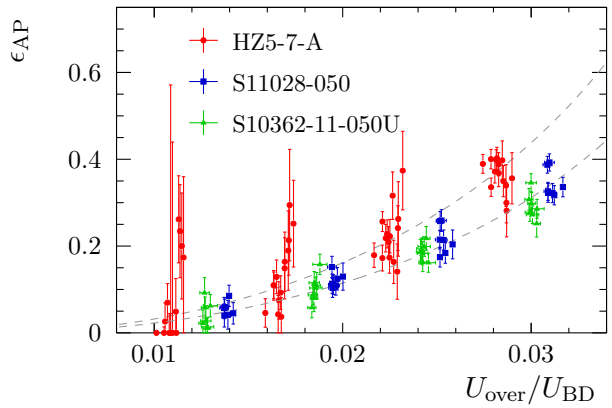

Figure 4.26: Comparison of ϵ_{AP} of sensors HZ5-7-A, S11028-050 and S10362-11-050U. Results of fitting Eq. (4.31) to data of HZ5-7-A and to the collective data of S11028-050 and S10362-11-050U are illustrated by dashed curves.

Table 4.6: Parameters $r_{\text{th. gen.}}$, $\alpha'_{\text{BD,dark}}$ and α'_{AP} derived from fitting Eq. (4.32) and (4.31) to data of $r_{\text{th. BD}}$ and ϵ_{AP} shown in Fig. 4.24 and 4.26, respectively.

Sensor	$r_{\text{th. gen.}}$ [MHz]	$\alpha'_{\text{BD,dark}}$	α'_{AP}
HZ5-7-A	1.176 ± 0.014	161 ± 10	25.6 ± 0.5
S11028-050/S10362-11-050U	0.936 ± 0.009	157 ± 10	18.27 ± 0.29

Parameter results given in Tab. 4.6 are similar to those in Tab. 4.5, though some differences exceed the range of the estimated uncertainty intervals. Both methods, fitting the mean DCR and evaluating dark count distributions, lead to estimates of generation rates as well as of after-pulse probabilities that are significantly higher in SiPM array HZ5-7-A than in single-channel SiPMs S11028-050 and S10362-11-050U. The active areas of four combined channels of HZ5-7-A on the one hand and of the single-channel SiPMs on the other hand differ only by 2 %, *cf.* Tab. 4.1. Hence, the discrepancy in $r_{\text{th. gen.}}$ is probably due to a larger depletion layer width or a higher density of defect levels in HZ5-7-A compared to the other two SiPMs. The different after-pulse probabilities can be caused by the same reasons. However, values of α'_{AP} can, to some extent, be explained by the gain per over-voltage G' which is higher in HZ5-7-A as discussed in the following paragraphs. A larger number of free carriers leads to a larger expectation value of carriers being trapped and subsequently triggering an after-pulse.

The gain G can be estimated by the quotient of measured dark current I_{dark} divided by the dark count rate r_{dark}. However, a correction for cross-talk, which leads to dark pulses having multiple of the 1 p.e. charge, has to be taken into account.

$$G \approx I_{\text{dark}} \cdot (1 - \epsilon_{\text{CT}}) \cdot r_{\text{dark}}^{-1} \tag{4.36}$$

Deviations from this relation may occur as a result of possible inaccuracies of the DCR and current measurements. At low over-voltages, the probability of missing pulses is increased due to the lower pulse height. Furthermore, leakage current that is independent of diode breakdown may be included in the measured I_{dark}. This effect biases the gain estimate especially at low r_{dark} and low G. Both effects lead to an overestimate of gain.

Figure 4.27 shows the gain determined by Eq. (4.36) as a function of over-voltage. The cross-talk probability ϵ_{CT} of HZ5-7-A is used to calculate the correction factor. The value of G that is derived from the highest measured r_{dark} at maximum over-voltage is used to calculate the gain increase per over-voltage G', compare Eq. (4.23), since it is assumed to be the less affected by the described systematics. Table 4.7 provides the resulting G'. Corresponding linear functions are shown in Fig. 4.27 by dashed lines. Indeed, the gain estimate after Eq. (4.36) exceeds the values indicated by the dashed curve at lower U_{over}.

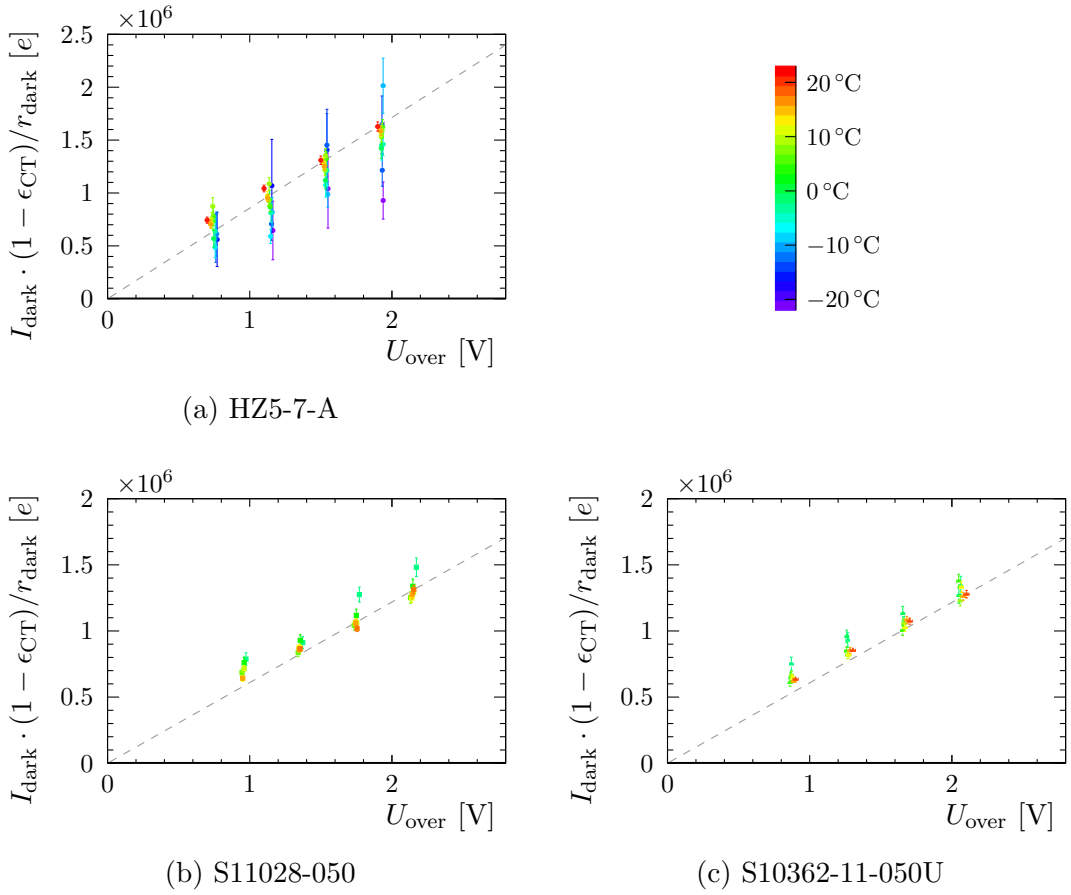

(a) HZ5-7-A

(b) S11028-050

(c) S10362-11-050U

Figure 4.27: Charge per 1 p.e. dark pulse as function of over-voltage.

Table 4.7: Estimate of gain increase per over-voltage G' after Eq. 4.36.

Sensor	G' $[10^5\,\mathrm{V}^{-1}]$
HZ5-7-A	8.57 ± 0.24
S11028-050	6.09 ± 0.16
S10362-11-050U	6.08 ± 0.14

Comparison of $\langle G'_i \rangle$ and G' corresponding to SiPM array HZ5-7-A from Tab. 4.2 and 4.7, respectively, enables a rough calibration of the ADC count measured with test setup A. It follows that

$$1 \text{ ADC count} \equiv (1.65 \pm 0.05) \cdot 10^4\, e\ . \tag{4.37}$$

4.5 Current-Voltage Characteristic

The current-voltage (I-U) characteristic of an SiPM above its breakdown voltage is ruled by the frequency of pixel breakdown and the SiPM gain G which is the number of released charge carriers per breakdown event. If one additionally assumes a leakage current I_{const} that occurs in the region around U_{BD}, independently of diode breakdown, and which hardly changes with relevant bias voltage variations, the measured dark current I_{dark} can be expressed as a function of U_{bias} by

$$I_{\text{dark}}(U_{\text{bias}}) = \begin{cases} I_{\text{const}} & \text{, if } U_{\text{bias}} \leq U_{\text{BD}} \\ \dfrac{I'_{\text{dark}} \cdot U_{\text{over}} \cdot \varepsilon_{\text{BD,dark}}(U_{\text{over}})}{(1-\epsilon_{\text{CT}}(U_{\text{over}})) \cdot (1-\epsilon_{\text{AP}}(U_{\text{over}}))} + I_{\text{const}} & \text{, if } U_{\text{bias}} > U_{\text{BD}} \end{cases} \tag{4.38}$$

with

$$U_{\text{over}} = U_{\text{bias}} - U_{\text{BD}}$$

where $\varepsilon_{\text{BD,dark}}$, ϵ_{CT} and ϵ_{AP} are given by Eq. (4.30), (4.26) and (4.31).

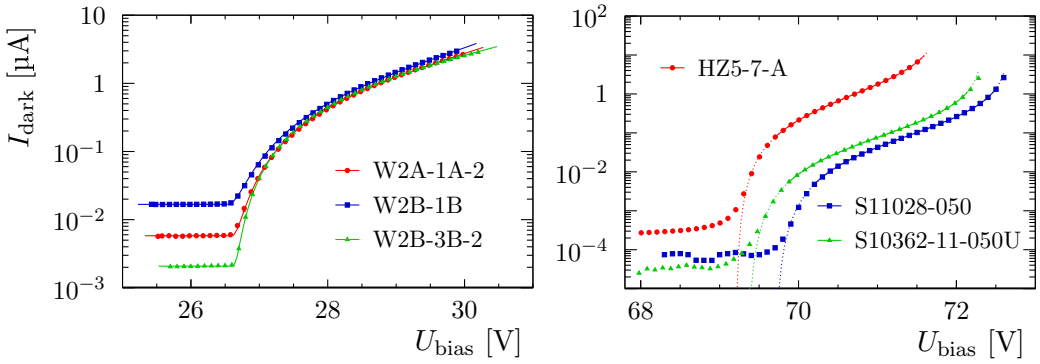

Figure 4.28: I-U characteristic of KETEK (left) and Hamamatsu SiPMs (right) measured at room temperature in darkness. Curves show fit results after Eq. (4.38). Dashed parts are outside of the fit range.

Figure 4.28 shows measured dark currents of KETEK and Hamamatsu SiPMs at temperatures that are given in Tab. 4.8. In the case of SiPM arrays, the illustrated current is the total of all SiPM channels which are connected to the measuring device in parallel, compare test setups C and D in Sec. 4.2.2. The results of fitting Eq. (4.38) to the acquired data points are also plotted in the figure. During the fit, parameters α_{BD} and α_{CT}, *cf.* Eq. (4.30) and (4.26), are fixed to values that have been inferred from signal spectrum analyses, see Sec. 4.3, Tab. 4.3. Parameter values of SiPM array HZ5-7-A are also used for single-channel SiPMs S11028-050 and S10362-11-050U, since no significant differences could be revealed in their signal spectra.

Table 4.8: Temperatures during *I-U* measurements shown in Fig. 4.28.

Sensor	T [°C]
HZ5-7-A	20.34
S11028-050	20.45
S10362-11-050U	20.45
W2A-1A-2	19.56
W2B-1B	19.56
W2B-3B-2	20.96

Table 4.9: Parameter results from fitting Eq. (4.38) to measured data of KETEK SiPMs shown in Fig. 4.28.

Sensor	U_{BD} [V]	α_{AP} [V^{-1}]	I_{const} [nA]	I'_{dark} [$\frac{\mathrm{nA}}{\mathrm{V}}$]
W2A-1A-2	26.602 ± 0.035	0.144 ± 0.014	5.806 ± 0.009	536 ± 35
W2B-1B	26.540 ± 0.017	0.157 ± 0.009	16.765 ± 0.012	570 ± 21
W2B-3B-2	26.6232 ± 0.0011	0.1331 ± 0.0013	2.079 ± 0.008	578.7 ± 2.5

When fitting Eq. (4.38) to data of KETEK SiPMs, the value of

$$(1 - \exp(-\alpha_{\mathrm{BD,dark}}\, U_{\mathrm{over}}))$$

in Eq. (4.30) is fixed to 1. Thus, no difference in the breakdown efficiency of free carriers produced by incoming photons or by thermal excitation is taken into account. The fit range comprises the whole voltage range of the characterisation measurement.

Fit results are provided in Tab. 4.9. The given uncertainties are statistical error estimates. They do not include possible systematic uncertainties, *e.g.* inaccurate values of fixed parameters or possible imperfections of the used fit function itself. However, the fitted curve in Fig. 4.28 shows a good description of measured data. The leakage current I_{const} may differ from the magnitude given in Tab. 4.9 when the *I-U* characterisation measurement is repeated. Hence, it is considered as being a systematic offset in the measured current rather than being a characteristic of the G-APDs.

If the SiPM gain is known, the thermal electron-hole pair generation rate can be calculated from the fit result of I'_{dark} by

$$r_{\mathrm{th.\,gen.}} = \frac{I'_{\mathrm{dark}}}{G' \cdot e} \ . \tag{4.39}$$

The gain per over-voltage of KETEK sensors is derived from G' of HZ5-7-A provided in Tab. 4.7 and the ratio of respective values of $\langle G'_i \rangle$ that are given as ADC count per volt in Tab. 4.2. This approach leads to the generation rates listed in Tab. 4.10.

Table 4.10: Thermal electron-hole pair generation rate calculated by Eq. (4.39) at temperatures given in Tab. 4.8.

Sensor	$r_{\text{th. gen.}}$ [MHz]
W2A-1A-2	3.56 ± 0.27
W2B-1B	2.88 ± 0.15
W2B-3B-2	5.43 ± 0.21

Table 4.11: Thermal generation rate $r_{\text{th. gen.}}$ normalised by total surface area A of G-APD pixels.

Sensor	$r_{\text{th. gen.}}/A$ [kHz mm^{-2}]
HZ5-7-A	1152 ± 14
S11028-050 / S10362-11-050U	936 ± 9
W2A-1A-2	380 ± 29
W2B-1B	307 ± 16
W2B-3B-2	516 ± 20

A comparison of thermal generation rates of KETEK and Hamamatsu SiPMs is provided by Tab. 4.11. The values of $r_{\text{th. gen.}}$ are normalised by the total pixel area A of the respective device, compare Tab. 4.1, and scaled to values corresponding to 20 °C using Eq. (4.10). Generation rates of KETEK SiPMs are by a factor of 2 to 3 lower than those observed with Hamamatsu SiPMs in dark count rate measurements.

The dark current of Hamamatsu SiPMs that is measured at voltages below U_{BD} is by about two orders of magnitude lower than I_{const} obtained with KETEK sensors. It cannot be adequately described by a constant nor by another simple expression. Therefore, a lower limit of the fit range is set where the current component that is also observed below the breakdown voltage is assumed to be negligible compared to the current that is induced by diode breakdowns. The value of I_{const} is hence fixed to 0.

The expression (4.38) has singularities at voltages where ϵ_{CT} or ϵ_{AP} equals 1. Instead of this unphysical behaviour, the current will saturate at larger over-voltages due to the finite number of pixels and their recovery time after breakdown. Also SiPM warming by larger currents and the resulting decrease of over-voltage at fixed bias will mitigate the divergence of dark current. For this reason, the fit range has an upper limit, and is chosen from $U_{\text{BD}} + 0.5\,\text{V}$ to $U_{\text{BD}} + 2.8\,\text{V}$. The described saturation is negligible in the performed characterisation of KETEK sensors because of their much lower cross-talk probability ϵ_{CT}.

The breakdown voltage of the tested Hamamatsu detectors is calculated by Eq. (4.28) using parameters from Tab. 4.4 and kept fix when fittig Eq. (4.38). In contrast to the analysis of I-U curves of KETEK devices, $\alpha_{\text{BD,dark}}$ is a free parameter

Table 4.12: Parameter results from fitting Eq. (4.38) to measured data of Hamamatsu SiPMs shown in Fig. 4.28. The value of U_{BD} is fixed in the fit process.

Sensor	U_{BD} [V]	$\alpha_{\mathrm{BD,dark}}$ [V^{-1}]	α_{AP} [V^{-1}]	I'_{dark} [$\frac{\mathrm{nA}}{\mathrm{V}}$]
HZ5-7-A	69.205	7.03 ± 0.24	0.4203 ± 0.0007	1379.9 ± 1.8
S11028-050	69.705	4.28 ± 0.16	0.2612 ± 0.0007	96.21 ± 0.23
S10362-11-050U	69.354	4.82 ± 0.08	0.2527 ± 0.0007	93.73 ± 0.13

of the fit. This enables a cross-check with results from dark count rate studies in Sec. 4.4.

Table 4.12 shows parameter values resulting from the fit as well as the previously calculated breakdown voltages. Uncertainties given in the table are small, since they do not comprise systematic uncertainties. However, the values obtained for $\alpha_{\mathrm{BD,dark}}$ and α_{AP} change easily by 10 % when varying the chosen fit range. Taking into account the uncertainties related with this analysis condition, the values of α_{AP} are compatible with 0.335 ± 0.032 for HZ5-7-A and 0.2678 ± 0.0031 for S11028-050 and S10362-11-050U estimated from α'_{AP} in Tab. 4.6 and the respective breakdown voltage.

Values of $\alpha_{\mathrm{BD,dark}}$ are by a factor of about 2 to 3 larger than correspondent values computed from α'_{AP} in Tab. 4.6. This could be a further indication that the measured dark count rate in Sec. 4.4 underestimates the real DCR at low over-voltages as discussed in the context of gain determination in the mentioned section.

The fit result for I'_{dark} enables to calculate the SiPM gain per over-voltage G' using the carrier generation rate $r_{\mathrm{th.\,gen.}}$ given in Tab. 4.6.

$$G' = \frac{I'_{\mathrm{dark}}}{r_{\mathrm{th.\,gen.}} \cdot e} \tag{4.40}$$

The dark current and generation rate in this equation must be corresponding to the same temperature. For this reason, I'_{dark} is normalised to 20 °C by Eq. (4.10). In the case of HZ5-7-A, it has furthermore to be taken into account that the measured generation rate in Tab. 4.6 is the sum over four channels, while the obtained I'_{dark} refers to the total current of all 32 channels of the SiPM array. Determined values of G' are provided in Tab. 4.13. They are consistent with numbers given in Tab. 4.7 which have been obtained by Eq. (4.36).

Temperature Dependence

The photon detection efficiencies, cross-talk and after-pulse probabilities studied in Sec. 4.3 and 4.4 do not exhibit a dependence on temperature. The same observation is made for the SiPM gain, which depends on the photo-diodes' capacitance, see Sec. 4.1 and 4.3. Hence, *I-U* curves measured in darkness at temperature T should be describable by means of a reference curve measured at T_{ref}, if the change of breakdown voltage ΔU_{BD}, which leads to a shift along the U-axis, and a scaling factor

Table 4.13: Gain per over-voltage G' derived from $r_{\text{th. gen.}}$ and I'_{dark} given by Tab. 4.6 and 4.12.

Sensor	G' $[10^5\,\text{V}^{-1}]$
HZ5-7-A	8.89 ± 0.11
S11028-050	6.18 ± 0.06
S10362-11-050U	6.02 ± 0.06

Table 4.14: Temperatures T_{ref} of *I-U* reference curves and parameters $U_{\text{bias,max}}(0\,°\text{C})$, $U'_{\text{bias,max}}$ defining the range of reference curve fits, see Eq. (4.43).

Sensor	T_{ref} [°C]	$U_{\text{bias,max}}(0\,°\text{C})$ [V]	$U'_{\text{bias,max}}$ $[\frac{\text{mV}}{°\text{C}}]$
S11028-050	21.4	70.362	55.9
S10362-11-050U	21.4	69.994	56.7
HZ5-7-A	19.4	69.71	56.66
HZ5-7-D	19.6	69.71	56.66
W2A-1A-2	19.6	26.83	22
W2B-1B	19.6	26.83	22
W2B-3B-2	20.6	26.83	22

$I_{\text{dark,rel}}$, which includes the temperature dependence of primary carrier generation, are taken into account, see Eq. (4.41). The leakage current measured below U_{BD}, which is represented by I_{const} in equation (4.38), may vary between the performed *I-U* scans. This bias is considered by the parameter I_{offset}.

$$I_{\text{dark}}\left(U_{\text{bias}} \mid T\right) = I_{\text{dark,rel}} \cdot I_{\text{dark}}\left(U_{\text{bias}} - \Delta U_{\text{BD}} \mid T_{\text{ref}}\right) + I_{\text{offset}} \tag{4.41}$$

According to Eq. (4.41), *I-U* reference curves obtained at T_{ref}, see Tab. 4.14, are fit to data points of *I-U* scans performed at several temperatures using the method of least squares. The reference curves $I_{\text{dark}}(U_{\text{bias}} \mid T_{\text{ref}})$ are determined by cubic spline interpolation of measured data points.

In the fit, the dark current data are weighted by an estimated uncertainty

$$\sigma(U_{\text{bias}}) = \sqrt{\sigma^2_{\text{low volt}} + I^2_{\text{dark,rel}}\sigma^2_{\text{ref}}(U_{\text{bias}} - \Delta U_{\text{BD}})}\ . \tag{4.42}$$

The uncertainty $\sigma_{\text{ref}}(U)$ is calculated by a linear interpolation of the standard deviations of I_{dark} that are obtained in the reference curve measurement at discrete values of U_{bias}. This value of σ_{ref} is scaled by the fit parameter $I_{\text{dark,rel}}$, which leads to a relative uncertainty of the dark current that is only dependent on (over-)voltage. However, at very low currents the observed standard deviation does no longer decrease proportionally to I_{dark}. In Eq. (4.42), this effect is taken into account by

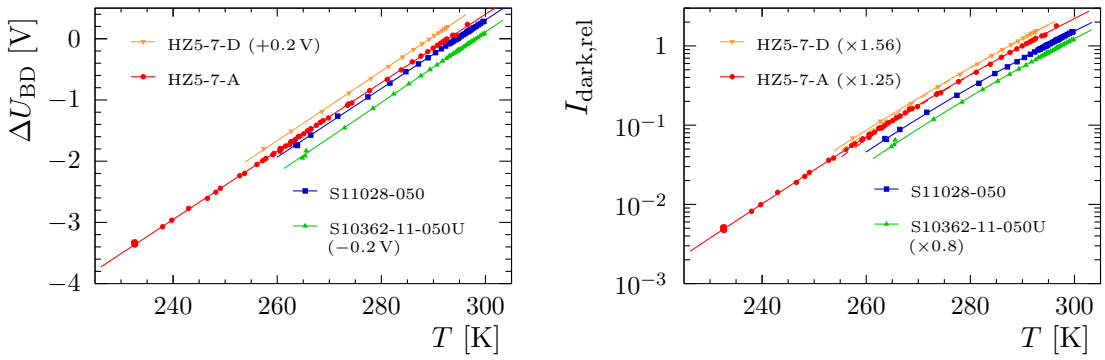

(a) Hamamatsu

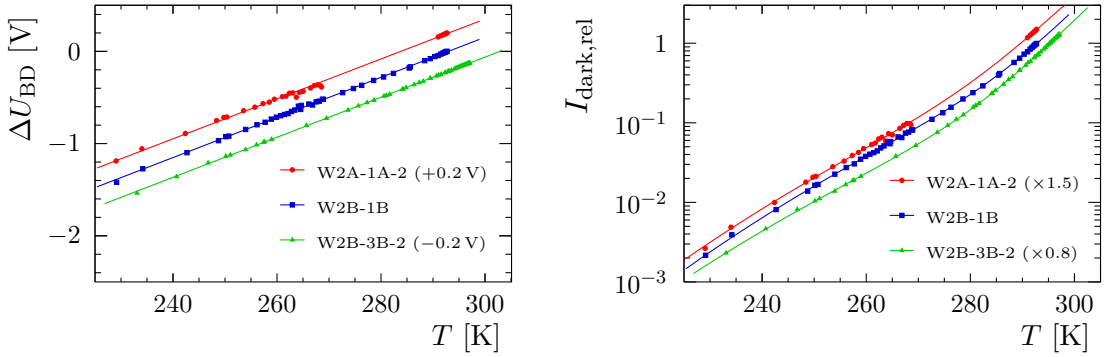

(b) KETEK

Figure 4.29: Change of breakdown voltage ΔU_{BD} and relative dark current $I_{\mathrm{dark,rel}}$ as function of temperature T. Data and fit curves are shifted or scaled by values given in parentheses to improve visibility of individual curves.

$\sigma_{\mathrm{low\,volt}}$ whose value is derived from the data points that shall be described by the reference curve via Eq. (4.41). It is the standard deviation of the dark current that is measured at the six lowest bias voltages of the respective I-U scan.

To provide a similar fit range with respect to the breakdown voltage for all analysed I-U curves, the considered data are limited by

$$U_{\mathrm{bias}} < U_{\mathrm{bias,max}}(0\,^{\circ}\mathrm{C}) + U'_{\mathrm{bias,max}} \cdot T[^{\circ}\mathrm{C}] \; . \tag{4.43}$$

Table 4.14 lists the used parameter values of $U_{\mathrm{bias,max}}(0\,^{\circ}\mathrm{C})$ and $U'_{\mathrm{bias,max}}$. The resulting maximum bias voltages correspond to about 1.7 V and 0.7 V over-voltage in the case of Hamamatsu and KETEK sensors, respectively.

Parameters obtained via the described fit procedure are illustrated in Fig. 4.29. The observed change in U_{BD} is proportional to the temperature change, as it is observed when analysing SiPM signal spectra, compare Fig. 4.16. Thus, a linear function, according to Eq. (4.28), is fitted to the data points $(T, \Delta U_{\mathrm{BD}})$.

$$\Delta U_{\mathrm{BD}}(T) = \Delta U_{\mathrm{BD}}(273.15\,\mathrm{K}) + U'_{\mathrm{BD}} \cdot (T - 273.15\,\mathrm{K}) \tag{4.44}$$

Table 4.15: Parameter results from fitting Eq. (4.44) to data shown in Fig. 4.29.

Sensor	$\Delta U_{\mathrm{BD}}(273.15\,\mathrm{K})$ [V]	U'_{BD} [$\mathrm{mV\,K^{-1}}$]
S11028-050	-1.197 ± 0.004	55.99 ± 0.21
S10362-11-050U	-1.237 ± 0.006	57.62 ± 0.28
HZ5-7-A	-1.0993 ± 0.0017	55.89 ± 0.09
HZ5-7-D	-1.118 ± 0.004	56.82 ± 0.27
W2A-1A-2	-0.4306 ± 0.0030	21.65 ± 0.16
W2B-1B	-0.4306 ± 0.0012	21.74 ± 0.08
W2B-3B-2	-0.4457 ± 0.0009	21.72 ± 0.05

The fit results are provided by Tab. 4.15. The derivatives of breakdown voltage with respect to the temperature, U'_{BD}, are in agreement with those found by analysis of signal spectra, see Tab. 4.4. The relative change in breakdown voltage $U'_{\mathrm{BD}}/U_{\mathrm{BD}}$ is similar for the studied Hamamatsu and KETEK SiPMs. Its value is about $8 \cdot 10^{-4}\,\mathrm{K^{-1}}$ at room temperature.

The generation of free carriers in the depletion layer of the G-APD pixels, which is the source of dark count and dark current, can occur via different mechanisms. Two general temperature dependencies are considered in the following equation.

$$I_{\mathrm{dark(,rel)}}(T) = I_{\mathrm{SRH}}(T) + I_{\mathrm{diff}}(T) \tag{4.45}$$

with

$$\begin{aligned} I_{\mathrm{i}}(T) &= I_{\mathrm{i}}(T_{\mathrm{ref}}) \cdot \left(\frac{T}{T_{\mathrm{ref}}}\right)^{a_i} \cdot \exp\left(-\frac{E_{\mathrm{A,i}}}{b_i\, k_{\mathrm{B}}} \cdot \left(\frac{1}{T} - \frac{1}{T_{\mathrm{ref}}}\right)\right) \ , \\ & i \in \{\mathrm{SRH}, \mathrm{diff}\} \ , \quad T_{\mathrm{ref}} = 293.15\,\mathrm{K} \end{aligned} \tag{4.46}$$

and

$$\begin{aligned} a_{\mathrm{SRH}} &= 2 & b_{\mathrm{SRH}} &= 2 \\ a_{\mathrm{diff}} &= 3 & b_{\mathrm{diff}} &= 1 \end{aligned} \tag{4.47}$$

The carrier generation described by Shockley-Read-Hall (SRH) statistics is due to carrier capture and emission by trap levels in the band gap [79,95]. The corresponding temperature dependence given by Eq. (4.46) and (4.47) is an approximation for trap levels close to the intrinsic Fermi level. Only these traps are efficient SRH generation centres. The value of the activation energy $E_{\mathrm{A,SRH}}$ is approximately equal to the band gap E_{G}. However, especially in the high-field region of the p-n junction, the SRH generation rate can be enhanced by trap-assisted tunnelling [84]. This effect leads to a value of $E_{\mathrm{A,SRH}}$ that is lower than E_{G}.

The temperature dependence of carrier diffusion into the space charge region of the p-n junction is taken into account by $I_{\mathrm{diff}}(T)$. Its activation energy $E_{\mathrm{A,diff}}$ is equal to E_{G}.

Table 4.16: Parameters obtained from fitting Eq. (4.45) to data of Hamamatsu sensors shown in Fig. 4.29. The value of I_{diff} is fixed to 0. Solid fit curves of HZ5-7-A and HZ5-7-D in Fig. 4.29 correspond to fit results where $E_{\mathrm{A,SRH}}$ is fixed to 1.12 eV. Parameters listed without uncertainties are fixed.

Sensor	$I_{\mathrm{SRH}}(293\,\mathrm{K})$	$E_{\mathrm{A,SRH}}$ [eV]	$I_{\mathrm{SRH2}}(293\,\mathrm{K})$	$E_{\mathrm{A,SRH2}}$ [eV]
S11028-050	0.8995 ± 0.0024	1.083 ± 0.005	0	—
S10362-11-050U	0.8881 ± 0.0024	1.121 ± 0.006	0	—
HZ5-7-A	1.038 ± 0.005	1.089 ± 0.008	0	—
HZ5-7-D	1.028 ± 0.007	1.099 ± 0.012	0	—
HZ5-7-A	0.968 ± 0.010	1.12	0.066 ± 0.007	0.591 ± 0.019
HZ5-7-D	0.963 ± 0.010	1.12	0.059 ± 0.006	0.59

The expression given by Eq. (4.45) to (4.47) is fit to the $I_{\mathrm{dark,rel}}(T)$ data obtained from the analysis of *I-U* curves, see Fig. 4.29. Resulting parameters are shown in Tab. 4.16 and 4.17 and discussed in the following.

The data of single-channel SiPMs from Hamamatsu can be described by only taking into account the SRH term $I_{\mathrm{SRH}}(T)$. However, data of SiPM arrays HZ5-7-A and HZ5-7-D show deviations from the fitted function, when only one SRH-like term is considered. For this reason, the fit range has been restricted to $T > 273\,\mathrm{K}$, where the temperature dependence according to SRH statistics provides a suitable description and shows an activation energy close to E_{G}. If a second SRH term $I_{\mathrm{SRH2}}(T)$, which allows for the influence of tunnelling or of a further trap level, is included in Eq. (4.45), the fit functions show a good agreement with data in the whole data range. In this case, the value of $E_{\mathrm{A,SRH}}$ has been fixed to 1.12 eV according to the band gap at room temperature. In the fit of HZ5-7-D data, the parameter $E_{\mathrm{A,SRH2}}$ is fixed as well, since its fit result becomes negative, else. The fit result for $E_{\mathrm{A,SRH2}}$ obtained from HZ5-7-A data is more reliable due to the larger temperature range. It is therefore also used to describe HZ5-7-D data.

The temperature dependence of $I_{\mathrm{dark,rel}}$ of tested KETEK SiPM arrays differs from that of the Hamamatsu devices. A significant impact of carrier diffusion is observed, which has not been seen with Hamamatsu sensors. Parameters from fitting Eq. (4.45) are given in Tab. 4.17. For sensor W2A-1A-2, the energy $E_{\mathrm{A,diff}}$ is fixed to the band gap, because the used data cover only a small part of the temperature range where I_{diff} is dominating.

The quality of describing the temperature-dependent dark current by a single *I-U* reference curve of the particular SiPM, shifted by $\Delta U_{\mathrm{BD}}(T)$ and scaled by $I_{\mathrm{dark,rel}}(T)$, is illustrated in Fig. 4.30. The values of $\Delta U_{\mathrm{BD}}(T)$ and $I_{\mathrm{dark,rel}}(T)$ are calculated by Eq. (4.44) and (4.45) using parameters given in Tab. 4.15, 4.16 and 4.17. Data points of Hamamatsu sensors are in good agreement for over-voltages less than 2.2 V. The increasing scattering of data points below the breakdown voltage

Table 4.17: Parameters obtained from fitting Eq. (4.45) to data of KETEK sensors shown in Fig. 4.29. Parameters listed without uncertainties are fixed.

Sensor	$I_{\text{diff}}(293\,\text{K})$	$E_{\text{A,diff}}$ [eV]	$I_{\text{SRH}}(293\,\text{K})$	$E_{\text{A,SRH}}$ [eV]
W2A-1A-2	0.724 ± 0.021	1.12	0.320 ± 0.010	0.836 ± 0.011
W2B-1B	0.636 ± 0.013	1.21 ± 0.04	0.410 ± 0.012	0.858 ± 0.009
W2B-3B-2	0.675 ± 0.014	1.153 ± 0.020	0.259 ± 0.012	0.791 ± 0.014

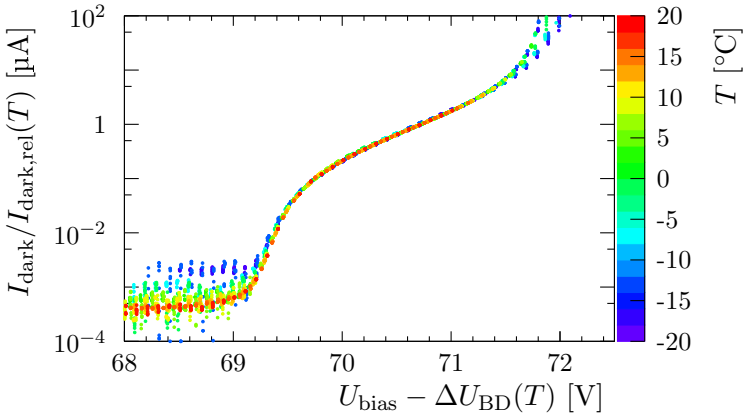

(a) Hamamatsu (HZ5-7-A)

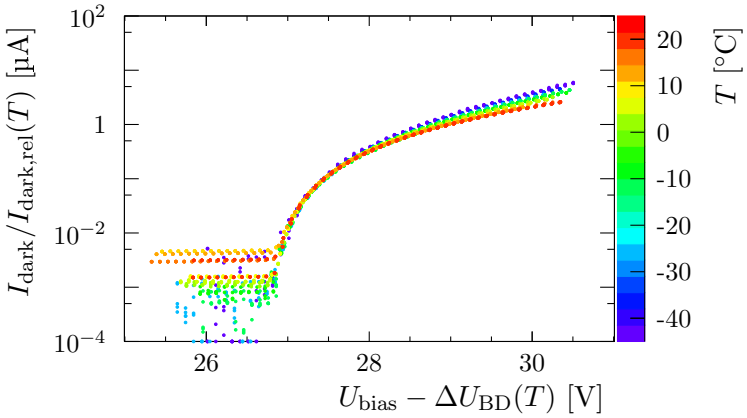

(b) KETEK (W2B-3B-2)

Figure 4.30: Example I-U curves corrected for temperature dependence of breakdown voltage and carrier generation after Eq. (4.44) and (4.45) using parameters given in Tab. 4.16 and 4.17.

with decreasing temperature is a result of the increased relative uncertainty of the measurement at low currents.

For KETEK sensors, the shifted and scaled I-U reference curve can only be used to approximate $I_{\text{dark}}(U_{\text{bias}} \mid T)$ at over-voltages from about 0.4 V to 0.8 V. At higher

Table 4.18: Parameter results from fitting Eq. (4.28) to data shown in Fig. 4.31.

Sensor	$U_{\mathrm{BD}}(273.15\,\mathrm{K})$ [V]	U'_{BD} [$\mathrm{mV\,K^{-1}}$]
W2A-1A-2	26.1436 ± 0.0030	22.31 ± 0.16
W2B-1B	26.0987 ± 0.0017	22.53 ± 0.11
W2B-3B-2	26.1506 ± 0.0009	22.43 ± 0.05

over-voltages, the data show a systematic deviation from the shape of the *I-U* curve that is measured at room temperature. The deviation increases with increasing over-voltage and decreasing temperature.

The discrepancy of *I-U* curve shapes at different temperatures can be explained by carrier generation rates that depend on voltage. This effect may occur due to the voltage dependence of the tunnelling probability. It is taken into account by fitting Eq. (4.38), with I'_{dark} being replaced by

$$I'_{\mathrm{dark}} \rightarrow I'_{\mathrm{dark}} + I''_{\mathrm{dark}} \cdot U_{\mathrm{over}} \ , \tag{4.48}$$

to the measured *I-U* data. Furthermore, a linear function is used instead of the constant I_{const} to improve the description of the breakdown-independent leakage current. The parameters of this linear function are derived from the dark current at bias voltages less than U_{BD} and fixed when fitting Eq. (4.38).

Figure 4.31 shows examples of *I-U* data, measured at four different temperatures, and the corresponding fit curves. It also visualises the derived temperature dependence of parameters U_{BD}, I'_{dark} and I''_{dark}. These temperature dependences are described by Eq. (4.28) and (4.45). Corresponding fit parameters are listed in Tab. 4.18 and 4.19. The given uncertainties only include statistical uncertainties found by the fit algorithm.

In contrast to the fit of an *I-U* reference curve, the data description by Eq. (4.38) does not only provide the change of breakdown voltage with temperature $\Delta U_{\mathrm{BD}}(T)$, but also the absolute value $U_{\mathrm{BD}}(T)$ for all evaluated *I-U* curve measurements. The determined change of breakdown voltage per temperature change U'_{BD} is by about 3 % higher when Eq. (4.38) instead of a reference curve is fit to the data, compare Tab. 4.15 and 4.18.

A contribution of carrier diffusion to the measured dark current is only seen in I'_{dark}, which determines the fraction of dark current that is independent of over-voltage. This is due to the fact that the diffusion current is close to its saturation level at the applied bias voltages. The relative fraction of dark current, that results from over-voltage dependent generation rates, decreases with increasing temperature, especially due to the higher contribution from diffusion to the total current. However, it is still about 24 % for sensors W2A-1A-2, W2B-1B and about 15 % for sensor W2B-3B-2 at room temperature and 3 V over-voltage.

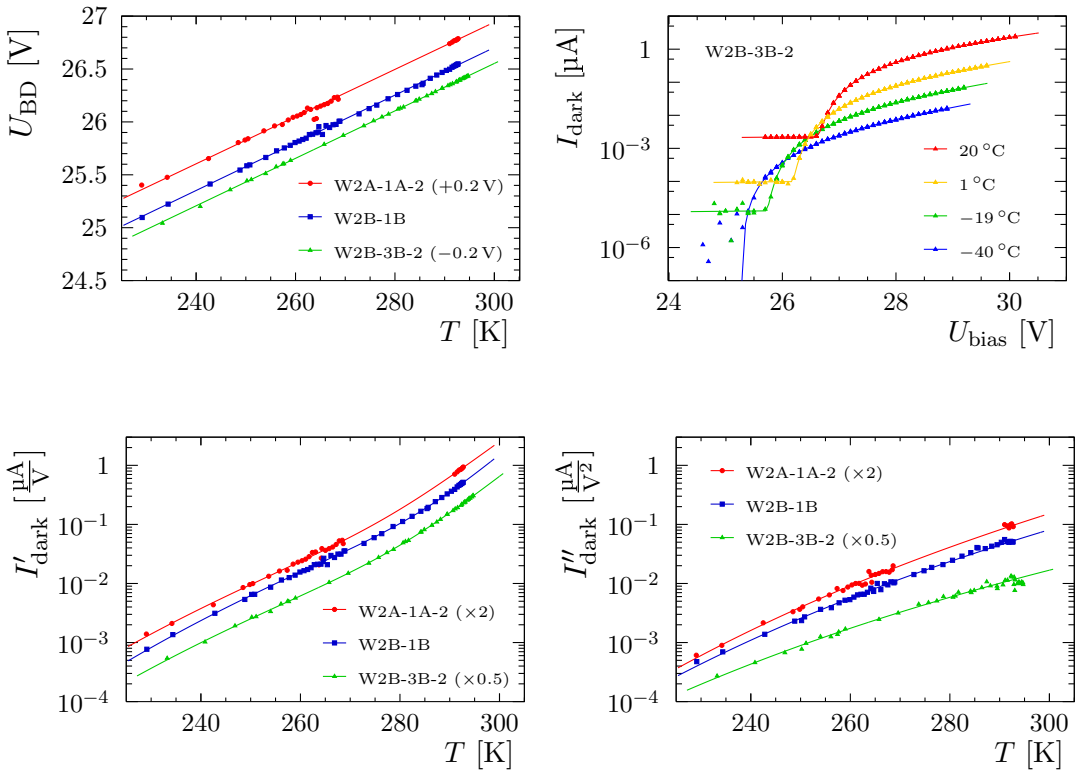

Figure 4.31: Temperature dependence of breakdown voltage U_{BD} and dark current coefficients I'_{dark}, I''_{dark} used in Eq. (4.38) with (4.48). Parameters are determined by fitting Eq. (4.38) to I-U data of KETEK SiPMs. Four exemplary I-U data sets and corresponding fit curves are shown in the top right plot.

Table 4.19: Parameter results from fitting Eq. (4.45) to data of KETEK sensors shown in Fig. 4.31. Prime and double prime symbols identify parameters determining the temperature dependence of I'_{dark} and I''_{dark}, respectively. Parameters listed without uncertainties are fixed.

Sensor	$I'_{diff}(293\,K)$ $[\frac{nA}{V}]$	$E'_{A,diff}$ [eV]	$I'_{SRH}(293\,K)$ $[\frac{nA}{V}]$	$E'_{A,SRH}$ [eV]
W2A-1A-2	367 ± 20	1.11 ± 0.15	121 ± 24	0.86 ± 0.05
W2B-1B	347 ± 12	1.30 ± 0.07	197 ± 10	0.919 ± 0.016
W2B-3B-2	356 ± 8	1.171 ± 0.028	132 ± 7	0.866 ± 0.017

Sensor	$I''_{diff}(293\,K)$ $[\frac{nA}{V^2}]$	$E''_{A,diff}$ [eV]	$I''_{SRH}(293\,K)$ $[\frac{nA}{V^2}]$	$E''_{A,SRH}$ [eV]
W2A-1A-2	0	—	49.6 ± 1.8	0.850 ± 0.012
W2B-1B	0	—	54.1 ± 1.2	0.799 ± 0.009
W2B-3B-2	0	—	23.7 ± 0.5	0.665 ± 0.009

4.6 Radiation Damage

The silicon photomultipliers used to read out the fibres of the LHCb SciFi Tracker have to withstand a radiation level that is expected to cause considerable damage. Hadrons and other particles with sufficient energy lead to the displacement of silicon atoms from their site in the lattice, resulting in a remaining vacancy and an interstitial defect. In addition to these point defects, the primarily displaced atom will generate cluster defects at the end of its track, if the recoil energy is higher than about 5 keV [96]. The defects may act as carrier generation centres leading to an increased leakage current and dark count rate, as trapping centres for electrons and holes, and change the effective doping concentration.

Damages in the silicon bulk are assumed to be proportional to the non-ionising energy loss (NIEL) of the incident radiation, which is referred to as *NIEL scaling hypothesis* [97]. If the displacement damage cross-section D of a given particle type and energy is known, the particle fluence Φ can be expressed by an equivalent fluence Φ_{eq} of neutrons having a kinetic energy of 1 MeV, which would induce the same damage. This common practice enables the comparison of silicon detector deteriorations observed in different radiation environments.

The 1 MeV-neutron-equivalent fluence expected in the upgraded tracking stations of the LHCb detector is obtained from FLUKA simulations [71]. The proposed total luminosity of $50\,\text{fb}^{-1}$ involves a maximum fluence at the locations of the SciFi Tracker's SiPMs of about $6 \cdot 10^{11}\,\text{cm}^{-2}$ to $8 \cdot 10^{11}\,\text{cm}^{-2}$. These values result from the cross-sections of proton-proton collisions of 72 mb and 100 mb, respectively, that are considered in the FLUKA simulations. Reference [71] states the necessity of an additional safety factor of two due to uncertainties in the simulation.

The impact of radiation on the performance of Hamamatsu MPPCs has been studied at proton beam facilities and with sensors that were installed at the LHCb detector *in situ*. These tests and their results are described in the following.

4.6.1 Proton Irradiation

Irradiations of four Hamamatsu MPPC 5883 sensors have been executed at the proton accelerators of the *Centre Antoine Lacassagne* (CAL) in Nice and the *Maier-Leibnitz-Laboratorium* (MLL) at Forschungszentrum Garching near Munich.

The accelerator of CAL is a medical cyclotron used for the treatment of ocular melanoma. The kinetic energy of protons leaving the cyclotron decreases from 65 MeV to 62 MeV at the end of the beam line [98]. The lateral beam profile is defined by collimators and shows a flat dose distribution. Its extent on the target's surface can be verified using an optical light source.

The particle fluence at CAL is monitored by two parallel plate ionisation chambers which are traversed by the proton beam. Monitor units are calibrated against another ionisation chamber that is used to obtain the energy deposition at the target position [99]. The uncertainty of dose measurements with ionisation chambers quoted by Ref. [98] is 4 %. However, comparative Faraday cup measurements, which

Table 4.20: Proton energy E_p and total proton fluence Φ_p accumulated during irradiations at MLL and CAL. The corresponding neutron-equivalent fluence Φ_{eq} is calculated using NIEL scaling factors found in Ref. [100].

Sensor	E_p [MeV]	Φ_p [$10^9\,cm^{-2}$]	Φ_{eq} [$10^9\,cm^{-2}$]
HS5-24-A	21.0	2.37 ± 0.11	6.4 ± 0.6
HS5-24-C	21.0	1.44 ± 0.10	3.9 ± 0.4
HZ5-26-B	60.9	65.3 ± 1.3	108 ± 4
HZ5-26-D	60.9	493 ± 10	819 ± 30

can be related to monitor units, provide a fluence uncertainty that is estimated to be less than 1 % [99]. In the following, an uncertainty of 2 % is considered for the proton fluence that is derived from the monitor chamber measurement.

At MLL, a tandem accelerator provides protons of about 24 MeV kinetic energy. The beam is periodically deflected by two pairs of electrodes to scan the opening of a PVC plate that defines the irradiated area. This practice is employed to achieve a homogeneous fluence over the surface of the tested SiPM array despite an inhomogeneous beam profile. The proton fluence at the SiPM is determined by the duration of exposure to the beam and beam current measurements using a Faraday cup that is inserted into the beam line before and after each irradiation. These currents have to be scaled by a calibration factor obtained from measuring the current ratio passing the PVC aperture. The current measurement uncertainties lead to a relative uncertainty of the inferred proton fluence that is large compared to that of irradiations at CAL, compare Table 4.20.

The mean kinetic energies of protons provided by the accelerators at CAL and MLL were 62 MeV and 23.75 MeV. The decrease of these energies caused by the particles' path through air, the beam window of the light-tight box which contains the SiPMs and the coating of the sensors' active volume is estimated by a GEANT4 simulation. The obtained mean energies of protons when reaching the silicon diodes are 60.9 MeV and 21.0 MeV, respectively.

NIEL scaling factors are taken from Ref. [100]. The obtained values for proton energies 60.9 MeV and 21.0 MeV are 1.660 ± 0.031 and 2.70 ± 0.08. Uncertainties are estimated from the differences of the two data sets, that are provided by Ref. [100]. Table 4.20 lists proton energies E_p, total proton fluences Φ_p and corresponding 1 MeV-neutron-equivalent fluences Φ_{eq}, that have been applied to the four tested SiPM arrays. The total proton fluence has been achieved by multiple successive irradiations. The fluence and duration of each irradiation can be found in Appendix D.

Signal Spectra

During the irradiations, SiPM arrays were connected to test setup A, see Sec. 4.2.2, Fig. 4.3. This technically allowed for measurements of signal spectra and currents in

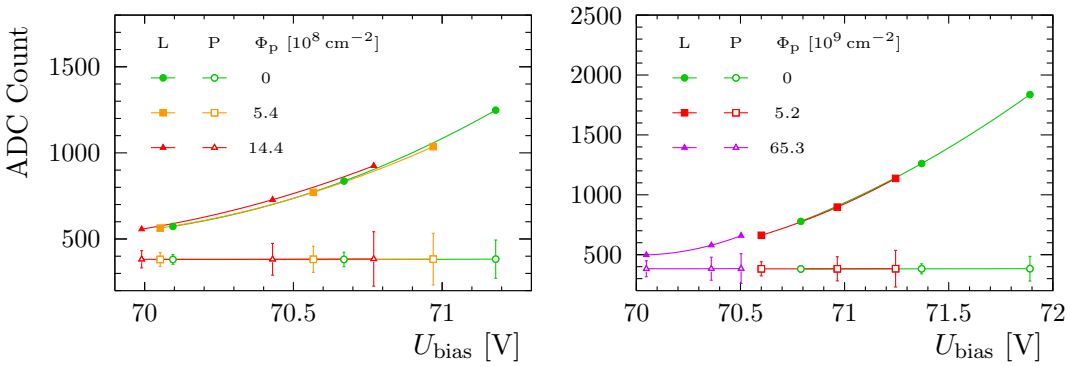

(a) $E_p = 21.0\,\mathrm{MeV}$ (b) $E_p = 60.9\,\mathrm{MeV}$

Figure 4.32: Mean ADC count of signal spectra acquired under sensor illumination by LED pulses (L) and of pedestal distributions (P). Vertical bars illustrate the standard deviation of the pedestal signal. Curves are obtained by cubic spline interpolation of the data points. Data are from two exemplary SiPM channels which have been irradiated at MLL (a) and CAL (b) with proton energies E_p and accumulated fluences Φ_p.

individual SiPM channels. However, the radiation-induced dark current caused two effects that disturbed these measurements. The increasing current lead to a change in the voltage drop at a series resistance on the FE-Board. Thus, the reverse voltage at the SiPM decreased with increasing fluence, since the applied bias voltage was not adjusted to this effect. Furthermore, the radiation-induced dark count rate, which is associated with the dark current, induced a widened pedestal distribution in signal spectra after irradiation. Thus, the determination of individual n-photon-equivalent peaks (compare Sec. 4.3) became difficult and eventually impossible. Signal spectra, that have been recorded immediately after the proton irradiation, are therefore not usable for an explicit analysis of gain, PDE and cross-talk.

Nevertheless, the spectrum's mean value at defined over-voltage and illumination should remain unaffected as long as no radiation effect except for a widened pedestal peak occurs and if the pedestal's mean is unchanged. Indeed, the expectation value of signals, that are measured under illumination by LED pulses with constant light intensity, does not show a dependence on the accumulated proton fluence, see Fig. 4.32.

After a period of about 30 months storage at room temperature, the characterisation of irradiated SiPM arrays by means of measurement setup A was repeated. A decrease of dark current by more than a factor of two, which is attributed to the annealing of radiation-induced defects, and cooling of sensors lead to a reduction of noise that was appropriate to enable signal spectra analyses as described in Sec. 4.3. Spectra were measured at temperatures given in Tab. 4.21.

Figures 4.33 and 4.34 show the observed gain, detected photon number and cross-talk probability of individual SiPM channels at several over-voltages before and 30 months after irradiation. Three of the four irradiated arrays show an increased

Table 4.21: Temperatures T_{before} and T_{after} during measurement of signal spectra before and 30 months after proton irradiation.

Sensor	T_{before} [°C]	T_{after} [°C]
HS5-24-A	24	−18
HS5-24-C	24	−18
HZ5-26-B	26	−20
HZ5-26-D	26	−39

gain per over-voltage after irradiation. The cross-talk probability of all four sensors appears to be slightly reduced. However, no proportionality of these parameters and the radiation level is found. It cannot be excluded that changes are artefacts due to systematic uncertainties of the measurement or of the signal spectrum analysis.

The mean number of detected photons per LED pulse μ_{phot}, which is derived from signal spectrum fits, is normalised so that it corresponds to a value of 1 at 1.5 V over-voltage in each SiPM channel. The necessary interpolation is done by fitting exponential functions to measured data as explained in Sec. 4.3. The resulting data points shown in Fig. 4.33 and 4.34 exhibit a similar dependence of the number of detected photons on over-voltage before and after irradiation.

I-U Characteristic

Current-voltage curves were measured at several temperatures after a period of about 27 months since irradiation of the sensors. The *I-U* curve of non-irradiated SiPM array HZ5-7-A is fitted to the acquired data points according to Eq. (4.41). The resulting values of the difference in breakdown voltage ΔU_{BD} and the relative dark current $I_{\text{dark,rel}}$ are plotted as function of temperature in Fig. 4.35.

Fitting the linear equation (4.44) to data of ΔU_{BD} leads to parameter values provided in Tab. 4.22. The obtained dependence of breakdown voltage on temperature, given by U'_{BD}, is consistent with that of non-irradiated Hamamatsu SiPMs of the same type, *cf.* Tab. 4.15. An absolute value of U_{BD} at a particular temperature can be calculated from parameters in Tab. 4.22 and the breakdown voltage associated with the used reference *I-U* curve of sensor HZ5-7-A. The latter is obtained from numbers provided by Tab. 4.4 and 4.15. Breakdown voltages of irradiated SiPM arrays, that are computed from *I-U* characterisation results, agree with values derived from signal spectra measured immediately before irradiation. Therefore, it is concluded that the breakdown voltage is not affected by radiation levels corresponding to the applied proton fluences.

Two terms, $I_{\text{init,rel}}$ and $I_{\text{rad,rel}}$, representing the initial carrier generation in a non-irradiated sensor and the radiation-induced leakage current, are used to describe the measured dark current after irradiation relative to the non-irradiated reference.

$$I_{\text{dark,rel}}(T) = I_{\text{init,rel}}(T) + I_{\text{rad,rel}}(T) \tag{4.49}$$

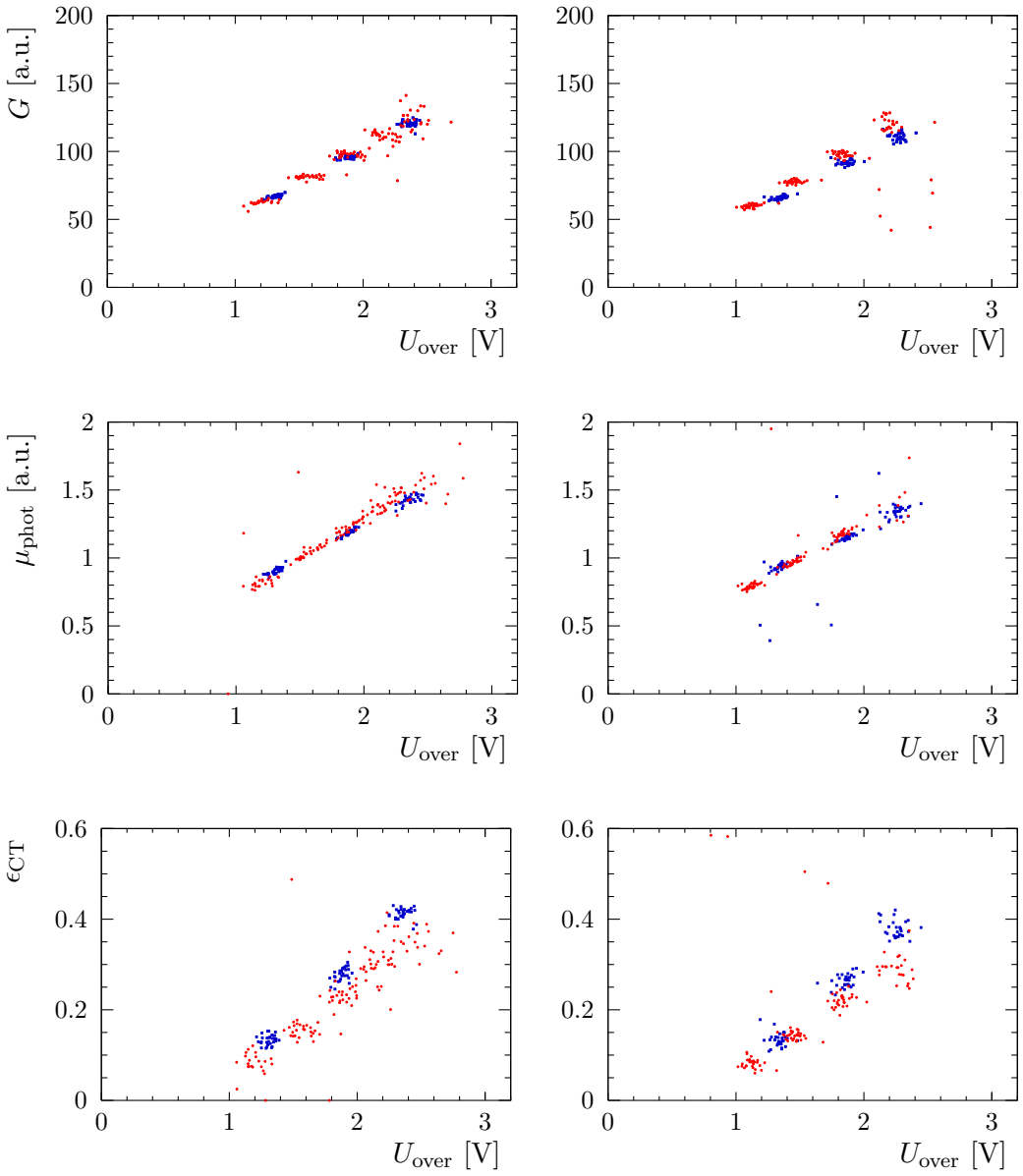

Figure 4.33: Gain G, mean number of detected photons per LED pulse μ_{phot} (normalised) and cross-talk probability ϵ_{CT} as a function of over-voltage U_{over}. Data points are obtained from signal spectra of individual channels of the respective SiPM array. Measurements were taken immediately before and 30 months after proton irradiation at CAL.

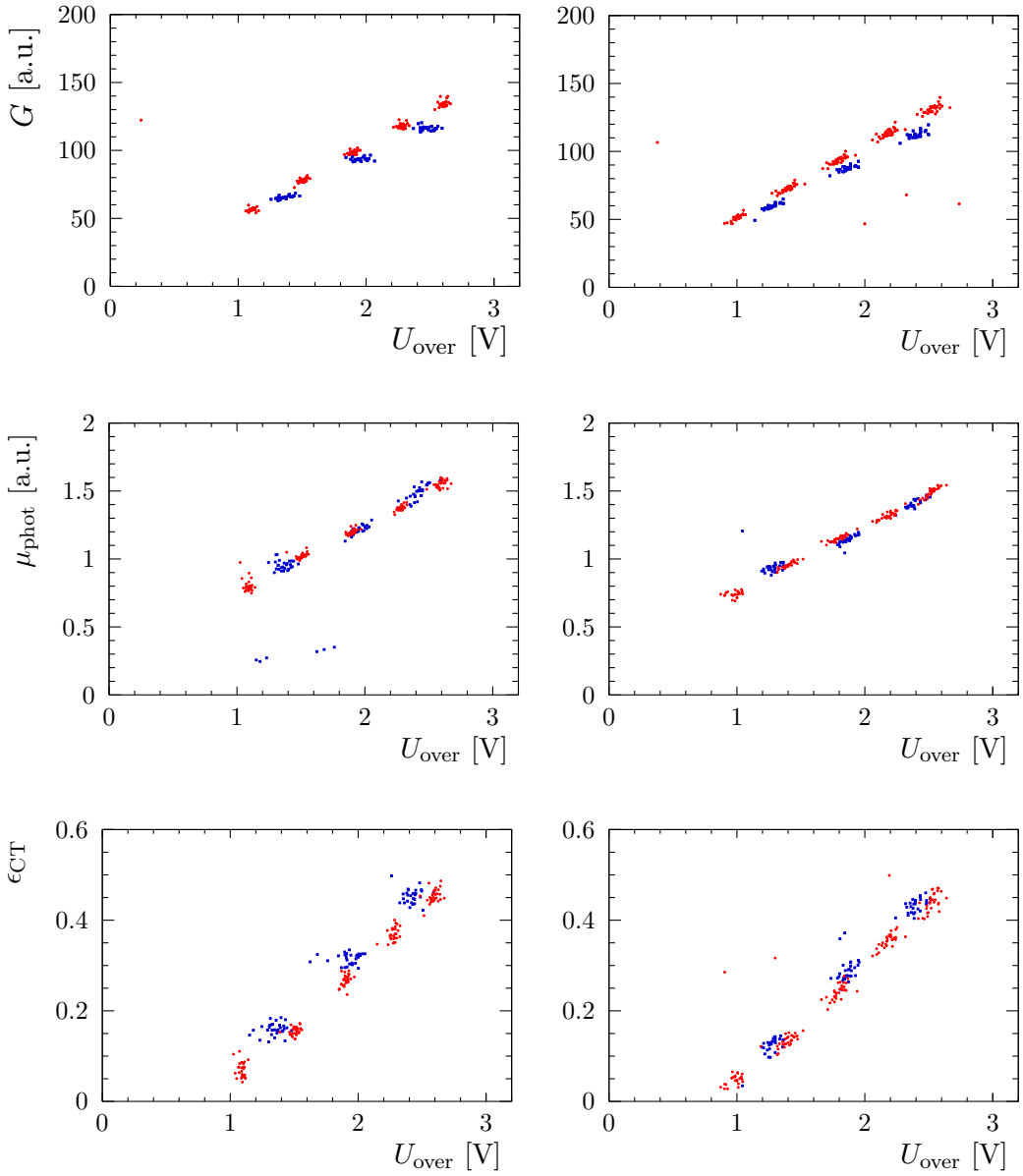

Figure 4.34: Gain G, mean number of detected photons per LED pulse μ_{phot} (normalised) and cross-talk probability ϵ_{CT} as a function of over-voltage U_{over}. Data points are obtained from signal spectra of individual channels of the respective SiPM array. Measurements were taken immediately before and 30 months after proton irradiation at MLL.

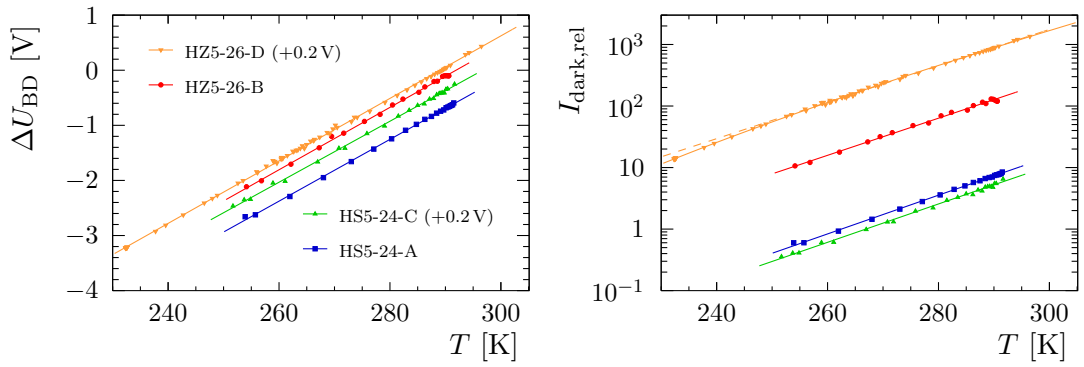

(a) (b)

Figure 4.35: Difference in breakdown voltage ΔU_{BD} (a) and dark current $I_{\mathrm{dark,rel}}$ (b) of SiPM arrays, 27 month after irradiation, relative to *I-U* reference curve of non-irradiated sensor HZ5-7-A as function of temperature T.

Table 4.22: Parameter results from fitting Eq. (4.44) to data shown in Fig. 4.35a.

Sensor	$\Delta U_{\mathrm{BD}}(273.15\,\mathrm{K})$ [V]	U'_{BD} [mV K^{-1}]
HS5-24-A	-1.639 ± 0.005	56.05 ± 0.31
HS5-24-C	-1.505 ± 0.006	55.35 ± 0.39
HZ5-26-B	-1.062 ± 0.006	56.61 ± 0.43
HZ5-26-D	-1.100 ± 0.003	56.71 ± 0.13

The value of $I_{\mathrm{init,rel}}(T)$ is calculated using two SRH terms according to Eq. (4.46) and (4.47) with parameters given in Tab. 4.16 for sensor HZ5-7-A. The following two expressions are used to parametrise the radiation-induced current component.

$$I_{\mathrm{rad,rel}}(T) = I_{\mathrm{SRH}}(T) + I_{\mathrm{SRH2}}(T) \tag{4.50}$$

$$I_{\mathrm{rad,rel}}(T) = I_{\mathrm{expo}}(T_{\mathrm{ref}}) \cdot \exp\left(\alpha_T (T - T_{\mathrm{ref}})\right) \tag{4.51}$$

While the first equation corresponds to carrier generation according to SRH statistics with two components having different activation energies, *cf.* Eq. (4.46), the second equation describes the radiation-induced dark current by a simple exponential function relative to the current at reference temperature T_{ref}.

Fitting Eq. (4.49) to data of HZ5-26-D with $I_{\mathrm{rad,rel}}(T)$ being described by Eq. (4.50) yields parameters listed in Tab. 4.23. One of the two activation energies, $E_{\mathrm{A,SRH}}$, has been fixed to 1.12 eV, which is equivalent to a defect level in the mid band gap. The fit result is shown by a solid line in Fig. 4.35b.

The found parameter values provide an appropriate description of data points in the investigated temperature range. However, all combinations of the three free parameters exhibit correlation coefficients greater than 0.9. Hence, the fit result does not enable an explicit physical interpretation, *e.g.* of the activation energy being the result of a distinct defect level.

Table 4.23: Parameters obtained from fitting Eq. (4.49) with $I_{\mathrm{rad,rel}}(T)$ being described by Eq. (4.50) to data of HZ5-26-D shown in Fig. 4.35b.

$I_{\mathrm{SRH}}(293\,\mathrm{K})$	$E_{\mathrm{A,SRH}}$ [eV]	$I_{\mathrm{SRH2}}(293\,\mathrm{K})$	$E_{\mathrm{A,SRH2}}$ [eV]
464 ± 26	1.12	619 ± 21	0.657 ± 0.007

Table 4.24: Parameters obtained from fitting Eq. (4.49) with $I_{\mathrm{rad,rel}}(T)$ being described by Eq. (4.51) to data shown in Fig. 4.35b. The fit range is restricted to $T > 250\,\mathrm{K}$.

Sensor	$I_{\mathrm{expo}}(293\,\mathrm{K})$	α_T $[10^{-3}\,\mathrm{K}^{-1}]$
HS5-24-A	8.16 ± 0.08	70.9 ± 0.6
HS5-24-C	5.52 ± 0.11	69.4 ± 1.0
HZ5-26-B	157.0 ± 2.9	69.4 ± 1.0
HZ5-26-D	1100 ± 9	68.10 ± 0.33

Using Eq. (4.51) instead of Eq. (4.50), when fitting Eq. (4.49) to HZ5-26-D data, offers a less accurate description of the observed dark current. The sum of square residuals χ^2 is by a factor of five greater, if Eq. (4.51) is used. However, this discrepancy of the two parametrisations of $I_{\mathrm{rad,rel}}(T)$ disappears, if only data in the temperature range $T > 250\,\mathrm{K}$ are taken into account. In this case, the χ^2 values are of the same magnitude for both descriptions. The dashed line in Fig. 4.35b illustrates the corresponding fit curve using Eq. (4.51) and its extrapolation to values below 250 K. Parameter values of this curve are given in Tab. 4.24.

Fit results that are provided for sensors HS5-24-A, HS5-24-C and HZ5-26-B in Tab. 4.24 and Fig. 4.35b have been obtained by taking Eq. (4.51) into account for the description of $I_{\mathrm{rad,rel}}(T)$. Results from using Eq. (4.50) are not stated due to the two following facts. In the temperature range of respective data, both descriptions, Eq. (4.50) and (4.51), provide the same accuracy. The correlations of parameters in the case of using Eq. (4.50) are even higher than those obtained in the analysis of HZ5-26-D data.

The quality of describing *I-U* curves of the irradiated SiPMs by a reference curve measured with a non-irradiated sensor is illustrated in Fig. 4.36. After correction of temperature effects on breakdown voltage and dark current, *I-U* data are in good agreement with the reference curve for over-voltages less than about 2 V. The current of irradiated sensors is normalised according to the values of $I_{\mathrm{expo}}(293\,\mathrm{K})$ and $I_{\mathrm{SRH}}(293\,\mathrm{K}) + I_{\mathrm{SRH2}}(293\,\mathrm{K})$ of array HZ5-26-B and HZ5-26-D, respectively, *cf.* Tab. 4.23 and 4.24. The similarity of *I-U* curves before and after irradiation is consistent with the observation of gain, PDE and cross-talk being hardly affected by the applied proton fluence, which has been discussed before.

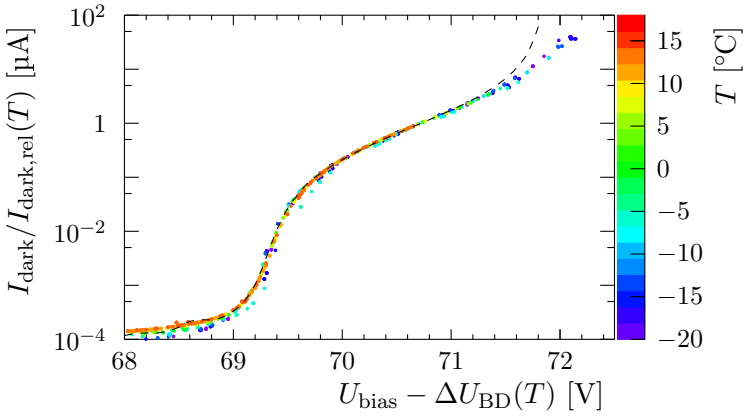

(a) HZ5-26-B

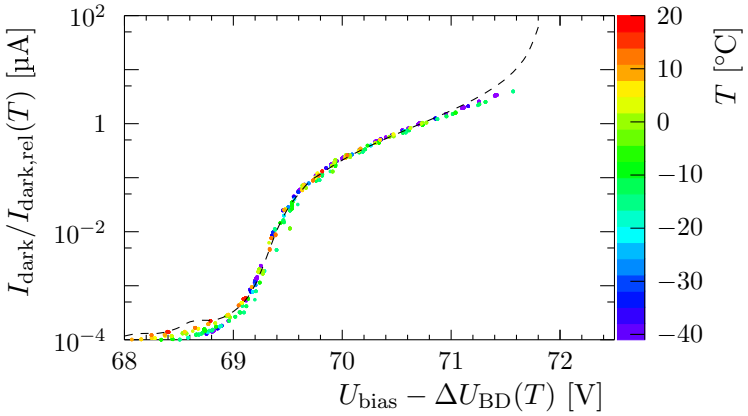

(b) HZ5-26-D

Figure 4.36: Example *I-U* curves normalised by radiation-induced multiplication of dark current and corrected for temperature dependence of breakdown voltage and carrier generation after Eq. (4.49). The radiation-induced dark current of HZ5-26-B and HZ5-26-D is described by Eq. (4.51) and (4.50), respectively, using parameters given in Tab. 4.24 and 4.23. The dashed line shows the current-voltage dependence of the non-irradiated sensor HZ5-7-A used as reference.

The temperature dependence of $I_{\mathrm{rad,rel}}$, which is given by the coefficient α_T in Tab. 4.24, is similar for all four proton-irradiated SiPM arrays. Though, it significantly differs from the temperature dependence of dark current before irradiation. The dark current of non-irradiated SiPMs decreases by about a factor of two per 8 K temperature reduction. After irradiation, a temperature decrease of about 10 K is needed to achieve the same factor.

The radiation-induced dark current per particle fluence at 293 K is computed by fitting a linear equation to data given in Tab. 4.24 and Tab. 4.20. The resulting proportionality factors are provided in Tab. 4.25. The damage per neutron-equivalent

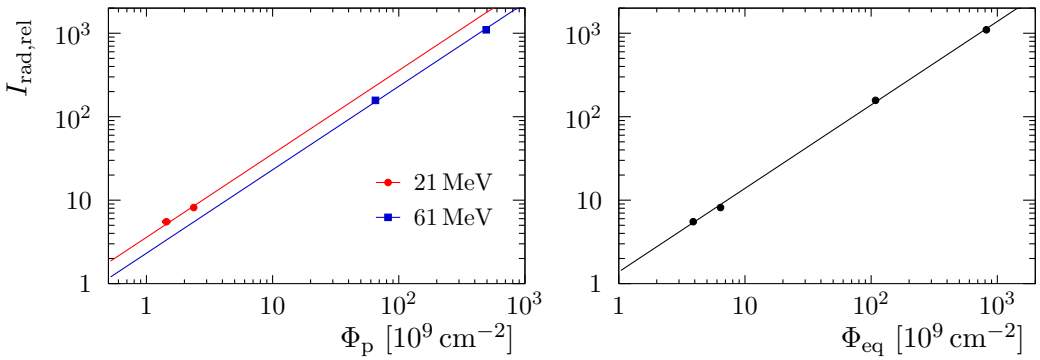

Figure 4.37: Radiation-induced relative dark current $I_{\mathrm{rad,rel}}$ *vs.* proton and 1 MeV-neutron-equivalent fluence, Φ_{p} and Φ_{eq}, at 293 K, 27 month after irradiation. Different proton energies are indicated by different markers and colours in the left plot.

Table 4.25: Radiation-induced relative dark current $I_{\mathrm{rad,rel}}$ per proton and 1 MeV-neutron-equivalent fluence, Φ_{p} and Φ_{eq}, at 293 K, 27 month after irradiation.

E_{p} [MeV]	$\frac{\Delta I_{\mathrm{rad,rel}}}{\Delta\Phi_{\mathrm{p}}}$ [10^{-9} cm^2]	$\frac{\Delta I_{\mathrm{rad,rel}}}{\Delta\Phi_{\mathrm{eq}}}$ [10^{-9} cm^2]
21.0	3.57 ± 0.14	1.32 ± 0.18
60.9	2.30 ± 0.04	1.38 ± 0.06
Weighted Mean		1.38 ± 0.06

fluence Φ_{eq} is consistent for the two applied proton energies, in accordance with the NIEL scaling hypothesis. Data points and the derived proportionality constants are visualised in Fig. 4.37.

The proportionality of radiation-induced current and neutron-equivalent fluence in combination with the fact, that no significant influence of the applied proton radiation on the SiPM characteristics, except for the magnitude of the dark current, has been observed, leads to the assumption that the measured current increase is proportional to the carrier generation rate of radiation-induced defects in the depletion layer of the SiPM pixels. Making this assumption, one can compute the radiation-induced primary carrier generation rate $r_{\mathrm{rad.\text{-}ind.\,gen.}}$ per pixel area A and fluence Φ_{eq} at 20 °C from numbers given in Tab. 4.11, 4.16 and 4.25.

$$\begin{aligned} \frac{r_{\mathrm{rad.\text{-}ind.\,gen.}}}{A\,\Phi_{\mathrm{eq}}} &= \left(\frac{r_{\mathrm{th.\,gen.}}}{A} \cdot I^{-1}_{\mathrm{dark,rel}}(293\,\mathrm{K})\right)_{\mathrm{HZ5\text{-}7\text{-}A}} \cdot \frac{\Delta I_{\mathrm{rad,rel}}}{\Delta\Phi_{\mathrm{eq}}} \\ &= (1.53 \pm 0.07) \cdot \frac{\mathrm{MHz}}{\mathrm{mm}^2} \cdot 10^{-9}\,\mathrm{cm}^2 \end{aligned} \tag{4.52}$$

4.6.2 In Situ Irradiation

SiPM arrays and single-channel SiPMs were installed in the LHCb cavern in the years 2011 and 2012, respectively, during detector operation in LHC Run 1. The *in situ* test of SiPMs was intended to facilitate the study of radiation damages and their annealing in a realistic environment. The tested Hamamatsu MPPC S11028-050 comprises a thermoelectric cooler which allowed to cool the SiPM to $-10\,^{\circ}\mathrm{C}$ during operation. Over-voltage was permanently applied to all tested SiPMs.

The SiPMs were mounted below the bottom support rail of the TT, *cf.* Sec. 2.2, Fig. 2.2, since an installation at the proposed location of the SciFi Tracker's photodetectors was not possible. The 1 MeV-neutron-equivalent fluence per proton-proton (pp) collision was about $8 \cdot 10^{-5}\,\mathrm{cm}^{-2}$ at the mounting point of the tested sensors [101]. This value has been obtained from FLUKA simulations and is by a factor of two lower than the neutron-equivalent fluence per collision expected at the SiPMs of the LHCb SciFi Tracker [71]. The uncertainty of FLUKA results is not precisely known, hence an explicit value is not provided by Ref. [101] and [71]. Instead, the references recommend to take a safety factor of two into account.

The number of pp collisions can be calculated from the delivered luminosity and the total cross-section of pp interactions σ_{tot}. The latter is obtained from Ref. [102], which quotes a value of 96.4 mb at centre-of-mass energy 7 TeV and 98.7 mb at 8 TeV. The given centre-of-mass energies are those provided by the LHC in the years 2011 and 2012, respectively. Table 4.26 lists the *in situ* irradiated sensors, the integrated luminosity $\int \mathcal{L}$ that has been delivered during their presence in the cavern, the corresponding number of pp collisions N_{coll} and the estimated neutron-equivalent fluence Φ_{eq}.

Signal Spectra

A characterisation of SiPM arrays HZ5-8-A and HZ5-8-D by means of test setup A has been performed before installation and about 17 months after removal from the LHCb cavern. The measurements were taken at a temperature of $23\,^{\circ}\mathrm{C}$ before and $-17\,^{\circ}\mathrm{C}$ after irradiation.

Table 4.26: *In situ* irradiated SiPMs, integrated luminosity delivered during their presence in the LHCb cavern, corresponding number of proton-proton collisions and estimated 1 MeV-neutron-equivalent fluence derived from FLUKA simulations [101].

Sensor	$\int \mathcal{L}$ [fb^{-1}]	$N_{\mathrm{coll}}[10^{14}]$	Φ_{eq} [10^9 cm^{-2}]
HZ5-8-A	1.219	1.175	9.40
HZ5-8-D	1.219	1.175	9.40
S10362-11-050U	2.132	2.104	16.8
S11028-050	2.132	2.104	16.8

Table 4.27: Parameter values of $U_{\mathrm{BD}}(0\,^{\circ}\mathrm{C})$ and U'_{BD} determining the breakdown voltage of *in situ* irradiated SiPMs according to Eq. (4.28).

Sensor	$U_{\mathrm{BD}}(0\,^{\circ}\mathrm{C})$ [V]	U'_{BD} [mV K^{-1}]
S11028-050	68.540 ± 0.006	57.0 ± 0.6
S10362-11-050U	68.230 ± 0.008	56.3 ± 1.0

The obtained values of gain G, mean number of detected photons μ_{phot} and cross-talk probability ϵ_{CT} are shown in Fig. 4.38. The mean photon number is normalised so that it corresponds to a value of 1 at 1.5 V over-voltage, as it is done with results from proton-irradiated sensors, *cf.* Sec. 4.6.1. The parameters G and μ_{phot} show the same dependence on U_{over} before and after the *in situ* irradiation test. The cross-talk probability measured 17 months after removal from the cavern is slightly lower than before irradiation.

The characterisation of single-channel SiPMs S10362-11-050U and S11028-050 described in Sec. 4.3 has been repeated after the *in situ* irradiation. Figure 4.39 shows the measured breakdown voltage as a function of temperature. Parameters obtained from fitting the linear function (4.28) to measured data are provided in Tab. 4.27. The results for $U_{\mathrm{BD}}(0\,^{\circ}\mathrm{C})$ and U'_{BD} agree with measurements before irradiation (see Tab. 4.4), if the measurement accuracy of the used Keithley SourceMeter of about ± 50 mV [103] is considered in addition to the statistical uncertainties derived from the fits, that are given in Tab. 4.4 and 4.27.

Figure 4.40 shows the mean number of detected photons per LED pulse and the cross-talk probability as function of relative over-voltage at several temperatures measured after irradiation. The data agree with those obtained before irradiation except for a decreased cross-talk probability of sensor S11028-050, compare Fig. 4.17.

The discrepancy of ϵ_{CT} before and after irradiation is contradictory to the sensor's *I-U* characteristic, which remained unaffected by the radiation except for an overall increase of dark current, compare Fig. 4.43. The parametrisation used to fit SiPM signal spectra could be a possible source of this inconsistency. The signal's baseline is shifted subsequent to pixel breakdowns occurring at high frequency, compare Fig. 4.49. The probability of sampling a signal at shifted baseline increases with dark count rate and thus with radiation damage. The effect is visible as a tail of signal peaks to lower pulse integrals in Fig. 4.41. An exponentially modified Gaussian distribution is used to describe these signals, *cf.* Sec. 4.3. However, fitting this parametrisation to data shown in Fig. 4.41 reveals inaccuracies in the reproduction of the measured signal spectrum. The width of signal peaks is partially overestimated, their maximum is underestimated. While the determination of SiPM gain is hardly affected by this inaccuracy, the derived value of cross-talk probability ϵ_{CT} is sensitive to the correct attribution of measured signals to the number of G-APD pixels having fired and thus to an accurate parametrisation of signal distributions.

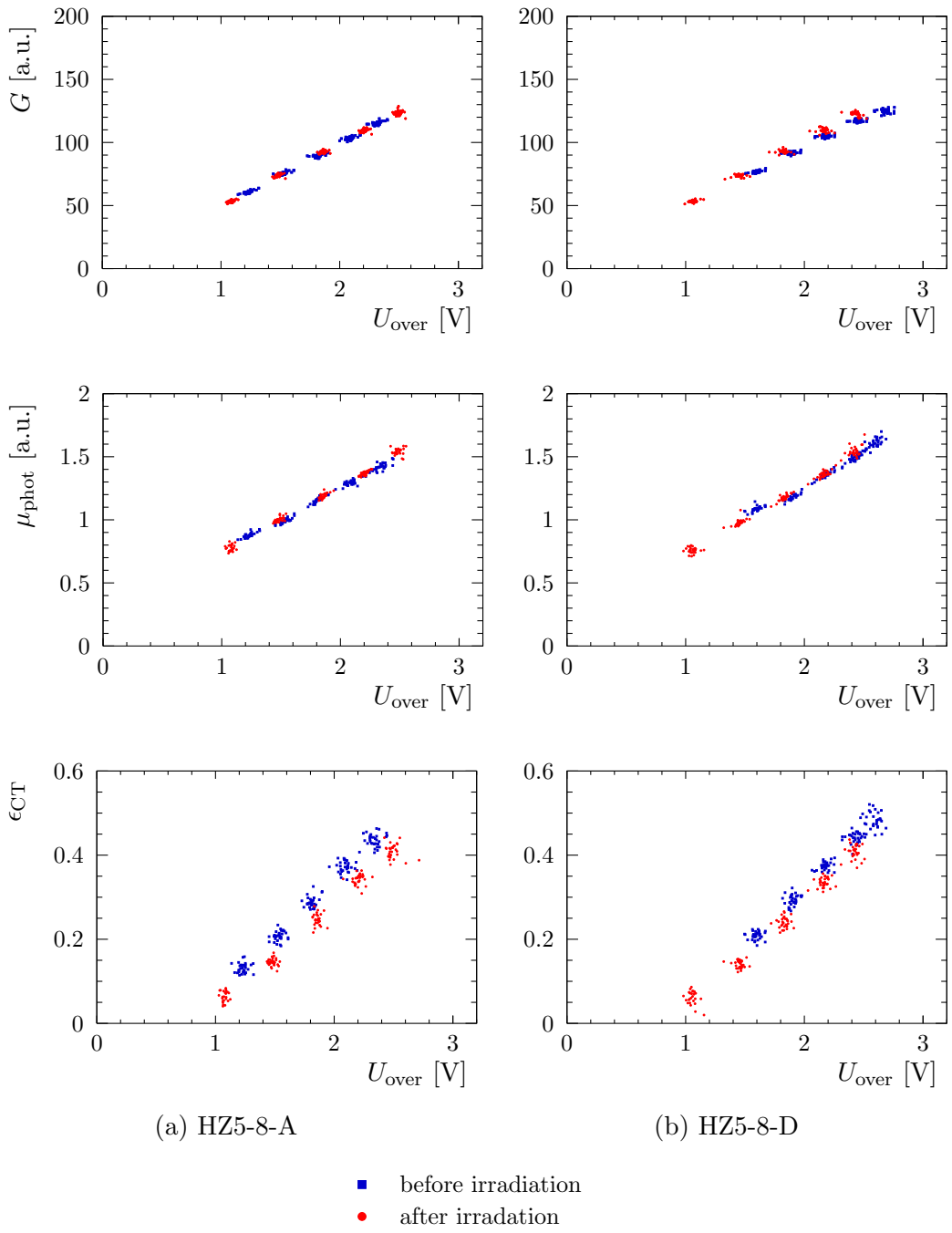

(a) HZ5-8-A (b) HZ5-8-D

Figure 4.38: Gain G, mean number of detected photons per LED pulse μ_{phot} (normalised) and cross-talk probability ϵ_{CT} as a function of over-voltage U_{over}. Data points are obtained from signal spectra of individual channels of the respective SiPM array.

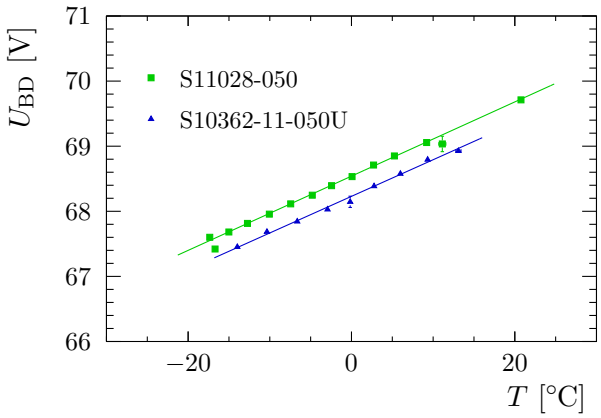

Figure 4.39: Dependence of breakdown voltage U_{BD} on temperature T after irradiation.

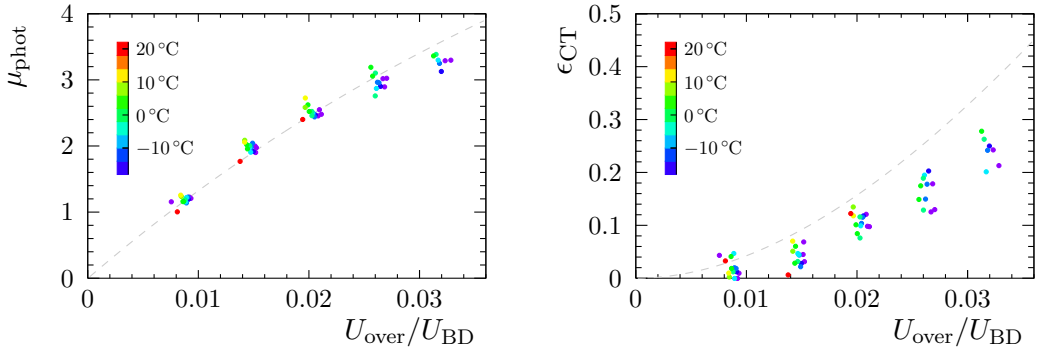

(a) S11028-050

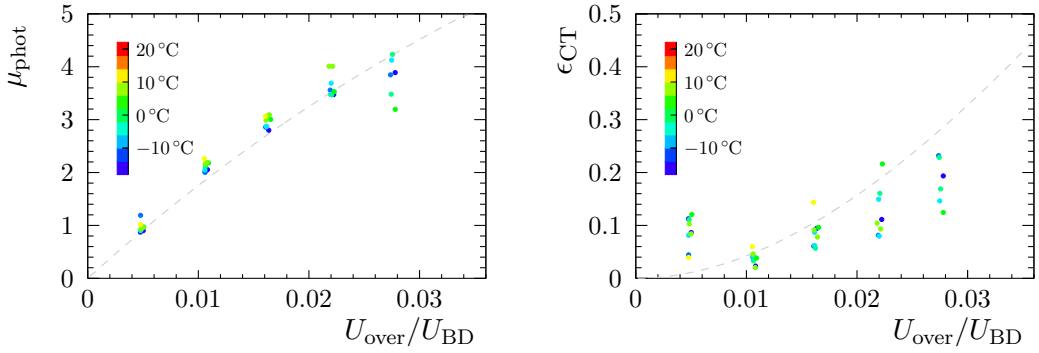

(b) S10362-11-050U

Figure 4.40: Mean number of detected photons per LED pulse μ_{phot} and cross-talk probability ϵ_{CT} of sensors S11028-050 and S10362-11-050U measured with setup B at several temperatures after irradiation. Dashed lines indicate the corresponding curves obtained for non-irradiated sensor HZ5-7-A with test setup A. Compare Fig. 4.17.

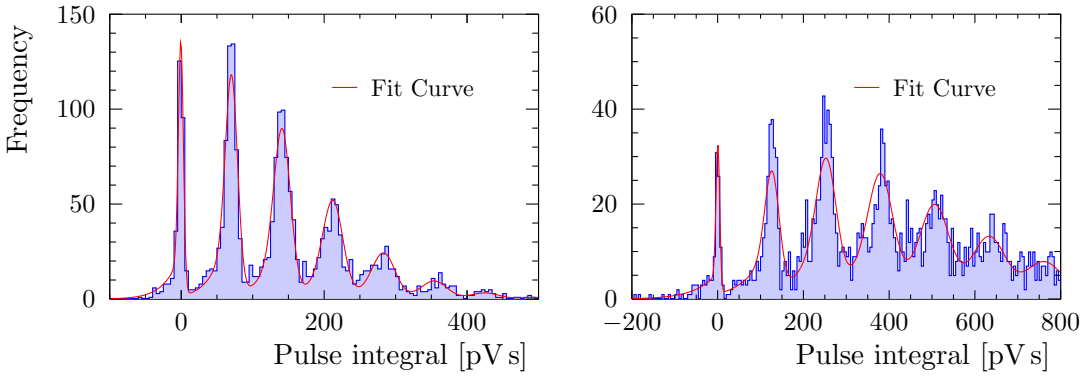

Figure 4.41: SiPM signal spectra of S11028-050 measured with test setup B at over-voltages 1.03 V (left) and 1.83 V (right) after irradiation. The ambient temperature during measurement is −17.3 °C.

I-U Characteristic

During their presence in the LHCb cavern, the tested SiPM arrays and single-channel sensors were connected to test setups C and D, see Sec. 4.2.2. Besides application of bias voltage, these setups allowed the execution of *I-U* scans, which were repeated once per hour. Thus, the change of breakdown voltage ΔU_{BD} and the dark current $I_{\mathrm{dark,rel}}$ relative to reference *I-U* curves, that were measured before irradiation, could be observed *in situ* by fitting the reference curves to the acquired data as described by Eq. (4.41) in Sec. 4.5.

The dependence of ΔU_{BD} and $I_{\mathrm{dark,rel}}$ on temperature has been studied before installation and after removal from the LHCb cavern. Additionally, the thermoelectric cooler of MPPC S11028-050 enabled temperature scans of this particular sensor *in situ*, which were executed during technical stops of the LHC. Arrows and Roman numerals in Fig.4.45, 4.46 and 4.47 indicate the dates, at which the temperature dependence of *I-U* characteristics was measured. The obtained values of ΔU_{BD} and $I_{\mathrm{dark,rel}}$ are visualised in Fig. 4.42.

The values of ΔU_{BD} are independent of radiation level and annealing time. Fitting linear function (4.44) to measured data leads to parameters given in Tab. 4.28. For each tested SiPM, the results are consistent within their uncertainties.

The relative dark current $I_{\mathrm{dark,rel}}$ is described by Eq. (4.49). In this equation, the dark current before irradiation, $I_{\mathrm{init,rel}}(T)$, is taken into account as it is given for the respective SiPM in Sec. 4.5. Since the temperature dependence of SiPM array HZ5-8-A has not been determined before installation in the LHCb cavern, parameters of HZ5-7-A are used for this sensor. Equation (4.51) is used to parametrise the radiation-induced current $I_{\mathrm{rad,rel}}(T)$. Results from fitting Eq. (4.49) to data of $I_{\mathrm{dark,rel}}$ are provided in Tab. 4.29.

The coefficients α_{T} show a variation that is larger than given by their uncertainty estimates. It is not clear, if this variation is due to systematic errors or a result of diverse radiation-induced defects that are contributing to the dark current with different temperature dependences and annealing rates.

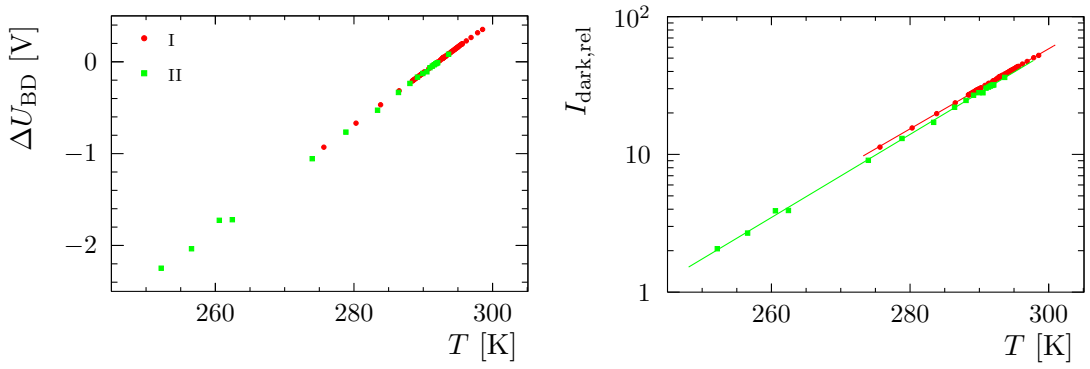

(a) HZ5-8-A

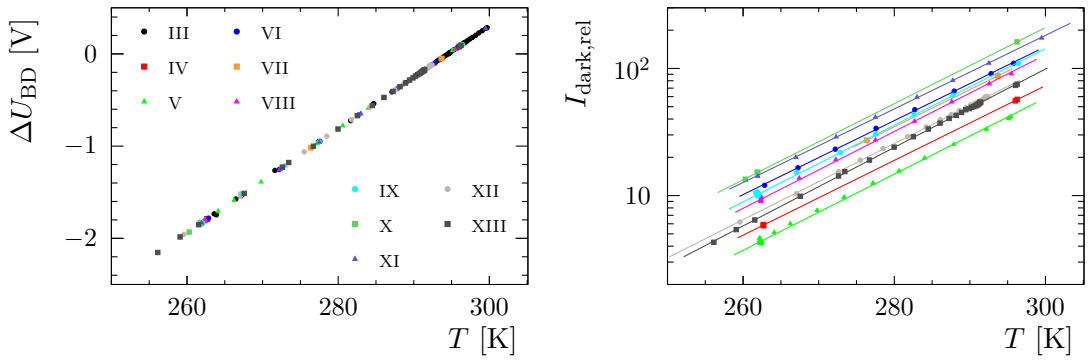

(b) S11028-050

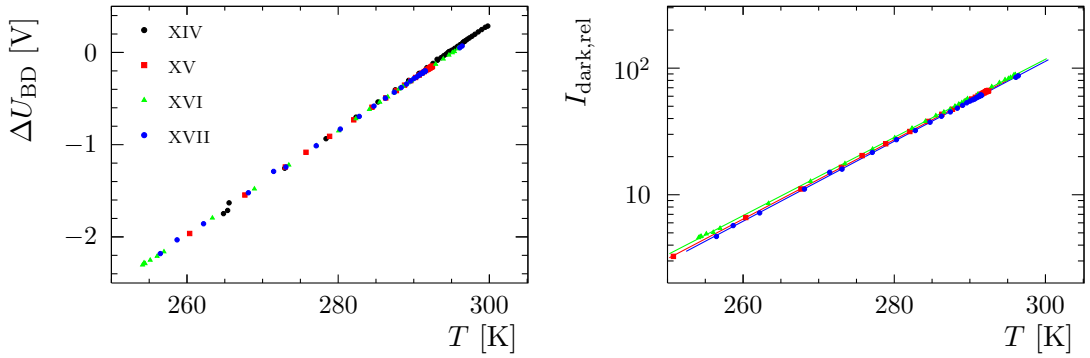

(c) S10362-11-050U

Figure 4.42: Change of breakdown voltage ΔU_{BD} and relative dark current $I_{\mathrm{dark,rel}}$ as functions of temperature T.

Table 4.28: Parameter results from fitting Eq. (4.44) to data shown in Fig. 4.42.

Measurement	$\Delta U_{\mathrm{BD}}(273.15\,\mathrm{K})$ [V]	U'_{BD} [mV K^{-1}]
HZ5-8-A		
I	-1.068 ± 0.007	56.23 ± 0.38
II	-1.081 ± 0.005	56.57 ± 0.35
S11028-050		
III	-1.197 ± 0.004	55.99 ± 0.21
IV	-1.201 ± 0.005	56.09 ± 0.29
V	-1.1984 ± 0.0020	56.21 ± 0.18
VI	-1.200 ± 0.005	56.13 ± 0.36
VII	-1.197 ± 0.010	55.85 ± 0.65
VIII	-1.2024 ± 0.0029	56.22 ± 0.24
IX	-1.2015 ± 0.0026	56.30 ± 0.23
X	-1.206 ± 0.005	56.23 ± 0.37
XI	-1.202 ± 0.005	56.11 ± 0.33
XII	-1.1939 ± 0.0034	55.83 ± 0.21
XIII	-1.1986 ± 0.0032	56.03 ± 0.20
S10362-11-050U		
XIV	-1.237 ± 0.006	57.62 ± 0.28
XV	-1.238 ± 0.004	56.50 ± 0.22
XVI	-1.2372 ± 0.0024	56.32 ± 0.14
XVII	-1.2337 ± 0.0032	56.22 ± 0.20

The exemplary plots in Fig. 4.43 show that *I-U* curves measured at different temperatures are in good agreement after normalisation according to the parameters given in Tab. 4.28 and Tab. 4.29. The normalised curves are furthermore consistent with the *I-U* characteristic obtained before irradiation.

Figure 4.44 shows the relative dark current of SiPMs S11028-050 and S10362-11-050U in the course of LHC operation in 2012. The dark current of S11028-050 is significantly reduced compared to S10362-11-050U by cooling down to $-10\,^{\circ}\mathrm{C}$. However, it exceeds the current of S10362-11-050U when the cooling is switched off in technical stops. This excess is due to decelerated annealing of radiation damages at lower temperatures. Annealing effects also have to be considered when describing $I_{\mathrm{rad,rel}}$ of non-cooled SiPMs HZ5-8-A and S10362-11-050U as a function of time.

The following approach is chosen to determine the dependence of radiation-induced dark current on the number of *pp* collisions N_{coll} and time t. The current $I_{\mathrm{rad,rel}}$ is described by a sum of currents I_i, each representing a damage with individual annealing time constant τ_i. The change of I_i per time is given by its increase per *pp* collision $\frac{\Delta I_i}{\Delta N_{\mathrm{coll}}}$, the collisions per time, which are calculated from the luminosity $\mathcal{L}$ and the total *pp* cross-section σ_{tot}, and its annealing according to an exponential

Table 4.29: Parameters obtained from fitting Eq. (4.49) with $I_{\mathrm{rad,rel}}(T)$ being described by Eq. (4.51) to data shown in Fig. 4.42.

Measurement	$I_{\mathrm{expo}}(293\,\mathrm{K})$	α_T $[10^{-3}\,\mathrm{K}^{-1}]$
HZ5-8-A		
I	35.99 ± 0.06	66.5 ± 0.5
II	33.82 ± 0.26	69.0 ± 0.5
S11028-050		
III	-0.07 ± 0.19	0.1 ± 0.5
IV	46.0 ± 0.4	67.7 ± 0.4
V	36.24 ± 0.23	68.89 ± 0.23
VI	94.9 ± 0.7	67.1 ± 0.4
VII	85.1 ± 0.8	67.5 ± 0.8
VIII	80.3 ± 0.6	69.67 ± 0.30
IX	90.0 ± 0.8	69.55 ± 0.29
X	132.8 ± 1.7	69.1 ± 0.5
XI	117.0 ± 0.8	66.8 ± 0.4
XII	63.84 ± 0.21	69.06 ± 0.27
XIII	61.18 ± 0.21	71.19 ± 0.27
S10362-11-050U		
XIV	$(3 \pm 20) \cdot 10^{-5}$	-140 ± 230
XV	69.42 ± 0.24	71.97 ± 0.28
XVI	71.38 ± 0.25	70.91 ± 0.19
XVII	67.97 ± 0.24	72.55 ± 0.27

function with the mentioned time constant.

$$I_{\mathrm{rad(,rel)}} = \sum_{i=0}^{5} I_i \tag{4.53}$$

with

$$\frac{\mathrm{d}I_i}{\mathrm{d}t} = \frac{\Delta I_i}{\Delta N_{\mathrm{coll}}} \cdot \mathcal{L}(t) \cdot \sigma_{\mathrm{tot}} - \frac{1}{\tau_i} \cdot I_i \tag{4.54}$$

Due to the luminosity levelling at the *pp* interaction point of the LHCb experiment, see Sec. 2.2, the luminosity $\mathcal{L}(t)$ can be approximated by a constant for the duration of an LHC fill. Thus, the current $I_i(t)$ resulting from *pp* collisions of a single LHC fill is given by

$$I_i(t) = \begin{cases} 0 & \text{if } t \leq t_{\mathrm{s}}, \\ \frac{\Delta I_i}{\Delta N_{\mathrm{coll}}}\,\mathcal{L}\,\sigma_{\mathrm{tot}}\,\tau_i\,\left(1 - \exp\left(-\frac{t-t_{\mathrm{s}}}{\tau_i}\right)\right) & \text{if } t_{\mathrm{s}} < t \leq t_{\mathrm{e}}, \\ \frac{\Delta I_i}{\Delta N_{\mathrm{coll}}}\,\mathcal{L}\,\sigma_{\mathrm{tot}}\,\tau_i\,\left(1 - \exp\left(-\frac{t_{\mathrm{e}}-t_{\mathrm{s}}}{\tau_i}\right)\right)\,\exp\left(-\frac{t-t_{\mathrm{e}}}{\tau_i}\right) & \text{if } t_{\mathrm{e}} < t, \end{cases} \tag{4.55}$$

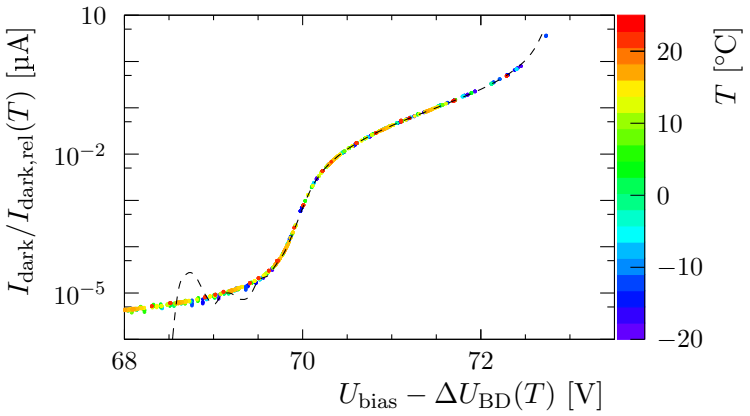

(a) S11028-050

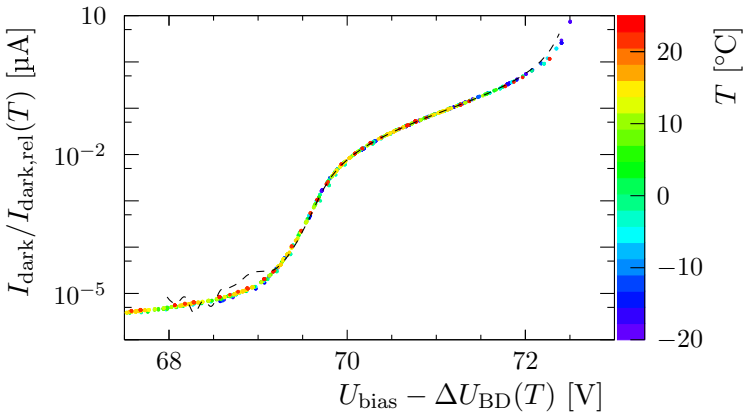

(b) S10362-11-050U

Figure 4.43: Example *I-U* curves normalised by radiation-induced multiplication of dark current and corrected for temperature dependence of breakdown voltage and carrier generation according to Eq. (4.49). The radiation-induced dark current is described by (4.51) using parameters given in Tab. 4.29. Presented data are from measurements XIII and XVII. The dashed line shows the current-voltage dependence before irradiation used as reference.

with t_s and t_e being the start and end time of the fill. The total radiation-induced dark current is then given by the sum of currents from all fills during which the SiPM was installed in the LHCb cavern.

Annealing times τ_i are taken from Ref. [104] and listed in Tab. 4.30. According to the value of τ_0, the component I_0 represents the non-annealing fraction of radiation-induced current. Time constants given in Ref. [104] are determined at room temperature. However, annealing rates are strongly temperature dependent. This effect can be included by a scaling factor according to Ref. [105]

$$\Theta(T) = \exp\left(\frac{E_\text{I}}{k_\text{B}}\left(\frac{1}{293.15\,\text{K}} - \frac{1}{T}\right)\right) \quad , \tag{4.56}$$

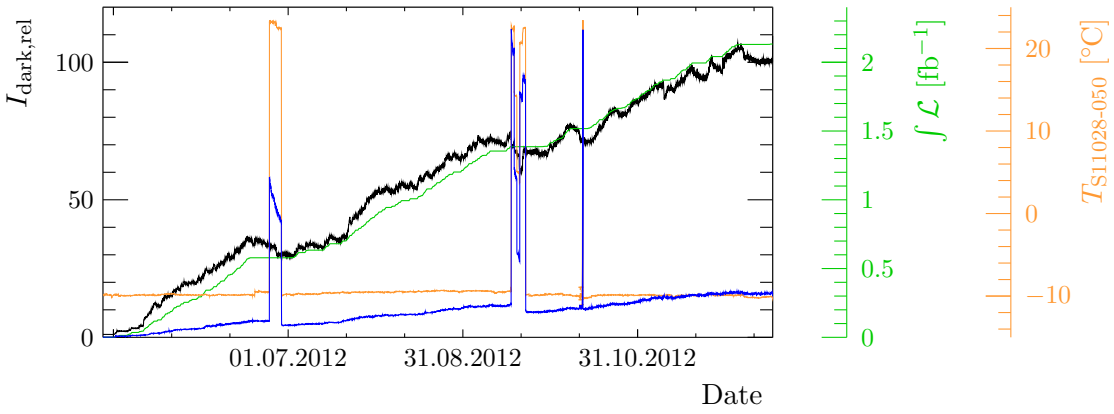

Figure 4.44: Relative dark current $I_{\mathrm{dark,rel}}$ of SiPMs S11028-050 (blue) and S10362-11-050U (black), integrated luminosity $\int \mathcal{L}$ (green) and temperature $T_{\mathrm{S11028\text{-}050}}$ of sensor S11028-050 (orange) in the course of LHC operation in 2012.

Table 4.30: Annealing time constants for not type inverted silicon detectors at room temperature, taken from Ref. [104].

τ_0	τ_1	τ_2	τ_3	τ_4	τ_5	Unit
∞	$5.34 \cdot 10^6$	$8.85 \cdot 10^5$	$6.54 \cdot 10^4$	$7.14 \cdot 10^3$	$1.07 \cdot 10^3$	s

which increases the time constants τ_i, if the temperature is lowered. The activation energy E_{I} quoted in Ref. [105] and [106] is $(1.09 \pm 0.14)\,\mathrm{eV}$ and $(1.11 \pm 0.05)\,\mathrm{eV}$, respectively. Therefore, a value of 1.1 eV is used to describe the temperature dependence of annealing rates of the irradiated SiPMs.

The described model of radiation-induced dark current and its annealing is fitted to the data from *in situ* irradiated SiPMs shown in Fig. 4.45, 4.46 and 4.47. The $I_{\mathrm{rad,rel}}$ data are obtained by subtraction of the initial dark current $I_{\mathrm{init,rel}}(T)$ from the measured value of $I_{\mathrm{dark,rel}}$. The result is scaled to a value equivalent to 20 °C by means of Eq. (4.51). In this calculation, the coefficient α_T is set to $69 \cdot 10^{-3}\,\mathrm{K}^{-1}$ with an uncertainty estimate of $\pm 2 \cdot 10^{-3}\,\mathrm{K}^{-1}$ being considered, which takes into account the variation of measured values in Tab. 4.29. This uncertainty in temperature scaling is the source of relatively large errors estimates for data from SiPM S11028-050, that are obtained at low temperatures, see Fig. 4.46.

The temperatures of sensors HZ5-8-A and S10362-11-050U are derived from the measured shift of breakdown voltage ΔU_{BD}, which is not affected by the radiation. The temperature of S11028-050 is determined by means of the thermistor included in the device, compare test setup D, Fig. 4.6. While the scaling of $I_{\mathrm{rad,rel}}$ by Eq. (4.51) is done using the respective measured temperature T, the scaling factor $\Theta(T)$ of annealing rates is calculated with T being approximated by step functions. The used approximation of T is shown by an orange line in Fig. 4.45 to 4.47.

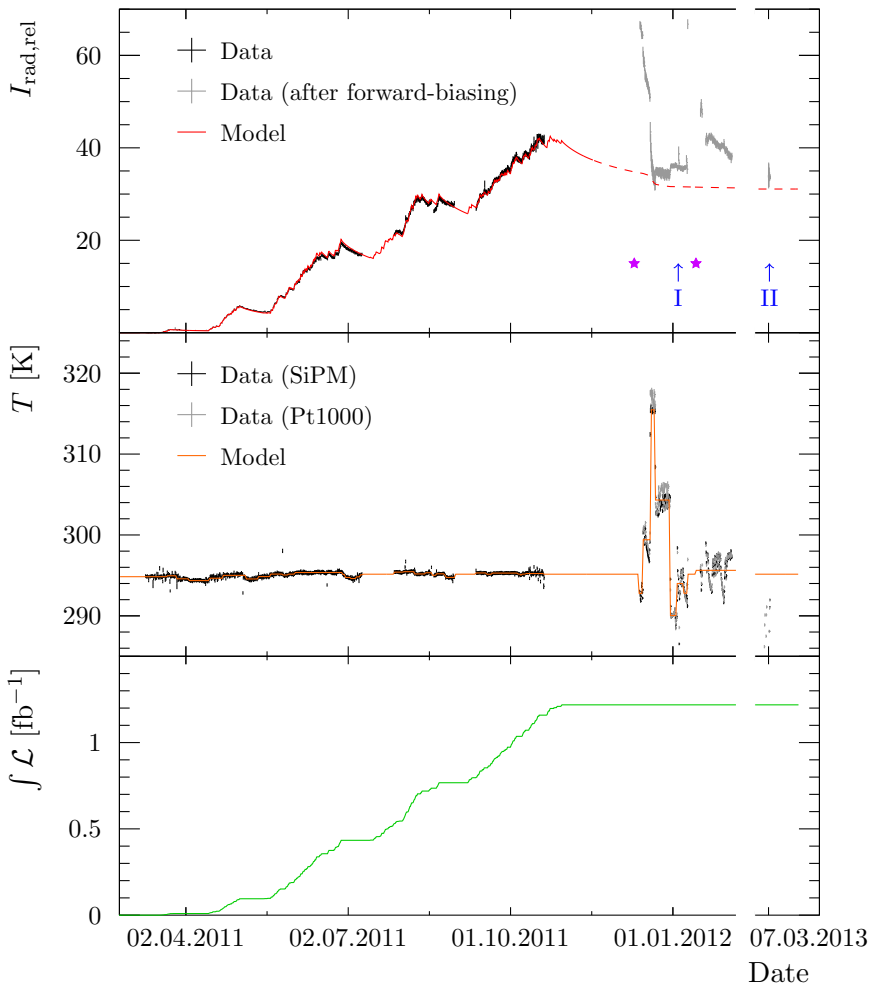

Figure 4.45: Radiation-induced relative dark current $I_{\mathrm{rad,rel}}$ of SiPM HZ5-8-A, sensor temperature T and integrated delivered luminosity $\int \mathcal{L}$ as functions of time. The dark current is scaled to values equivalent to 20 °C. Violet stars identify the dates of forward bias application. Arrows and Roman numerals indicate measurements of I-U curves as function of T. In addition to temperatures derived from the shift of U_{BD}, temperatures measured by means of a Pt1000 element are shown in grey colour in the mid plot.

In the case of HZ5-8-A, the fit range is restricted to times before removal of the SiPM from the cavern. The extrapolation of the fit curve beyond this range is indicated by a dashed line in Fig. 4.45. After removal from the LHCb cavern and transport to the laboratory, the channels of SiPM array HZ5-8-A were tested under forward bias voltage. Subsequently, a significantly increased dark current was measured, which is identified by grey colour in Fig. 4.45. After a period of annealing, a second application of forward bias voltage increased the leakage current once again. This observation leads to the assumption that forward bias possibly enhances the damaging effect of radiation or restores already annealed defects.

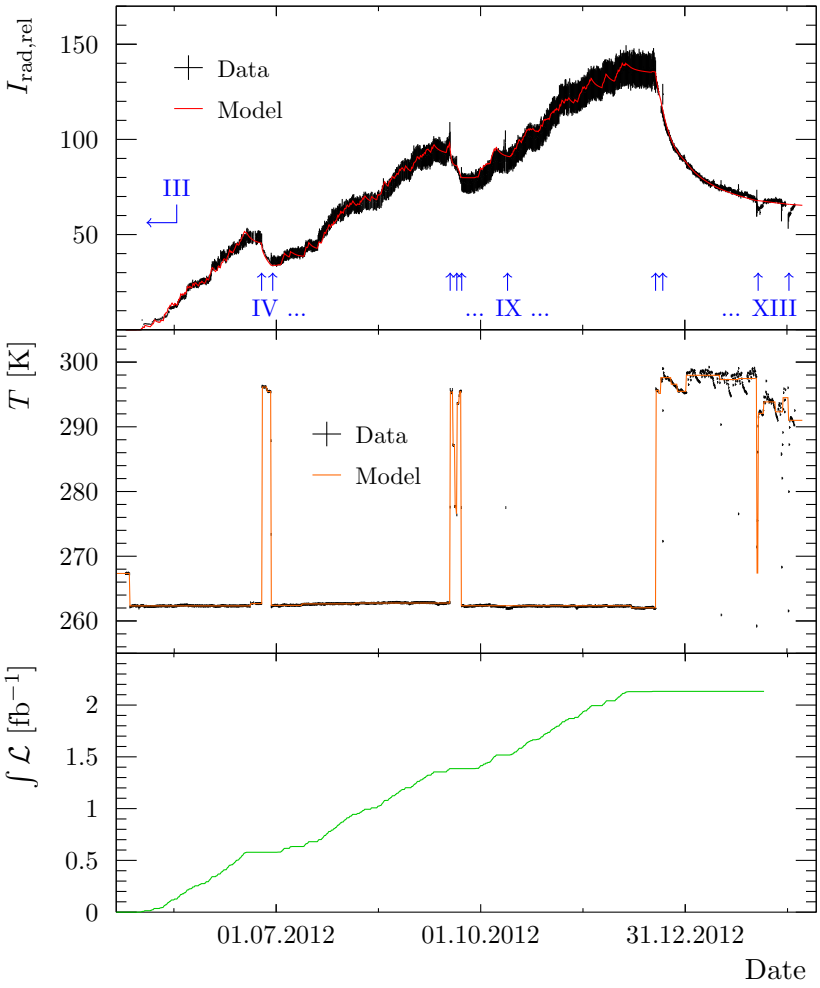

Figure 4.46: Radiation-induced relative dark current $I_{\mathrm{rad,rel}}$ of SiPM S11028-050, sensor temperature T and integrated delivered luminosity $\int \mathcal{L}$ as functions of time. The dark current is scaled to values equivalent to 20 °C. Arrows and Roman numerals indicate measurements of I-U curves as function of T.

Fit results for $\frac{\Delta I_i}{\Delta N_{\mathrm{coll}}}$ are provided in Tab. 4.31. The component $\frac{\Delta I_5}{\Delta N_{\mathrm{coll}}}$ is only taken into account when fitting data of S11028-050, since τ_5 is less than 20 min at room temperature, whereas I-U curves are sampled only once per hour.

The parameters $\frac{\Delta I_i}{\Delta N_{\mathrm{coll}}}$ are a measure of radiation-induced dark current relative to the respective I-U curve used as reference. The equivalent increase of radiation-induced primary carrier generation rate per neutron-equivalent fluence and active sensor area, $\frac{\Delta r_i}{\Delta \Phi_{\mathrm{eq}}} A^{-1}$, can be calculated according to Eq. (4.52) using parameters given in Tab. 4.11 and 4.16. The neutron-equivalent fluence per pp collision is obtained from FLUKA simulations as quoted at the beginning of this section. The calculated values of rate increase per fluence and area are provided in Tab. 4.32.

Numbers given in Tab. 4.32 reveal variations of parameter results for the different sensors that are large compared to the provided uncertainty estimates. These

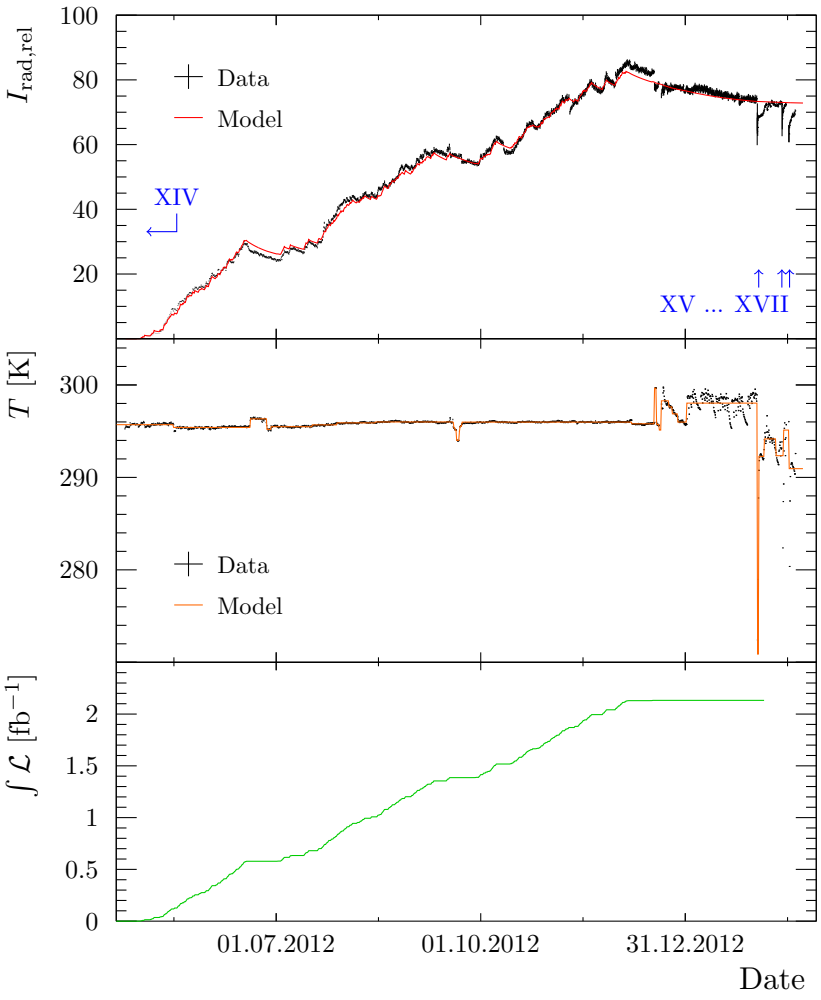

Figure 4.47: Radiation-induced relative dark current $I_{\mathrm{rad,rel}}$ of SiPM S10362-11-050U, sensor temperature T and integrated delivered luminosity $\int \mathcal{L}$ as functions of time. The dark current is scaled to values equivalent to 20 °C. Arrows and Roman numerals indicate measurements of I-U curves as function of T.

estimates comprise uncertainties derived from fitting I-U curves, the temperature scaling of $I_{\mathrm{rad,rel}}$ and fitting the discussed model of radiation damage to values of $I_{\mathrm{rad,rel}}$, as well as uncertainties given in Tab. 4.11 and 4.16. Possible sources of not included systematic uncertainties are the luminosity $\mathcal{L}$, the annealing time constants τ_i and the activation energy of annealing rates E_{I}, which could vary for different annealing processes.

The description of radiation-induced dark current by Eq. (4.53) and (4.54) is equivalent to contributions from independent defect types, each annealing at specific rate τ_i^{-1} in a single-step first order process. However, the used formulae should only be seen as an empirical parametrisation of observed leakage currents instead of being the description of a physical model, since the background of annealing mechanisms is still not understood [106]. The possible relevance of annealing processes of higher

Table 4.31: Fit results for components $\frac{\Delta I_i}{\Delta N_{\text{coll}}}$ of radiation-induced current increase per *pp* collision at 20 °C, relative to the corresponding reference *I-U* curve of the non-irradiated sensor.

Sensor	$\frac{\Delta I_0}{\Delta N_{\text{coll}}}$	$\frac{\Delta I_1}{\Delta N_{\text{coll}}}$	$\frac{\Delta I_2}{\Delta N_{\text{coll}}}$	Unit
HZ5-8-A	2.646 ± 0.006	2.876 ± 0.022	2.99 ± 0.05	10^{-13}
S11028-050	2.775 ± 0.006	1.862 ± 0.016	2.755 ± 0.023	
S10362-11-050U	3.400 ± 0.006	2.391 ± 0.029	1.40 ± 0.08	

Sensor	$\frac{\Delta I_3}{\Delta N_{\text{coll}}}$	$\frac{\Delta I_4}{\Delta N_{\text{coll}}}$	$\frac{\Delta I_5}{\Delta N_{\text{coll}}}$	Unit
HZ5-8-A	1.71 ± 0.26	4.3 ± 1.2	—	10^{-13}
S11028-050	0.30 ± 0.07	1.72 ± 0.19	11.4 ± 0.4	
S10362-11-050U	0.2 ± 0.5	1.5 ± 1.8	—	

Table 4.32: Components $\frac{\Delta r_i}{\Delta \Phi_{\text{eq}}} A^{-1}$ of the radiation-induced primary carrier generation rate per neutron-equivalent fluence and pixel area at 20 °C, calculated from fit results in Tab. 4.31.

Sensor	$\frac{\Delta r_0}{\Delta \Phi_{\text{eq}}} A^{-1}$	$\frac{\Delta r_1}{\Delta \Phi_{\text{eq}}} A^{-1}$	$\frac{\Delta r_2}{\Delta \Phi_{\text{eq}}} A^{-1}$	Unit
HZ5-8-A	3.67 ± 0.05	3.99 ± 0.06	4.15 ± 0.09	$\frac{\text{MHz}}{10^9\,\text{cm}^{-2}\cdot\text{mm}^2}$
S11028-050	3.61 ± 0.05	2.422 ± 0.032	3.58 ± 0.05	
S10362-11-050U	4.48 ± 0.05	3.15 ± 0.05	1.85 ± 0.11	

Sensor	$\frac{\Delta r_3}{\Delta \Phi_{\text{eq}}} A^{-1}$	$\frac{\Delta r_4}{\Delta \Phi_{\text{eq}}} A^{-1}$	$\frac{\Delta r_5}{\Delta \Phi_{\text{eq}}} A^{-1}$	Unit
HZ5-8-A	2.4 ± 0.4	5.9 ± 1.6	—	$\frac{\text{MHz}}{10^9\,\text{cm}^{-2}\cdot\text{mm}^2}$
S11028-050	0.39 ± 0.09	2.24 ± 0.25	14.9 ± 0.5	
S10362-11-050U	0.3 ± 0.6	2.0 ± 2.4	—	

order and via multiple steps could be a cause for the inconsistent results when using the described parametrisation.

Relative amplitudes of leakage current components with certain annealing time, which are determined by the *in situ* irradiations of SiPMs, are different from those quoted in Ref. [104]. This observation might hint at an influence of defects additional to those, which are relevant for the radiation-induced dark current in silicon detectors operated below their breakdown voltage. A further hint is the different current–temperature dependence. For irradiated silicon detectors operated below breakdown, the dependence can be described by Eq. (4.46) according to SRH statistics with an effective band gap $E_{\text{A,SRH}}$ similar to that of non-irradiated silicon, see Ref. [107, 108]. The dark current of irradiated SiPMs shows a significantly smaller change with temperature, compare Eq. (4.50),(4.51) and Tab. 4.23,4.24,4.29.

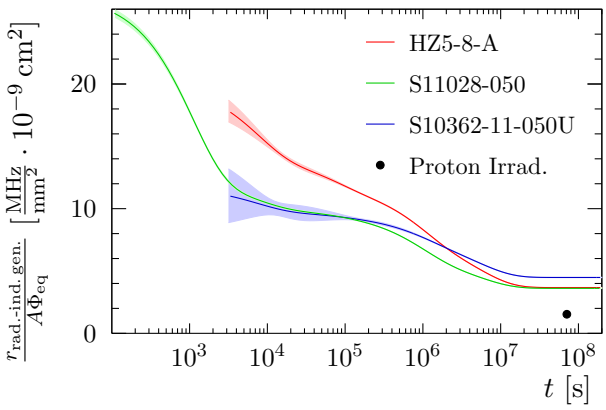

Figure 4.48: Annealing of the radiation-induced primary carrier generation per pixel area and neutron-equivalent fluence.

Figure 4.48 illustrates the decrease of radiation-induced carrier generation at 20 °C as obtained from the *in situ* irradiations. The curves show the annealing of a damage induced by an irradiation at time $t = 0$. If the 1 MeV-neutron-equivalent fluence Φ_{eq} is accumulated within a duration t_{irrad} that is short compared to the considered annealing time constants, the following approximation can be made, which is used in the plot.

$$\frac{r_{\text{rad.-ind. gen.}}}{A\,\Phi_{\text{eq}}}(t) \approx \sum_{i=0}^{5} \frac{\Delta r_i}{\Delta\Phi_{\text{eq}}}\, A^{-1}\, \exp\left(-\frac{t}{\tau_i}\right) \tag{4.57}$$

The figure also shows the value of $r_{\text{rad.-ind. gen.}}/(A\,\Phi_{\text{eq}})$ obtained from proton irradiations of SiPM arrays, *cf.* Sec. 4.6.1. It is by more than a factor two lower than the rates at equivalent time derived from the *in situ* tests. Possible reasons for this discrepancy are discussed in the following.

The particle flux of the proton irradiations has been many orders of magnitude higher than *in situ*. The resulting high defect concentrations could affect the annealing in the case of processes of higher than first order. Also a mixture of diverse particles and energies is present in the LHCb cavern in contrast to the mono-energetic protons used for irradiations at CAL and MLL. Of course, an influence of these irradiation conditions on the resulting damage would imply a deviation from the NIEL scaling hypothesis.

Reference [106] states a long-term annealing of radiation-induced leakage current instead of the non-annealing component quoted by Ref. [104], which is considered here. However, no clear evidence for such a long-term annealing is found in the data of *in situ* irradiated SiPMs.

An underestimation of the neutron-equivalent fluence occurring at the mounting point of tested SiPMs in the LHCb cavern could be a further explanation for the discrepancy of results from proton and *in situ* irradiations. In this case, it has to be

considered that fluence estimates for the upgraded LHCb detector could be too low as well.

It is concluded that results from the *in situ* irradiations should be used to achieve a conservative estimate of the radiation-induced dark count rate of SiPMs used in the LHCb SciFi Tracker, rather than results from the proton irradiations. The dark count rate in a single SiPM channel resulting from a neutron-equivalent fluence of $8 \cdot 10^{11}\,\mathrm{cm}^{-2}$, according to the full data taking period of the upgraded LHCb detector [71], is thus estimated to be about 345 MHz at 20 °C. [3] It is calculated by means of Eq. (4.29), with $r_{\mathrm{th.\,gen.}}$ being derived from the maximum value of $\frac{\Delta r_0}{\Delta \Phi_{\mathrm{eq}}} A^{-1}$ in Tab. 4.32, which is about $4.5 \cdot 10^{-9}\,\mathrm{MHz\,mm^{-2}\,cm^2}$. The sensitive area A of the SiPM channel is considered to be the same as in the Hamamatsu MPPC 5883, see Tab. 4.1. Values of 0.3 and 0.2 are used for $\varepsilon_{\mathrm{BD,dark}}$ and ϵ_{AP} according to an over-voltage of 1.5 V, see Sec. 4.3 and 4.4.

SiPMs in the LHCb SciFi Tracker will be cooled to −40 °C to reduce the high dark count rate and thus diminish the frequency of fake hits [23]. Heating the photo-sensors to 40 °C during shutdown periods is proposed to allow annealing processes. Therefore, only the non-annealing damage is considered in the provided dark count rate estimate.

Dark Count Rate

In the previous paragraphs, the increase of SiPM dark current resulting from irradiation has been solely ascribed to an increase of the dark count rate. This has been motivated by the fact that no significant changes of gain, PDE, cross-talk and *I-U* characteristic are observed. The dark count rate of SiPM S11028-050 has been measured after *in situ* irradiation to verify this conclusion.

Figure 4.49 shows a typical waveform of the irradiated SiPM measured with test setup B, *cf.* Sec. 4.2.2. The signal's baseline is shifted subsequent to diode breakdowns occurring at high frequency. This effect deteriorates the measurement of dark count rates, which is done by measuring the frequency of exceeding a certain threshold level. Furthermore, simultaneous dark pulses cannot be distinguished by this method. Therefore, only measurements at less than −6 °C are taken into account in this study.

The measured data are analysed in the same way as described in Sec. 4.4. Figure 4.50 shows the measured dark count rate r_{dark}, the thermal breakdown rate $r_{\mathrm{th.\,BD}}$ and the after-pulse probability ϵ_{AP} measured at several temperatures and over-voltages. A curve according to Eq. (4.31) is fitted to data of ϵ_{AP}. The value of α'_{AP} is the only free parameter in this fit. Other parameters occurring in Eq. (4.31) are fixed to values obtained before irradiation, since a significant radiation effect on cross-talk and breakdown efficiency has not been observed. The resulting value of α'_{AP} is 18.9 ± 1.3, which is consistent with the measurement before irradiation, see

[3] A value of 250 MHz is quoted in the TDR (Ref. [23]), since a different parametrisation of the radiation damage and a different fluence estimate were taken into account when the report was written.

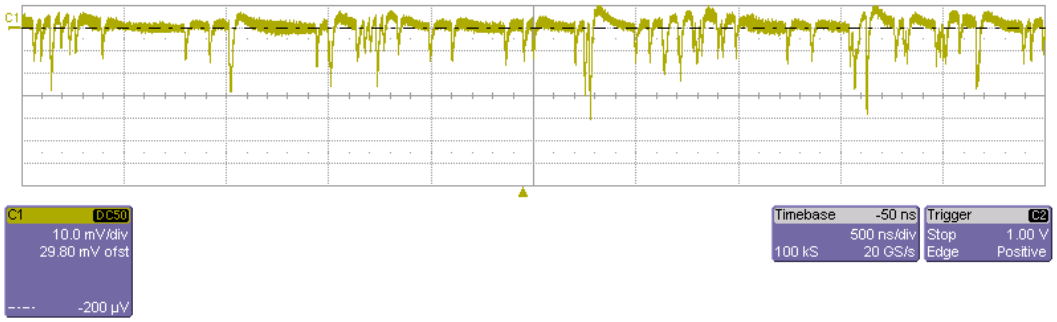

Figure 4.49: Waveform sampled by the digital oscilloscope of setup B (see Sec. 4.2.2) during SiPM characterisation after *in situ* irradiation.

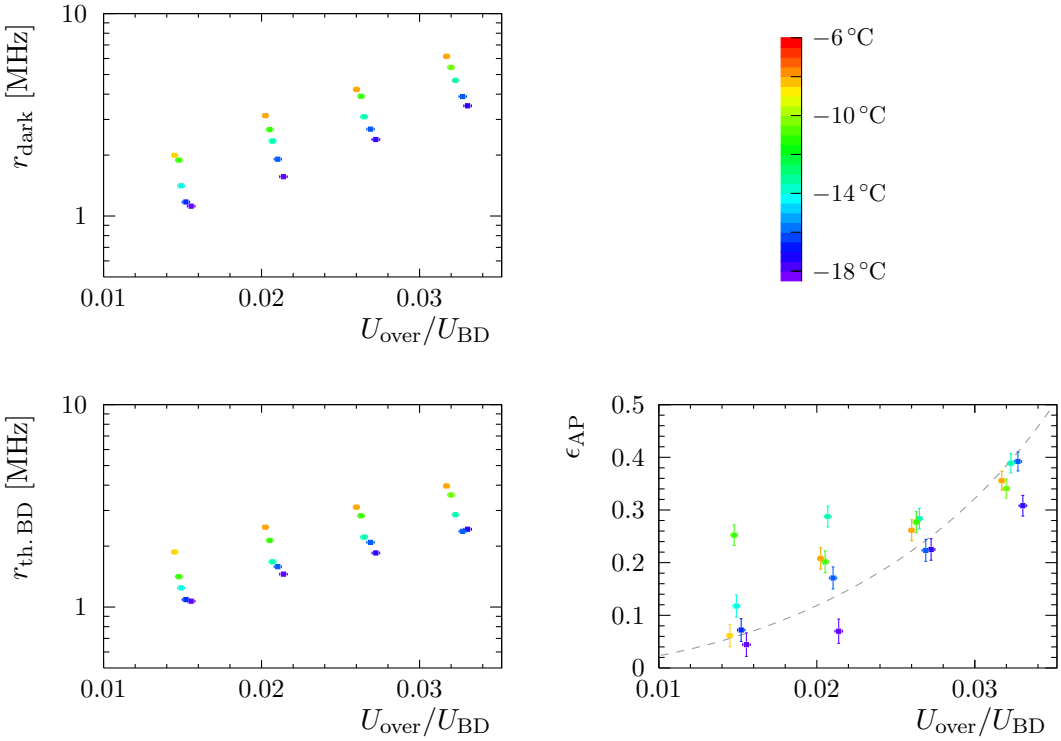

Figure 4.50: Dark count rate r_{dark}, thermal breakdown rate $r_{\mathrm{th.\,BD}}$ and after-pulse probability ϵ_{AP} measured at different temperatures and over-voltages.

Tab. 4.6. The stated uncertainty includes a factor $\sqrt{\chi^2/\mathrm{NDF}}$ to account for the apparent underestimation of data variation by the pure statistical error from the dark count distribution fit, which is illustrated by error bars in Fig. 4.50.

The radiation-induced dark count rate $r_{\mathrm{dark,rad}}$ and thermal breakdown rate $r_{\mathrm{th.\,BD,rad}}$ are obtained by subtraction of rates measured before irradiation from r_{dark} and $r_{\mathrm{th.\,BD}}$. Data shown in Fig. 4.51 are scaled to 20 °C. The considered temperature dependence is equivalent to Eq. (4.51) with $\alpha_T = 69.2 \cdot 10^{-3}\,\mathrm{K}^{-1}$. Fitting Eq. (4.29) and (4.32) to respective data yields the parameters $r_{\mathrm{th.\,gen.,rad}}$, $\alpha'_{\mathrm{BD,dark}}$ and α'_{AP}

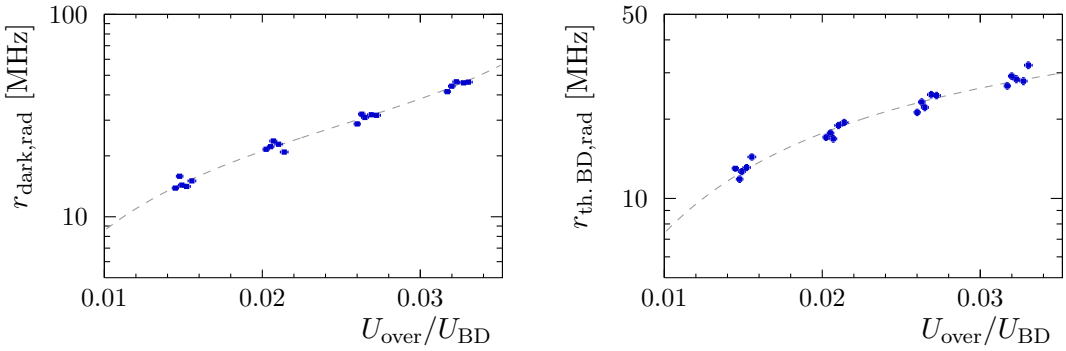

Figure 4.51: Radiation-induced dark count rate $r_{\mathrm{dark,rad}}$ and thermal breakdown rate $r_{\mathrm{th.\,BD,rad}}$ scaled to 20 °C.

Table 4.33: Parameters $r_{\mathrm{th.\,gen.,rad}}$, $\alpha'_{\mathrm{BD,dark}}$ and α'_{AP} derived from (a) fitting Eq. (4.29) to radiation-induced dark count rates $r_{\mathrm{dark,rad}}$ shown in Fig. 4.51 and (b) fitting Eq. (4.32) and (4.31) to data of $r_{\mathrm{th.\,BD,rad}}$ and ϵ_{AP} shown in Fig. 4.51 and 4.50.

	$r_{\mathrm{th.\,gen.,rad}}$ [MHz]	$\alpha'_{\mathrm{BD,dark}}$	α'_{AP}
(a)	71 ± 4	151 ± 37	16.8 ± 1.7
(b)	69.4 ± 1.9	122 ± 16	18.9 ± 1.3

provided in Tab. 4.33. The dependence of cross-talk on relative over-voltage has been fixed to its value obtained before irradiation.

Parameters in Tab. 4.33 show the consistency of results from the two analysis methods, (a) fitting the mean dark count rate and (b) analysing parameters derived from the dark count distribution. Values of $\alpha'_{\mathrm{BD,dark}}$ and α'_{AP} also agree with those found before irradiation, see Tab. 4.5 and 4.6.

To allow a comparison of the obtained radiation-induced thermal carrier generation $r_{\mathrm{th.\,gen.,rad}}$ and the radiation-induced relative dark current $I_{\mathrm{rad,rel}}$, both values are divided by the respective rate and current, that were measured before irradiation, see Tab. 4.5, 4.6 and 4.16. The results are provided in Tab. 4.34. The identifiers (a) and (b) refer to rates determined via analysis of mean dark count rates and dark count distributions, respectively. The ratio of currents (c) is obtained from the last current measurement before disconnection of the SiPM from test setup D and installation in setup B for the purpose of dark count rate measurements. The time between the two measurements was about two days. The value identified by (d) is due to an extrapolation of the fitted model of radiation-induced dark current (see Fig. 4.46) to the time of DCR measurements. Numbers in Tab. 4.34 are in good agreement, which confirms the assumption that the radiation-induced increase of dark current is proportional to an increase of thermal carrier generation.

Table 4.34: Ratios of thermal carrier generations rates $r_{\text{th. gen.,rad}}$ and relative dark current $I_{\text{rad,rel}}$ resulting from *in situ* irradiation to respective parameters $r_{\text{th. gen.}}$ and $I_{\text{dark,rel}}$ obtained before irradiation. See text for details.

$\frac{r_{\text{th. gen.,rad}}}{r_{\text{th. gen.}}}$		$\frac{I_{\text{rad,rel}}}{I_{\text{dark,rel}}}$	
(a)	(b)	(c)	(d)
75 ± 5	74.2 ± 2.2	72.3 ± 1.1	72.8

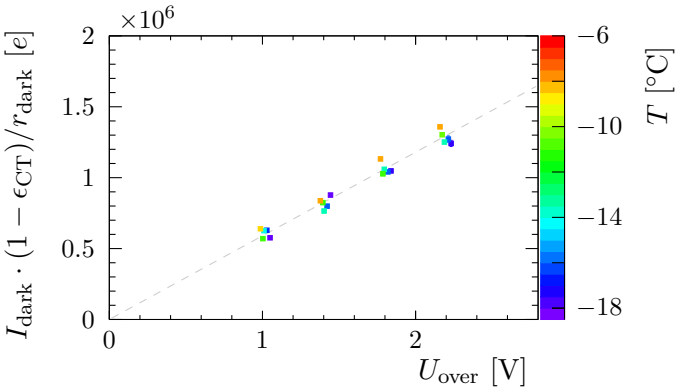

Figure 4.52: Charge per 1 p.e. dark pulse as function of over-voltage measured with SiPM S11028-050 after *in situ* irradiation.

A determination of SiPM gain per over-voltage G' is done by fitting a linear function to the cross-talk corrected dark current per dark count rate, see Fig. 4.52. The resulting value of G' is $(5.90 \pm 0.07) \cdot 10^5\,\text{V}^{-1}$. It is in accordance with the estimate of the sensor's gain before irradiation provided in Tab. 4.7.

4.7 Conclusion and Outlook

Silicon photomultipliers have been proposed for the readout of scintillating fibres in the LHCb SciFi Tracker. They enable single photon detection at relatively low bias voltage, they are robust, unaffected by magnetic fields and cost-effective. However, thermally initiated diode breakdown and after-pulsing can induce a significant dark count rate (DCR). This SiPM noise is able to exceed detection thresholds set in the proposed readout electronics of the LHCb SciFi Tracker, if inter-pixel cross-talk or random coincidence of multiple dark count events occur. In addition to the initial DCR, SiPMs will be harmed by the radiation environment of the upgraded LHCb detector.

SiPMs have therefore been studied in the years 2010 to 2013 to determine their suitability for fibre readout in the LHCb SciFi tracker. The following sensor types have been characterised in these studies.

- Hamamatsu 32-channel SiPM arrays of type MPPC 5883
- Hamamatsu single-channel sensors MPPC S10362-11-050U and S11028-050
- Three prototypes of 32-channel arrays from KETEK

The radiation hardness of MPPC 5883 arrays from Hamamatsu has been investigated by proton irradiation and *in situ* measurements. The single-channel SiPMs have a similar pixel structure and were therefore chosen for further *in situ* tests. The built-in thermoelectric cooler of device S11028-050 has enabled cooling during the irradiation test and facilitated temperature scans. During the evolution of the LHCb SciFi Tracker, SiPM manufacturers could further improve the characteristics of their sensors. The prototypes, tested in this work, were produced for LHCb by the manufacturer KETEK.

Signal Spectra

Measurements of SiPM signal spectra have been taken to determine gain, photon detection efficiency (PDE) and cross-talk probability. In particular, the dependence of these parameters on the applied bias voltage and on temperature have been studied. Tested sensors from Hamamatsu and KETEK show similar dependences of the PDE on relative over-voltage. The KETEK prototypes revealed a reduction of cross-talk probability by one to two orders of magnitude compared to the tested Hamamatsu devices. The decreased cross-talk enables operation at higher over-voltages and thus at higher PDE and gain while keeping the same noise level.

Determined breakdown voltages show a linear dependence on temperature. No significant change of gain, PDE or cross-talk in the temperature range from about $-20\,^{\circ}\mathrm{C}$ to $20\,^{\circ}\mathrm{C}$ has been observed when the effect on breakdown voltage is taken into account.

Dark Count Rate

The temperature dependence of dark count rates, that have been measured with non-irradiated Hamamatsu SiPMs, is consistent with a description according to Shockley-Read-Hall (SRH) statistics of defect levels close to the mid band gap. The simultaneous measurement of dark count rate and dark current has been used to determine the SiPM gain at several over-voltages. The obtained values are consistent for different temperatures in the above mentioned range.

The effects of thermal breakdown rate and after-pulsing on the total dark count rate have been distinguished by two different approaches. On the one hand, an expression taking these characteristics into account has been fit to the mean dark count rate as a function of over-voltage. On the other hand, a theoretical model has been found to describe the distribution of dark counts, that are recorded in a certain time period, by the effects of thermal breakdown rate and after-pulsing. This method enables the distinction of contributions from the two effects even at discrete voltages, in contrast to the previous approach. Both methods agree in the derived voltage dependences of thermal breakdown rate and after-pulse probability as well as in the determined rates of thermal carrier generation. The obtained after-pulsing probabilities do not show a temperature dependence.

Current–Voltage Characteristics

A function describing the current–voltage characteristic of SiPMs above their breakdown voltage has been derived from the characteristics of gain, breakdown efficiency, cross-talk and after-pulsing. From results of fitting this function to data it has been inferred that thermal generation rates and after-pulse probabilities are significantly less in the tested KETEK prototypes compared to the tested Hamamatsu devices.

The study of current–voltage curves enables the determination of temperature effects on breakdown voltage and dark current. The linear dependence of breakdown voltage on temperature has been confirmed for all tested sensors. The dark current of Hamamatsu SiPMs has been shown to accord to SRH statistics with an effective band gap of about 1.1 eV for temperatures above 260 K. At lower temperatures, a second SRH term with only about half the activation energy had to be added for a sufficient description of the data. While the temperature dependence of dark current in Hamamatsu sensors is consistent with carrier generation mainly via traps close to mid gap, the current in KETEK SiPMs is dominated by a term describing the temperature dependence of carrier diffusion. A smaller fraction of KETEK dark current is described by activation energies less than 1 eV and shows a deviating dependence on voltage. The observed behaviour might hint at tunnelling processes being responsible for the corresponding carrier generation.

The characterisation studies of non-irradiated sensors have shown that the KETEK prototypes are superior to the tested Hamamatsu sensors. However, in the time since the presented measurements, Hamamatsu has also established new devices with significantly decreased DCR, cross-talk and after-pulse probability. These devices enable operation at higher over-voltage and thus better PDE as well.

Irradiation Tests

Irradiation tests of Hamamatsu SiPMs have been performed at the proton beam facilities of the *Centre Antoine Lacassagne* in Nice and the *Maier-Leibnitz-Laboratorium* at Forschungszentrum Garching near Munich. Furthermore, SiPMs have been installed in the LHCb cavern during data taking in the years 2011 and 2012 to provide *in situ* measurements.

No significant radiation-induced changes of gain, PDE, cross-talk or after-pulse probability have been observed for 1 MeV-neutron-equivalent fluences up to about $8 \cdot 10^{11}\,\mathrm{cm}^{-2}$. Also, breakdown voltages are the same before and after irradiation, their dependence on temperature has not been changed. Current–voltage curves remained unaffected except for an overall multiplication of dark current.

The increased dark current measured after proton irradiations shows a linear dependence on the applied neutron-equivalent fluence, which accords to the NIEL scaling hypothesis. However, the temperature dependence of radiation-induced dark current is found to be significantly different from the dependence of the initial current before irradiation and thus from the current–temperature dependence of radiated silicon detectors, that are operated below breakdown. The temperature dependence of radiation-induced dark current corresponds to a change by about a factor two per 10 K.

Dark currents that were measured *in situ* have been described by a model of damage and annealing. It accounts for an SiPM deterioration, that is proportional to the luminosity, and a set of different annealing time constants, that have been obtained from literature. Although the evolution of dark currents can be described by the fitted model, the resulting fit parameters are not fully consistent for the three tested sensors. The relative amplitudes of dark current fractions with certain annealing time differ from those obtained from literature for silicon detectors. This observation, together with the different temperature dependence, hints at radiation-induced defects that are responsible for dark currents in SiPMs but not relevant for currents in silicon diodes operated below the breakdown voltage.

It has been inferred that the radiation-induced dark count rate is proportional to the current increase, since all other characteristics have shown no radiation effect. This conclusion has been confirmed by an explicit comparison of dark count rate and dark current measurements with an *in situ* irradiated sensor.

The estimates for the non-annealing dark current per fluence, derived from *in situ* tests, show a maximum variation of about 20 %. They exceed the corresponding value obtained from proton irradiations by more than a factor two. Despite the lower uncertainty of fluences in the proton irradiation tests, it has been concluded that results from the *in situ* tests should be used for a conservative estimate of radiation effects in the upgraded LHCb detector, also because *in situ* measurements correspond to a more realistic particle distribution and dose rate. The resulting value of radiation-induced dark count rate per channel of an SiPM array, that is comparable to Hamamatsu MPPC 5883, is about 345 MHz at 20 °C and 1.5 V over-voltage.

Since no radiation effect except for an increased dark count rate has been observed at fluences relevant for the LHCb upgrade, it has been concluded that fibre readout by SiPMs is a feasible technology. The occurring dark count rates will be reduced by cooling the SiPMs to about $-40\,°\mathrm{C}$.

Obtained SiPM characteristics have been used as parameters in detector simulations by the LHCb SciFi Tracker collaboration whose goal is the determination of hit efficiencies, noise rates and thus tracking performance.

5 Conclusion

The upgrade of the LHCb detector will enable a major improvement of sensitivities to key observables in the indirect search for New Physics. This will be achieved by reduced statistical uncertainties when using a data sample of $50\,\mathrm{fb}^{-1}$, which will be recorded over ten years of upgrade operation. A new trigger scheme, which comprises detector readout at the full LHC bunch crossing rate of 40 MHz, will remove the current limitations posed by the hardware trigger stage. In particular, analyses of decays with hadronic final states will benefit from this measure. The upgraded detector is designed to be operable at luminosities up to $2 \cdot 10^{33}\,\mathrm{cm}^{-2}\,\mathrm{s}^{-1}$.

The current LHCb downstream tracking system, consisting of silicon strips in the Inner Tracker (IT) and gas drift tubes in the Outer Tracker (OT), has to be replaced by a new detector design to ensure high tracking performances at operational conditions of the LHCb upgrade. A complete replacement of the downstream tracking system by scintillating fibres (SciFi) with silicon photomultiplier (SiPM) readout has been proposed since it provides the necessary granularity and thus hit resolution for particle tracking at relatively low costs. The use of a single technology for the whole acceptance enables more efficient track finding algorithms and facilitates production, alignment, operation and maintenance of the sub-detector.

However, it has to be shown that the LHCb SciFi Tracker technology is able to provide the necessary hit resolution at low noise rates and to withstand the radiation environment of the upgraded LHCb detector. For this purpose, scintillating fibre and silicon photomultiplier studies have been performed.

A comprehensive SciFi simulation has been developed using the GEANT4 toolkit. Several simulation studies have been presented in this work. In particular, the simulation has been used to describe measurements of fibre irradiation tests and to estimate the decrease in the number of detectable photons during the data taking period of the upgraded detector. The developed fibre simulation is used in research and development (R&D) studies by several groups of the LHCb collaboration and to infer parametrisations that can be used in the overall detector simulation. Thus, its results contribute to the development of clustering and tracking procedures. In addition to the simulations, a measurement of signal timing has been made. The derived photon propagation times have also been an input to the overall detector simulation by the LHCb SciFi Tracker group.

Measurements with silicon photomultipliers have been presented, revealing the dependency of several characteristics on bias voltage and temperature. Especially, the crucial proof of radiation hardness has been made by irradiations with protons and *in situ* tests in the LHCb cavern. It has been shown that the only significant radiation effect at fluences relevant for the LHCb upgrade is a high dark count rate.

The resulting noise rate can be kept at a sufficiently low level by cooling the SiPMs. Characterisation of SiPM prototypes, that have been established during the time of R&D studies for the LHCb SciFi Tracker, have shown the manufacturers' ability to reduce cross-talk and after-pulsing.

The studies presented in this thesis have been the base for further R&D by the LHCb collaboration and set the ground for the formation of the LHCb SciFi Tracker group with now more than 20 institutes participating. The proton irradiation tests of SiPMs have contributed to the *Letter of Intent for the LHCb Upgrade* [13] which has been published in early 2011. The *in situ* irradiations have provided further input to the viability assessment of the SciFi Tracker technology [109] which took place in 2013. It has been concluded, that the SciFi Tracker technology is feasible to satisfy the requirements of tracking performance. The LHCb collaboration has therefore decided to replace the complete downstream tracking system by the new SciFi Tracker during the LHC Long Shutdown 2. Results from studies described in this thesis have contributed to the *LHCb Tracker Upgrade Technical Design Report* [23].

Appendices

A ^{90}Sr Spectrum

The excitation of scintillating fibres by electrons emitted from a ^{90}Sr source is simulated using the β spectrum (c) shown in Fig. A.1. The spectrum has been calculated by piecewise integration of the continuous spectrum (b) which has been determined using formulae and numbers from Ref. [110]. For comparison, the energy spectrum (a) according to Ref. [111] is also drawn.

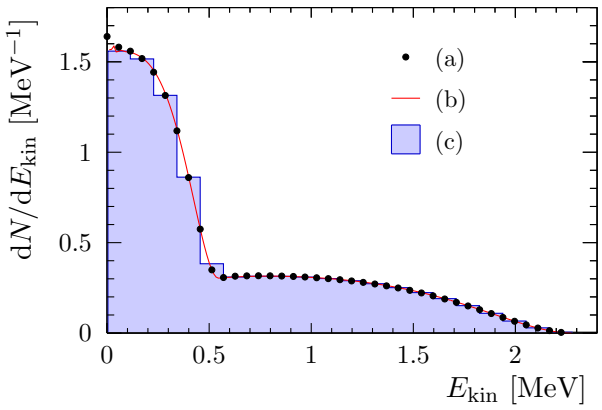

Figure A.1: Energy spectrum of electrons from ^{90}Sr decay, (a) taken from Ref. [111], (b) calculated using formulae and numbers from Ref. [110] and (c) used in the fibre simulation.

B Photon Detection Efficiencies

The following photo-sensors have been used in fibre irradiation tests by the LHCb SciFi Tracker collaboration, see Sec. 3.2.6.

- Ketek SiPM
- Newport 818-UV photodiode
- Hamamatsu MPPC C11208-02

Figure B.1 shows the wavelength-dependent photon detection efficiencies (PDE) of these devices, that have been taken into account to reproduce the measurements in simulation. The PDEs are scaled to have a maximum of 1. Thus, photon detection is maximised in the simulation to reduce statistical fluctuations while preserving wavelength effects. This procedure does not harm the quality of derived results, since they do not depend on the absolute photon number per particle hit.

The PDE of Hamamatsu SiPMs given in Ref. [23] is used to determine the absolute number of detected photons per particle crossing a fibre mat (Sec. 3.2.5). Its wavelength dependence is illustrated by Figure B.2.

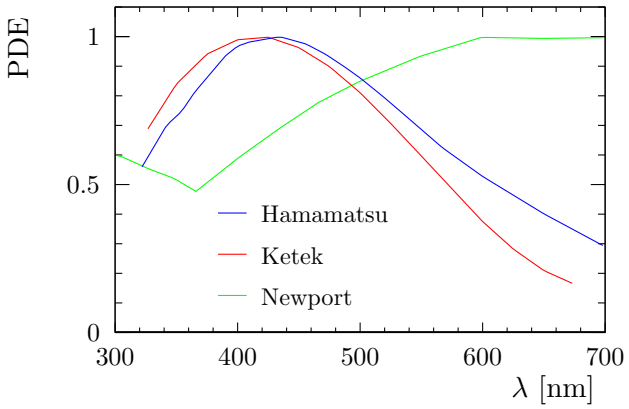

Figure B.1: Wavelength-dependent PDE of photo-sensors used in fibre irradiation tests. Curves are taken from Ref. [112](Hamamatsu), [72](Ketek) and [113](Newport) and scaled to have a maximum of 1.

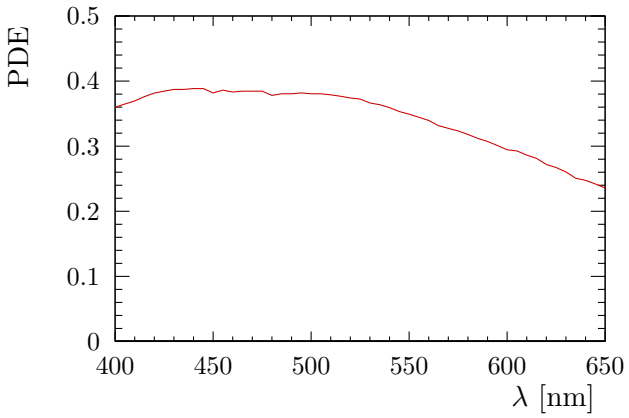

Figure B.2: Wavelength-dependent PDE of Hamamatsu SiPM taken from Ref. [23].

d

C UV LED Characteristics

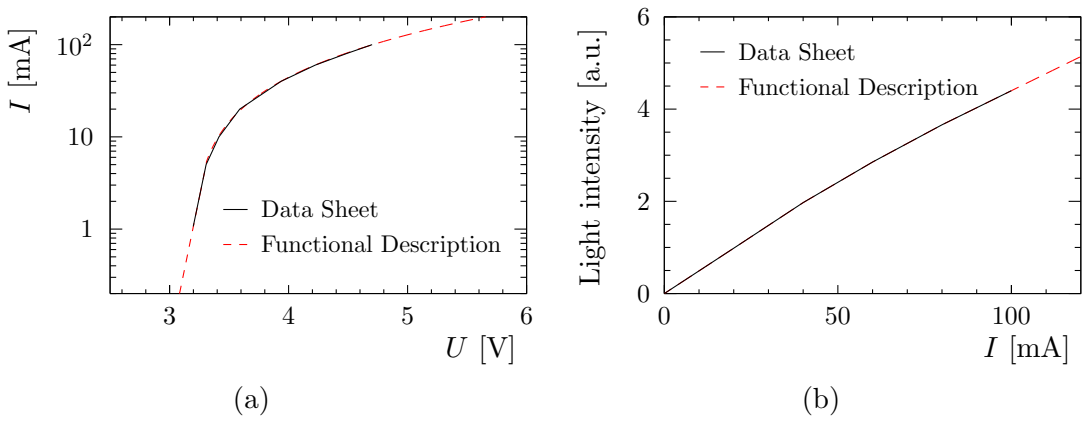

Figure C.1: Current–voltage characteristic (a) and dependence of light emission on forward current (b) of UV LED used in timing measurements of scintillating fibre, see Sec. 3.3. Curves obtained from the data sheet [114] and functional descriptions used to determine LED pulse shapes shown in Fig. 3.56 are illustrated.

D Proton Irradiations

The following tables list duration and proton fluence Φ_p of SiPM irradiations performed at the *Centre Antoine Lacassagne* in Nice and the *Maier-Leibnitz-Laboratorium* at Forschungszentrum Garching near Munich. Hamamatsu SiPM arrays have been irradiated with protons of 61 MeV (sensors HZ5-26-B, HZ5-26-D) and 21 MeV (sensors HS5-24-A, HS5-24-C) kinetic energy, respectively. The 1 MeV-neutron-equivalent fluence Φ_{eq} is calculated using scaling factors from Ref. [100].

Table D.1: HZ5-26-B

Number	Duration [s]	Φ_p [10^9 cm^{-2}]	Φ_{eq} [10^9 cm^{-2}]
1	18	1.302 ± 0.006	
2	16	1.302 ± 0.006	
3	18	1.302 ± 0.006	
4	16	1.308 ± 0.006	
5	26	1.359 ± 0.006	
6	122	6.439 ± 0.006	
7	28	13.274 ± 0.032	
8	196	13.000 ± 0.006	
9	191	13.000 ± 0.006	
10	190	13.000 ± 0.006	
Total fluence		65.29 ± 0.04	106 ± 5

Table D.2: HZ5-26-D

Number	Duration [s]	Φ_p [10^9 cm^{-2}]	Φ_{eq} [10^9 cm^{-2}]
1 to 10	2	0.134 ± 0.006	
11	7	18.7 ± 0.9	
12	15	41.8 ± 2.1	
13	14	41.4 ± 2.1	
14	18	26.198 ± 0.006	
15	19	26.140 ± 0.006	
16	19	26.147 ± 0.006	
17	19	26.147 ± 0.006	
18	19	26.147 ± 0.006	
19	19	26.153 ± 0.006	
20	19	26.147 ± 0.006	
21	18	26.134 ± 0.006	
22	19	26.134 ± 0.006	
23	18	26.140 ± 0.006	
24	19	26.140 ± 0.006	
25	19	26.140 ± 0.006	
26	19	26.134 ± 0.006	
27	18	26.134 ± 0.006	
28	17	23.958 ± 0.006	
Total fluence		493.2 ± 3.1	800 ± 40

f

Table D.3: HS5-24-A

Number	Duration [s]	Φ_p [$10^8\,cm^{-2}$]	Φ_{eq} [$10^8\,cm^{-2}$]
1	60	5.8 ± 0.8	
2	60	5.7 ± 0.4	
3	60	6.5 ± 0.4	
4	60	5.8 ± 0.6	
Total fluence		23.7 ± 1.1	67 ± 5

Table D.4: HS5-24-C

Number	Duration [s]	Φ_p [$10^8\,cm^{-2}$]	Φ_{eq} [$10^8\,cm^{-2}$]
1	60	5.4 ± 0.6	
2	60	4.7 ± 0.6	
3	60	4.3 ± 0.6	
Total fluence		14.4 ± 1.0	40.6 ± 3.5

Bibliography

[1] S. L. Glashow, *Partial-symmetries of weak interactions*, Nuclear Physics **22** (1961), no. 4, 579.

[2] A. Salam and J. Ward, *Electromagnetic and weak interactions*, Physics Letters **13** (1964), no. 2, 168.

[3] S. Weinberg, *A Model of Leptons*, Phys. Rev. Lett. **19** (1967) 1264.

[4] G. Aad *et al.*, *Observation of a new particle in the search for the Standard Model Higgs boson with the ATLAS detector at the LHC*, Physics Letters B **716** (2012), no. 1, 1.

[5] S. Chatrchyan *et al.*, *Observation of a new boson at a mass of 125 GeV with the CMS experiment at the LHC*, Physics Letters B **716** (2012), no. 1, 30.

[6] Planck Collaboration, R. Adam *et al.*, *Planck 2015 results. I. Overview of products and scientific results*, `arXiv:1502.01582`.

[7] A. D. Sakharov, *Violation of CP invariance, C asymmetry, and baryon asymmetry of the universe*, Pis'ma Zh. Eksp. Teor. Fiz **5** (1967) 32.

[8] LHCb Collaboration, A. A. Alves *et al.*, *The LHCb Detector at the LHC*, Journal of Instrumentation **3** (2008), no. 08, S08005.

[9] LHCb collaboration, R. Aaij *et al.*, *LHCb Detector Performance*, Int. J. Mod. Phys. A **30** (2014) 1530022, `arXiv:1412.6352`.

[10] LHCb, R. Aaij *et al.*, *First Evidence for the Decay $B_s^0 \to \mu^+\mu^-$*, Phys. Rev. Lett. **110** (2013), no. 2, 021801, `arXiv:1211.2674`.

[11] LHCb Collaboration, R. Aaij *et al.*, A. Bharucha *et al.*, *Implications of LHCb measurements and future prospects*, The European Physical Journal C **73** (2013), no. 4, 2373. 178 p.

[12] T. Gershon, *Updated sensitivity projections for the LHCb Upgrade*, Tech. Rep. LHCb-PUB-2013-015. CERN-LHCb-PUB-2013-015, CERN, Geneva, Sep, 2013.

[13] LHCb Collaboration, *Letter of Intent for the LHCb Upgrade*, Tech. Rep. CERN-LHCC-2011-001. LHCC-I-018, CERN, Geneva, Mar, 2011.

[14] LHCb, CMS, V. Khachatryan *et al.*, *Observation of the rare $B_s^0 \to \mu^+\mu^-$ decay from the combined analysis of CMS and LHCb data*, Nature **522** (2015) 68, arXiv:1411.4413.

[15] M. Schlupp, *Precision tests of the Standard Model using key observables of CP violation and rare decays*, PhD thesis, Technische Universität Dortmund, 2015.

[16] N. Cabibbo, *Unitary Symmetry and Leptonic Decays*, Phys. Rev. Lett. **10** (1963) 531.

[17] M. Kobayashi and T. Maskawa, *CP-Violation in the Renormalizable Theory of Weak Interaction*, Progress of Theoretical Physics **49** (1973), no. 2, 652.

[18] T. M. Karbach, *Improved constraints on γ: CKM2014 update*, in *8th International Workshop on the CKM Unitarity Triangle (CKM2014) Vienna, Austria, September 8-12, 2014*, 2014. arXiv:1411.4600.

[19] J. Brod and J. Zupan, *The ultimate theoretical error on γ from $B \to DK$ decays*, JHEP **01** (2014) 051, arXiv:1308.5663.

[20] LHCb, R. Aaij *et al.*, *First measurement of the CP-violating phase in $B_s^0 \to \phi\phi$ decays*, Phys. Rev. Lett. **110** (2013), no. 24, 241802, arXiv:1303.7125.

[21] R. Jacobsson, *Performance of the LHCb detector during the LHC proton runs 2010 – 2012*, in *Nuclear Science Symposium and Medical Imaging Conference (NSS/MIC), 2012 IEEE*, pp. 1479–1486, Oct, 2012. doi: 10.1109/NSSMIC.2012.6551357.

[22] LHCb collaboration, I. Bediaga *et al.*, *Framework TDR for the LHCb Upgrade: Technical Design Report*, Tech. Rep. CERN-LHCC-2012-007. LHCb-TDR-12, CERN, Geneva, Apr, 2012.

[23] LHCb Collaboration, *LHCb Tracker Upgrade Technical Design Report*, Tech. Rep. CERN-LHCC-2014-001. LHCB-TDR-015, CERN, Geneva, Feb, 2014.

[24] LHCb Collaboration, *LHCb VELO Upgrade Technical Design Report*, Tech. Rep. CERN-LHCC-2013-021. LHCB-TDR-013, CERN, Geneva, Nov, 2013.

[25] LHCb Collaboration, *LHCb PID Upgrade Technical Design Report*, Tech. Rep. CERN-LHCC-2013-022. LHCB-TDR-014, CERN, Geneva, Nov, 2013.

[26] LHCb Outer Tracker group, *Performance of the LHCb Outer Tracker*, Journal of Instrumentation **9** (2014), no. 01, P01002.

[27] M. Tobin, *The {LHCb} silicon tracker*, Nuclear Instruments and Methods in Physics Research Section A: Accelerators, Spectrometers, Detectors and Associated Equipment **732** (2013) 168, Vienna Conference on Instrumentation 2013.

[28] LHCb SciFi, B. D. Leverington, *The LHCb Upgrade Scintillating Fibre Tracker*, in *Proceedings of Technology and Instrumentation in Particle Physics 2014, PoS(TIPP2014)113*, June, 2014.

[29] GEANT4 collaboration, S. Agostinelli *et al.*, GEANT4– *a simulation toolkit*, Nuclear Instruments and Methods in Physics Research Section A: Accelerators, Spectrometers, Detectors and Associated Equipment **506** (2003), no. 3, 250.

[30] GEANT4 collaboration, J. Allison *et al.*, GEANT4 *developments and applications*, Nuclear Science, IEEE Transactions on **53** (2006) 270.

[31] Kuraray Co., Ltd., Kuraray Nihonbashi Building, 1-6, 3-Chome, Nihonbashi; Chuo-ku, Tokyo 103-8254, Japan, *Scintillation Materials.* Product Catalogue.

[32] F. D. Brooks, *Development of Organic Scintillators*, Nucl. Instrum. Meth. **162** (1979) 477.

[33] I. A. Berlman, *Handbook of Fluorescence Spectra of Aromatic Molecules*, Academic Press, New York and London, 2. ed., 1971.

[34] L. J. Basile, *Transfer of excitation energy in rigid solutions of organic scintillators*, Trans. Faraday Soc. **60** (1964) 1702.

[35] C. D'Ambrosio *et al.*, *Organic scintillators with large Stokes shifts dissolved in polystyrene*, Nuclear Instruments and Methods in Physics Research Section A: Accelerators, Spectrometers, Detectors and Associated Equipment **307** (1991), no. 2–3, 430.

[36] T. Förster, *Zwischenmolekulare Energiewanderung und Fluoreszenz*, Annalen der Physik **437** (1948), no. 1-2, 55.

[37] T. Förster, *10th Spiers Memorial Lecture. Transfer mechanisms of electronic excitation*, Discuss. Faraday Soc. **27** (1959) 7.

[38] P. Rebourgeard *et al.*, *Fabrication and measurements of plastic scintillating fibers*, Nuclear Instruments and Methods in Physics Research Section A: Accelerators, Spectrometers, Detectors and Associated Equipment **427** (1999), no. 3, 543.

[39] N. Sultanova, S. Kasarova, and I. Nikolov, *Dispersion Properties of Optical Polymers*, Acta Physica Polonica A **116** (2009), no. 4, 585, Proceedings of the International School and Conference on Photonics, PHOTONICA09.

[40] M. Vasilopoulou *et al.*, *Highly transparent partially fluorinated methacrylate polymers for optical waveguides*, Microelectronic Engineering **86** (2009), no. 4–6, 1142, {MNE} '08 The 34th International Conference on Micro- and Nano-Engineering (MNE).

[41] Sellmeier, *Zur Erklärung der abnormen Farbenfolge im Spectrum einiger Substanzen*, Annalen der Physik **219** (1871), no. 6, 272.

[42] T. Kaino, *Preparation of plastic optical fibers for near-IR region transmission*, Journal of Polymer Science Part A: Polymer Chemistry **25** (1987), no. 1, 37.

[43] W. Groh, *Overtone absorption in macromolecules for polymer optical fibers*, Die Makromolekulare Chemie **189** (1988), no. 12, 2861.

[44] Y. Takezawa, N. Taketani, S. Tanno, and S. Ohara, *Empirical prediction method of intrinsic light scattering loss of transparent amorphous polymers*, Journal of Applied Polymer Science **46** (1992), no. 11, 2033.

[45] J. Q. Stewart, *Generalizations of the Rayleigh Formula for Molecular Scattering*, J. Opt. Soc. Am. **11** (1925) 581.

[46] M. Dettenmaier and E. W. Fischer, *Untersuchungen zu den Orientierungs- und Dichtefluktuationen in amorphen Polymeren mit Hilfe der Lichtstreuung*, Die Makromolekulare Chemie **177** (1976), no. 4, 1185.

[47] C. Emslie, *Polymer optical fibres*, Journal of Materials Science **23** (1988), no. 7, 2281.

[48] C. D'Ambrosio *et al.*, *Reflection losses in polystyrene fibres*, Nuclear Instruments and Methods in Physics Research Section A: Accelerators, Spectrometers, Detectors and Associated Equipment **306** (1991), no. 3, 549.

[49] H. Blumenfeld, E. Gaillard, and P. Rebourgeard, *Measurement of the reflection coefficient at the core-cladding interface in plastic scintillating fibers*, Nuclear Instruments and Methods in Physics Research Section A: Accelerators, Spectrometers, Detectors and Associated Equipment **309** (1991), no. 1–2, 169.

[50] J. Alitti *et al.*, *The design and construction of a scintillating fiber tracking detector*, Nuclear Instruments and Methods in Physics Research Section A: Accelerators, Spectrometers, Detectors and Associated Equipment **273** (1988), no. 1, 135.

[51] H. Leutz, *Scintillating fibres*, Nuclear Instruments and Methods in Physics Research Section A: Accelerators, Spectrometers, Detectors and Associated Equipment **364** (1995), no. 3, 422.

[52] M. Hoek, *Design and Construction of a Scintillating Fibre Tracker for measuring Hard Exclusive Reactions at HERMES*, PhD thesis, Justus-Liebig-Universität Gießen, 2006, doi: 10.3204/DESY-THESIS-2006-027.

[53] Hamamatsu Photonics K.K., Solid State Division, *C10082CA/C10083CA series: Mini-spectrometers, high sensitivity type (integrated with back-thinned type CCD image sensor)*, August, 2013. Data Sheet.

[54] J. Wallace, M. Sinclair, K. Gillen, and R. Clough, *Color center annealing in γ - irradiated polystyrene, under vacuum and air atmospheres*, Radiation Physics and Chemistry **41** (1993), no. 1–2, 85.

[55] W. Busjan, K. Wick, and T. Zoufal, *Shortlived absorption centers in plastic scintillators and their influence on the fluorescence light yield*, Nuclear Instruments and Methods in Physics Research Section B: Beam Interactions with Materials and Atoms **152** (1999), no. 1, 89.

[56] A. Bross and A. Pla-Dalmau, *Radiation damage of plastic scintillators*, Nuclear Science, IEEE Transactions on **39** (1992) 1199.

[57] T. Zoufal, *Beeinträchtigung der optischen Eigenschaften und Veränderung der Fluoreszenz von Kunststoffszintillatoren durch Röntgenstrahlung*, PhD thesis, Universität Hamburg, 2002, doi: 10.3204/DESY-THESIS-2002-013.

[58] B. D. Leverington, 2013 and 2014. Private communication.

[59] R. Clough, K. Gillen, G. Malone, and J. Wallace, *Color formation in irradiated polymers*, Radiation Physics and Chemistry **48** (1996), no. 5, 583.

[60] J. Gaynor, G. Schueneman, P. Schuman, and J. P. Harmon, *Effects of fluorinated substituents on the refractive index and optical radiation resistance of methacrylates*, Journal of Applied Polymer Science **50** (1993), no. 9, 1645.

[61] P. R. H. Bertolucci *et al.*, *Radiation effects of low refractive index, fluorinated methacrylate polymers for fiber cladding*, Polymer Engineering & Science **38** (1998), no. 4, 699.

[62] T. Förster, *Experimentelle und theoretische Untersuchung des zwischenmolekularen Übergangs von Elektronenanregungsenergie*, Zeitschrift für Naturforschung **4a** (1949), no. 5, 321.

[63] J. B. Birks, *Energy transfer in organic systems VI. Fluorescence response functions and scintillation pulse shapes*, Journal of Physics B: Atomic and Molecular Physics **1** (1968), no. 5, 946.

[64] C. Hawkes *et al.*, *Decay time and light yield measurements for plastic scintillating fibers*, Nuclear Instruments and Methods in Physics Research Section A: Accelerators, Spectrometers, Detectors and Associated Equipment **292** (1990), no. 2, 329.

[65] J. Flournoy, *Measurement of decay times of fast scintillating fibers*, Radiation Physics and Chemistry **41** (1993), no. 1–2, 389.

[66] R. Brun and F. Rademakers, *ROOT – An object oriented data analysis framework*, Nuclear Instruments and Methods in Physics Research Section A: Accelerators, Spectrometers, Detectors and Associated Equipment **389** (1997), no. 1–2, 81, New Computing Techniques in Physics Research V.

[67] M. Deckenhoff, *Simulation of Scintillating Fibres in Geant4*, Tech. Rep. LHCb-PUB-2014-023. CERN-LHCb-PUB-2014-023. LHCb-INT-2014-009, CERN, Geneva, Feb, 2014.

[68] K. Koike, *Design of Plastic Optical Fiber for Home Network*, PhD thesis, Keio University, March, 2010.

[69] Kuraray Co., Ltd., 2014. Private communication.

[70] C. Joram and T. Schneider, *Mirroring of fibre ends for the LHCb SciFi project*, Tech. Rep. LHCb-PUB-2014-020. CERN-LHCb-PUB-2014-020. LHCb-INT-2013-060, CERN, Geneva, Feb, 2014.

[71] N. Lopez March and M. Karacson, *Radiation studies for the LHCb tracker upgrade*, Tech. Rep. LHCb-PUB-2014-022. CERN-LHCb-PUB-2014-022. LHCb-INT-2013-003, CERN, Geneva, Feb, 2014.

[72] C. Joram, T. Schneider, and P. Shatalov, *Measurements and radiation tests on scintillating fibres for the LHCb SciFi project*, Tech. Rep. LHCb-PUB-2014-021. CERN-LHCb-PUB-2014-021. LHCb-INT-2013-002, CERN, Geneva, Feb, 2014.

[73] R. Ekelhof, PhD thesis, Technische Universität Dortmund, 2015, in preparation.

[74] R. Ekelhof, 2014. Private communication.

[75] W. H. Richardson, *Bayesian-based iterative method of image restoration*, J. Opt. Soc. Am. **62** (1972) 55.

[76] L. B. Lucy, *An iterative technique for the rectification of observed distributions*, The Astronomical Journal **79** (1974) 745.

[77] D. Renker, *Geiger-mode avalanche photodiodes, history, properties and problems*, Nuclear Instruments and Methods in Physics Research Section A: Accelerators, Spectrometers, Detectors and Associated Equipment **567** (2006), no. 1, 48, Proceedings of the 4th International Conference on New Developments in Photodetection – BEAUNE 2005.

[78] B. Dolgoshein *et al.*, *Status report on silicon photomultiplier development and its applications*, Nuclear Instruments and Methods in Physics Research Section A: Accelerators, Spectrometers, Detectors and Associated Equipment **563** (2006), no. 2, 368, TRDs for the Third Millenium – Proceedings of the 3rd Workshop on Advanced Transition Radiation Detectors for Accelerators and Space Applications.

[79] S. M. Sze and K. K. Ng, *Physics of Semiconductor Devices*, Wiley Interscience, Hoboken, NJ, 3. ed., 2007.

[80] A. Lacaita, F. Zappa, S. Bigliardi, and M. Manfredi, *On the bremsstrahlung origin of hot-carrier-induced photons in silicon devices*, Electron Devices, IEEE Transactions on **40** (1993) 577.

[81] Y. Du and F. Retière, *After-pulsing and cross-talk in multi-pixel photon counters*, Nuclear Instruments and Methods in Physics Research Section A: Accelerators, Spectrometers, Detectors and Associated Equipment **596** (2008), no. 3, 396.

[82] W. Shockley and W. T. Read, *Statistics of the Recombinations of Holes and Electrons*, Phys. Rev. **87** (1952) 835.

[83] R. N. Hall, *Electron-Hole Recombination in Germanium*, Phys. Rev. **87** (1952) 387.

[84] G. Collazuol *et al.*, *Studies of silicon photomultipliers at cryogenic temperatures*, Nuclear Instruments and Methods in Physics Research Section A: Accelerators, Spectrometers, Detectors and Associated Equipment **628** (2011), no. 1, 389, {VCI} 2010 Proceedings of the 12th International Vienna Conference on Instrumentation.

[85] B. Beischer *et al.*, *A high-resolution scintillating fiber tracker with silicon photomultiplier array readout*, Nuclear Instruments and Methods in Physics Research Section A: Accelerators, Spectrometers, Detectors and Associated Equipment **622** (2010), no. 3, 542.

[86] DKE Deutsche Kommission Elektrotechnik Elektronik Informationstechnik im DIN und VDE, *Industrial platinum resistance thermometers and platinum temperature sensors (IEC 60751:2008)*, May, 2009. German version EN 60751:2008.

[87] Analog Devices, Inc., *AD7719: Low Voltage, Low Power, Factory-Calibrated 16-/24-Bit Dual* $\Sigma - \Delta$ *ADC*, April, 2003. Data Sheet, Rev A.

[88] Keithley Instruments, Inc., *Model 2010: Low Noise 7½-Digit Autoranging Multimeter*. Data Sheet.

[89] Hamamatsu Photonics K.K., Solid State Division, *S11028 series: Thermoelectrically cooled MPPC for photon counting*, January, 2011. Data Sheet.

[90] J. S. Steinhart and S. R. Hart, *Calibration curves for thermistors*, Deep Sea Research and Oceanographic Abstracts **15** (1968), no. 4, 497.

[91] N.V. Philips, *Multimeter PM2525*, 1987. Operation Manual.

[92] V. Balagura *et al.*, *Study of scintillator strip with wavelength shifting fiber and silicon photomultiplier*, Nuclear Instruments and Methods in Physics Research Section A: Accelerators, Spectrometers, Detectors and Associated Equipment **564** (2006), no. 1, 590.

[93] H. Dautet *et al.*, *Photon counting techniques with silicon avalanche photodiodes*, Appl. Opt. **32** (1993) 3894.

[94] W. G. Oldham, R. Samuelson, and P. Antognetti, *Triggering phenomena in avalanche diodes*, Electron Devices, IEEE Transactions on **19** (1972) 1056.

[95] C.-T. Sah, R. Noyce, and W. Shockley, *Carrier Generation and Recombination in P-N Junctions and P-N Junction Characteristics*, Proceedings of the IRE **45** (1957) 1228.

[96] G. Lindström, *Radiation damage in silicon detectors*, Nuclear Instruments and Methods in Physics Research Section A: Accelerators, Spectrometers, Detectors and Associated Equipment **512** (2003), no. 1–2, 30, Proceedings of the 9th European Symposium on Semiconductor Detectors: New Developments on Radiation Detectors.

[97] G. Lindström, M. Moll, and E. Fretwurst, *Radiation hardness of silicon detectors – a challenge from high-energy physics*, Nuclear Instruments and Methods in Physics Research Section A: Accelerators, Spectrometers, Detectors and Associated Equipment **426** (1999), no. 1, 1.

[98] J. Hérault, N. Iborra, B. Serrano, and P. Chauvel, *Monte Carlo simulation of a protontherapy platform devoted to ocular melanoma*, Medical Physics **32** (2005), no. 4, 910.

[99] R. Cambria *et al.*, *Proton beam dosimetry: A comparison between the Faraday cup and an ionization chamber*, Physics in Medicine and Biology **42** (1997), no. 6, 1185.

[100] A. Vasilescu (INPE Bucharest) and G. Lindstroem (University of Hamburg), *Displacement damage in silicon*, online compilation, version from 15.08.2000, http://rd50.web.cern.ch/RD50/NIEL/.

[101] M. Karacson, 2012. Private communication.

[102] D. A. Fagundes, M. J. Menon, and P. V. R. G. Silva, *On the rise of proton–proton cross-sections at high energies*, Journal of Physics G: Nuclear and Particle Physics **40** (2013), no. 6, 065005.

[103] Keithley Instruments, Inc., *Series 2600A: System SourceMeter Instruments*, 2008. Data Sheet.

[104] R. Wunstorf, *Systematische Untersuchungen zur Strahlenresistenz von Silizium-Detektoren für die Verwendung in Hochenergiephysik-Experimenten*, PhD thesis, Universität Hamburg, October, 1992, DESY FH1K 92-01.

[105] H. Feick, *Radiation Tolerance of Silicon Particle Detectors for High-Energy Physics Experiments*, PhD thesis, Universität Hamburg, August, 1997, DESY F35D-97-08.

[106] M. Moll, *Radiation Damage in Silicon Particle Detectors - Microscopic Defects and Macroscopic Properties*, PhD thesis, Universität Hamburg, December, 1999, DESY-THESIS-1999-040.

[107] RD50, A. Chilingarov, *Generation current temperature scaling*, Tech. Rep. PH-EP-Tech-Note-2013-001, CERN, Geneva, Jan, 2013.

[108] LHCb VELO group, A. Affolder *et al.*, *Radiation damage in the LHCb Vertex Locator*, J. Instrum. **8** (2013) P08002. 23 p.

[109] A. Bay *et al.*, *Viability Assessment of a Scintillating Fibre Tracker for the LHCb Upgrade*, Tech. Rep. LHCb-PUB-2014-015. CERN-LHCb-PUB-2014-015. LHCb-INT-2013-004, CERN, Geneva, Feb, 2014.

[110] H. Behrens and J. Jänecke, *Numerical Tables for Beta-Decay and Electron Capture*, in *Landolt-Börnstein - Group I Elementary Particles, Nuclei and Atoms 4* (H. Schopper, ed.). SpringerMaterials, 1969. doi: 10.1007/b19939.

[111] *Appendix A: Compilation of Physical Data*, Journal of the ICRU **4** (2004), no. 2, 87.

[112] Hamamatsu Photonics K.K., Solid State Division, *C11208 series: Photon counting module with built-in TE-cooled MPPC*, September, 2011. Data Sheet.

[113] Newport Corporation, 1791 Deere Avenue, Irvine, CA 92606, USA, *818 Series Calibrated Photodiode Sensors*. Data Sheet.

[114] Nichia Corporation, 491 Oka, Kaminaka-Cho, Anan-Shi, Tokushima 774-8601, Japan, *Specifications for Nichia UV LED Model: NSHU590B*. Data Sheet.